

VILNIUS UNIVERSITY
FACULTY OF CHEMISTRY
DEPARTMENT OF PHYSICAL CHEMISTRY

VIDA KRIKŠTOLAITYTĖ

**DESIGN AND CHARACTERISATION OF THE ELECTRODES OF
ENZYMATIC BIOFUEL CELLS**

Doctoral Dissertation

Physical Sciences, Chemistry (03 P)

Vilnius, 2014

The dissertation was prepared at Vilnius University Faculty of Chemistry and Malmö University Faculty of Health and Society in the period of 2009 – 2013.

Scientific supervisor:

prof. habil. dr. Arūnas Ramanavičius (Vilnius University, Physical Sciences, Chemistry – 03P).

Scientific co-supervisor:

prof. dr. Tautgirdas Ruzgas (Malmö University, Physical Sciences, Biochemistry – 04P).

Contents

ABREVIATIONS.....	6
INTRODUCTION	8
1. LITERATURE REVIEW	13
1.1. Enzymatic biofuel cells	13
1.1.1. Operating principle	13
1.1.2. Key performance characteristics.....	14
1.1.3. Application niches	18
1.1.4. Demands and problems in the design of practically beneficial EFCs.....	20
1.1.5. Development perspectives.....	23
1.2. Redox enzymes.....	23
1.2.1. General structural properties.....	24
1.2.2. Main aspects of biocatalysis.....	24
1.2.3. Redox enzymes for glucose oxidation.....	27
1.2.4. Redox enzymes for O ₂ reduction.....	37
1.2.5. Peroxidase/oxidase based cathode.....	43
1.3. Design considerations of EBFC electrodes	46
1.3.1. Electron transfer mechanisms in redox enzymes	47
1.3.2. Mediated electron transfer based coupling.....	49
1.3.3. Direct electron transfer based wiring of redox enzymes.....	52
1.4. Gold nanoparticles	55
1.4.1. Synthesis of gold nanoparticles.....	56
1.4.2. Adsorption of redox enzymes on AuNP surface: improved bioelectrocatalysis...	58
1.5. Surface functionalization of a planar gold and AuNPs	60
1.5.1. A planar gold: an advantageous electrode material in EBFC design.....	61
1.5.2. Self-assembled monolayers of thiols	61
1.5.3. Polyelectrolyte films.....	63
1.6. Assembly of mono- and multi-layers of AuNPs on solid surfaces.....	64
1.6.1. DLVO theory: the role for NP stability and assembly.....	65
1.6.2. Drop-casting self-assembly	66
1.6.3. Layer-by-layer self-assembly.....	67
1.7. Characterisation of bioelectrocatalytic AuNP-enzyme nanostructures by E-QCM-D technique	72
1.7.1. QCM-D method: the principle.....	72

2. MATERIALS, EQUIPMENT, AND METHODS	76
2.1. Materials	76
2.1.1. Reagents.....	76
2.1.2. Solutions.....	78
2.1.3. Redox enzymes.....	78
2.2. Equipment.....	82
2.3. Methods	82
2.3.1. Synthesis of N-(6-mercapto) hexylpyridinium chloride	82
2.3.2. Synthesis of phenanthroline derivatives.....	82
2.3.3. AuNP synthesis.....	83
2.3.4. AuNP size estimation.....	84
2.3.5. AuNP ξ -potential estimation by electrophoretic light scattering	84
2.3.6. Enzyme homogeneous activity measurements	84
2.3.7. Electrode preparation	84
2.3.8. Evaluation of formed PTP layer by ATR-FTIR spectroscopy	88
2.3.9. Electrochemical measurements.....	88
2.3.10. E-QCM-D measurements and data analysis.....	90
2.3.11. Evaluation of kinetic constants characterising bioelectrocatalytic reduction of O ₂ at laccase modified AuNPs	94
3. RESULTS AND DISCUSSION.....	95
3.1. Enzymatic polymerisation of polythiophene by immobilised glucose oxidase	95
3.1.1. Dependence of $K_{m(app.)}$ and I_{max} values of GRE/GOx/PTP-modified electrodes on the duration of PTP polymerisation	95
3.1.2. ATR-FTIR evaluation of PTP formed by GOx and H ₂ O ₂ induced polymerisation... ..	98
3.1.3. Stability of GRE/GOx/PTP-modified electrodes	99
3.2 Evaluation of 1,10-phenanthroline derivatives as ET mediators for anodic biocatalyst glucose oxidase	102
3.2.1. Amperometric studies.....	102
3.2.2. Potentiometric studies.....	105
3.3. Development and characterisation of glucose powered EBFCs	106
3.3.1. Mediated glucose-powered EBFC based on anode and cathode modified by GOx	106
3.3.2. Mediator-less carbohydrate/O ₂ EBFCs with improved CDH based bioanode	111
3.4. Bioelectrocatalytic reduction of O ₂ by laccase at AuNP monolayers.....	125
3.4.1. Adsorption of PLL	127

3.4.2. Sequential adsorption of Lc, AuNPs, and Lc.....	128
3.4.3. Evaluation of kinetic constants of bioelectrocatalytic reduction of O ₂ at Lc modified AuNPs.....	134
3.5. Evaluation of physicochemical properties of mono-and multi-layers of AuNPs	138
3.5.1. MHP and PLL adsorption	139
3.5.2. Self-assembly of AuNP monolayers	140
3.5.3. Self-assembly of AuNP multilayers	144
3.6. Bioelectrocatalytic reduction of O ₂ by laccase differently incorporated into AuNP multilayers.....	145
CONCLUSIONS	149
LIST OF PUBLICATIONS AND CONFERENCE CONTRIBUTION	151
SUPPLEMENTARY INFORMATION	155
1. Synthesis and Characterization of N-(6-mercapto)hexylpyridinium (MHP)	155
1.1. General procedures.....	155
1.2. Synthesis of 2-(6-chlorohexyl)isothiuronium chloride (compound 1)	155
1.3. Synthesis of 6-chlorohexane-1-thiol (compound 2).....	156
1.4. Synthesis of N-(6-mercapto)hexylpyridinium chloride (compound 3).....	156
2. Evaluation of the QCM-D electrode working area by cyclic voltammetry.....	157
3. Surface concentration of nanoparticles: parameter λ	158
4. Δf - ΔD plot for the PLL- <i>Th</i> Lc-AuNPs- <i>Th</i> Lc film	159
REFERENCES	160
ACKNOWLEDGMENTS	185

ABREVIATIONS

5AP	5-amino-1,10-phenanthroline
AuNP(s)	Gold nanoparticle(s)
BFC(s)	Biofuel cell(s)
CP(s)	Conducting polymer(s)
<i>Ct</i> CDH	Cellobiose dehydrogenase from <i>Corynascus thermophilus</i>
CV	Cyclic voltammogram
DET	Direct electron transfer
EFBC(s)	Enzymatic biofuel cells
ET	Electron transfer
GRE	Graphite rod electrode
GO _x	Glucose oxidase
<i>Hi</i> CDH	Cellobiose dehydrogenase from <i>Humicola Insolens</i>
HRP	Horseradish peroxidase
K_m	Michaelis constant
LbL	Layer-by-layer
LSV	Linear sweep voltammogram
MHP	N-(6-mercapto) hexylpyridinium
<i>Mv</i> BO _x	Bilirubin oxidase from <i>Myrothecium verrucaria</i>
MW	Molecular weight
NHE	Standard (normal) hydrogen electrode
PDB	Protein data bank
PDs	Phenanthroline derivatives
pI	Isoelectric point
PLL	Poly-L-lysine
PMS	Phenazine methosulfate
PTP	Polythiophene
QCM-D	Quartz crystal microbalance with dissipation monitoring
RDE	Rotating disk electrode
RSA	Random sequential adsorption
SAM	Self-assembled monolayer

SEM	Scanning electron microscopy
<i>TaLc</i>	Laccase from <i>Trichaptum abietinum</i>
<i>ThLc</i>	Laccase from <i>Trametes hirsuta</i>
UHQ	Ultra high quality (water)

INTRODUCTION

Enzymatic biofuel cells (EBFCs) are a type of fuel cells that use purified redox enzymes as catalysts to convert chemical energy into electrical energy *via* biochemical reactions [1]. The use of highly substrate-specific and highly active redox enzymes as biocatalysts, the exploitation of cheap, renewable, and ecological biofuel oxidised at minimal overpotential, and mild EBFC reaction conditions raise a special interest and possibilities to employ EBFCs in very delicate niches such as implantable/attachable devices, e.g., implantable/attachable power sources and self-powered biosensors [2], and low energy consuming devices, e.g., small portable electronic devices [3]. Most prominent are so-called glucose/oxygen (O₂) powered EBFCs since glucose and O₂ are involved in metabolism of most living organisms, and thus these EBFCs might be used for biomedical purposes, e.g., self-powered biosensors in blood, tears, saliva, etc.

Despite the aforementioned advantages, the development of practically beneficial EBFCs is still challenging due to relatively low power output and short-term operational stability. Unlike abiotic FCs, which typically afford power densities in the order of mW cm⁻² to kW cm⁻² [4], EBFCs generate power densities in the order of μW cm⁻² to mW cm⁻² [5, 6]. It is also well addressed in scientific literature that portable EBFCs should approximately be stable in operation for at least one week or, in the case of a surgical procedure, for more than one year [3]. As reported in some research, the operational stability of EBFC electrodes may last for a few weeks or months [7] but not several years as it is required for the biomedical devices intended for implantation.

The general knowledge from the development of EBFCs is that in the majority of cases anodic electrodes limit the performance of overall carbohydrate/O₂ EBFCs [8]. Thus, the way to improve the characteristics of an overall EBFC is first the optimisation of the operation of an anodic part of the EBFC. For this reason, the main focus when designing carbohydrate/O₂ EBFCs has been devoted to study the bioelectrocatalysis on an anodic electrode. In this

work two quite different anodic enzymes considering many different aspects, i.e., glucose oxidase (GOx) and cellobiose dehydrogenase (CDH), have been chosen to design mediated and direct electron transfer (ET) based carbohydrate/O₂ EBFCs. GOx has been the first enzyme employed in EBFC design [9]. It demonstrates high catalytic activity and selectivity to glucose [10]. Unfortunately, its active center is located deep inside the insulating protein shell of the enzyme [11], and, thus, the electrons from the GOx cannot be transferred to the electrode surface *via* direct ET [12]. For this reason, different ET mediator molecules are employed to pick up the electrons from the redox centre of GOx and deliver them to an electrode [13]. Especially the usage of ET mediators, partly insoluble in aqueous solvents, should be emphasised, since they can be immobilised on an electrode in order to avoid their leaking from the electrode surface. ET mediator properties of five phenanthroline derivatives with different functional groups were investigated using GOx immobilised on graphite rod electrodes (Chapter 3.2.). While seeking the improvement of the stability of GOx-modified electrodes, the advantage of GOx catalysed enzymatic polymerisation of conductive polymers was taken. The GOx immobilised on the surface of the electrode is then covered by the thin layer of conducting polymer (Chapter 3.1.).

In comparison to GOx, CDH enzyme is an advantageous enzyme due to its broad spectrum of substrate, low sensitivity to O₂, and the ability of direct ET (DET). While a weakness of utilising CDH enzyme is the fact that glucose is not the natural substrate of the enzyme. Thus, the catalytic efficiency is significantly lower compared to GOx based EBFCs. However, the enzymes which are able to demonstrate DET in combination with differently prepared three-dimensional (3D) nanostructures have great perspectives in the area of biomedical applications.

Enzyme molecules arranged in 3D structures may not only increase the current density but also improve the apparent stability of EBFCs. In the present work negatively charged citrate-coated gold nanoparticles (AuNPs) were exploited as they are stable, electrically conductive, and biocompatible

building blocks for nanostructuring of surfaces. It is very important that for the careful fundamental studies of enzyme bioelectrocatalysis on a single AuNP level, the size, shape, and surface characteristics of AuNPs can relatively simply be controlled and monitored. As a model enzyme for these studies, the laccase (Lc) enzyme was employed since it shows DET on AuNPs, but not on planar gold surfaces. Moreover, it is a relatively cheap, widely studied enzyme, and its physicochemical properties are well characterised.

It should be pointed out that the basic principles of EBFCs and seeking to fulfil their stability and power demands have been under investigation for a while, and some progress has been achieved [14]. So far, the flexibility of EBFC electrodes has not been investigated at all and, thereby, in this work the very first studies addressing the flexibility problem have been performed. It is very important to be aware if EBFCs deposited, e.g., on catheters, withstand mechanical load as well as how does the flexibility correlate with the functionality of biomedical devices.

The objectives of the doctoral thesis were following:

1. to design carbohydrate/O₂ enzymatic biofuel cells (EBFCs);
2. to determine the factors limiting the performance of EBFCs;
3. to characterise the bioelectrochemical properties of the enzymes adsorbed onto conductive AuNP nanostructures and evaluate the viscoelasticity of the nanostructures.

Therefore, the tasks of the present thesis were formulated as follows:

1. to exploit carbohydrate oxidising enzymes (GOx, CDH) in the design of anodic electrodes;
2. to employ immobilised GOx enzyme for the enzymatic polymerisation of polythiophene;
3. to utilise O₂ and hydrogen peroxide reducing enzymes (bilirubin oxidase, horseradish peroxidase, and laccase) in the development of cathodic electrodes;

4. to develop mediated and direct ET based carbohydrate/O₂ EBFCs;
5. to assess the reactions and processes limiting the performance of separate anodic and cathodic electrodes;
6. to determine the number of the laccase molecules adsorbed on a single AuNP, as well as evaluate the kinetic constants characterising O₂ reduction on laccase-modified AuNP monolayers of different density;
7. to assemble the mono- and multi-layer nanostructures of AuNPs on planar thiol/polyelectrolytes modified gold surfaces while controlling the assembly by the ionic strength of AuNP dispersion;
8. to assess the viscoelastic properties of the nanostructures consisted of AuNPs using different inter-linker molecules (thiols, polyelectrolytes);
9. to compare the bioelectroreduction of O₂ at mono- and multi-layer structures of AuNPs modified with laccase enzyme.

Scientific novelty:

1. The very first enzymatic polymerisation of polythiophene was carried out using GOx immobilised on the surface of an electrode;
2. For the first time 1,10-phenanthroline derivatives (PDs) were employed as ET mediators for GOx enzyme. The best ET mediator, 5-amino-1,10-phenanthroline (5AP) compound, when cross-linked with GOx, was utilised in the design of the anodic electrode of a glucose/O₂ EBFC;
3. A positively charged bi-functional thiol, N-(6-mercapto) hexylpyridinium (MHP), for the first time was exploited to electrostatically attach the cellobiose dehydrogenase (CDH) enzymes from *Corynascus thermophilus* (CtCDH) and *Humicola insolens* (HiCDH) to the AuNP surface. This coupling enabled the DET between the enzymes and the AuNP modified gold surface;

4. The DET between the *Hi*CDH enzyme the surface of AuNPs was established for the first time. Accordingly *Hi*CDH was used as an anodic biocatalyst in the designing DET based carbohydrate (lactose, glucose)/O₂ EBFCs;
5. The evaluation of bioelectrocatalysis on a single laccase-modified AuNP was unprecedentedly performed when combining electrochemical methods and Quartz crystal microbalance with dissipation technique (E-QCM-D);
6. For the first time the QCM-D analysis was utilised to assess the viscoelastic properties of AuNP-enzymes based biocatalytic structures.

Statements for defence:

1. GOx enables enzymatic polymerisation of polythiophene *via* its catalytic cycle during glucose oxidation. PTP coated GOx enzyme demonstrates improved stability characteristics;
2. 5AP acts as an ET mediator for GOx enzyme, and can accordingly be exploited to design an anode of mediated glucose-powered EBFC when crosslinked with GOx;
3. MHP compound enables direct ET based coupling of CDH enzymes on the surface of AuNPs;
4. *Hi*CDH demonstrates the resistance to substrate inhibition by lactose. Thus, the enzyme might be employed as an anodic biocatalyst in the designing of EBFC operating in the presence of high carbohydrate concentration;
5. Combining electrostatically driven assembly of AuNPs on surfaces and E-QCM-D measurements enable the assessment of bioelectrocatalysis at a single Lc modified AuNP. The bioelectrocatalysis at a single NP depends on the surface density of NPs;
6. PLL/AuND based multilayer is a highly conductive nanostructure suitable for DET based immobilisation of Lc enzyme.

1. LITERATURE REVIEW

1.1. Enzymatic biofuel cells

Fuel cells are electrochemical devices which convert chemical energy into electrochemical energy *via* chemical reactions [4]. Biofuel cells (BFCs) are a type of fuel cells that use biocatalysts instead of inorganic or organic, i.e., metal and carbon, catalysts to catalyse chemical reactions [15]. Three types of biocatalysts can be employed in BFC design: complete living cells [16], purified enzymes [8], and organelles [17]. This work was solely focused on the studies of enzyme catalysed so-called enzymatic biofuel cells (EBFCs) including the design and characterisation of their separate electrodes.

1.1.1. Operating principle

To ensure a high reaction velocity of oxidation-reduction reactions at EBFC electrodes, oxidoreductases (redox enzymes) are used in the electrode construction. Redox enzymes usually catalyse biochemical oxidation-reduction reactions in a very selective manner and, thereby, extract electrical energy from a very specific biological compounds [18]. In some cases redox enzymes can be employed in multi-enzyme cascades together with enzymes belonging to other classes in order to extract electrical energy from more complex substances [19].

Like a traditional abiotic fuel cell [4], an EBFC is a galvanic cell consisted of two electrodes: an anode and a cathode. At the anode biofuel oxidation occurs and the electrons, extracted during this process, are provided to the electrode. On the contrary, at the cathode biooxidant reduction takes place and the electrons, consumed during the reaction, are taken from the electrode (Fig. 1) [15, 20, 21]. When EBFC electrodes are immersed in an electrolyte solution, containing a certain amount of biofuel and biooxidant, and connected through an external circuit, electrons flow from the anode to the cathode and thus generate electrical power [15].

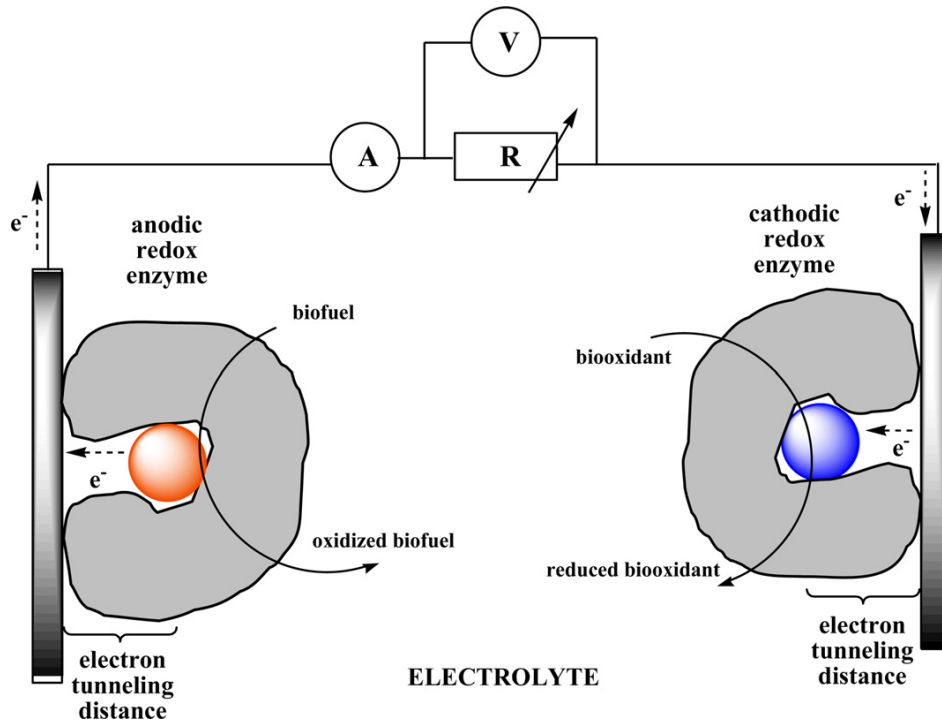


Figure 1. General scheme of the operating principle of an EBFC. Adopted from [20].

Any substance which is oxidised by a living organism, e.g., various carbohydrates, amino acids, alcohols, etc., can be utilised as a biofuel since it is obvious that a certain enzyme (or even a few enzymes) catalysing oxidation of each specific compound must exist, while O_2 and peroxides are usually exploited as a biooxidant [1].

Most prominent are so-called glucose/ O_2 powered EBFCs since both glucose and O_2 are involved in metabolism of most living organisms, and, thus, these EBFCs might be used for biomedical purposes, e.g., self-powered biosensors in blood, tears, saliva, etc.

1.1.2. Key performance characteristics

The prime parameter which is considered in EBFC design is power output. The power output (P_{cell}) of an EBFC is directly proportional to the current achieved at different cell voltages and thus is calculated after multiplying the values of the current (I) and the EBFC voltage (U_{cell}). These parameters are experimentally obtained from so-called EBFC polarisation curve [22]:

$$P_{cell} = U_{cell} \times I \quad (1)$$

The power output is often divided by the surface area (A) of an EBFC electrode in order to uniformly characterise the performance of EBFCs:

$$\text{Power density} = \frac{P_{\text{cell}}}{A} \quad (2)$$

A polarisation curve is a plot of potential as a function of the current (or the current density) generated by the EBFC while altering external electric load or *vice versa*. This means that polarisation curves can either be recorded potentiostatically (an external potential is changing) or galvanostatically (an external current is varying). Polarisation curves themselves are used for better understanding of the limitations (later denoted as overvoltage losses) of EBFCs such as enzyme kinetics, internal resistance drop, mass transport (Fig. 2a), etc., while their recalculation to power curves enables the estimation of the maximal power (or power density) of EBFCs (Fig. 2b) [23].

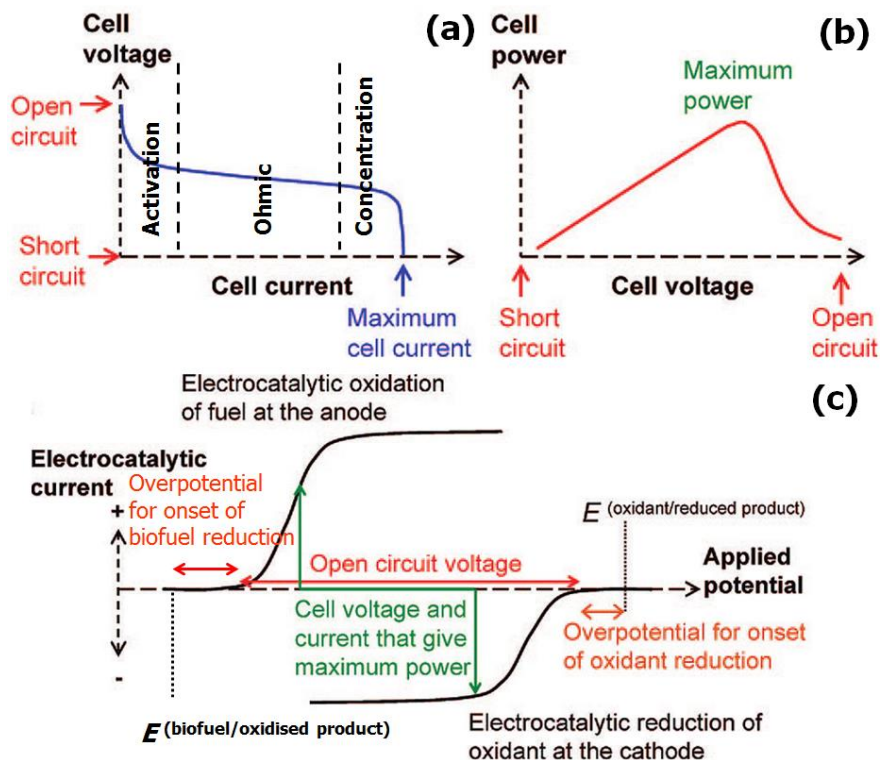


Figure 2. Different ways for plotting the data of EBFC performance characteristics: (a) polarisation curve (current-voltage) of the complete EBFC with the different polarisation types indicated; (b) power curve vs. cell voltage; (c) polarisation curves of individual EBFC bioelectrodes. Adopted with changes from [1].

The highest voltage in a polarisation curve, termed open-circuit voltage (OCV), is achieved at *open circuit* conditions when there is no current flow (no work is done) in an external circuit. OCV provides the information about thermodynamics of an EBFC. The OCV value for a particular EBFC is experimentally determined by the difference between the onset potential for biocatalysis at the cathodic and anodic electrodes, respectively (Fig. 2c) [1]. Theoretically the voltage (or the OCV in the case of *open circuit* conditions) of a cell is defined as the difference between thermodynamic potentials of the biooxidant/reduced product redox couple at a cathode and biofuel/oxidised product redox couple at an anode, adjusted to all nonstandard conditions of EBFC operation:

$$U_{cell} = E_{cathode} - E_{anode} \quad (3)$$

However, the experimentally estimated value of U_{cell} is usually lower than that theoretically expected as the result of overpotential at separate EBFC electrodes.

Thereby, the overpotential (η) of individual electrodes can be described as the difference between the experimentally measured potential ($E_{measured}$) and the equilibrium ($E_{eq.}$) potential [22]:

$$\eta = E_{measured} - E_{eq.} \quad (4)$$

The equilibrium potential is in turn related to the formal potential ($E_{eq.}^0$) for a redox couple according to well-known Nernst equation [24]:

$$E_{eq.} = E_{eq.}^0 + \frac{RT}{nF} \ln \left(\frac{c_O}{c_R} \right) \quad (5),$$

where R denotes the universal gas constant ($8.314 \text{ J mol}^{-1} \text{ K}^{-1}$), T stands for the absolute temperature (K), n is the number of electrons involved in a reaction, F denotes the Faraday constant (96485.4 C), c_O and c_R are the concentrations of oxidised and reduced species (M).

There are three types of η contributing to the total overvoltage (η_{total}) across an EBFC, i.e., activation (η_{act}), ohmic (η_{iR}), and concentration (η_{conc}) [15]:

$$\eta_{total} = \eta_{act} + \eta_{iR} + \eta_{conc} \quad (6)$$

Each type of η contributes to the overall shape of a polarisation curve for an EBFC, as illustrated in Fig. 2a. η_{act} predominantly arises at low current due to a finite rate of reaction at an electrode which is determined by the rate of heterogeneous ET. η_{iR} , called either ohmic or internal resistance drop, describes the polarisation that occurs in an EBFC at higher current due to resistances associated with the electrolyte and electrical connections. And, finally, η_{conc} describes the mass transport limitations of a bioelectrochemical reaction and it is the predominant contributor to electrode polarisation at large currents. For bioelectrochemical reactions that proceed with small activation overpotentials, the concentration of reagent at the surface of the electrode rapidly approaches zero [15].

Many redox enzymes, when comparing with metal catalysts, operate very close to the thermodynamic potential of their substrate/product couple having minimal η . Yet some enzymes demand a larger η than others to catalyse the same reaction. For example, the reduction of O₂ by plant laccases [25] requires several hundred mV larger η than fungal laccases [26]. The former are less advantageous biocatalysts to use them in EBFC design since they lower the value of U_{cell} of a complete EBFC.

When anodic and cathodic electrodes are fully electrically connected through so-called *short circuit* without an applied load, U_{cell} is equal to zero, and no useful work is performed. Thereby, significant power output may be achieved only when an EBFC operates between two limiting cases of an EBFC polarisation curve, i.e., between *open* and *short circuit* conditions, when U_{cell} is between OCV and 0 (Figs. 2a and 2b).

In conclusion, the maximum power density and thus current density as well as the OCV describe the performance of an overall EBFC. The operational stability of an EBFC should also be considered as an important parameter since it describes the viability of an EBFC.

1.1.3. Application niches

The use of highly substrate-specific and highly active redox enzymes as biocatalysts, the exploitation of cheap, renewable, and ecological biofuel oxidised at minimal overpotential, and mild EBFC reaction conditions raise the special interest and possibilities to employ EBFCs in very delicate niches such as implantable/attachable devices, e.g., implantable/attachable power sources and self-powered biosensors [2], and general low energy consuming devices, e.g., small portable electronic devices [3].

Specifically, the general requirement for all above mentioned devices is the miniaturisation of their electric power source as it constitutes the biggest part (size and weight) of complete devices. This is only possible to accomplish using EBFCs since redox enzymes are usually characterised by very high substrate-selectivity and thus EBFC construction does not necessitate separating anodic and cathodic parts. The absence of a separation membrane automatically leads to the diminution in the EBFC size. Other electric power sources such as abiotic FCs or batteries do not comply with the requirements of further reduction in device size because: (i) conventional FCs do not provide sufficient substrate selectivity (e.g., one of the most widely used metal catalyst platinum catalyses both glucose oxidation and O₂ reduction, thereby, glucose and O₂ must be supplied in separated containers to make the oxidation process solely possible on one electrode and the reduction process, respectively, on another), (ii) batteries are closed electrochemical systems having electrolyte storage containers and thus the energy capacities of batteries do not scale with size due to the need for casings and seals.

Also, enzymes are attractive biocatalysts due to their ability to utilise abundant biological fuels (e.g., glucose) along with ubiquitous O₂ as a biooxidant and operate in physiological conditions, where conventional FCs are inefficient. Thereby, EBFCs as self-contained devices, i.e., self-powered and wireless gadgets, might be integrated into biologically relevant technologies or products, e.g., as monitoring devices in cell culture applications, in food

storage and manufacture technologies, as well as attached to or implanted in living organisms for different purposes, viz., sensing, stimulation, delivery, etc.

Moreover, EBFCs might power small portable electronic devices in *on site* conditions, e.g., by simply refuelling with lemonade or any other carbohydrate containing solution, if carbohydrate/O₂EBFC was integrated as a power source. In 2010 Sony company reported a glucose/O₂ EBFC unit with multi-stacked structure which successfully operated a radio-controlled car (16.5 g) as well as in the memory-type Walkman (Fig. 3a). [27].

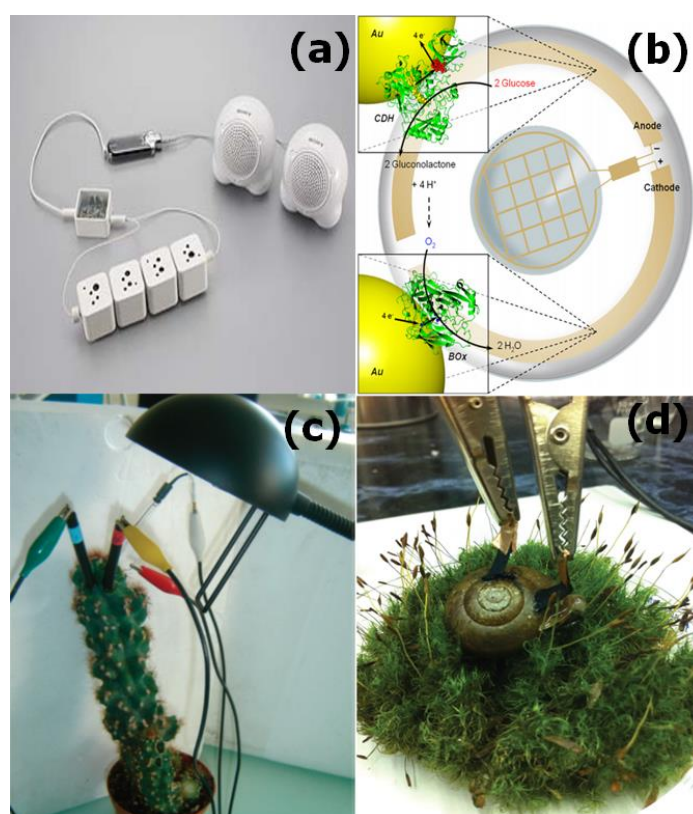


Figure 3. Some examples of EBFCs as a part of (a) a mp3 player [28] and (b) contact lense [29], or inserted in (c) a cactus [30] and snail [31]

Taking advantages of EBFC properties, EBFCs were inserted and tested in rats [32], cockroaches [33], clams [34], snail [31] (Fig. 3) or lobsters [35]. Katz and co-workers demonstrated that EBFCs connected in series or in parallel deliver enough power to supply an electric motor [34] and a cardiac pacemaker [35]. Flexer and Mano attached EBFC electrodes to a cactus in order to monitor photosynthesis process (Fig. 3) [30]. In light of these

examples, one of the promising EBFC application niches seems to be their use in non-invasive contact situations e.g., contact lenses [29], where most of *in vivo* shortcomings (immunoresponse, etc) are evaded (Fig. 3).

There are some more merits of EBFCs which make their use advantageous over the employment of abiotic FCs and batteries. For example, enzyme production is renewable and relatively inexpensive when comparing with the high cost and future scarcity of noble metals employed as catalysts in most of FC devices. Also, redox enzyme themselves and the products of enzymatic reactions can be considered as relatively safe in implantable situations as well as being ecologically disposable, while batteries cause ecological problems due to the toxicity of their waste if disposed improperly.

In summary, EBFCs are not yet used in everyday applications, but this may change in the future if EBFCs having better performance characteristics, such as power density and operational stability, are developed.

1.1.4. Demands and problems in the design of practically beneficial EFCs

Despite the aforementioned advantages, the development of practically beneficial EBFCs is still challenging due to relatively low power output and short-term operational stability. Unlike abiotic FCs, which typically afford power densities in the order of mW cm^{-2} to kW cm^{-2} [4], EFCs generate power densities in the order of $\mu\text{W cm}^{-2}$ to mW cm^{-2} (Fig. 4) [5, 6]. Even though the power output provided by already existing EBFCs is sufficient to power some small low-energy consuming electronic devices, if generated at a high enough cell voltage, there is still the deficiency in power output to use EBFCs in more general applications demanding power output of $10\text{-}100 \text{ mW cm}^{-2}$ [3, 22].

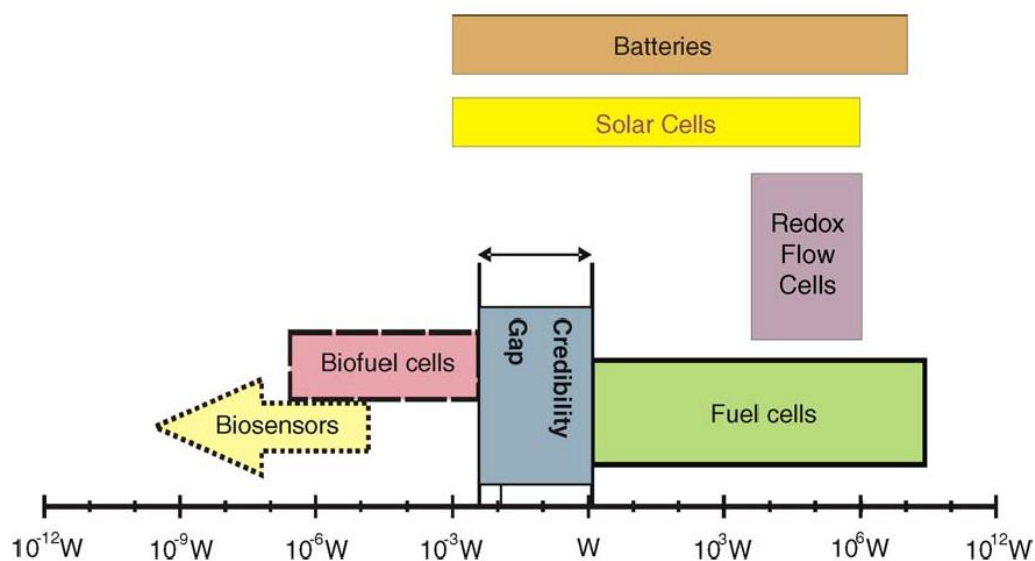


Figure 4. Schematic representation of the power ranges provided by biosensors, biofuel cells, inorganic FCs and batteries showing the free room for further EFC development. Adopted from [22].

It is also well addressed in scientific literature that portable EBFCs should approximately be stable in operation for at least one week or, in the case of a surgical procedure, for more than one year [3]. As reported in some research articles, the operational stability of EBFC electrodes may last for a few weeks or months [7] but not several years as it is required for implantable biomedical devices.

In order to improve the performance of EBFCs and their operational stability, several potent factors should be considered. First of all, the biocatalytic activity and stability of enzymes bound to the surface of EBFC electrodes should be high enough. Secondly, the electron transfer (ET) between the enzyme active centre and electrically conducting electrode materials should be rapid. These two considerations can be only useful if a high quantity of enzyme molecules can be immobilised on the electrode surface. However, the majority of redox enzymes are unable to achieve efficient direct ET (DET) between their active centre and a planar electrode surface as their redox centres are deeply imbedded in their protein shells [36]. This means that only a limited number of enzymes are available for the construction of direct ET based EBFCs. Moreover, even though enzymes are capable of very high activity in

comparison to conventional metal or carbon catalysts, generally reaching catalytic turnover numbers of 10^3 s^{-1} or higher [37], they are usually rather large molecules which results to low activity to volume ratio. The maximal theoretically possible current density which might be achieved assuming the complete monolayer coverage by fully active and properly connected enzyme molecules of 58 nm^2 cross section with an activity of 600 s^{-1} , is only in the range of $200 \mu\text{A cm}^{-2}$ as stated by Katz [38]. Thereby, multilayers of enzymes are likely to be demanded in order to increase the current density. Enzyme molecules arranged in three-dimensional structures may also increase the apparent stability of EBFCs. All these improvements are possible if the maximal current density of an EBFC is limited by the enzyme kinetics. In the case, when the high amount of enzyme is immobilised, the maximal current density is limited by substrate diffusion rather than enzyme kinetics, and thus some enzyme molecules can detach from the electrode surface or lose their catalytic activity without changing the magnitude of the maximal current density. Additionally, the relatively high values of Michaelis constant (K_m) of carbohydrate oxidising enzymes (often greater than 10 mM, Chapter 1.2.3.), do not allow the maximal turnover of enzyme to be exploited, especially considering *in vivo* conditions where low substrate concentration is present. For example, the concentration of glucose in human blood is approximately 5 mM [39] or even lower in other human physiological fluids such as saliva ($\sim 0.08 \text{ mM}$) [40] and tears (0.001-0.005 mM) [41]. This means that the active sites of glucose oxidising enzymes are not substrate saturated by the levels of glucose available in human physiological fluids. O_2 powered cathodic biocatalysts are characterised by quite high K_m value as well.

An incomplete biofuel oxidation is another important problem from a power-density perspective. The complete oxidation of glucose molecule to water and CO_2 with a release of 24 electrons involves around 10 enzymes which carry out particular chemical transformations [42]. When one enzyme, e.g., glucose oxidase, is employed for partial glucose oxidation, only two electrons are extracted from one glucose molecule. Thereby, multi-enzyme

cascade based EBFCs holds a great perspective in the designing of EBFCs with enhanced power output [6].

It should be pointed out that the basic principles of EBFCs and seeking to fulfil their stability and power demands have been under investigation for a while, and some progress has been achieved [14]. So far, the flexibility of EBFC electrodes has not been investigated at all and, thereby, in this work the very first studies addressing the flexibility problem have been performed. It is very important to be aware if EBFCs deposited, e.g., on catheters, withstand mechanical load as well as how does the flexibility correlate with the functionality of biomedical devices.

1.1.5. Development perspectives

The continuous interest in EBFC development is motivated by the fact that there are many enzymes capable of all sorts of chemical transformations in a variety of conditions, and that most of them are yet to be discovered and exploited for energy conversion. Further, as genomics and proteomics become more sophisticated, one can expect that the ability to engineer enzymes for power generation will also improve [43]. Moreover, new electrode materials are recently being rapidly developed as well as rational ways to electrically connect enzymes to electrodes [44]. Finally, the knowledge gained from research on EBFCs is important from a purely scientific perspective in order to understand how activity and stability of enzymes can be controlled by the interface between the adsorbed enzyme and the surface.

1.2. Redox enzymes

Oxidoreductases, often abbreviated to redox enzymes, are a large class of enzymes catalysing oxidation-reduction reactions in microbial, plant or animal organisms where electrons are selectively transferred from one biological molecule (a reductant) to another (an oxidant) [18, 45]. Replacing the oxidant molecule by an anodic electrode and the reductant molecule accordingly by a cathodic electrode, redox enzymes, thereby, can be employed in EBFC development. So far, there are about 1500 enzymes referred to

oxidoreductases (<http://www.enzyme-database.org/stats.php>), yet only a small fraction of them can successfully be utilised as EBFC biocatalysts due to the difficulty to achieve sufficient (if at all) electrical contact between their redox active centre and the electrode surface.

1.2.1. General structural properties

Generally enzymes are rather large globular protein molecules formed by a polypeptide chain which is a consecutive sequence of interlinked amino acids. To accomplish their biocatalytic activity, redox enzymes employ various redox-active centres [46]. The redox centres are shielded by the polypeptide backbone which can modulate their substrate-selectivity, catalytic activity, stability, and inhibition-resistance. Common redox centres include particular amino acids (e.g., tyrosine or cysteine) and non-proteinaceous part so-called cofactor which can either be classified as organic (e.g., FAD) or inorganic (e.g., metal ions) [18]. Cofactors tightly bound to enzymes are called prosthetic groups, while those loosely bound to enzymes and releasing from redox centres during the catalytic reaction are referred to coenzymes. The intact active enzyme with its cofactor is called a holoenzyme, while solely protein part without cofactor is called an apoenzyme [37].

1.2.2. Main aspects of biocatalysis

On the whole, some enzymes catalyse one-substrate enzymatic reactions accordingly yielding one product and the native enzyme, while others catalyse more than one substrate enzymatic reactions *via* more complex biocatalytic mechanisms accordingly releasing more than one product. Specifically, redox enzymes catalyse redox reactions including two substrates and thus produce two products *via* two possible mechanisms: sequential or non-sequential. In the sequential mechanism, both substrates bind to the enzyme (in a certain order or randomly) and the reaction proceeds releasing two products from the enzyme. Whilst, in the non-sequential mechanism, also known as the Ping-Pong mechanism, the second substrate does not bind to the enzyme before the first product is dissociated. The enzyme changes its characteristics (e.g., oxidation

state, conformation) during the reaction with the first substrate, and recovers its native state after the reaction with the second substrate (Fig. 5) [37]. Thereby, the enzyme is involved in the reaction but not consumed.

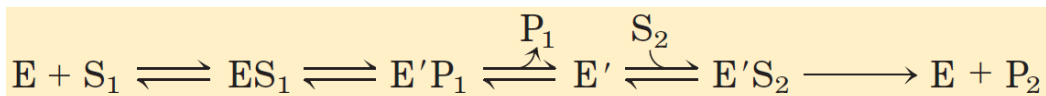


Figure 5. Schematic representation of a Ping-Pong mechanism. E and E' denote the native and the intermediate state of an enzyme, S_1 and S_2 stand for the first and the second substrate, P_1 and P_2 define the first and the second product.

All the redox enzymes studied in this thesis catalyse redox reactions *via* Ping-Pong mechanism (Chapters 1.2.3.-1.2.5.).

The rate of a simple one-substrate enzymatic reaction, that is, the rate of product formation (v) is described by well-known Michaelis-Menten equation:

$$v = v_{max} \frac{[S]}{K_m + [S]} = (7),$$

where, v_{max} is the maximal rate of enzymatic reaction ($M \text{ min}^{-1}$), $[S]$ stands for the substrate concentration (M), and the K_m is the Michaelis constant representing the substrate concentration at which the reaction rate is a half of v_{max} (M).

The initial enzymatic reaction rate increases with increasing substrate concentration as long as it achieves the maximal value when all enzyme molecules are saturated by substrate molecules, that is, under conditions when the enzyme concentration is much lower than the substrate concentration (Fig. 6).

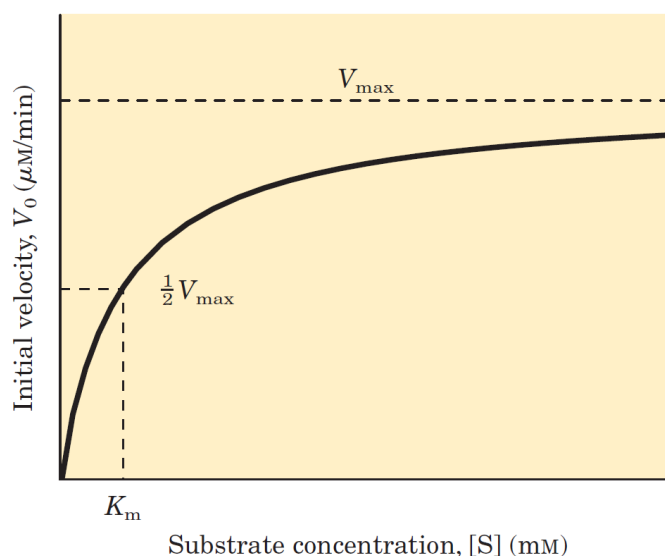


Figure 6. Dependence of an enzymatic reaction on substrate concentration. Adopted from [31].

Thereby, the maximal rate is directly proportional to the enzyme concentration and the rate constant limiting the whole enzymatic reaction which is generally denoted as a reaction rate limiting constant k_{cat} :

$$v_{max} = k_{cat} \times [E] \quad (8)$$

The constant k_{cat} is a first-order rate constant and hence has units of reciprocal time (s^{-1}). It is also called the turnover number. It is equivalent to the number of substrate molecules converted to product per second on a single enzyme molecule when the enzyme is saturated with a substrate [37].

The rate equation for the enzymatic reactions including two-substrate binding *via* the Ping-Pong mechanism is more complicated and expressed as follows:

$$v = \frac{v_{max}}{\frac{K_m^{S_1}}{S_1} + \frac{K_m^{S_2}}{S_2} + 1} \quad (9),$$

where $K_m^{S_1}$ and $K_m^{S_2}$ are Michaelis constants for the first and second substrate, respectively.

However, in the case when the saturation concentration for one of the two substrates is achieved, the enzyme catalysed redox reaction can be simply described by the former Michaelis-Menten equation (Eq. 7).

1.2.3. Redox enzymes for glucose oxidation

The most common and intuitive biofuel for EBFCs is glucose due to its high abundance in nature and essential role in human metabolism. It is an aldohexose carbohydrate and from the two stereoisomers only the dextrorotatory (D-glucose) is biologically active. Glucose is involved in the glycolysis metabolic pathway, where it is oxidised to pyruvate, which further enters the citric acid cycle. Eventually, after series of chemical transformations with a release of energy, glucose is broken down to CO₂ and water [47].

Most glucose-oxidising enzymes target the C1 hydroxyl group of β-D-glucopyranose (hereafter referred to simply as ‘glucose’, Fig. 7), liberating two electrons and forming D-gluconolactone which spontaneously hydrolyses to D-gluconate.

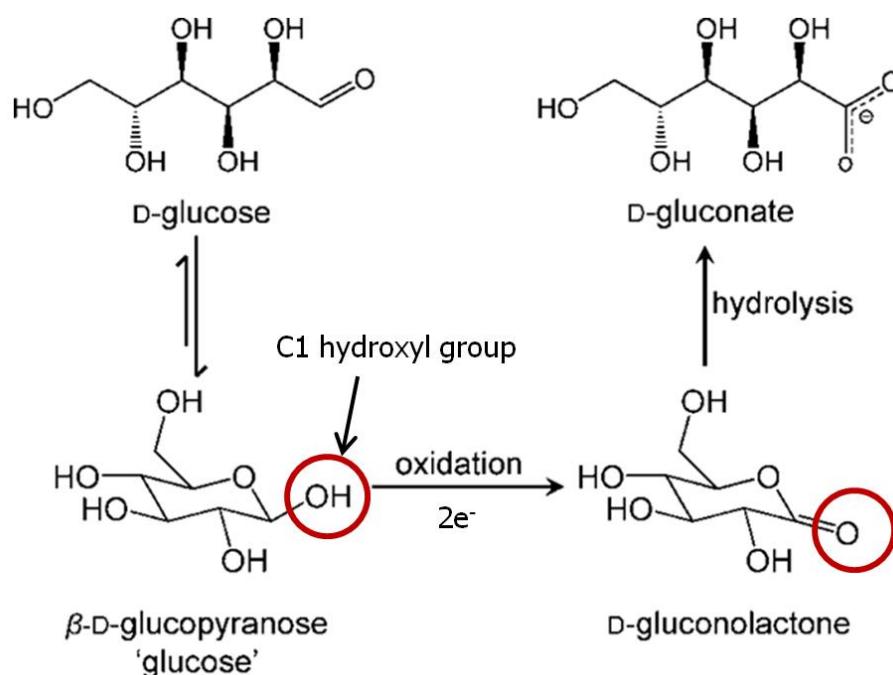


Figure 7. Biologically relevant forms of D-glucose and its oxidised product D-gluconolactone. Adapted with changes from [1].

The oxidation reaction of glucose is catalysed by a range of oxidase and dehydrogenase enzymes that differ in their cofactors and natural electron acceptors (Table 1). Enzymes using O₂ as the electron acceptor are classified as oxidases, whereas those using another acceptor, such as a heme-based protein (cytochrome), are classified as dehydrogenases.

Table 1. Enzymes catalysing the oxidation of glucose.

Enzyme	EC Number	Cofactor	Half-Cell Reaction
Glucose oxidase (GOx)	1.1.3.4	FAD	Glucose \rightarrow glucono- δ -lactone + 2H ⁺ + 2e ⁻
Glucose dehydrogenase (GDH)	1.1.1.47	NAD	See above
Glucose dehydrogenase (GDH)	1.1.5.2	PQQ	See above
Cellobiose dehydrogenase (CDH)	1.1.99.18.	FAD, heme	See above

Below, the particular glucose oxidising enzymes, which were investigated in this work, are discussed with the purpose of giving the understanding of their biological, structural, and electrochemical nature.

1.2.3.1. Glucose oxidase

Glucose oxidase (GOx), β -D-glucose:O₂ 1-oxidoreductase; EC 1.1.2.3.4, is an extracellular flavoprotein, naturally found in many sources such as red algae [48], citrus fruits [49], bacteria [50], insects (e.g., bees) [51], and fungi (e.g., *Aspergillus* and *Penicillium*) [52, 53], etc. The main biological function of GOx is the protection against bacterial and fungal pathogens through the production of peroxide as the result of its catalytic activity (Eqs. 10-11) [54]. In this work the fungal GOx from *Aspergillus niger* was used.

While playing still not well appreciated role in the nature, GOx has become a very important enzyme in the biotechnology industry [54]. It has been the first enzyme employed in EBFC design [9], and it is further widely

employed in the development of glucose biosensors and EBFCs due to its long-term stability when immobilised [55] as well as high catalytic activity and selectivity to glucose [10]. Moreover, GOx production is cheap since the effective recombinant technology to produce the enzyme using microorganisms, specifically yeast from *Saccharomyces cerevisiae*, has been developed [56].

GOx from *Aspergillus niger* is a homodimer of around $5 \times 6 \times 8$ nm consisting of two identical 80 kDa subunits, each containing a flavin adenine dinucleotide (FAD) as a prosthetic group [11]. The enzyme, like many extracellular proteins, is highly glycosylated and contains approximately 16 % of neutral sugar and 2 % of amino sugars [57]. GOx also contains 3 cysteine residues and 8 potential sites for N-linked glycosylation [58]. The crystal structure of GOx monomer as well as oxidised (native) and reduced forms of the cofactor FAD, which is responsible for the catalytic function of GOx, are shown in Fig. 8.

GOx catalyses the oxidation of β -D-glucose to D-glucono- δ -lactone while the fused ring structure of flavin mononucleotide (the isoalloxazine ring) is undergoing reversible reduction, thus a hydrogen atom is being bound to each of the two doubly bound nitrogen in the flavin group (Fig. 8b and Eq. 10). Then reduced GOx recovers its native (oxidised) form using molecular oxygen as an electron acceptor (Eq. 11), and D-glucono- δ -lactone spontaneously hydrolyses to gluconic acid (Eq. 12) [59].

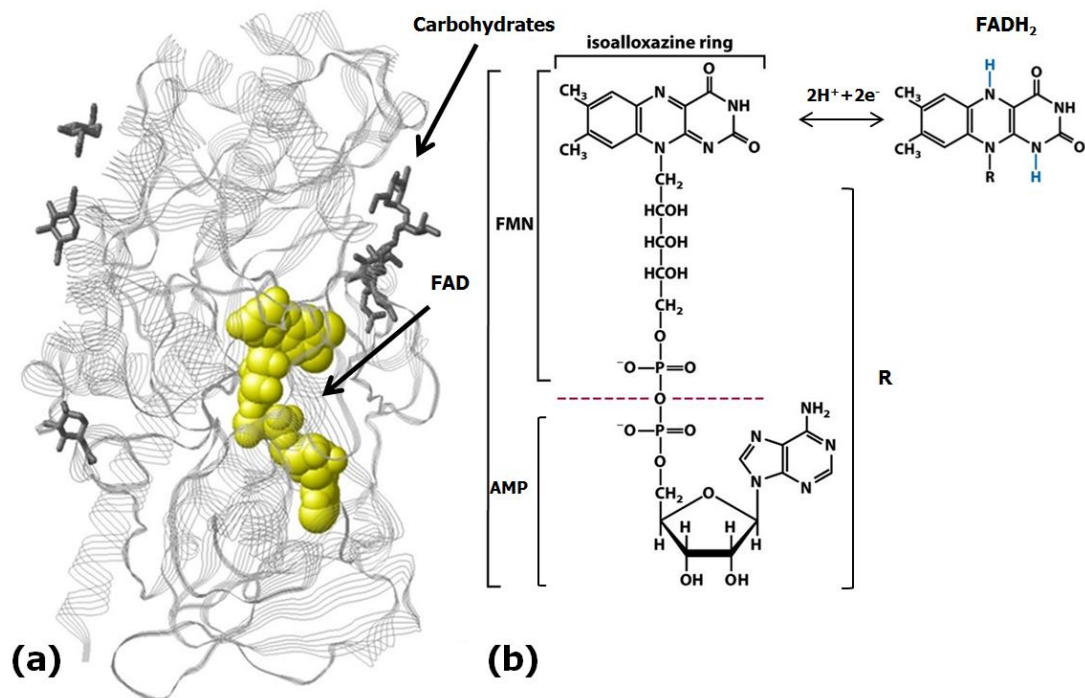
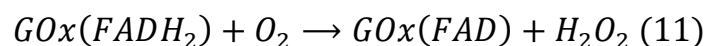
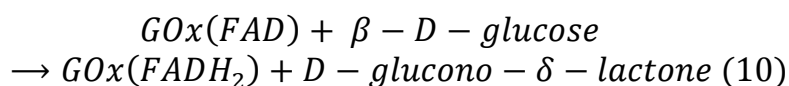
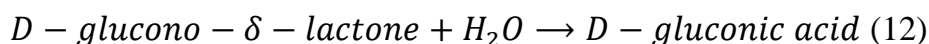


Figure 8. (a) Crystal structure of the monomer of the GOx from *Aspergillus niger* (PDB ID: 1CF3) [11]. The proteinaceous backbone is shown as light grey ribbons, the carbohydrates are represented as dark grey sticks, and cofactor FAD is depicted as yellow spheres. Abbreviations: FAD - flavin adenine dinucleotide, FMN - flavin mononucleotide, AMP - adenosine monophosphate. (b) Molecular structure of FAD including its oxidised and reduced forms.

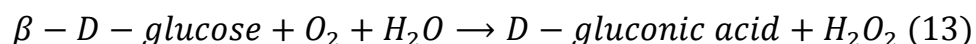
Catalytic reactions:



Spontaneous non-catalytic reaction:

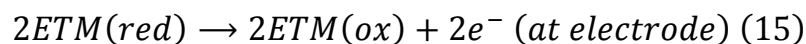
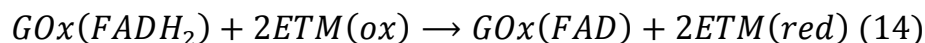


Overall reaction:



The FAD cofactor is located deep inside the insulating protein shell of the enzyme [11]. Thus, the electrons from the reduced FAD cannot be transferred to the electrode surface *via* DET [12]. For this reason, different ET mediator molecules, such as ferrocene derivatives, can be employed to pick up the

electrons from the redox centre of GOx and deliver them to an electrode [13]. In such electrode designs, glucose oxidation reaction (Eq. 10) is followed by redox reactions:



where ETM(ox) and ETM(red) are oxidised and reduced forms of ET mediator.

Different strategies for the immobilisation of RMs on the surface of electrodes have been used to prevent the diffusion of RMs in a solution, i.e., their leaking out from the enzyme-electrode interface. For example, RMs were attached to osmium polymers [60], conducting polymers such as polypyrrole [61] or directly connected to the electrode surface *via* bi-functional binding agents [38].

Considering the possibility to use the GOx enzyme in the designing of implantable EBFCs, it is important to keep in mind that the optimal conditions for the catalytic activity of GOx differ from those existing, e.g., in human blood. Specifically, the concentration of glucose and NaCl in human blood is approximately 5 mM and 150 mM, respectively, and pH is around 7.4 [39]. While GOx has an optimal pH of 5-6 [62], is specific for β -D-glucose with a K_m of 33-110 mM [59, 63] and can be inhibited by halide ions, but with a much higher effect at lower pHs [64].

1.2.3.2. Enzymatic polymerisation of conducting polymers by GOx: polythiophene synthesis

Polythiophene (PTP) is composed of thiophene molecules, which are 5-membered heterocyclic compounds with sulphur as a heteroatom. Investigation related to the preparation of PTP compounds and the characterisation of their electrochemical properties has intensified only during the last few decades [65, 66].

PTP can be synthesised by means of photoinduced [67], chemical [68] or electrochemical [69] synthesis. In electrochemical polymerisation, a potential is applied across a certain electrolyte solution containing thiophene,

producing a conductive PTP film on the anode. During electrochemical synthesis thin and predictable polymer layer forms on the electrode surface but the conditions of the reaction (strongly acidic solution, high monomer concentration, high potential of polymerisation reaction initiation) might have a negative influence on the enzyme conformation, which is entrapped within the PTP layer, formed during this polymerisation reaction [70, 71]. On the other hand, chemical synthesis is superior owing to a wider choice of monomers and using certain catalysts, as it is possible to synthesise less branched polymers. Some examples of oxidisers initiating polymerisation of PTP are FeCl_3 , H_2O_2 , CuClO_4 , etc. [72, 73]. It is possible to entrap a variety of molecules into the PTP-based layer in order to change its parameters, such as electrical conductivity [74]. Owing to the diffusional permeability of the polymer, a decent substrate and product mobility towards/outwards the enzyme is retained. Consequently, the resulting PTP polymer layers serve as an excellent basis/matrix to design stable and electrochemically effective biosensors or biofuel cells. However, it is impossible to obtain reproducible thin polymer layers by chemical synthesis, since during this process amorphous polymer suspension is formed [75].

In order to avoid problems, which occur during electrochemical and chemical PTP synthesis, an excellent alternative method is enzyme catalysed polymerisation. This simple technique does not require a highly acidic medium, strong oxidising agent and, the enzyme acts as a catalyst for the polymerisation reaction. Enzymatic synthesis also allows the control of regioregularity and stereochemistry of the resulting polymer [76]. Enzymatic polymerisation has been proven by polypyrrole and polyaniline synthesis using horseradish peroxidase [77-80], laccase [81, 82], soybean peroxidase [83], royal palm tree peroxidase [84] and GOx [85, 86], enzymes, which mostly catalyse the generation of respective monomer free radicals. These free radicals undergo coupling to produce dimers. Successive oxidation and coupling reactions lead to a polymer formation. In previous studies an advantage of the enzymatically by glucose oxidase (GOx) produced hydrogen

peroxide to polymerise aniline and pyrrole in a broad pH conditions ranging from 2.0 to 9.0 was taken [85-90].

In the dissertation environmentally friendly *green* PTP synthesis was applied since no hazardous oxidisers and/or polymerisation initiators were exploited for the initiation of polymerisation reaction. Polymerisation solution used for the coating of graphite rod electrodes (GRE) with adsorbed GOx by PTP layer was composed of three main components: thiophene, glucose and dissolved O₂. GOx immobilised on a GRE catalysed oxidation of glucose by O₂, while gluconolactone (Eq. 10) and hydrogen peroxide (Eq. 11) were produced. Then, glucono-1,5-lactone was hydrolysed to gluconic acid (Eq. 12). Owing to the formation of these compounds, solution pH near the surface of immobilised enzyme decreased, while hydrogen peroxide gradient increased. These conditions favoured the formation of PTP film in close proximity to the electrode surface and, thereby, covering the GOx adsorbed on the GRE surface with a thin polymer layer (Fig. 9).

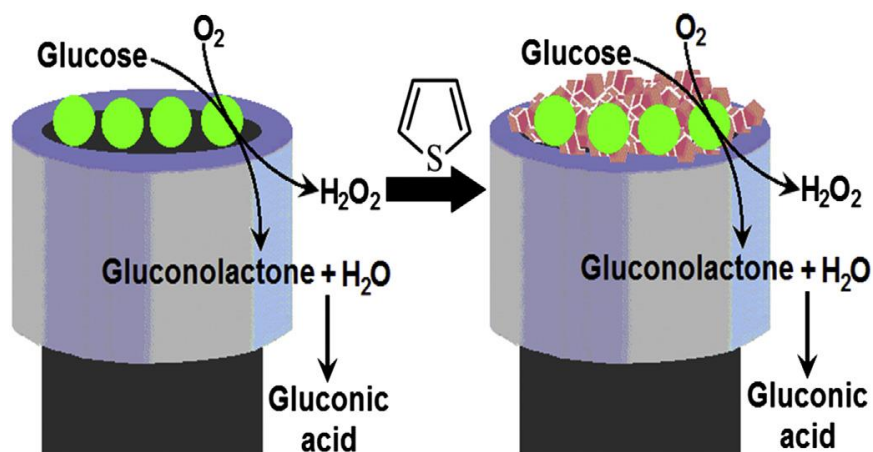


Figure 9. Schematic representation illustrating the coating of the GRE/GOx electrode by PTP layer.

The proper incorporation of biomolecules, e.g., enzymes, within conducting polymer layer may provide many advantages such as enhanced biocatalytic stability, easy protection against the negative environmental impact, e.g., contamination by microbes and undesirable electrochemical interactions, and allows the application of modified electrodes in a wider range

of experimental conditions (pH and temperature) [86]. This routine can be used to modulate bioelectrokinetic parameters, e.g., K_m and maximal rate of biochemical reactions in a certain range [86, 88]. These kinetic parameters are very important in biosensor design. For such purpose polypyrrole, polyaniline, and polythiophene are most commonly used [91].

1.2.3.3. Cellobiose dehydrogenase

Cellobiose dehydrogenase (CDH), cellobiose: acceptor 1-oxidoreductase; EC 1.1.99.18, is an extracellular flavocytochrome protein secreted by wood-degrading, phytopathogenic or saprotrophic fungi within the phyla of *Basidiomycota* and *Ascomycota* [92]. The biological function of CDH has been under discussions for a few recent years while it was generally suggested that the enzyme takes a part in the degradation of the ligno-cellulose matrix in wood. This assumption was supported by the identification of novel electron acceptors for CDH [93, 94].

CDH is a monomeric enzyme consisting of two distinct domains, a dehydrogenase domain (CDH_{DH}) with FAD as a prosthetic group and a cytochrome domain (CDH_{CIT}) carrying haem b as a prosthetic group. The larger CDH_{DH} domain serves as a catalytically active site, whereas the smaller CDH_{CIT} domain acts as an ET protein between CDH_{CIT} and a terminal electron acceptor. The domains are connected through a flexible linker of 20 amino acids which allows efficient inner ET between the domains. The crystal structure of the intact enzyme is not available yet, but the two domains have been separately crystallised for *Phanerochaete chrysosporium* CDH, and their structure was then revealed by X-ray crystallography [95, 96]. In the following description it is assumed that different species of CDH have a similar crystal structure. The crystal structure of the enzyme along with the redox transformations of its cofactors are shown in Fig. 10. The molecular mass of CDH ranges from 85 up to 101 kDa depending on the degree of glycosylation which can account for up to 16 % of the molecular mass [97].

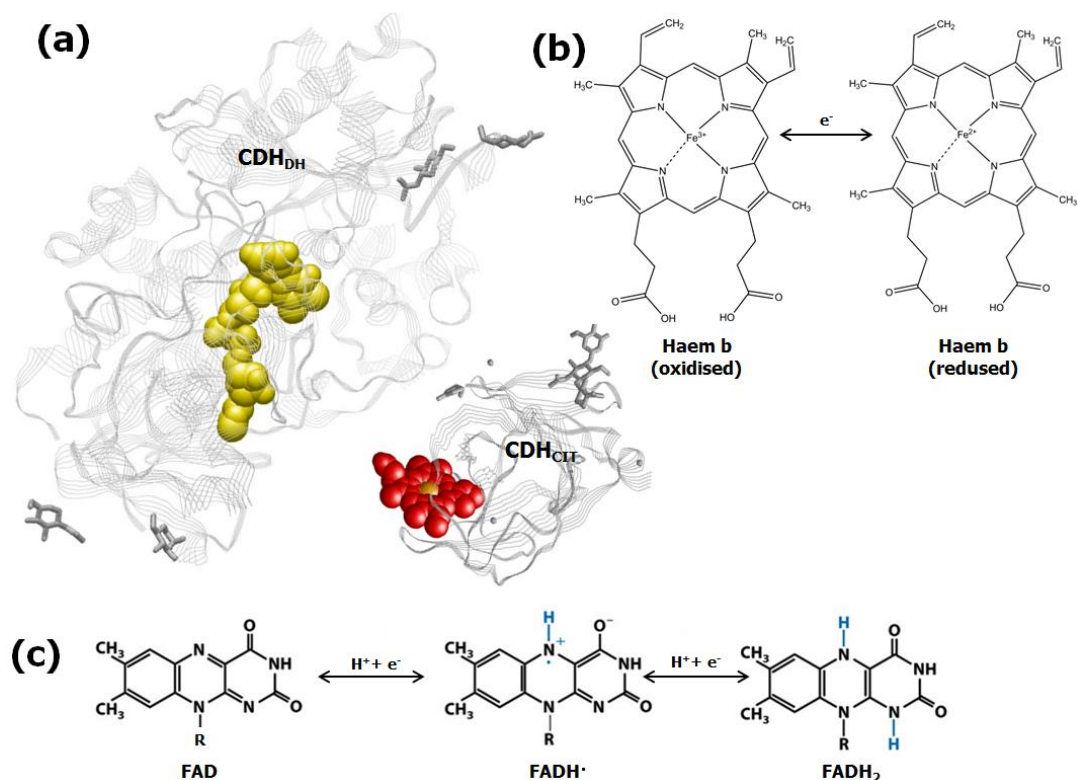


Figure 10. (a) Crystal structure of CDH, presented using the CDH_{DH} (PDB ID: 1KDG [96]) and the CDH_{CIT} (PDB ID: 1D7B [95]) domains of *Phanerochaete chrysosporium* CDH. The proteinaceous backbone is shown as light grey ribbons, the carbohydrates are represented as dark grey sticks, the cofactors FAD and haem b are depicted as yellow and red spheres, respectively. Redox transformations of the cofactors (B) haem b and (C) FAD (only showing the part involved in the redox reaction).

CDH preferably oxidises the β -1,4-linked disaccharides, such as cellobiose, lactose, or cello-oligosaccharides. However, depending on the origin of the enzyme, may also oxidise some monosaccharides including glucose although with lower catalytic efficiencies than di- or oligo-saccharides. Thereby, CDHs extracted from different origins have been divided into two classes. The class I includes CDHs from *Basidiomycetes* which demonstrate narrow substrate specificity, comprising mainly oligo- and disaccharide oxidation, and have the highest catalytic activity in slightly acidic pHs (~3.5-4.0). Whilst, the class II emerges CDHs from *Ascomycetes* that display broader substrate spectrum, i.e., are also able to oxidise monosaccharides, e.g., glucose, with fairly high K_m values, and show a great variety in their optimal pH for IET [97, 98]. Specifically, according to pH-dependent pattern of the biocatalytic activity, the class II referred CDHs are further divided into three

groups featuring acidic, intermediate, or neutral-alkaline pH optima [99]. The acidic group exhibits a narrow activity at around pH 5, the intermediate group also has a maximum activity at around pH 5-6, but a much broader pH profile and, the last neutral-alkaline group demonstrates a pH optimum between 6 and 9 [100, 101]. The highest biocatalytic activity at neutral pH makes the third group CDHs, i.e., CDHs from *Humicola insolens* (*HiCDH*), *Corynascus thermophilus* (*CtCDH*), especially valuable as bioanode enzymes in the designing of glucose powered EBFCs aiming their use in physiological solutions [29]. In comparison to GOx, CDH is an advantageous enzyme due to its broad spectrum of substrate, low sensitivity to O₂, the ability of DET and unlike GDH does not require a soluble cofactor. Additionally, the production of *HiCDH* and *CtCDH* enzymes is already possible at large scale as well as the genetic engineering protocols are available to regulate specificity, activity, and glycosylation of the enzymes [102, 103].

In CDH_{DH} domain an aldose, e.g., glucose, is oxidised at the C1 position (only the β-anomer is a substrate for CDH) into its corresponding lactone and concurrently the FAD in the active site of the CDH_{DH} is fully reduced to FADH₂ (Fig. 11).

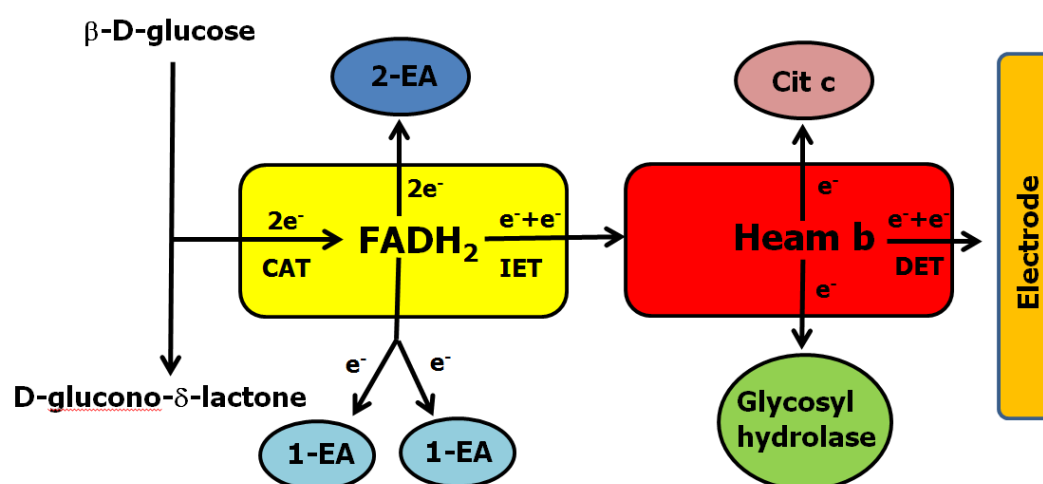


Figure 11. ET in CDH from the substrate, e.g., glucose, to various terminal electron acceptors. One- and two-electron acceptors (EA) can be reduced directly by the FADH₂ in the CDH_{DH}. Alternatively, electrons can be transferred by IET to the haem b in the CDH_{CYT}, which works as a relay for the reduction of macromolecular electron acceptors like glycosyl hydrolases, cyt c or an electrode.

Re-oxidation of CDH_{DH} can occur either directly at the (reduced) CDH_{DH} domain by transfer of reduction equivalents to a two- (e.g. quinones) and one (e.g., Os³⁺ complex) electron acceptor or, alternatively, electrons can be sequentially shuttled from the reduced FAD to the haem b cofactor, followed by consecutive reduction of two one-electron acceptors (ferric iron complexes, cytochrome c, glycosyl hydrolases) or donation of the electrons directly to the electrode (Fig. 11). Cyt c is one of only a few one-electron acceptors which solely act with CDH_{CYT}, thereby can be used to evaluate IET [97].

1.2.4. Redox enzymes for O₂ reduction

O₂ is a typical oxidant in abiotic FCs used in the form of pure gas or air. On the other hand, O₂ is essential for the respiration in all aerobic organisms and its ubiquity in human physiological solutions directs its application as an oxidant in potentially implantable EBFC systems. Moreover, O₂ has a high reduction potential (+0.818 V) which thus enables high voltage output of the complete EBFC. The respective half-cell reactions and enzymes used for the bioelectrochemical reduction of O₂ are listed in Table 2 below.

Table 2. Enzymes catalysing the reduction of O₂.

Enzyme	EC Number	Cofactor	Half-Cell Reaction
Laccase	1.10.3.2	Cu	$O_2 + 4H^+ + 4e^- \rightarrow 2H_2O$
Bilirubin oxidase	1.3.3.5	Cu	See above
Cytochrome c oxidase	1.9.3.1	Cu, Fe/heme	See above

Since laccase or bilirubin oxidase enzymes catalyse the O₂ reduction reaction and exhibit DET at electrodes, they were used and investigated as a cathode enzymes in this work.

1.2.4.1. Laccase

Laccase (Lc), benzenediol: O₂ oxidoreductase; EC 1.10.3.2, is multi-copper protein typically found in plants and fungi [104]. Lc is among of a few enzymes that have been studied since the late 19th century when discovered in the Japanese lacquer tree *Rhus vernicifera* in 1883 [105]. It was the first redox enzyme for which DET based bioelectrocatalysis was demonstrated [106]. Plant Lcs participate in the radical-based formation of lignin [107], whereas in fungi Lcs have been shown to be associated with a large number of physiological processes including morphogenesis, pathogenicity, stress defence, and lignin degradation [108]. There are also some reports describing Lc activity in insects [109] and bacteria [110] where its function is still quite controversial.

Lcs belong to the group of blue multicopper oxidases (BMCOs), characterised by the presence of at least four Cu atoms as a prosthetic group, which play an important role in the enzyme catalytic mechanisms. Cu atoms are distributed in different binding sites and are classified into three types, according to specific spectroscopic (UV/visible and electronic paramagnetic resonance (EPR) spectroscopy) and functional characteristics: one Cu ion in type 1 (T1) site, together with at least three additional Cu ions, i.e., one Cu ion in type 2 (T2) site and two Cu ions in type 3 (T3) site, arranged in a tri-nuclear T2/T3 cluster (TNC) (Fig. 12a). T1 Cu at its oxidised resting state absorbs the light at approximately 610 nm and thus gives rise to a noticeable blue colour of the enzyme. T2 Cu does not confer colour but is EPR detectable, and T3 Cu bi-nuclear gives a weak absorbance in the near UV region but no detectable EPR signal [108, 111].

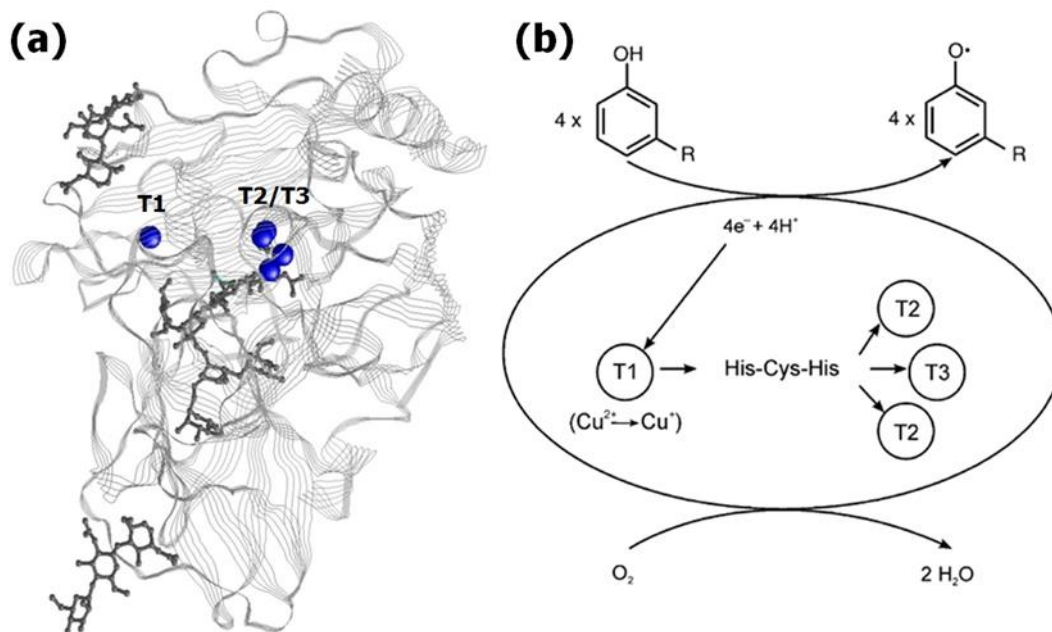


Figure 12. (a) The crystal structure of the Lc from *Trametes hirsuta* (PDB ID: 3V9C). The proteinaceous backbone is shown as light grey ribbons, the carbohydrates are represented as dark grey sticks, and the Cu ions are depicted as blue spheres. (b) Catalytic cycle of the Lc enzyme. Adopted from [104].

In general, Lc catalyses a one electron oxidation of a wide variety of organic and inorganic compounds, including mono-, di-, and polyphenols, aminophenols, methoxyphenols, aromatic amines, etc. The oxidation proceeds at the T1 site, and the extracted electrons are transferred through a highly conserved His-Cys-His tri-peptide motif, to the T2/T3 site, where the four electron reduction of O₂ to water concomitantly occurs (Fig. 12b). The Lc enzyme has low specificity for reducing substrates, in contrast to its strong preference for O₂ as an oxidising substrate [112]. The one electron substrate oxidation is coupled to the four electron reduction of O₂, thus the reaction mechanism is not straightforward. Lc must operate as a battery, storing electrons from individual substrate oxidation reaction to reduce O₂ [113]. The overall reaction describing the O₂ bioreduction to water is written in Table 2.

Lcs extracted from different organisms show considerable heterogeneity in their structural, physicochemical, and kinetic properties such as redox potential (T1 site), molecular weight, glycosylation extent, pI, optimal catalysis conditions, etc., which are possibly attributed to the diversity of their natural

environmental conditions and the function they perform. The redox potential of the T1 Cu site varies between 430 and 780 mV (vs. NHE) as determined by potentiometric titrations of different Lcs [114]. Consequently, all Lcs can be divided into three groups depending on the potential value: low, middle and high potential Lcs [115]. Both Lcs studied in this work, i.e., Lc from *Trametes hirsuta* (*ThLc*) [116] and recently discovered Lc from *Trichaptum abietinum* (*TaLc*), are fungal Lcs referred to high potential Lcs. Only a few studies were performed to evaluate the redox potential of T2 and T3 Cu sites due to the difficulty of finding the conditions at which redox processes at these sites limits the catalysis. As mentioned above, fungal Lcs are of special interest in bioelectrochemistry due to their high redox potential comparing to, e.g., plant Lcs [25, 26] as well as due to the simplicity of their discovery and purification. Most fungal Lcs are extracellular proteins, but intracellular Lcs have also been described in fungi [117]. The localisation and a broad substrate selectivity of the enzyme is probably connected with the diversity of its physiological functions. It is worth to mention that several Lc isoenzymes have been detected in many fungal species. A fungal Lc is typically a monomeric protein. The molecular mass varies in the range of 60-70 kDa with a significant part comprised of carbohydrates. The extent of glycosylation usually ranges between 10 % and 25 %, but in some Lcs carbohydrates constitute more than 30 % of the total weight of the enzyme, (e.g., in *Coriolopsis fulvocinnerea* - 32 % [118]) [104]. A few fungal Lcs, however, exhibit a homodimeric [119] or even oligomeric structure [120]. The electrostatic surface potential distribution of fungal Lcs reveals a dominance of negative charges, which is in accordance with the acidic pI of around pH 4.0 (range = 2.6-6.9) [121].

In many bioelectrocatalytic applications the heterogeneous DET from an electrode to the T1 site of Lc typically occurs if the enzyme is properly oriented. DET is possible to achieve because the T1 centre is located only ~ 6Å away from the protein surface. This distance is small enough for tunnelling of electrons quite efficiently [114]. Interesting is the fact that the electron tunnelling distance from the T1 site to the T2/T3 TNC is ~ 13Å, which is the

same as the distance between the FAD cofactor in GOx and the surface of the enzyme. In GOx, the 13Å distance makes DET extremely difficult, while BMCOs can easily transfer electrons across this distance due to an efficient electron coupling between Cu T2/T3 and T1 sites [122].

Despite feasible DET, fungal Lcs have a few key obstacles to be functional biocatalysts in physiological conditions or fluids which have pH close to the neutral. Firstly, fungal Lcs typically exhibit pH optima in the acidic pH range, even though they are more stable in alkaline than in acidic pH range [123]. Secondly, the activity of Lc is inhibited by anions such as halides [124]. Yet, for operation in living organisms, where the pH is lower, e.g., grapes, high redox potential Lcs are the most suitable cathodic biocatalysts [125]. Also, the Lc enzyme is an extremely interesting enzyme for the fundamental study of DET process.

1.2.4.2. Bilirubin oxidase

Bilirubin oxidase (BOx), bilirubin: O₂ oxidoreductase; EC 1.3.3.5, is a subgroup of BMCOs naturally found in fungi [126] and bacteria [127]. The enzyme was first discovered and described in the early 80's [126, 128]. Similar to Lcs, the BOx enzyme has 4 Cu ions as a prosthetic group in its active centre, typically arranged to T1, T2/T3 sites (Fig. 13a), as well as catalyses the reduction of O₂ to water (without formation of highly reactive O₂ species) *via* reaction presented in Table 2 [129]. A natural reducing substrate of BOx is bilirubin, a breakdown end product of heme metabolism, which is accordingly oxidised to biliverdin (Fig. 13b) while concomitantly reducing O₂ to water (Fig. 13a) [126].

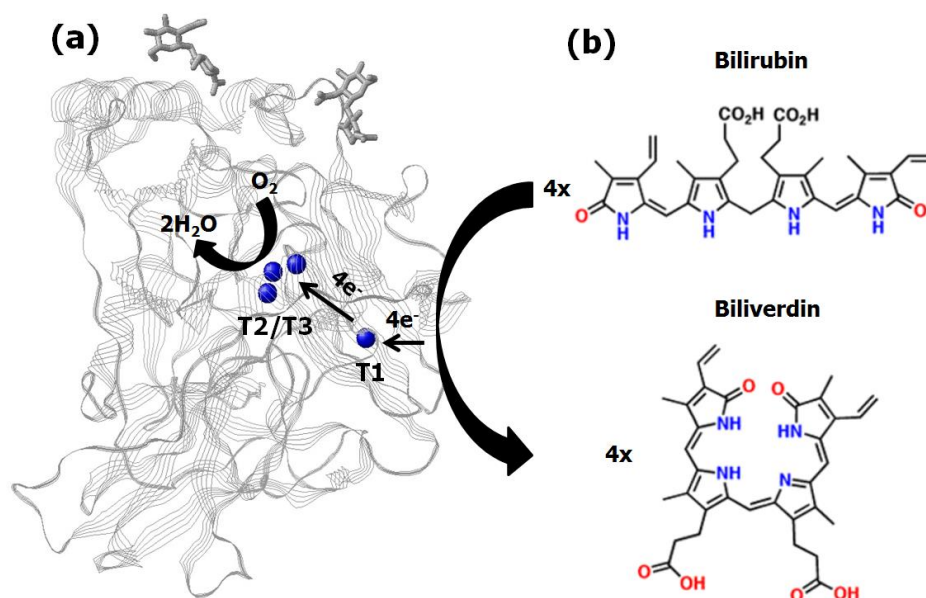


Figure 13. (a) The crystal structure of BOx from *Myrothecium verrucaria* (PDB ID: 2XLL) [130]. The proteinaceous backbone is shown as light grey ribbons, the carbohydrates are represented as dark grey sticks, and the Cu ions are depicted as blue spheres. (b) The oxidation of bilirubin to biliverdin.

A wide range of other substrates can be also oxidised in a one-electron process, e.g., 2,2'-azino-bis(3-ethylbenzothiazoline-6-sulphonic acid) (ABTS, commonly used with BMCOs to assess reaction kinetics), syringaldazine, or 2,6-dimethoxyphenol [131].

At first sight, both fungal Lcs and BOxs, having a redox potential up to 780 mV [114] and 670 mV [132], respectively, seem to be extremely interesting to employ them as O₂ reducing biocatalysts for the designing of implantable EBFCs. However, as mentioned above (Chapter 1.2.4.1), Lcs from fungi have pH optima in the acidic region as well as are inhibited by halide ions which make them unsuitable for biocathodes in the designing of EBFCs supposed to operate in vertebrate (e.g., human) tissues and fluids. Whilst, BOx is tolerant to Cl⁻ ions and demonstrates high catalytic activity in neutral pH, though its redox potential is lower ~100 mV comparing with fungal Lcs [131]. According to these circumstances, most probably determined by a protein part of enzyme (apoenzyme), the BOx enzyme is considered as the best cathodic biocatalyst so far operating in physiological conditions. BOx as an O₂ biocatalyst of an EBFC was first employed by Ikeda and co-workers in 2001,

who demonstrated that the enzyme catalyses the reduction of O₂ to water at potentials higher than 0.7 V in the presence of ABTS as a redox mediator [133]. Prior to this, BOx had widely been used in an enzymatic amperometric bilirubin biosensors [134]. Even though the usage of redox mediators can significantly increase a current density of an EBFC, soluble mediators are undesirable in the design of implantable EBFCs. Thus, suitable wiring and orientation of BOx molecules are required instead. DET between BOx and different electrode materials (metal and carbon, etc.) has been achieved using different immobilisation strategies in attempts to appropriately orient the enzyme for efficient ET [135]. Cathodes based on BOx can often generate current densities in the mA cm⁻² range; the maximum current being limited by O₂ diffusion to the electrode surface [14].

Highly purified BOx from *Myrothecium verrucaria* (*MvBOx*) was employed in these studies to create biocathode of a mediator-less carbohydrate/ O₂ EBFCs. *MvBOx* is a slightly glycosylated monomeric enzyme having a molecular weight of about 60 kDa [136] and an pI of ~4.1 [128].

1.2.5. Peroxidase/oxidase based cathode

The concept of peroxidase/oxidase biocathodes powered by the reduction of hydrogen peroxide, in situ generated by oxidases, can be an alternative to BMCO based cathodes of EBFCs. In general, depending on the oxidase enzyme co-immobilised with peroxidase, EBFCs can be powered by different substrates such as glucose [137] or ethanol [138]. In glucose EBFCs, glucose oxidase (GOx) co-immobilised with different peroxidases (e.g., horseradish peroxidase, microperoxidase-8, and microperoxidase-11) has been generally employed. The choice of redox enzymes for a bi-enzyme based cathode is determined by their catalytic activity in conditions where they are intended to operate. For example, the main requirement for the bi-enzyme couple imposed to be used in human samples, such as blood, saliva, is their high catalytic activity and stability in physiological conditions.

Peroxidase/oxidase bi-enzyme system acts *via* a consecutive mechanism. First, the reducing substrate, e.g., glucose, is oxidised by an oxidase while

forming hydrogen peroxide. Second, the produced hydrogen is accordingly used as a substrate for a peroxidase. The peroxidase catalyses the reduction of hydrogen peroxide to water and, during this reaction, the oxidised state of the enzyme is recovered to its reduced state accepting electrons from the electrode (Fig. 14).

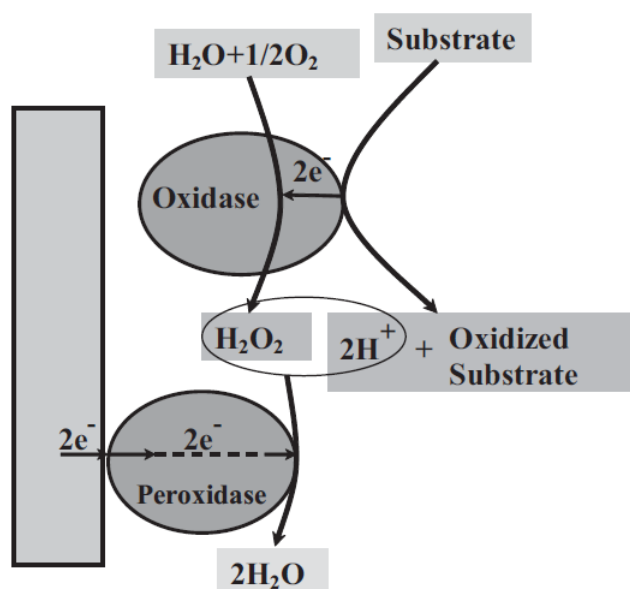


Figure 14. Schematic illustration of the mechanism of a peroxidase/oxidase based cathode. Adopted from [139]

In this work the horseradish peroxidase (HRP)/GOx enzymatic couple was employed and studied as a biocathode in glucose powered EBFC. The choice of these enzymes was mainly based on their commercial availability, low price, and high stability and activity in physiological conditions. More information about GOx and HRP enzymes is provided in Chapters 1.2.3.1 and 1.2.5.1., respectively.

1.2.5.1. Horseradish peroxidase

Horseradish peroxidase (HRP, EC 1.11.1.7) is isolated from horseradish roots (*Amoracia rusticana*) and belongs to the ferroporphyrin group of peroxidases. The root of the plant contains a number of distinctive peroxidase isoenzymes of which the C isoenzyme (HRP C) is the most abundant [140], and was employed in this work to construct a peroxidase/oxidase based biocathode.

HRP C is a monomeric enzyme which consists of 308 amino acid residues and two different types of metal centre, i.e., iron (III) protoporphyrin IX (usually referred to as the ‘haem group’) and two Ca^{2+} ions (Fig 15a) [141]. Both are essential for the structural and functional integrity of the enzyme. For example, the loss of one Ca^{2+} ion decreases the enzyme activity by 40 %. [142].

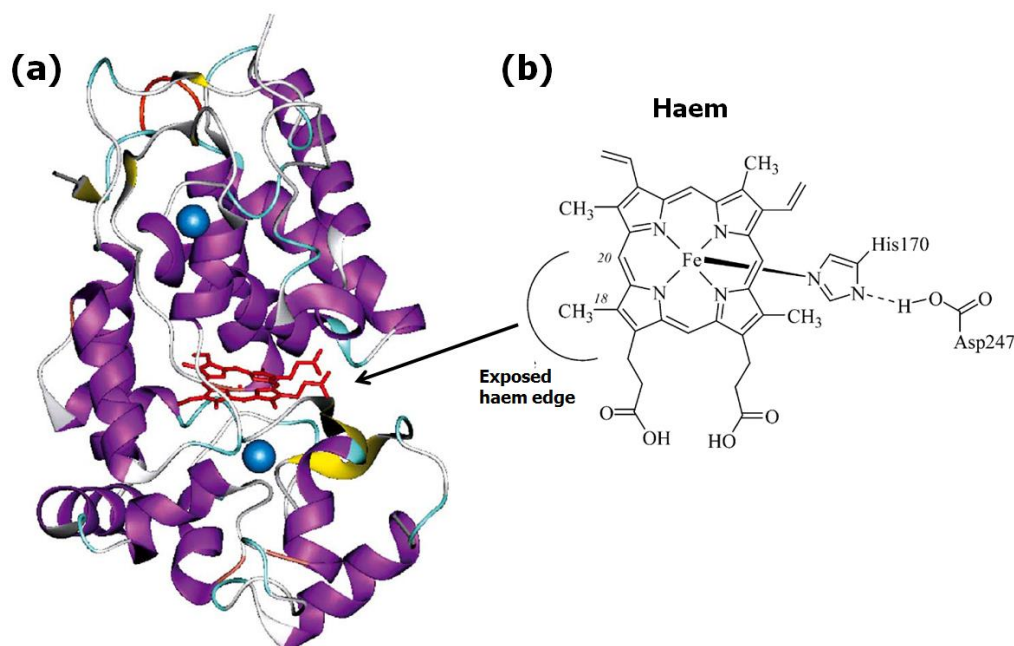
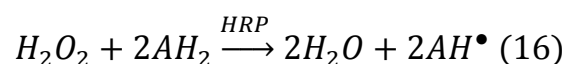


Figure 15. (a) The crystal structure of HRP C (PDB ID: 1H5A) [142]. The haem cofactor is presented as red sticks and Ca^{2+} ions as blue spheres, respectively. (b) The molecular structure of the haem cofactor. Aromatic substrates are oxidised at the exposed haem edge without binding to haem iron. Adapted with changes from [142].

The enzyme contains four highly conserved disulfide bridges and is considerably glycosylated (~21% by weight). The carbohydrate composition consists of galactose, arabinose, xylose, fucose, mannose, mannosamine, and galactosamine depending upon the specific isoenzyme. Their constitution affects the stability of the enzyme [143]. Its molecular weight (~44 kDa) includes the polypeptide chain (33890 Da), haem plus Ca^{2+} ions (~700 Da), and carbohydrates (~9400 Da). The isoelectric point for HRP C is approximately 9.0 [141]. The optimal pH is 7.0 [144], and the enzyme demonstrates high stability in the pH range of 5.0-9.0 [145].

Horseradish peroxidase catalyses the oxidation of small organic and inorganic molecules by hydrogen peroxide that are able to approach the Fe-porphyrin. Most reactions catalysed by HRP C and other horseradish peroxidase isoenzymes can be expressed by the following equation:



in which AH_2 and AH^\bullet represent a reducing substrate and its radical product, respectively. Typical reducing substrates include aromatic phenols, phenolic acids, and indoles [140].

Many physiological roles have been assigned to HRP isoenzymes including indole-3-acetic acid metabolism, lignification, cross-linking of cell wall polymers, suberin formation and contribution to defence against infection [140].

It was previously shown that the distance between the haem cofactor and the surface of the HRP enzyme is $\sim 10 \text{ \AA}$, which enables quite effective DET. So far, the DET between HRP and different electrodes, e.g., carbon [146], graphite [147], gold [148], has been established. In the respect of DET properties, HRP has been employed as a biocatalyst to power cathodes by hydrogen peroxide reduction when immobilised alone [149] or co-immobilised with oxidase in the construction of bi-enzyme system [137] (Chapter 1.2.5.). It can be noticed that HRP has an enormous number of applications in the area of diagnostic, biosensing, and biotechnology due to its high stability in aqueous solution. Thus, HRP is one of the most studied redox enzymes [140].

1.3. Design considerations of EBFC electrodes

To increase the lifetime of EBFC a substantial amount of enzymes at the surface of an electrode must immobilised. Considering the fact that enzymes are proteins, they display a weak three-dimensional structure; thus, the immobilisation methodology must provide the enzyme with an adequate microenvironment that enables its native structural conformation to ensure the high catalytic activity of an immobilised enzyme [42, 150]. The proper orientation of enzyme molecules has also to be kept in mind during the

immobilisation procedure in order to achieve appropriate electrical contact between the enzyme active centre and the electrode. The ET contact is one of the most critical points when constructing mediator-less, that is, DET based EBFCs [151]. DET based bioelectrocatalysis is only possible to establish using a small group of redox enzymes. This is established by the structure of the proteinaceous environment determining the presence or absence of natural ET pathways (Fig. 16a; Chapter 1.3.3.) [152]. In all other cases, when DET is not sufficient enough (or not achievable at all), redox compounds so-called mediators must be employed to shuttle the electrons between an enzyme and an electrode (Fig. 16b; Chapter 1.3.2.) [153].

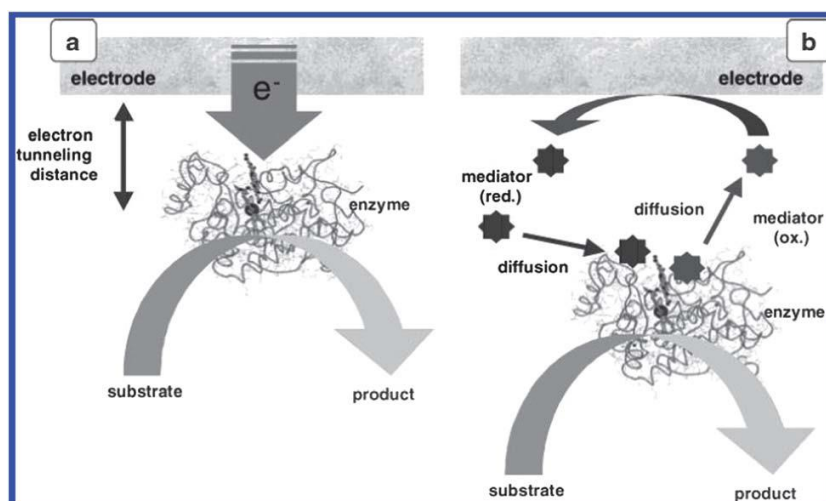


Figure 16. Two approaches to transfer the electrons between the active site of an enzyme and an electrode: (a) DET and (b) ET *via* ET mediator.s Adopted from [154].

1.3.1. Electron transfer mechanisms in redox enzymes

From a bioelectrochemical point of view, in the early 1990s Guo and Hill divided redox enzymes into two groups, i.e., intrinsic and extrinsic, and characterised them as follows [155]. In intrinsic redox enzymes, the catalytic reaction occurs within deeply localised redox-active sites which are very often buried into the protein matrix. The latter is generally assumed to behave as an electric insulator. Since intrinsic redox enzymes do not have natural built-in redox partners as well as ET pathways connecting the redox centres to their surface, for these enzymes efficient DET reactions at electrodes are less

probable and may require either: (1) the sites of the catalytic reaction to be close to the protein surface, (2) the deformation of an enzyme without loss of its catalytic activity, (3) the projection of an electrode surface into the enzyme, or (4) the introduction of ET pathways by modification of an enzyme [155]. GOx, which belongs to the intrinsic group of redox enzymes, has its FAD cofactor deeply hidden into the glycoproteinaceous shell and, thus, the enzyme or the electrode needs to be modified to achieve DET (Chapter 1.2.3.1.). For example, it is believed that the deglycosylation of GOx enabled the establishment of significant DET [156]. Yet, some intrinsic redox enzymes, e.g., peroxidases, demonstrate DET due to the cofactor exposed on their surface (heme in this case) leading to short distances of electron tunnelling (Chapter 1.2.5.1.) [147]. In extrinsic redox enzymes a built-in natural redox mediator or polypeptide based ET pathways exist within the enzyme connecting the active site to the enzyme exterior; this naturally facilitates DET [155]. To realise efficient DET, a proper orientation of the redox enzyme onto the electrode so that the site of the electron-tunnelling pathways faces the electrode becomes important [152]. According to this definition, CDH is a good example of an extrinsic enzyme (Chapter 1.2.3.2).

Much work has been done to understand the factors which determine electron flow through enzymes. According to quantum mechanical theory, the rate of ET (k_{ET}) from a donor to an acceptor is expressed as follows:

$$k_{ET} = (H_{DA})^2 \exp(-\beta(d - d_0)) \exp\left(-\frac{(\Delta G + \lambda)^2}{4RT\lambda}\right) \quad (17),$$

where H_{DA} is the electron-nuclear coupling at the distance d_0 , β is a tunnelling decay factor for a given electron donor/acceptor pair in a defined medium, d and d_0 are the actual distance and van der Waals distance (the closest distance) between a donor and an acceptor, ΔG is the free energy change, and λ is the reorganization energy accompanying the ET process [157]. This equation is called Marcus equation and, among other ET-determining parameters, describes, e.g., exponential dependence of ET rate on the distance between an electron donor and acceptor. Conclusion from this dependence is that the k_{ET}

becomes negligible at donor-acceptor separation beyond 1.5 nm [158]. This means that DET can only take place when an electrode is placed within this distance to an enzyme cofactor in the active site; whereas a shorter distance makes the ET so efficient that the enzymatic reaction kinetics becomes a rate-determining step [159].

1.3.2. Mediated electron transfer based coupling

In the case of mediated electron transfer (MET), synthetic or biological charge carriers so-called ET mediators are used to shuttle electrons between the active centre of an enzyme and an electrode. ET mediators can exchange electrons with a variety of redox enzymes instead of natural electron donor or acceptor. It is usually a small organic dye molecule or organometallic complex, which may be dissolved in solution or immobilised on the electrode through the linker which allows its free movement but no escape from the surface. In this work for mediated systems both an insoluble mediator and redox enzymes were attached to the electrode in order to avoid mediator leaking from the electrode surface.

There are both advantages and disadvantages to using ET mediators. In their favour, they are essential if the active centre of an enzyme is hidden into the apoenzyme and is consequently unable to exchange electrons directly with the electrode surface (e.g., intrinsic redox enzymes). Analogously, they are also requisite if the enzyme preferentially attaches in a nonelectroactive orientation on the electrode surface, however, this attachment may be very stable. Finally, mediators are necessary for coupling to multilayers of enzyme on the electrode surface (raising the catalytic density) because, otherwise, only the lower layer will lie within the electron tunnelling distance from the electrode surface. In these cases, redox polymers can be used to create a conductive matrix extending from the electrode surface, hence, 3D-electrode.

Characteristic requirements of mediator species include stability and selectivity of both oxidised and reduced forms of the species and the redox chemistry

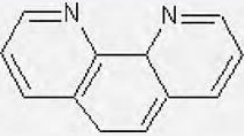
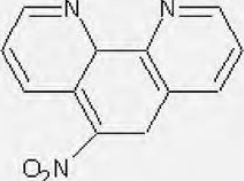
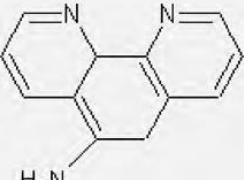
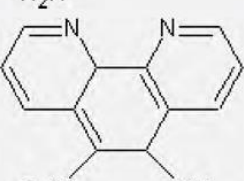
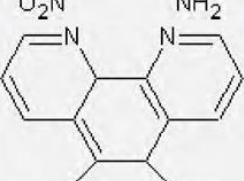
must be reversible, thus, requiring low overpotential [42]. The absence of pH – dependence of redox potential is also desired.

In MET, the thermodynamic redox potential of mediator now dictates the maximum voltage of an EBFC. In practice, a redox potential which is more positive for oxidative biocatalysis (at anode) and more negative for reductive biocatalysis (at cathode) is required in order to provide a driving force for ET between enzyme active site and mediator. These both requirements result to the voltage losses in an EBFC. A major challenge in MET is, therefore, to achieve the best compromise between driving force and current, in order to maximise power output [21]. Other possible difficulties connected with the utilisation of MET in the designing of EBFCs are briefly mentioned in Chapter 1.3.3.

1.3.2.1. An example of ET mediators: 1,10-phenanthroline derivatives

In the thesis, five different 1,10-phenanthroline derivatives (PDs), i.e., 1,10-phenanthroline monohydrate; 5-nitro-1,10-phenanthroline; 5-amino-1,10-phenanthroline; 5-amino,6-nitro-1,10-phenanthroline and 5,6-diamino-1,10-phenanthroline, having different functional groups have been investigated electrochemically in order to determine their ability to act as ET mediators for glucose oxidase (GOx). Afterwards, 5-amino-1,10-phenanthroline, as the best ET mediator for GOx among the investigated PDs, was employed to construct GOx based anode in the designing a complete glucose powered EBFC (Chapter 3.3.1.).

Table 3. The abbreviations and molecular structures of phenanthroline derivatives used in the present studies.

Abbreviation	Name of the PDs	Molecular structure
PMH	1,10-Phenanthroline monohydrate	
5NP	5-Nitro-1,10-phenanthroline	
5AP	5-Amino-1,10-phenanthroline	
5A6NP	5-Amino,6-nitro-1,10-phenanthroline	
56DAP	5,6-Diamino-1,10-phenanthroline	

PDs are classic bi-dentate ligands chelating transition metal ions which play an important role in coordination chemistry. PDs are rigid planar, hydrophobic, hetero-atomic systems in which nitrogen atoms are well placed to act cooperatively in the binding of metal ions [160]. Chemical properties of PDs depend on the positions and characteristics of the substituting radicals bound to 1,10-phenanthroline [161, 162]. Due to the combination of structural and chemical properties the PD-metal complexes (mainly PD-osmium and PD-ruthenium) have been actively studied for their spectroscopic, redox, and electrochemical properties [163-165]. However, most of these metal complexes are not commercially available and their synthesis is very complicated as well as time-consuming. Due to relatively simple and rapid preparation of PDs their use as ET mediators in the designing of new biosensors and biofuel cells was

tested in this thesis. So far, despite of some bioelectrochemical studies devoted to the investigation of PDs-metal complexes [163, 166], there have been no published studies on similar investigations of PDs that were not involved into metal complexes.

1.3.3. Direct electron transfer based wiring of redox enzymes

Although, DET was already first demonstrated for several redox enzymes in the 1970s [106] and had afterwards been used in electroanalytical applications, it had not been employed in EBFC design until 2006 when researchers developed biocathodes for the reduction of O_2 using laccase [167] and bilirubin oxidase [168], and bioanodes employing glucose oxidase [169]. The DET based design allows significant simplification and improvement in the construction of EBFCs; no soluble compounds need to be added, mediator caused voltage losses can be avoided, and possibly toxic mediator compounds can be excluded. These factors also simplify miniaturisation and practical realisation of efficient and simple biodevices [20].

Generally, in order to classify a redox enzyme as DET active, when immobilised on the surface of an electrode, an electrochemical signal should be observed in the absence of an enzyme substrate revealing the electrochemistry of the enzyme-bound cofactor (Fig. 17a), and a catalytic current should be registered in the presence of an enzyme substrate (Fig. 17b) [152].

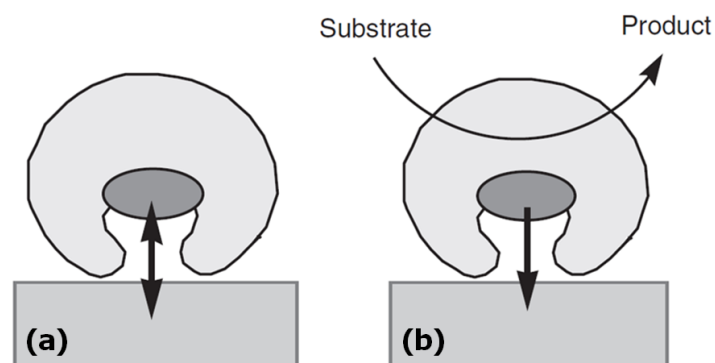


Figure 17. Schematic representation of the electron transfer pathway in DET between a redox enzyme and an electrode: (a) in the absence of the enzyme substrate, (b) in the presence of the enzyme substrate.

As it has already been mentioned in chapter 1.3.1., DET across the enzyme-electrode interface is solely possible using those intrinsic redox enzymes in which active centre appears close enough to the protein surface, (Fig. 18a) or, extrinsic enzymes having intermolecular ET pathways and the centres of electron relay (or small proteins as built-in redox mediators) which lie close to each other as well as to the surface an enzyme (Fig. 18b). According to the Marcus equation (Eq. 17), the critical separation distance, which allows to achieve a sufficiently high rate of ET for the enzyme bioelectrocatalysis demonstrating turnover frequencies in the range of 10^3 - 10^4 s⁻¹, is ~ 15 Å [158].

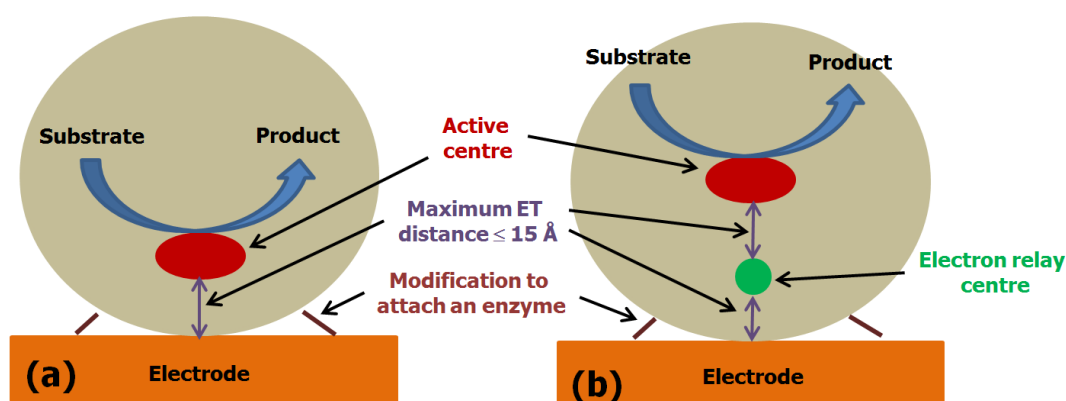


Figure 18. Cartoon depicting an enzyme molecule immobilised on an electrode surface in DET contact to the electrode: (a) the active site itself or (b) the centre of electron relay appears close to the protein surface.

DET pathway can be established by linking these enzymes strongly to the electrode in the proper orientation, either by directed covalent or strong, non-covalent bonding, such as multisite electrostatic interactions. Strong attachment can lead to enhanced stability of the enzyme immobilised on an electrode, and may also increase the electro-active surface coverage by assuming only the most favourable orientation. For this purpose, the surface functionalisation procedures by different reactive compounds are generally performed.

1.3.3.1. Exploitation of nanotechnologies

In the case of DET based bioelectrocatalysis, only the lowest layer of immobilised enzyme molecules, i.e., monolayer, lies within the electron shuttling distance. Thus, nanostructured i.e., high-surface area, surfaces must be used to increase the surface area of an electrode and adsorb sufficient amount of enzyme molecules. Another strategy could be the immobilisation of the enzyme inside a highly conductive matrix such as nanoporous material, in which DET can occur in any direction [23]. In addition, some research efforts have also been made to improve the activity and stability of immobilised enzymes by using nanostructures [14]. It is also worth mentioning, that the direct adsorption of enzymes on bulk electrode surfaces may frequently result in their denaturation and loss of biocatalytic activity [170]. While, the adsorption of enzymes on the surfaces of nanomaterials, having nano-size dimensions comparable to those of biomolecules, can maintain the natural conformation/structure of enzymes and, hence, their functionality.

The attractiveness of nanomaterials relies not only on their ability to act as effective immobilisation matrices, but also on their unique electronic, magnetic, optical, physical, and chemical properties that are completely different from bulk materials, and can advantageously be combined with the functioning of biomolecules, thus contributing to improved bioelectrode performance in terms of power of the EBFCs [44]. All above mentioned properties are influenced by the percentage of the total number of atoms in the nanomaterial that are interfacial. For example, if gold nanoparticles are assumed to be spherical, a 1.3 nm diameter gold particle has 88% of its atoms on the surface; a 2.0 nm particle has 58% surface atoms; a 5 nm particles has 23% surface atoms; a 10 nm particle has 11.5% surface atoms; a 50 nm particle has 2.3% surface atoms; a 100 nm particle has 1.2% surface atoms; and a 1000 nm particle has 0.2% surface atoms [171].

It is now fairly inexpensive to purchase or synthesise many different types of nanomaterials, such as nanoporous media, nanotubes, nanoparticles, and nanofibers [172] (Fig. 19).

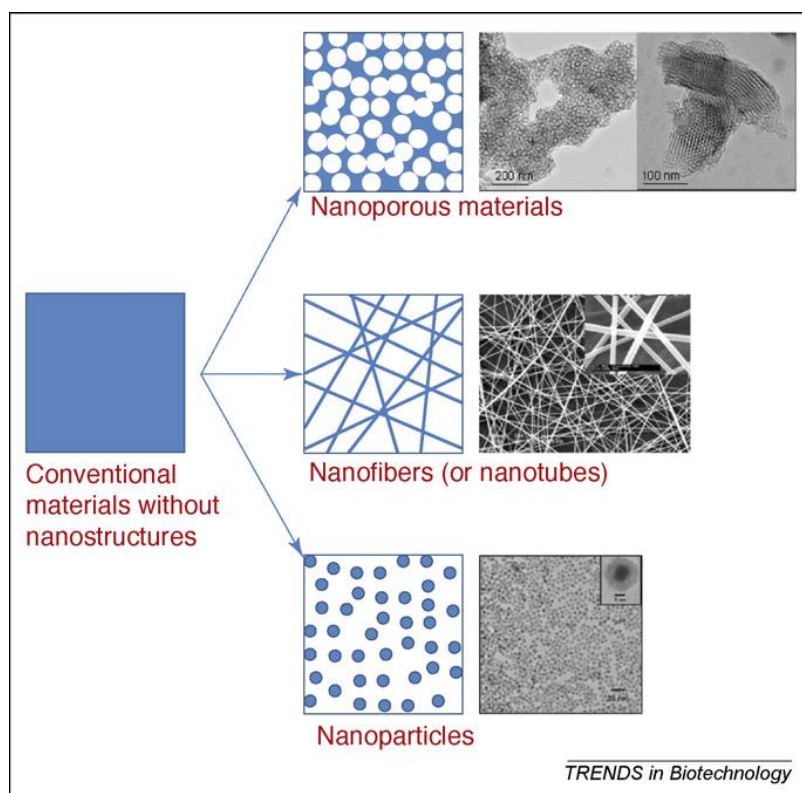


Figure 19. Illustration of nanostructured materials. Shown are transmission electron microscope (TEM) images of nanoporous silica (top panel) and magnetic nanoparticles (bottom panel), as well as scanning electron microscope (SEM) images of electrospun nanofibers (middle panel). Adopted from [173].

In this work gold nanoparticle modified gold electrodes were used to construct DET based wiring of redox enzymes in order to construct membraneless carbohydrate/O₂ EBFCs, as well as evaluate the DET based bioelectrocatalysis at a single nanoparticle modified with Lc molecules.

1.4. Gold nanoparticles

To design high current density mediatorless EBFCs, gold nanoparticles (AuNPs) have often been used as a stable, electrically conductive, and biocompatible nanomaterial [8, 14, 29]. This choice can be justified by the fact that synthesis protocols of stable, size-shape-controlled monodispersed AuNPs are well developed (Chapter 1.4.1.). Additionally, surface charge and other surface properties, such as hydrophobicity/hydrophilicity, of AuNPs can easily be regulated using self-assembled monolayers (SAMs) of small surface active compounds, e.g., thiols, which provide additional advantages in optimising

DET reactions of bioelectrodes (Chapter 1.5.) [174]. It is very important that for the careful fundamental studies of enzyme bioelectrocatalysis on a single AuNP, the size, shape, and surface characteristics of AuNPs can simply be controlled and monitored.

1.4.1. Synthesis of gold nanoparticles

The synthesis methods of AuNPs described in this chapter follow the so-called “bottom-up” strategy. (“Top-down” techniques, which are mechanically or anywise based on diminishing processes using bulk metals, will not be considered here). “Bottom-up” strategies predominantly employ chemical or electrochemical reduction of metal salts in solution [175]. Here are two main protocols of the chemical synthesis of AuNPs reviewed, which provide the formation of AuNPs of well-defined shape and size, thus making them excellent building blocks for the controllable construction of nanostructures.

The first and, so far, the most popular method used for chemical AuNP synthesis is the reduction of gold salt (AuCl_4^-) in aqueous solution containing sodium citrate where citrate ions act as both synthesis initiators (while reducing AuCl_4^-) and AuNP size controllers and stabilizers (when capping on the surface of the emerged AuNPs). This a very simple approach, introduced by Turkevich et al. in the 1950s [176] and later refined by Frens [177], yields roughly spherical AuNPs in a tuneable range of the sizes of 15-150 nm [177].

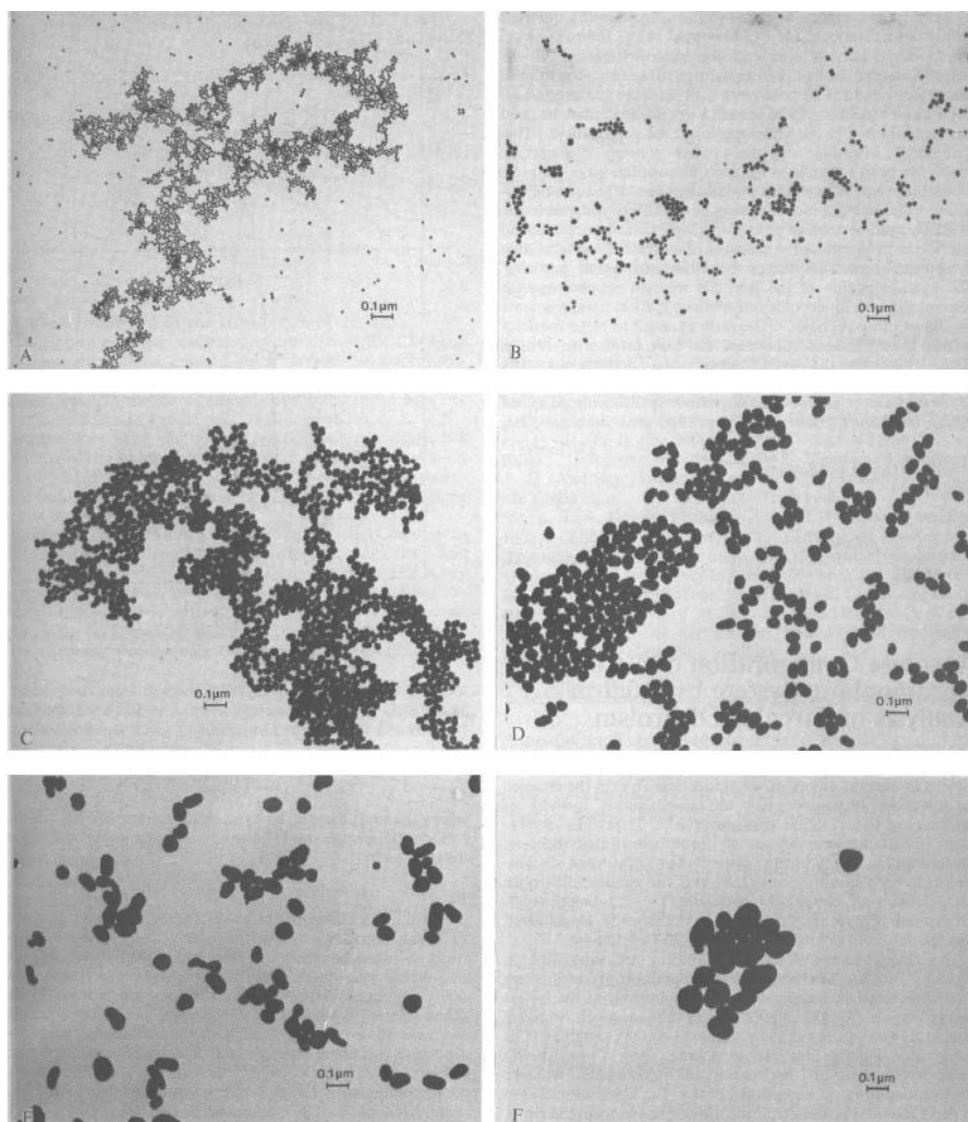


Figure 20. Electron micrographs of the gold sols with sizes of 16 nm (A), 24.5 nm (B), 41 nm (C), 71.5 nm (D), 97.5 nm (E), 147 nm (F). Adopted from [177].

The size is controlled by the initial citrate to AuCl_4^- ratio, where higher ratios give smaller particles. For the preparation of smaller AuNPs (<10 nm), the use of an additional reductive agent, e.g., tannic acid is optimal [178]. During the synthesis, citrate ions adhere loosely to the gold core, providing the AuNP surface with a negative net charge that stabilizes the NP in the solution. However, the stability is susceptible to the binding of charged compounds, pH changes, and addition of salts and that, in turn, as are further discussed in the following chapters, takes an advantage to be exploited to assembly the mono- and multi-layers of AuNPs of different density as well as well distinct physicochemical properties (i.e, conductivity, flexibility, etc.).

The second commonly used method for AuNP synthesis was established in 1994 by Brust et al. [179]. In this method, the reduction of AuCl_4^- is not performed in aqueous solution, but the salt is transferred to an organic solvent using a transfer agent. In the organic solvent, the Au ions are reduced by addition of a reducing agent, commonly NaBH_4 . In the presence of long-chain alkane thiols, which bind to the nanoparticle surface, the nanoparticles are stabilized due to steric interaction between alkane chains of different particles. In contrast to the Turkevich-Frens method, this protocol yields particles that are thermally and air stable, and can easily be transferred between different organic solvents. By altering the thiol to AuCl_4^- ratio in the preparation, AuNPs with narrow size distributions having mean core diameters ranging between 1.5 and 5.2 nm can be produced [180]. The core size decreases with increasing thiol to gold ratio. Alkanethiol stabilised AuNPs have gained attention since they constitute a NP analogue to the flat substrate SAMs. As the conventional SAMs, these NPs have shown promising results regarding the possibility to provide surface functionality to the particles [181]

Since the AuNPs using the former Turkevich-Frens method are obtained in water, thus, being compatible with enzyme immobilisation, this synthesis approach was utilised to prepare negatively charged citrate-coated AuNPs in the range of 15-40 nm. AuNPs were used to construct conductive platforms for DET based coupling of enzymes in this work.

1.4.2. Adsorption of redox enzymes on AuNP surface: improved bioelectrocatalysis

For the adsorption of enzymes on AuNP modified surfaces, different approaches, such as direct immobilisation [182, 183], immobilisation using self-assembled monolayers of thiols [184], polyelectrolyte films, etc., have been used, as well as reconstitution on the surface *via* apo-enzyme was exploited [185, 186]. In all these cases, DET based bioelectrocatalysis was established. The observed DET can simplistically be explained by the fact that a AuNP comes into close contact with the active centre of an enzyme and functions as an intermediate electron hopping site in the heterogeneous ET

pathway [187]. It is worth noting that quite few enzymes, e.g., bilirubin oxidase [182], laccase [183], can achieve very effective bioelectrocatalysis when immobilised directly on unmodified, i.e., negatively charged citrate-coated AuNPs. In most of other cases, the AuNP surface has to be modified by particular surface active compounds to optimise the enzyme adsorption on the surface; otherwise, the enzymes adsorb in improper orientation or/and lose their native conformation (hence, their activity) due to random and nonoptimised positioning on the AuNP surface (Fig. 21).

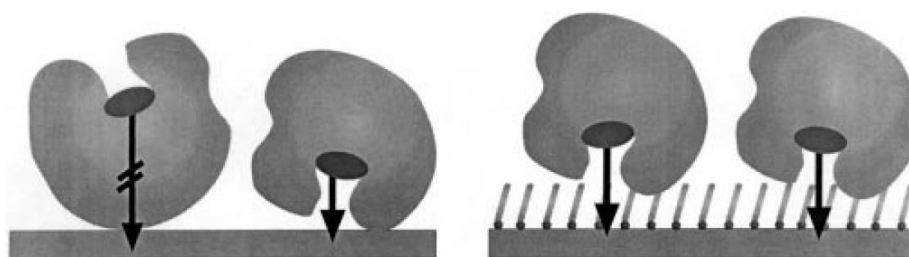


Figure 21. Enzymes immobilised by non-specific absorption (left) and in an orientated way on a chemically functionalised surface (right). Adopted from [188].

Besides chemical patterns, enzyme conformation (and, of course, bioelectrocatalysis) is also affected by the surface topology and size of AuNPs. On the whole, it is difficult to predict how bioelectrocatalysis of different enzymes correlates with the size of AuNPs, since in some cases higher bioelectrocatalytic currents were observed at smaller NPs [189] while in other ones, oppositively, at larger AuNPs [190]. The current understanding is that the bioelectrocatalytic activity of the enzymes, adsorbed on different size AuNPs, is dependent not only on the enzyme-AuNP interaction, but also on other components of the bioelectrocatalytic layers, e.g., thiols or polyelectrolytes used to (inter)link AuNPs [191].

The selection of conditions for the successful DET based wiring of enzymes on the AuNP surface mainly depend on the enzyme size and structural as well as surface properties, such as pI, the degree of hydrophobicity/hydrophilicity. In general, adsorption of enzymes (proteins) on solid surfaces is a very complex process, which involves structural changes in

the enzyme, dehydration of parts of the enzyme and the surface, and direct interactions (electrostatic, hydrogen bond formation, van der Waals interactions) between the enzyme and the surface [192].

1.5. Surface functionalization of a planar gold and AuNPs

In this chapter the functionalization approaches of the surface of a planar gold (Au) and AuNPs, employed to design DET based EBFC electrodes, are briefly described. The aim of the modification of the surface of a planar Au with certain chemical groups is directed to optimise the effective assembly of AuNPs by a rational approach (Chapter 1.6.3.) While the chemical treatment of the surface of AuNPs may be prerequisite for the establishment of a suitable environment for the DET based binding of certain redox enzymes (Chapter 1.4.2.) or, for the (inter)linking of another layer of AuNPs in the case of the assembly of 3D AuNP structure. In fact, any mono- or bi-functional molecule that has a tendency to bind with Au and AuNP surfaces has potential to be used as an (inter)linker or a binding ligand, respectively. The choice of a particular chemical compound, envisaged to be used for surface functionalization, mainly depends on surface properties of both the surface used for the modification (a planar gold and/or AuNPs) and the elements intended to be attached to that surface (AuNPs and/or enzymes). Additionally, operational conditions such as solution pH, ionic strength, etc., should be considered.

In this work the advantage of surface modification by self-assembled monolayers of thiols and polyelectrolyte films has been taken. More detailed explanations of gold/AuNP surface functionalization by thiols and polyelectrolytes in general, as well as the justification of the choice of a particular thiol and polyelectrolyte used to functionalise the gold and negatively charged citrate-coated AuNP surfaces in the present studies, are given in the following sections of this chapter.

1.5.1. A planar gold: an advantageous electrode material in EBFC design

In the studies of DET based bioelectrocatalysis, a planar gold (Au) was used as a bulk electrode material due to the several main reasons. First of all, thin films of Au are common surfaces used for a number of existing spectroscopic and other analytical techniques, including quartz crystal microbalance with dissipation (QCM-D) technique. QCM-D was used for the careful characterisation of bioelectrocatalysis of EBFC electrodes in this work. Second, Au is a reasonably inert metal: it does not oxidise at temperatures below its melting point, as well as does not react with atmospheric O₂ and most chemicals. Third, Au is known as a reasonably biocompatible material which does not show toxicity to eukaryotic cells [193]. This property is especially valuable considering the fact that the EBFCs, containing gold electrodes in their construction, may be used *in vivo* conditions. Finally, as described below, Au binds different thiols and polyelectrolytes with a high affinity, thus, the functionalised Au surface can be exploited to assembly 3D structures as scaffolds for the designing of beneficial DET based EBFC electrodes [171].

1.5.2. Self-assembled monolayers of thiols

In general, self-assembled monolayers (SAMs) of organic molecules are molecular assemblies formed spontaneously on surfaces by adsorption and further organised into more or less ordered domains [171]. In this section the main features of the SAM of thiols, as well as their formation and properties on Au/AuNP surfaces are reviewed.

Thiols are organic sulphur-based compounds that contain a sulfhydryl head group –SH and an alkyl chain which represents an alkane, alkene, or other carbon-containing group of atoms (Fig. 22). Considering the number of functional groups involved in the structure of a thiol molecule, thiols are accordingly divided into mono- and bi-functional thiols. Mono-functional thiols are consisted of hydrophilic sulfhydryl group as a head group and an alkyl chain as a hydrophobic tail. While bi-functional thiols contain either two distinct functional groups, i.e., a sulfhydryl head group and other hydrophilic terminal group, or two sulfhydryl groups considering so-called di-thiols.

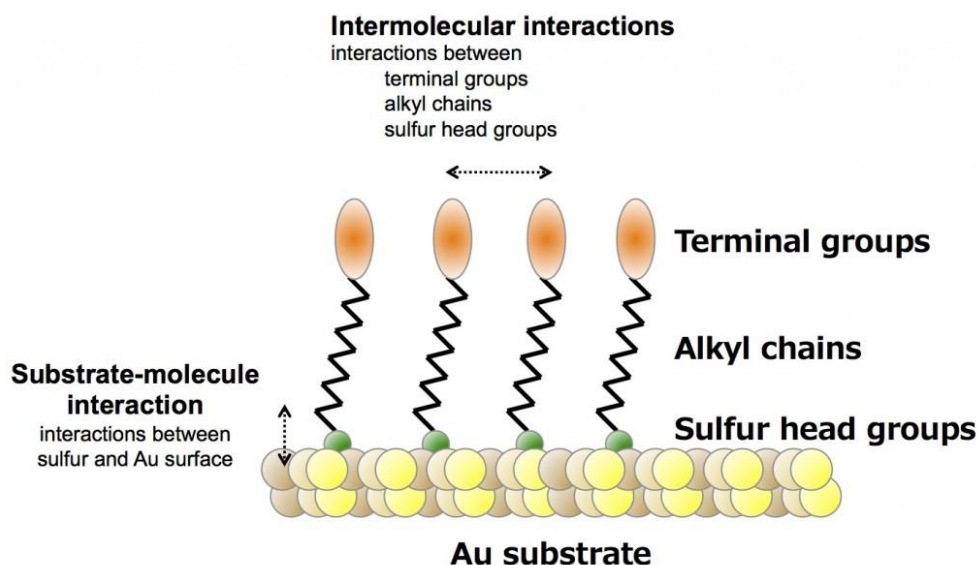


Figure 22. Schematic diagram of single-crystalline SAM of alkanethiolates supported on a gold surface with a (111) crystal structure. The characteristics of the SAM are highlighted. Adopted from [171].

SAMs of thiols has become a very common approach to functionalise Au surfaces (both planar and curved, e.g., AuNPs) since thiol molecules organise a stable structure on gold surfaces *via* strong covalent interaction between a sulphur and gold atoms (S-Au⁰) [194]. The order of a SAM on the surface is affected by intermolecular interactions, e.g., van der Waals interaction between the alkyl chains, and electrostatic interactions between the sulphur head groups and between charged or polar terminal groups (in the case of bi-functional thiols) (Fig. 22). A SAM on a solid surface can be easily prepared by adding the drop of a certain thiol solution on a surface and just letting the thiol molecules to rearrange to a SAM for a few hours. A simple preparation procedure, good stability under ambient conditions, and easy control of chemical properties (polarity, surface charge, etc.) of the surface, when choosing the particular terminal groups of a thiol molecule, enables the usage of SAMs to optimise the surface environment for the immobilisation of enzymes in DET facile orientation. The attachment of enzymes on the surface may be performed *via* hydrophobic, electrostatic, or covalent interactions. Usually hydrophobic interaction leads to enzyme unfolding and denaturation.

Thus, the positioning of enzymes on the surface of an electrode using either electrostatic or covalent interactions is desired. For this reason, bi-functional thiols having charged terminal groups, such as amino or carboxyl, are commonly used for enzyme immobilisation on an electrode without losing their bioelectrocatalytic activity.

SAMs are themselves nanostructures with a number of useful properties (Fig. 22). For example, the thickness of a SAM is typically 1-3 nm; they are the most elementary form of a nanometer-scale organic thin-film material.

In this work a novel bi-functional thiol, N-(6-mercapto)hexylpyridinium (MHP), was used, which contains a positively charged pyridinium group as a terminal group. MHP possesses a pH independent positive charge and effectively attracts negatively charged species from the solution [195, 196]. AuNPs modified by the SAM of MHP was exploited to electrostatically attach cellobiose dehydrogenase (CDH) enzymes at neutral pH where a total charge of these enzymes is negative (pI of CDH is ~4.2). The SAM of MHP was also exploited as an (inter)linker layer for the formation of mono- or multi-layers of negatively charged AuNPs by layer-by-layer assembly (Chapter 3.5.).

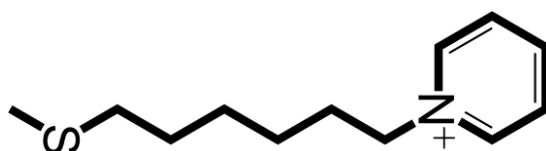


Figure 23. The molecular structure of N-(6-mercapto) hexylpyridinium (MHP).

1.5.3. Polyelectrolyte films

Polyelectrolytes (PEs) represent a unique class of polymers, which are macromolecules bearing highly charged groups. According to the charge they possess, PEs can be referred to polyanions, polycations, and polyampholytes (possess both cationic and anionic repeat groups). The fractional charge of the PE may be varied by changing the pH, counter-ion concentration, or ionic strength of the solution [197].

The electrostatic interaction between PEs and charged surfaces plays an important role in a large number of applications of interest in colloid and

interface science [197]. An example is the layer-by-layer (LbL) deposition, where a PE film acts as an (inter)layer to build different multi-layered structures on solid surfaces. The thickness of those multi-layered structures can be expanded from nanometres to micrometers. The self-assembly method of constructing layers from oppositely charged PEs and NPs is currently a very prospective approach with novel application possibilities in electrochemistry [198]; especially, when DET based bioelectrocatalysis is exploited and 3D conductive scaffolds for enzyme immobilisation are desired.

In this work a linear cationic biological polymer, poly-L-lysine (PLL) (Fig. 24), was employed to assembly mono- and multi-layers of negatively charged AuNPs using the consistent LbL methodology (Chapter 1.6.3.). The isoelectric point of PLL is ~ 9.0 , thus it is an excellent positively charged (inter)linker (modifier) of negatively charged surfaces in the solutions of pHs lower than 9.0. It is also important to emphasise that PLL is a biocompatible PE [199]. The two above mentioned facts are especially important for justifying the use of PLL films in the nanostructures intended to be used for biomedical applications.

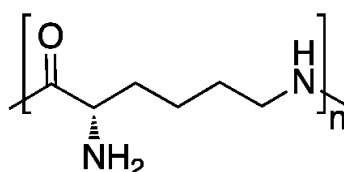


Figure 24. The molecular structure of repeating units in poly-L-lysine (PLL).

1.6. Assembly of mono- and multi-layers of AuNPs on solid surfaces

The crucial point in the preparation of conductive AuNP scaffolds for enzyme immobilisation, which enables effective DET based bioelectrocatalysis, has been the development of simple, reliable assembly routes to form highly dense AuNP films. However, the deposition of densely-packed AuNP films is complicated due to the fact that charged AuNPs are normally surrounded by so-called electric double layer, which strongly limits their approach to one another. Interactions between NPs and other types of interfaces can be predicted by the DLVO theory briefly described in the following chapter [200].

The following ways to overcome this limitation and to form highly dense AuNP structures in this work were used: (i) simple drop-casting of AuNP dispersion and allowing noncontrolled self-assembly during solvent evaporation (Chapter 1.6.2.); (ii) the layer-by-layer (LbL) assembly (highly controllable adsorption) driven by the optimisation of the AuNP-surface interaction when chemically modifying the surface as well as additionally reducing the interparticle repulsion while increasing ionic strength of the AuNP dispersion. The precise control over the assembly conditions using LbL deposition is responsible for the range of novel properties (e.g., flexibility) of the assembled AuNP nanostructures (Chapter 1.6.3.).

1.6.1. DLVO theory: the role for NP stability and assembly

The Derjaguin, Landau, Verwey and Overbeek (DLVO) theory [201] of colloidal stability defines an electrostatic repulsion and van der Waal's attraction as two main factors governing stability of the colloidal suspension. In addition to these two balancing potential energy contributions, steric interactions due to the coating play an important role when polymers or proteins are present on the colloid surface [192]. Within the DLVO-framework, all interactions between colloids and surfaces with electrostatic origin are treated and described in terms of distance-dependent interaction potentials, i.e. $U(D)$ where U is the free energy and D is the surface separation. The sum of attractive and repulsive interactions gives the characteristic total potential profile with a peak in the repulsive regime at a few nanometers of separation.

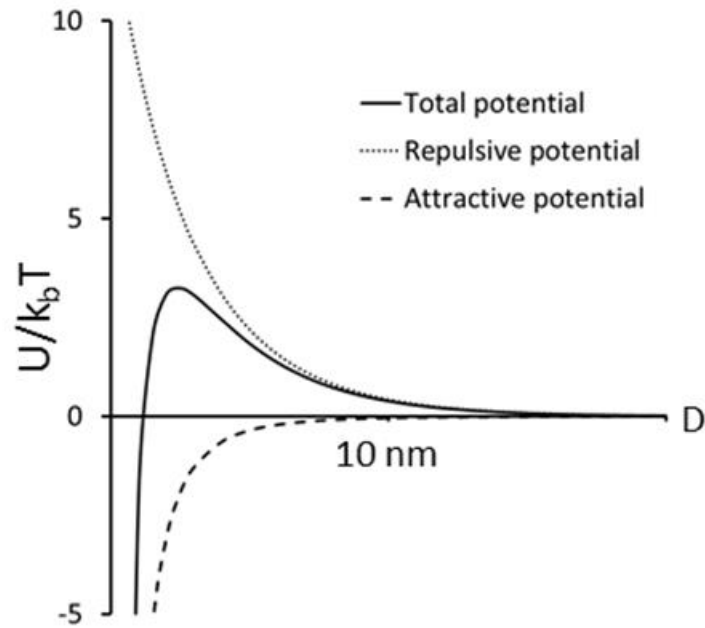


Figure 25. Distance dependent interaction potentials between two surfaces in accordance with DLVO-theory. The solid line is the sum of the attractive Van der Waals interactions and repulsive double layer interactions.

The interaction potential is commonly scaled to thermal energy, k_bT , where k_b is the Boltzman constant and T is the temperature. For considerations regarding particle stability, this scaling is highly relevant since the kinetic energy of approaching particles will be in the same range. Thus, it can be intuitively understood that in order to retain stability of particle dispersion for longer periods, the peak describing the repulsive potential must exceed a few k_bT .

1.6.2. Drop-casting self-assembly

A densely-packed self-assembly of NPs can be achieved on a solid surface by drop-casting approach when a solution of NPs is spread on a solid surface and, upon evaporation of the solvent, the long-range dispersion forces between the NPs or between the NPs and the surface cause the NPs to self-organise into mono- or multi-layer structures. At higher concentrations NP form multilayer regions rather than a monolayer with long range order [202].

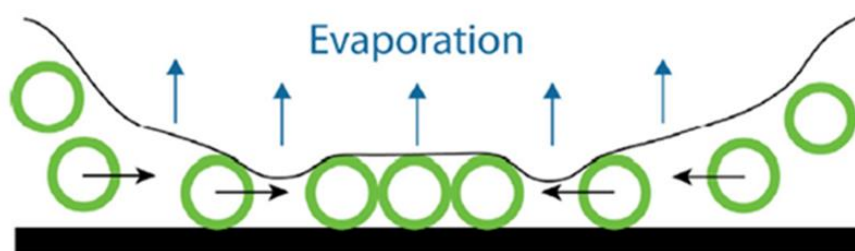


Figure 26. Self-assembly of colloidal NPs by drop-casting.

It has been demonstrated that simply drop-casted 3D structures of AuNPs, which were then impregnated with enzymes, enabled superior bioelectrocatalysis, that is, high current density and superior operational stability of enzymatic bioelectrodes [14, 203, 204]. These findings suggest that this simple approach of AuNP-nanostructure assembly could be employed to prepare efficient and possibly commercially competitive scaffolds of bioelectrochemical devices. Nevertheless, it should be kept in mind that the drop-casted films of AuNPs may have the problem of the reproducibility in surface coverage and thickness and, thereby, be not suitable for the careful fundamental studies and optimisation of enzyme bioelectrocatalysis, e.g., down to a single NP level. In the studies of the present work, drop-casted AuNP films were solely used to modify electrodes for the designing of carbohydrate/O₂ EBFCs for a proof-of-concept demonstration and performance characterisation, but not for the careful characterisation of the kinetics of bioelectrocatalytic processes at enzyme-single AuNP level.

For the latter studies, AuNP layers prepared by highly controllable stepwise assembly, described in the next chapter, were used.

1.6.3. Layer-by-layer self-assembly

The well-defined adsorption of charged AuNPs on a surface can be driven by electrostatic (or covalent) layer-by-layer (LbL) self-assembly, where a thin layer of an oppositely charged film, e.g., a SAM of thiols or polyelectrolyte film, is employed as an (inter)linker to adsorb AuNPs through electrostatic (or covalent) attraction (bonding).

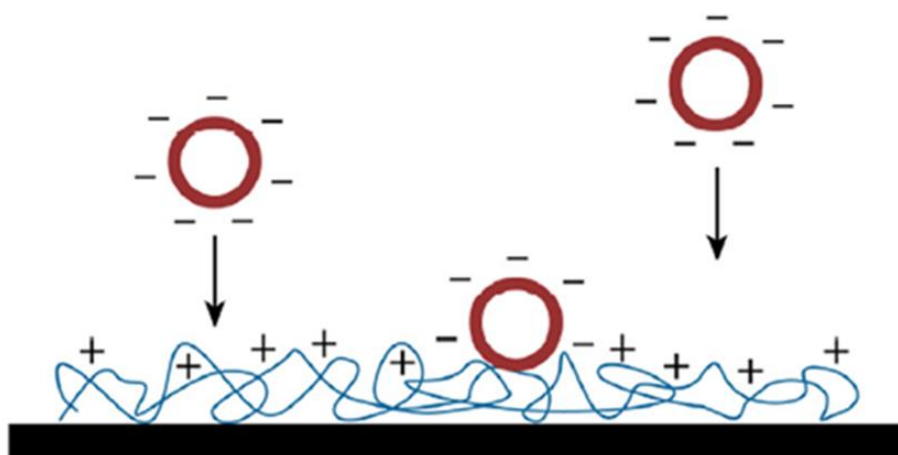


Figure 27. Schematic illustration of electrostatically driven self-assembly of colloidal NPs.

AuNP arrangement on the surface driven by electrostatic interaction can often be described by the model of random sequential adsorption (RSA). RSA results in non-crystalline patterns with short-range order [205]. In the simple RSA model particles adsorb sequentially at random positions on the surface; however, any adsorption event that leads to particle overlap is discounted. The limiting coverage in RSA is around 55% of the area, i.e., after that point it is no longer possible to adsorb more particles [206]. More detailed RSA model description is provided in chapter 1.6.3.1.

One of the main advantages of LbL deposition is the possibility to control the density of AuNP films, e.g., by changing the pH or ionic strength of AuNP dispersion. Thus, the method enables the possibility to assess the correlation between the surface density of AuNPs and the bioelectrocatalytic activity of enzymes adsorbed on the AuNP surface. Moreover, stepwise electrostatic self-assembly provides an opportunity to assemble well-ordered 3D bioelectrocatalytic structures of different thickness, as well as allows a variety of materials to be incorporated within the film structures. Therefore, the LbL assembly can be regarded as a versatile bottom-up nanofabrication technique in the designing of highly powerful DET based EBFC electrodes. It is also worth mentioning that the usage of different (inter)linkers to build a multilayer allows controlling not only bioelectrocatalytic but also viscoelastic properties of this

structure. The viscoelasticity/flexibility of the bioelectrocatalytic structures should be taken into account when considering their application for biomedical purposes. For this reason, two typical positively charged chemical compounds of different molecular weight, poly-L-lysine (PLL) and N-(6-mercapto) hexylpyridinium (MHP), were employed in the present work to electrostatically connect citrate stabilised negatively charged AuNPs. The difference in molecular weight between PLL and MHP is believed to play a crucial role in the adsorption of AuNPs, packing density, and viscoelastic properties of AuNP layer assembled on surfaces chemically modified by these compounds.

1.6.3.1. RSA model for interacting NPs in controlled assembly

Random sequential adsorption (RSA) assumes that NPs are placed one by one at random locations on a surface with uniform binding affinity [205]. In the case of hard NPs, each placement yields an irreversible and fixated NP unless the NP does not overlap with another already bound NP. If so, the placement is unsuccessful and the NP disappears from the surface. The maximum surface coverage that can be obtained by a RSA process is 54.7 % given that all objects are perfectly spherical, have the same size and only interact *via* their hard surfaces (Fig. 28) [206]. Initially all NPs that reach the surface will bind and the early adsorption will therefore be limited by the diffusion of NPs to the surface. Many studies show, that initially NP adsorption is a first-order rate process with respect to the NP concentration [207]. As the surface coverage increases and exclusion effects become important, the deposition rate quickly decreases and saturation coverage will be reached in the limit of long times.

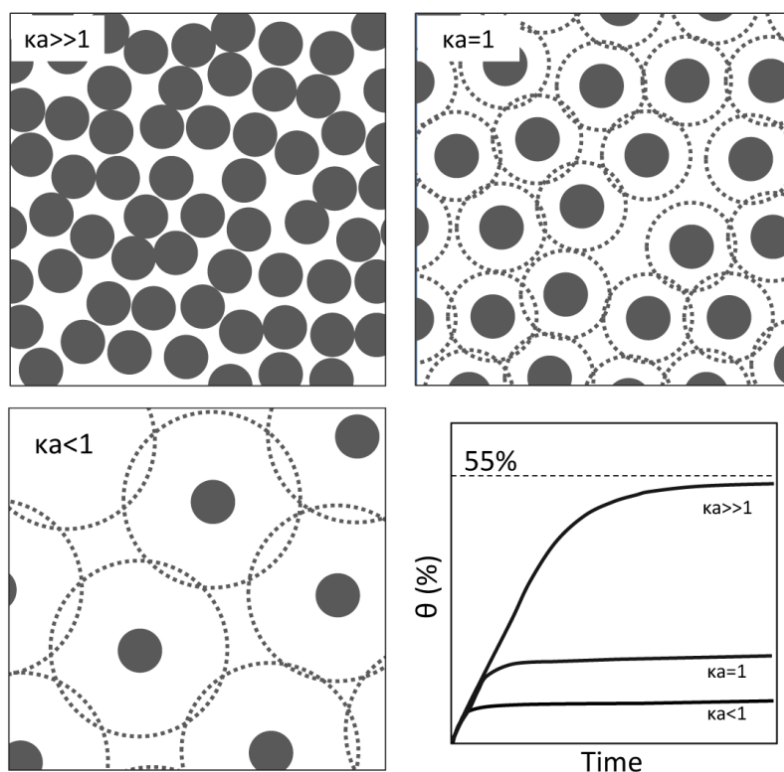


Figure 28. Schematic illustration of randomly adsorbed NPs deposited at different conditions defined by the screening parameter κa . For $\kappa a \leq 1$, the double-layer exceeds the hard core radius, thus acting as a soft shell surrounding the particles. Characteristic curves describing the kinetics of the random sequential adsorption are presented in the lower right corner. Adopted from [208].

As demonstrated in several studies, NPs interacting *via* double-layer repulsion were seen to assemble onto surfaces in accordance with the RSA process. However, according to the model introduced by Adamczyk, because of the electrical double-layers these NPs should be treated as soft spheres with hard cores, rather than purely hard NPs [209]. With decreasing ionic strength, the Debye length (κ^{-1}) increases and the distance of closest approach between particles will increase as well. Within the RSA approximation, increased long-range interactions are equivalent with a thicker soft shell around each particle. Thus, deposition at low ionic strength will give rise to saturation coverage (θ) well below the theoretical jamming limit of 55%. This effect is most relevant for the smallest nanometer-sized NPs, i.e. $\kappa a \leq 1$ (a is the NP radius) whereas it becomes negligible for larger micrometer-sized particles, i.e. $\kappa a \gg 1$, where the hard core exclusion effects dominate.

The dependence θ vs. $\kappa \cdot r_{NP}$ can be modelled by Eq. 18, where r_{NP} is a geometric (“hard”) radius of NPs and κ is a reciprocal of Debye length.

$$\theta = \theta_{jam} \left(\frac{r_{NP}}{r_{NP,eff}} \right)^2 = \theta_{jam} \left(\frac{r_{NP} \cdot \kappa}{r_{NP} \cdot \kappa + \lambda} \right)^2 = \theta_{jam} \left(\frac{r_{NP}}{r_{NP} + \lambda \cdot \kappa^{-1}} \right)^2 \quad (18)$$

$$\kappa = \sqrt{\frac{2F^2 z_i^2 c_i}{\varepsilon \varepsilon_0 RT}} \quad (19)$$

F and R are Faraday and Molar gas constants, respectively; z_i and c_i are the valence and the concentration of electrolyte ions; ε and ε_0 are the dielectric constant of the solution and vacuum, respectively; and T is absolute temperature.

In Eq. 18 $\theta_{jam} = 0.547$ [206]. Effective (“soft”) radius, $r_{NP,eff}$, of nanoparticles (Eq. 18) accounts for the repulsive as well as other forces acting between NPs, which result into a diluted NP monolayer, *i.e.*, $\theta < \theta_{jam}$. In case of electrostatic repulsion of NPs the effective radius can be estimated as a multiple of Debye screening length, $\lambda \kappa^{-1}$ (Eq. 18). Parameter λ , to the highest degree, accounts for the effect of electrical surface potential of NPs on θ [210, 211]. However, λ depends also on κ and r_{NP} [211] and obviously is dependent on all interactions that should be taken into theoretical modelling of inter-particle interaction potential at the interface. Kooij [212], however, demonstrated that accounting only for particle-particle electrostatic repulsion satisfactorily describes θ for diluted NP monolayer. Following this, the parameter λ was calculated by assessing inter-particle distance at which particle-particle electrostatic energy, U_{pp}^{dl} , is equal to kT .

$$\frac{U_{pp}^{dl}}{kT} = \frac{B_{pp}}{r} \cdot \exp[-\kappa \cdot r_{NP}(\bar{r} - 2)] \quad (20)$$

where $\bar{r} = r_{cc} / r_{NP}$ is the centre-to-centre distance between two nanoparticles divided by a geometric radius of NP. The coefficient B_{pp} is given by:

$$B_{pp} = \left(\frac{4\pi\varepsilon\varepsilon_0 \cdot kT \cdot r_{NP}}{e^2} \right) \left(\frac{\bar{\Psi}_p + 4\gamma\Lambda\kappa \cdot r_{NP}}{1 + \Lambda\kappa \cdot r_{NP}} \right)^2 \quad (21)$$

$$\bar{\Psi}_p = \frac{\Psi_p \cdot e}{kT}; \gamma = \tanh\left(\frac{\bar{\Psi}_p}{4}\right) \text{ and } \Lambda = \frac{\bar{\Psi}_p - 4\gamma}{2\gamma^3} \quad (22)$$

The equations describing electrostatic interparticle interaction were, in this work, used for assessing theoretical dependence of surface coverage, θ , by AuNPs on the ionic strength of the solution. It should be mentioned that $\theta = 1$ corresponds to hexagonal, close packing of AuNPs, when the maximal packing by RSA (θ_{jam}) reaches only 0.547 of the packing.

1.7. Characterisation of bioelectrocatalytic AuNP-enzyme nanostructures by E-QCM-D technique

The understanding the physicochemical properties, e.g., bioelectrochemical and viscoelastic properties, of AuNP-enzyme nanostructures and particularly their relationship to the structure and composition is a key step in order to manipulate and optimise their effective application in bioelectrochemistry. However, it is not a simple task to determine the total amount of the elements of each layer involved into bio-nanostructure. Electrochemical methods can in general only detect redox proteins and AuNPs that are in electronic contact with an electrode. In the present work electrochemical methods were thus combined with quartz crystal microbalance with dissipation (QCM-D) technique for quantifying the total amount of AuNPs and enzyme molecules attached to the surface of a gold sensor, as well as evaluate the bioelectrocatalytic properties of the AuNP-enzyme layer. Moreover, QCM-D also enabled the assessment of viscoelastic (rheological) characteristics of 2D and 3D nanobiostructures.

1.7.1. QCM-D method: the principle

The QCM-D technique is based on measuring the resonance characteristics of a quartz crystal oscillator operating in shear mode. Due to its piezoelectric properties, the mechanical oscillation of the quartz can be excited by applying an oscillating electric field across the crystal. Once excited, the free mechanical oscillation can be monitored by measuring the decaying electric field (i.e., mechanically caused voltage oscillations). From the analysis of

voltage decay curve the resonance frequency, f , and the dissipation, D , are deduced (Fig. 29). Tracking the changes of the two parameters, Δf and ΔD , induced by the material adsorbing on the crystal (gold surface), allows characterizing adsorption processes and structural changes of the surface adlayer in real time. The time resolution of the QCM-D technique is in principle limited by the decay time of the oscillation which is in the range of range of milliseconds.

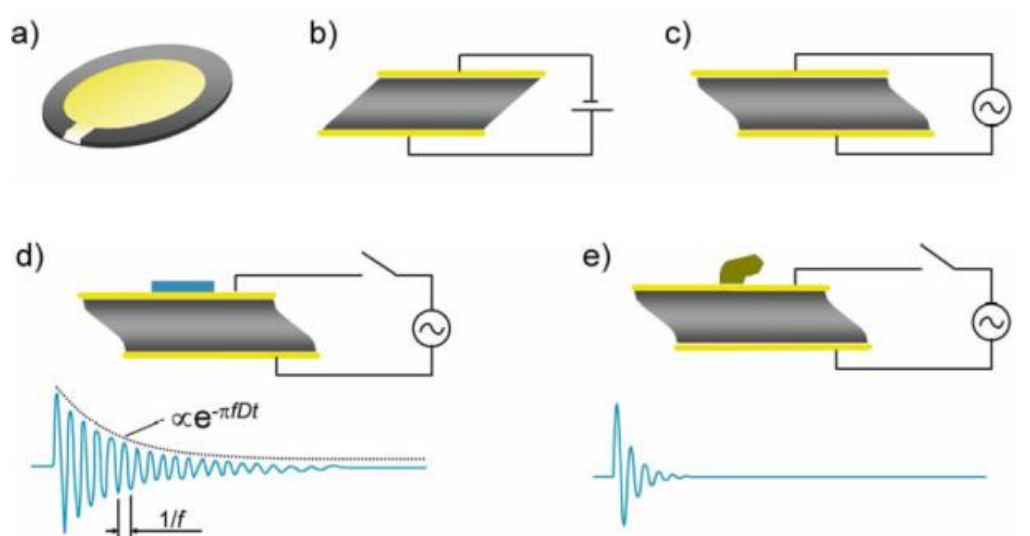


Figure 29. Schematic presentation of the QCM-D working principle. The piezoelectric quartz crystal is sandwiched between two gold electrodes (a). The application of an electric field across the crystal results in shear motion of the crystal (b). Resonance in the shear motion can be excited with an oscillating field (applied voltage) of appropriate frequency (c). After disconnecting the driving circuit, the freely decaying oscillation of the crystal is monitored by measuring a voltage decay on the electrodes (d, e). The temporal change in the crystal's movement, $A(t)$, can be fitted to the dependence $A(t) = A \exp(-\pi f D t) \sin(2\pi f t + \varphi)$ in order to extract the resonance frequency, f , and the dissipation, D . The attachment of a rigid mass (d) to the crystal's surface will mainly lead to a decrease in f ($D \approx 0$), while a soft (viscoelastic) mass (e) will strongly affect D . Monitoring changes in f and D allows thus to follow interfacial processes in real time.

1.7.1.1. Sauerbrey equation

In 1959 Sauerbrey published a paper [213] describing the linear relationship between applied load on the oscillating quartz crystal and the induced Δf_n . According to the Sauerbrey equation the mass can be calculated from Δf_n according to:

$$\Gamma = \frac{C}{n} \cdot \Delta f_n \quad (23)$$

where Δf_n , Γ , and n represent frequency change, adsorbed mass per unit area, and overtone number, respectively. C is the mass sensitivity constant ($17.7 \text{ ng/cm}^2 \times \text{Hz}^{-1}$). The relation holds under the assumption that the adsorbed mass is less than the mass of the crystal, is uniformly distributed and rigidly attached with no slip or deformation during the oscillation of the crystal. In other words it is applicable for non-dissipative, homogeneous stiff adsorbed films.

1.7.1.2. Modelling

Appropriate selection of analytical models to interpret QCM data is critical, and recent advances have allowed a more structured approach for specific experimental situations.

Most films dissipate energy due to their viscoelastic properties, therefore applying the Sauerbrey equation will result in an underestimation of the mass. The viscoelastic Voigt model provides a modelling from which the correct mass together with viscous and elastic components of the adsorbed film can be determined by including the dissipative energy loss in the fitting of Δf_n and ΔD_n at several overtones ($n = 3, 5, \text{ and } 7$) [214].

$$\Delta f = -\frac{1}{2\pi\rho_q h_q} \left(h_f \rho_f \omega - 2h_f \left(\frac{\eta_b}{\delta_b} \right)^2 \frac{\eta_f \omega^2}{\mu_f^2 + \omega^2 \eta_f^2} \right) \quad (24)$$

$$\Delta D = -\frac{1}{2\pi f \rho_q h_q} \left(2h_f \left(\frac{\eta_b}{\delta_b} \right)^2 \frac{\mu_f \omega}{\mu_f^2 + \omega^2 \eta_f^2} \right) \quad (25)$$

where ω is the angular frequency of oscillation ($\omega = 2\pi f$), μ the shear elasticity and η the shear viscosity. The viscous penetration depth of the shear wave in the bulk is denoted as δ_b and film thickness as h_f .

Strictly speaking, the underlying assumption for the viscoelastic model apply to a homogenous film [215], however, it is also used in the calculation of mass of films consisting of discrete NPs.

1.7.1.3. Model independent analysis (MIA)

For the adsorption of discrete NPs it was demonstrated by finite element modelling (FEM) that the dissipative energy loss originates from stiffness/strength of interaction in the surface-particle interface and the liquid surrounding the particle, also known as the hydration shell [216], that is dragged around by the particle during the crystal oscillation [217]. Therefore during deposition of particles the fractional amount of liquid surrounding the particles should decrease as the surface coverage increases and by that the dissipative energy loss [216]. Tellechea et al [218] presented so called a model independent analysis (MIA) of QCM-D data in which the theoretical 100% surface coverage is obtained as the intercept of $\Delta f_n/n$ from $\Delta D_n/\Delta f_n$ vs $\Delta f_n/n$ plot. Since the fractional trapped liquid is assumed to be diminished to occupy only the void spaces between the densely packed NPs the Sauerbrey relation holds for the calculation of the mass from the intercept of $\Delta f_n/n$ since the dissipation energy is assumed to approach zero. Using this method Ohlsson et al [219] has shown that the mean particle diameter can be determined as the apparent thickness of the adsorbed layer by dividing the Sauerbrey mass with the particle density (calculated as hexagonal prism average density). However the method requires a surface coverage of approximately 10-20 % as it is under these conditions the particles are close enough to share their hydration shells and by that decrease $\Delta D_n/(\Delta f_n/n)$ [220]. In this work the method was used to investigate if it holds for NPs adsorbed on different linkers and if it is applicable also at higher surface coverages.

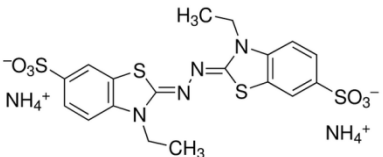
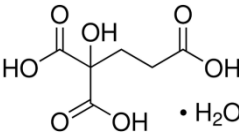
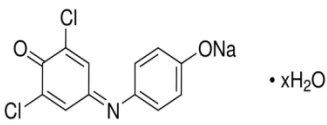
2. MATERIALS, EQUIPMENT, AND METHODS

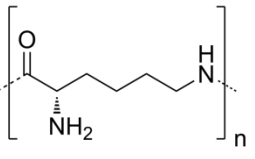
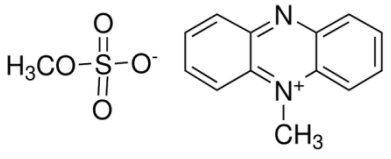
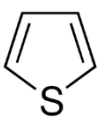
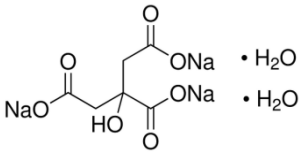
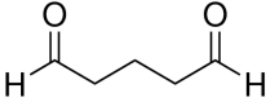
2.1. Materials

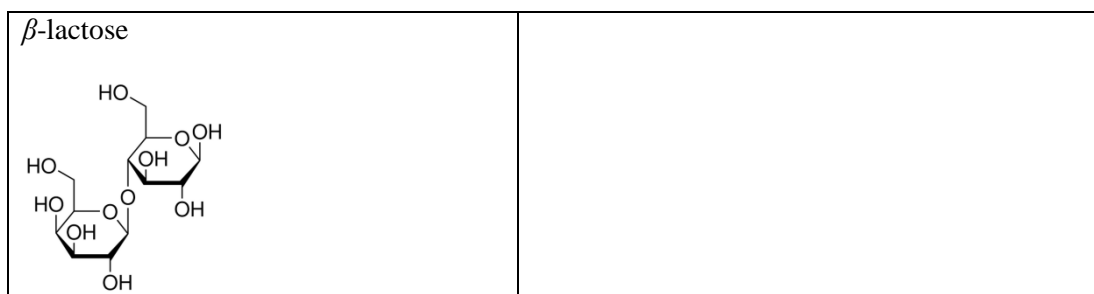
2.1.1. Reagents

All the chemicals were of analytical grade.

Table 4. The list of chemical reagents used for the PhD project and the sources where they were obtained:

Reagent	Source
Absolute ethanol (>99 %)	Kemetyl AB (Haninge, Sweden)
Ammonium sulphate ((NH ₄) ₂ SO ₄)	Sigma-Aldrich (St. Louis, MO, The USA)
2,2'-azino-bis(3-ethylbenzothiazoline-6-sulfonic acid) diammonium salt (ABTS) (C ₁₈ H ₂₄ N ₆ O ₆ S ₄)	
	
Citric acid monohydrate (HOC(COOH)(CH ₂ COOH) ₂ ·H ₂ O)	
	
2,6-dichloroindophenol sodium salt hydrate (DCIP) (C ₁₂ H ₆ Cl ₂ NNaO ₂ ·H ₂ O)	
	
Hydrogen peroxide (H ₂ O ₂)	
Hydrogen tetrachloroaurate(III) trihydrate (HAuCl ₄ ·3H ₂ O)	
Potassium chloride (KCl)	

Sodium chloride (NaCl)	
Sodium phosphate (Na ₂ HPO ₄)	
Sodium phosphate dibasic dihydrate (NaH ₂ PO ₄ ·2H ₂ O)	
Sodium sulphate (Na ₂ SO ₄)	
Poly-L-lysine (C ₆ H ₁₄ N ₂ O ₂) 0.1 % (w/v) in water with MW of 70-150 kDa (for calculations the average MW of 110 kDa was taken).	Sigma-Aldrich (Irvine, Ayrshire, The UK)
	
90% phenazine methosulfate	Sigma-Aldrich (Berlin, Germany)
	
Absolute ethanol (95%)	
Sodium fluoride (NaF)	
Sulphuric acid (H ₂ SO ₄)	
Thiophene	Merck (Darmstadt, Germany)
	
Trisodium citrate dihydrate (C ₆ H ₅ Na ₃ O ₇ ·2H ₂ O)	
	
25% glutaraldehyde	AppliChem GmbH (Darmstadt, Germany)
	
D-(+)-glucose	



2.1.2. Solutions

Buffers and all other solutions were prepared using ultra high quality (UHQ) water (18.2 M Ω ·cm) purified with PURELAB UHQ II system from ELGA Labwater (High Wycombe, UK).

Nitrogen (N₂), used to establish anaerobic conditions while bubbling through the working solutions, was obtained from AGA Gas AB (Sundbyberg, Sweden) and additionally purified using Gas Clean Filters from Varian BV (Middelburg, The Netherlands).

Buffer solutions used:

- (i) PBS (pH 4) - 50 mM phosphate buffer solution, pH 4, with 100 mM sodium sulphate, (pH adjusted with citric acid monohydrate);
- (ii) C-PBS (pH 3.4-5.4) - 50 mM citrate-phosphate buffer solution with 100 mM potassium chloride;
- (iii) PBS (pH 6.4-8.2) - 50 mM phosphate buffer solution with 100 mM potassium chloride;
- (iv) A-PBS (pH 6) - 50 mM acetate- phosphate buffer solution, pH 6.0, with 100 mM KCl.

The 1M solutions of glucose were prepared in a certain buffer solution at least 24 h before use to allow glucose to mutarotate and to reach the equilibrium of α - and β - forms.

2.1.3. Redox enzymes

Seven preparations of redox enzymes were used in the thesis work: (i) three anodic enzymes, *viz.*, cellobiose dehydrogenases (CDHs) from *Corynascus thermophilus* (CtCDH) and *Humicola insolens* (HiCDH), and glucose oxidase (GOx) from *Aspergillus niger*, and (ii) four cathodic enzymes – laccases (Lcs) from *Trametes hirsuta* (ThLc) and *Trichaptum abietinum* (ThLc), horseradish

peroxidase (HRP), and bilirubin oxidase from *Myrothecium verrucaria* (*MvBOx*). CDH, GOx, BOx, and HRP enzymes were exploited for the designing and characterisation of the complete glucose/O₂ EBFCs, whereas Lcs – for separate cathode studies on the 2D and 3D nanostructures of AuNPs.

2.1.3.1. Anodic redox enzymes

Highly purified *CtCDH*, kindly provided by Dr. Roland Ludwig (BOKU: University of Natural Resources and Life Sciences, Vienna, Austria), was purified from the culture supernatant of ascomycete *Corynascus thermophilus*, CBS 405.69, which was obtained from the Centraalbureau voor Schimmelcultures (Baarn, The Netherlands). The enzyme stock solution of 8.4 mg ml⁻¹ in a 20 mM sodium acetate buffer, pH 5.5, was stored frozen at -18 °C and used without further purification and characterisation.

HiCDH, recombinantly produced in the culture of ascomycete *Aspergillus oryzae* according to previously reported protocols [221], was provided by Novozymes A/S (Bagsvaerd, Denmark). The homogeneous preparation of *HiCDH* with a MW of 97 kDa, as confirmed by SDS-PAGE (Fig. 30), was stored in a 50 mM sodium acetate buffer, pH 5.5, at -18 °C.



Figure 30. SDS-PAGE of *HiCDH*. Line 1 - molecular mass rulers; lines 2-4 correspond to *HiCDH* preparations (0.6 µg, 1.3 µg, and 2.5 µg, respectively) applied on SDS-PAGE.

For electrode biomodification stock solutions of the CDH enzymes were thawed at +4 °C and diluted with UHQ water until 6 mg ml⁻¹ concentration was achieved.

GOx powder of 295 U mg⁻¹ enzymatic activity was purchased from Appli-Chem GmbH (Darmstadt, Germany) and used without further purification and characterisation. When needed, the GOx solution was freshly prepared in a A-PBS (pH 6) from lyophilised powder of the enzyme.

2.1.3.2. Cathodic redox enzymes

MvBOx was recombinantly produced in *Aspergillus oryzae*, in accordance with previously reported protocols [222] was provided by Novozymes A/S (Bagsvaerd, Denmark). The highly purified preparation of the enzyme, as confirmed by SDS-PAGE (Fig. 31), was stored in a 50 mM Tris/acetate buffer, pH 8 at -18 °C.

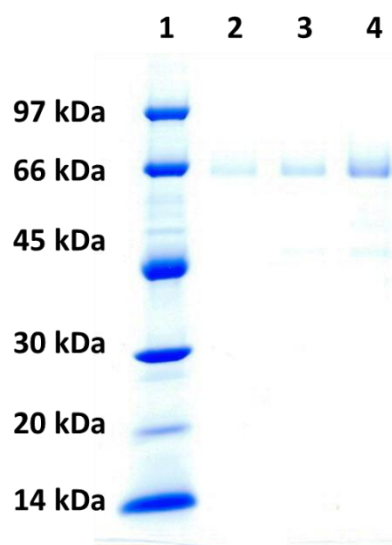


Figure 31. SDS-PAGE of *MvBOx* preparation. Line 1 - molecular mass rulers; lines 2-4 correspond to *MvBOx* preparations (0.6 µg, 1.3 µg, and 2.5 µg, respectively) applied on SDS-PAGE.

For biocathode modification stock solution of the *MvBOx* enzyme was thawed at +4 °C and diluted with UHQ water until 6 mg ml⁻¹ concentration was achieved.

HRP of 1000 U mg⁻¹ enzymatic activity, (for ABTS and 95% ethanol were obtained from Sigma-Aldrich (Berlin, Germany)). When needed, HRP solution was freshly prepared from lyophilised enzyme powder in A-PBS (pH 6).

Lc obtained from the basidiomycete *Trametes hirsuta* (*ThLc*), strain *T. hirsuta* 56, was provided by the laboratory collection of the Moscow State University of Engineering Ecology (Moscow, Russia). The homogeneous preparation of the enzyme with MW of 70 kDa (glycosylation 12%, pI 4.2) as verified by SDS-PAGE was isolated from a culture medium as described previously [116]. The stock solution of *ThLc* with 14.4 mg ml⁻¹ enzyme concentration in 100 mM phosphate buffer, pH 6.5, was stored frozen at -18 °C.

The homogeneous *TaLc* was purified at the Department of Molecular Microbiology and Biotechnology of VU Institute of Biochemistry (Vilnius, Lithuania). The purified enzyme appeared as a single band on 14 % SDS-PAGE (Fig. 32) showing MW of 51 kDa.

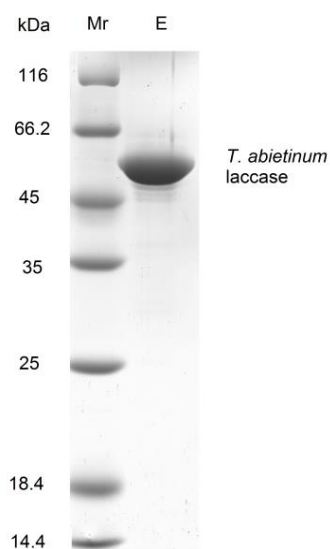


Figure 32. SDS-PAGE of the purified *TaLc*. Line Mr - molecular mass rulers; E - corresponds to the preparation of *TaLc* applied on SDS-PAGE.

2.2. Equipment

Potentiostats:

- a) Potentiostat PGSTAT 30 with GPES3 v3.2 software ECO-Chemie/Autolab (Utrecht, The Netherlands);
- b) Compact potentiostat Ivium CompactStat from Ivium Technologies (Eindhoven, Netherlands);
- c) Potentiostat EC Epsilon 50 from BASi (West Lafayette, IN, the USA).

Spectrophotometers:

Simultaneous electrochemical and quartz-crystal microbalance with dissipation (E-QCM-D) measurements were performed using the QWEM401 electrochemistry cell (Q-Sense, Gothenburg, Sweden).

NICOMPTM submicron particle sizer from Nicomp 380 ZLS (Santa Barbara, California).

2.3. Methods

2.3.1. Synthesis of N-(6-mercapto) hexylpyridinium chloride

N-(6-mercapto) hexylpyridinium (MHP) chloride was synthesised at the Department of Organic Chemistry, Centre for Physical Sciences and Technology (Vilnius, Lithuania). The synthesis scheme (SI, Fig. S1) and detailed description of synthesis procedure as well as analytical data of synthesised compounds are provided in Supplementary Information. MHP was dissolved in water at a concentration of 1 mM and used for experiments without further dilution

2.3.2. Synthesis of phenanthroline derivatives

1,10-phenanthroline monohydrate was commercial and the other phenanthroline derivatives (PDs) were synthesised by the procedure described [223]. The PDs were presented as PMH, 5NP, 5AP, 5A6NP, and 56DAP. Their full titles and chemical structures are given in Table 3. The 10mM solutions of PDs were prepared in organic solvent – acetonitrile.

2.3.3. AuNP synthesis

The dispersion of spherical gold nanoparticles (AuNPs) was prepared by following the reduction procedure of HAuCl_4 with sodium citrate in aqueous solution as reviewed elsewhere [224]. Briefly, 50 ml of 1 mM HAuCl_4 solution in water was heated to about 90 °C while stirring. Then, a certain amount (depending on a desired size of AuNPs, Fig. 33) of 1% (w/w) trisodium citrate solution was added to HAuCl_4 solution under vigorous stirring. The heating was continued for 15 min with stirring, and 10 min without stirring.

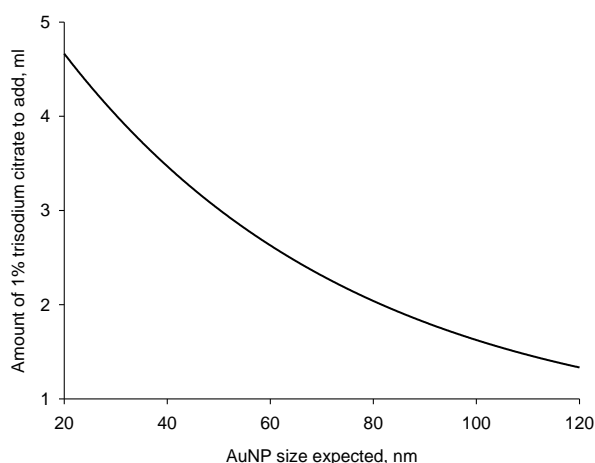


Figure 33. Graph for careful selection what volume of 1% (w/w) trisodium citrate solution should be added to 50 ml of 1 mM HAuCl_4 solution to get the desired size AuNPs. The method was derived experimentally by initial guidelines provided in [225].

For the E-QCM-D analysis, where experiments were carried out using the dispersions of AuNPs of different ionic strength, while changing the concentration of NaCl from 0 to 20 mM, sodium citrate was removed by dialysis procedure using cellulose membrane with a cut-off size of 12-14 kDa against UHQ water in the volumetric ratio of 1:50 for 12 h at +4 °C.

For electrochemical measurements solely, the non-dialysed AuNP dispersion was concentrated by centrifugation at 10000×g for 30 min in 1 ml Eppendorf tubes. Then, about 98 % of supernatant was removed, and the precipitated AuNPs were re-suspended by ultrasonication for 7 min using Transsonic 460/H from Elma GmbH&KG sonicator (Singen, Germany). Samples were then stored as 50 times concentrated AuNP dispersion at +4°C.

2.3.4. AuNP size estimation

2.3.4.1. Surface plasmon absorbance spectrophotometry

The size of AuNP was evaluated by comparing (overlapping) the optical absorption spectra against the extinction efficiency vs. wavelength generated by MiePlot software: <http://www.philiplaven.com/mieplot.htm> [226].

2.3.4.2. Atomic force microscopy

AuNP mean diameter and uncertainty as standard deviation was determined by recording NP diameter distribution using atomic force microscopy after drying their dispersion on mica surface pre-treated with PLL. Commercial AFM (MultiMode 8 SPM with a NanoScope V control unit, Bruker AXS, Santa Barbara, USA) was set to tapping mode in air and settings were continuously adjusted by the Scan Asystauto control software.

2.3.5. AuNP ξ -potential estimation by electrophoretic light scattering

A measurement cuvette and electrodes were cleaned with UHQ water. The cuvette was filled with 2.5 ml of AuNP dispersion (no dilution). Then the cuvette was connected with the electrodes and loaded in the instrument. The applied voltage was automatically set by the software and the 3 cycles of 100 s were applied.

2.3.6. Enzyme homogeneous activity measurements

The *ThLc* activity and electrochemical measurements were performed in 50 mM phosphate buffer (pH 4.0) containing 0.1 M Na₂SO₄ (adjusted by citric acid). The appearance of a coloured product during the oxidation of ABTS catalysed by *ThLc* was exploited to evaluate the activity (turnover number) of *ThLc*

2.3.7. Electrode preparation

2.3.7.1. Graphite rod electrode preparation

Graphite rod electrodes (GREs) (99.999%, low density, 0.3 cm diameter with active surface geometric area of 0.071 cm²), used as working electrodes, were purchased from Sigma-Aldrich (Berlin, Germany).

In order to obtain a smooth and clean surface of GREs before their modification, the electrodes were hand-polished with fine emery paper, rinsed with ethanol and UHQ water, and dried in air at room temperature. The basic method for rapid and simple electrode modification with a mediator and an enzyme was reported in the previous study [227].

2.3.7.2. Graphite rod electrode modification by GOx, and the GOx modified electrode coating by polythiophene layer

In order to prepare GOx-coated GREs, 3 μl of 40 mg ml^{-1} GOx solution were deposited on the electrode surface, later allowing the water to evaporate at room temperature. Afterwards, electrodes were stored for 20 h over the 5% solution of glutaraldehyde at +4 °C in a closed vessel as described in our previous studies [227] to cross-link enzymes adsorbed on the electrode surface. Before the experiments, the GOx-modified electrodes were washed with UHQ water to remove non-cross-linked enzyme molecules and the side surface of the electrodes was sealed into epoxy to prevent its contact with the solution.

To prepare GOx-modified GREs covered with additional polythiophene (PTP) layer (Chapter 3.1.), the electrodes were immersed into polymerisation solution, i.e., 50 mM A-PBS, pH 6.0, containing 200 mM of dispersed thiophene and 50 mM of dissolved glucose at room temperature, for a definite period of time. Additionally, control electrodes were prepared keeping the GRE/GOx-modified electrodes in A-PBS in the absence of one of the components, i.e., glucose or thiophene, essential for PTP polymerisation process. The first control electrode was incubated in A-PBS containing 50 mM of glucose ('control solution I') and the second one in A-PBS containing 200 mM of thiophene ('control solution II'), respectively. Prior to amperometric measurements, the GOx and GOx/PTP-modified GREs, further in the text denoted as GRE/GOx- and GRE/GOx/PTP-modified electrodes, respectively, were thoroughly washed with UHQ water.

2.3.7.3. Graphite rod electrode modification by 1,10-phenanthroline derivatives and enzymes

In order to screen different phenanthroline derivatives (PDs) as ET mediators for GOx enzyme (Chapter 3.2.), the cleaned GREs were consequently modified by PDs and GOx (GRE/PDs/GOx). For this purpose, 3 μl of 10 mM solution of a certain PD was dropped and distributed on the GRE surface for three times. After each drop, the electrode was dried at room temperature. The next drop was only added after completely drying the previously added one. The PDs-treated GRE surfaces were then modified with the 3 μl solution containing 10 mg ml^{-1} GOx and dried at room temperature. Then these modified electrodes were stored for 20 h over a 5% solution of glutaraldehyde at +4 °C in a closed vessel.

PDs/GOx-modified GREs were compared with the GRE, which was only modified with GOx. The six different surfaces that were prepared are further abbreviated in the thesis as follows: (i) GOx-modified GRE (GRE/GOx); (ii) PMH and GOx-modified GRE (GRE/PMH/GOx); (iii) 5AP and GOx-modified GRE (GRE/5AP/GOx); (iv) 5NP and GOx-modified GRE (GRE/5NP/GOx); (v) 5A6NP and GOx-modified GRE (GRE/5A6NP/GOx) and (vi) 56DAP and GOx-modified GRE (GRE/56DAP/GOx).

The GRE/5AP/GOx bioanodic electrode used in the designing of a complete glucose powered EFC (Chapter 3.3.1.) was prepared on the cleaned GRE three times dropping 3 μL of both the 10 mM of 5AP and 10 mg ml^{-1} of GOx solutions, respectively. After each drop (5AP and GOx, respectively), the electrode was dried at room temperature. The 5AP-, GOx-, and HRP-modified GREs were simply prepared three times putting and drying 3 μL of a certain solution (10 mM of 5AP, 10 mg ml^{-1} of GOx or 10 mg ml^{-1} of HRP) on the unmodified GRE surface. The biocathodic electrode based on a bienzyme system (GRE/HRP/GOx) was prepared by a similar drying procedure as described above, on the GRE surface adding one drop of the 10 mg ml^{-1} of HRP and GOx solutions, respectively. The modified electrodes were kept for 15 min over a 25 % glutaraldehyde solution at +4 °C in a closed vessel.

All modified electrodes were thoroughly rinsed with UHQ water to remove non-cross-linked enzyme molecules, dried at room temperature and, lastly, their lateral surface was isolated with a silicone tube. The prepared electrodes were stored in a closed vessel over A-PBS buffer, pH 6.0, at +4 °C until they were used in experiments.

2.3.7.4. Gold electrode cleaning and their modification by AuNPs and enzymes

Polycrystalline gold (Au) disk electrodes from Bioanalytical Systems (BASi) (West Lafayette, IN, the USA) with geometric areas of 0.031 cm² were mechanically cleaned by polishing on Microcloth from Buehler (Lake Bluff, IL, USA) using a 0.1 μm alumina suspension from Struers (Copenhagen, Denmark) to produce a mirror-like surface. The electrodes were rinsed with UHQ water, immersed in freshly prepared Pyranha solution (mixture of volumetric 3:1 concentrated H₂SO₄ and 30% H₂O₂ solution) for 20 min, and after washed with Milli-Q water. After that the Au electrodes were electrochemically cleaned in 0.5 M H₂SO₄ by cyclic voltammetry; 20 cycles between -0.1 V and +1.9 V vs. NHE at a scan rate of 0.1 V s⁻¹. Finally, the electrodes were rinsed with Milli-Q water and dried under the air flow before modification by gold nanoparticles (AuNPs). Three-dimensional (3D) AuNP modified Au electrodes were fabricated by the drop casting method, as reported in previous publications [8, 14, 29, 204]. Briefly, 1.5 μl of the concentrated AuNP dispersion was pipetted on top of the cleaned Au electrode and dried at room temperature. The casting and evaporation steps were repeated 5 times to build 3D AuNP layer on planar Au electrode; resulting electrode is denoted as Au/AuNP. Thereafter, the electrodes were rinsed with UHQ water.

For the cathode biomodification (Chapter 3.3.2.2.), 10 μl of *MvBOx* solution (6 mg ml⁻¹) was applied onto the Au/AuNP electrode surface. The electrodes were covered with an Eppendorf tube and left for incubation for 2 h. Afterwards, the electrodes were carefully rinsed with 50 mM phosphate buffer, pH 7.4.

For the anode biomodification (Chapter 3.3.2.1.), a positively charged thiol, i.e., MHP, was adsorbed on the Au/AuNP electrode surface before the CDH enzyme immobilisation. Specifically, 10 μl of 1 mM MHP solution was deposited on AuNP modified Au electrode and kept for 1 h under moisturised atmosphere at room temperature. The resulting thiol modified Au/AuNP electrode was thoroughly rinsed with UHQ water, and then a 3 μl drop of CDH enzyme solutions (6 mg ml^{-1}) was deposited on the thiol modified Au/AuNP electrodes as described above. The electrodes were kept under moisturised atmosphere for 30 min at room temperature, and then allowed to dry in air.

2.3.8. Evaluation of formed PTP layer by ATR-FTIR spectroscopy

IR spectroscopy measurements were performed by Frontier ATR-FTIR spectrometer from Perkin Elmer (The USA), which was equipped with mercury cadmium telluride (MCT)/liquid-nitrogen detector. Scanning resolution of 2 cm^{-1} was applied and the interval of scanning was in the range from 600 cm^{-1} to 4000 cm^{-1} . The PTP samples (Chapter 3.1.2.) for ATR-FTIR were prepared in aqueous solutions containing: (i) 200 mM of dispersed thiophene, 1 mg ml^{-1} of dissolved GOx and 50 mM of glucose; (ii) 200 mM of dispersed thiophene and 5 mM of dissolved H_2O_2 . The polymerisation lasted for 48 h at room temperature. After the polymerisation samples were lyophilised in order to get dried products of reaction. According to the same procedure a control sample containing only 200 mM of dispersed thiophene was prepared.

2.3.9. Electrochemical measurements

2.3.9.1. Electrochemical detection of PTP deposition

In order to verify the formation of PTP layer on the GOx modified electrode and its influence on the activity (Chapter 3.1.1.) and stability (Chapter 3.1.3.) of the enzyme, an amperometric sensor model was chosen. The relationship between amperometric signal and the substrate glucose was analysed using a two variable hyperbolic equation, which is in agreement with Michaelis-Menten kinetics (Eq. 7). Kinetic parameters, i.e., $K_{m(app.)}$ and the maximal

current intensity (I_{\max}), measured in glucose containing A-PBS, were correspondingly equated to the hyperbolic function parameters a and b. The raising $K_{m(app.)}$ and decreasing I_{\max} values were considered as the main evidence that GOx was covered by polymerisation products, which most likely formed a diffusional barrier for substrate glucose and/or EP mediator phenazine methosulfate.

Three-electrode electrochemical cell system was used for all amperometric measurements. GRE/GOx- and GRE/GOx/PTP-modified electrodes were used as working electrodes. Pt wire was used as a counter electrode. An Ag/AgCl electrode in 3 M KCl (Ag/AgCl/3M KCl) was used as a reference electrode. Anodic current (GOx- and GOx/PTP-modified GREs) dependence on glucose concentration was studied at +300 mV vs Ag/AgCl/3M KCl. All experiments were carried out inside a Faraday-cage in 50 mM A-PBS, pH 6.0, containing 100 mM KCl at ambient temperature (at 25 °C). Solution in electrochemical cell was stirred by magnetic stirrer at rotation rate of 120 rpm. Between the measurements, electrodes were stored in appropriate solutions (polymerisation solution, control solution I or II) at room temperature or, in the case of stability test, kept over A-PBS, pH 6.0, at 4°C in a closed vessel.

2.3.9.2. Amperometric and potentiometric studies of phenanthroline derivatives

Three-electrode electrochemical cell system was used for amperometric and accordingly two-electrode system for potentiometric measurements. The GRE/GOx or GREs/PDs/GOx were used as a working, Ag/AgCl_{sat.} (0.197 V vs. NHE) as a reference, and Pt wire was used as an auxiliary electrode. All amperometric and potentiometric experiments were performed at room temperature in A-PBS (pH 6). The solution was stirred continuously. Amperometric signal dependence on substrate concentration was studied at +600mV vs. Ag/AgCl_{sat.} and the responses were presented as plots representing changes in current vs. glucose concentration. In order to investigate the usage of PDs for the design of biofuel cells, the potentiometric measurements with

PDs-modified GRE/GOx electrodes and PDs non-modified GREs were performed.

2.3.9.3. Cyclic and linear voltammetry

Cyclic voltammograms used to characterise of the bioelectrochemical characteristics of individual EBFC electrodes were recorded using a three-electrode electrochemical cell in quiescent solutions. More details, e.g., scan rates and solution compositions, are given in captions of particular figures.

2.3.9.4. EFC performance characterisation

The main parameters of a complete EFC were obtained in a two-electrode electrochemical cell connecting a biocathode as a working electrode and a bioanode as a combined reference and counter electrode. Polarisation curves were obtained recording the current in the circuit while changing the voltage from open-circuit voltage (OCV) to 0 mV with a scan rate of 0.1 mV s⁻¹. The OCV was recorded as an absolute value. The power outputs of the EFC were calculated after multiplying the values of a current density and potential. Operational stability tests were performed in chronoamperometric mode at a potential corresponding to the potential of the EFC at its maximal power density. All measurements were performed in quiescent solutions, under aerobic conditions. The standard deviations using three separate measurements were calculated as an uncertainty of basic electrochemical parameters of complete EFCs.

2.3.10. E-QCM-D measurements and data analysis

In chapter 3.4. to quantify AuNPs and *ThLc* molecules attached to the surface, and to evaluate the bioelectrocatalytic properties of the AuNP-Lc layer on a planar gold electrode, simultaneous electrochemical and QCM-D measurements were performed using the QWEM401 electrochemistry cell (Q-Sense, Gothenburg, Sweden). All measurements were made at +22±0.02 °C. The planar surface of gold covered QCM-D sensor (Au_{QCM-D}) was modified with PLL, AuNPs and the enzyme by the following procedure. PLL was adsorbed on the QCM-D sensor and then *ThLc* was deposited. The resulting

structure was noted as Au_{QCM-D}-PLL-*ThLc*. Afterwards, the AuNP layer was adsorbed following by adsorption of *ThLc* (Au_{QCM-D}-PLL-*ThLc*-AuNPs-*ThLc*). We assumed that this final *ThLc* adsorption step resulted into the enzyme adsorption only on AuNPs since adsorption of *ThLc* directly on PLL covered gold sensor was already blocked by the first *ThLc* adsorption step.

The primary data from the QCM-D measurements are the changes in the resonant frequency (Δf) and the dissipation (ΔD) of energy of the oscillating QCM-D sensor. These changes have been recorded at the fundamental frequency of the crystal and three overtones (3rd, 5th, and 7th). An example of data from the typical experiment is shown in Fig. 55. Dissipation is defined as $D = E_{\text{dis}}/(2\pi E_{\text{st}})$, with E_{dis} being the energy dissipated during one period of oscillation and E_{st} being the energy stored [228]. The dissipation is dimensionless with dissipation units (DU). One DU corresponds to the ratio $E_{\text{dis}}/(2\pi E_{\text{st}})$ being equal to 10^{-6} .

Prior to use, the QCM-D gold sensor was rinsed with 99.5% pure ethanol and water, then dried under a flow of nitrogen gas, and placed in the Harrick plasma cleaner, model PDC-32G, for 10 min at the highest plasma intensity setting. For measurements the sensor was mounted into a QCM-D cell module and a stable baseline, *i.e.*, Δf and ΔD response *vs.* time, was obtained in water at a fixed flow rate of 100 $\mu\text{L}/\text{min}$. Except for enzyme adsorption, when the flow was stopped, all further steps of the experiment were carried out using the same flow rate. After the stabilisation of the baseline, PLL adsorption on the surface of the QCM-D gold sensor was obtained by pumping 0.002% PLL solution in water for 5 min. Next, the sensor was rinsed by pumping water for 10 min, which was sufficient to reach a new stable frequency and dissipation reading. The same washing procedure was repeated after adsorption of *ThLc* and AuNPs. Adsorption of the enzyme was achieved by filling the chamber above the electrode with 0.7 mg ml^{-1} *ThLc* in buffer solution (pH 4) and keeping it over the surface for 15 min while mixing occasionally (switching on pumping for a half minute each three minutes). AuNP assembly was conducted by passing the AuNP dispersion with different salt concentrations over the

electrode surface for 30 - 90 min. The Δf and ΔD values obtained after rinsing with water were used for calculations of mass since after rinsing the bulk density and viscosity remained the same as during the monitoring of the baseline.

Adsorption of PLL on Au_{QCM-D} and the first layer of *ThLc* resulted in relatively small Δf and negligible ΔD . Thus, the adsorbed mass of PLL was calculated using both Sauerbrey equation and Voigt modelling [229]. During AuNP and the second *ThLc* layer adsorption measurements with QCM-D quite large Δf and ΔD were observed (Fig. 55). Even though the magnitude of changes in D and f during the assembly of separate components of the PLL-*ThLc*-AuNPs-*ThLc* structure (especially, for the AuNP adsorption step) was quite different, the D/f ratio ranged from 0.001 (PLL) to 0.05 (*ThLc* and AuNPs) revealing that the entire structure was rigid (Fig. S4). The mass of all the PLL-*ThLc*-AuNPs-*ThLc* structure components could be evaluated using Sauerbrey formula but, to obtain better estimates of the adsorbed mass of the AuNP-enzyme layers, the Voigt viscoelastic model was fitted to the QCM-D data as it is recommended for the structures having significant D and f changes [230].

During the viscoelastic modelling the adsorbed layer density (or thickness) and two viscoelastic parameters, *i.e.*, shear viscosity and shear modulus, were set as fitting parameters. The fluid density ($\rho = 1 \text{ g/cm}^3$), fluid viscosity ($\mu = 1 \text{ g/ms}$), and thickness (or density) of adsorbed layer were set constant. The modelling was performed with QTools software using the 3rd, 5th, and 7th overtones.

The mass of the enzyme layer on the PLL treated QCM-D sensor, *i.e.*, *ThLc* in structure Au_{QCM-D}-PLL-*ThLc*, was calculated as a mass difference of the total mass of PLL and *ThLc* (protein) layer minus the mass of PLL layer measured before enzyme adsorption. The calculation of masses was done using Voigt modelling.

In order to fit the data of the adsorbed AuNP and *ThLc* layers having extremely different properties modelling was performed using a two-layer

system, *i.e.*, “layer 1” and “layer 2”. “Layer 1” corresponded to a structure Au_{QCM-D}-PLL-*ThLc*, and “layer 2” consisted of the AuNP layer in the structure Au_{QCM-D}-PLL-*ThLc*-AuNPs. In order to evaluate the viscoelastic properties and thickness of the PLL-*ThLc* layer (“layer 1”), it was assumed that the density of the adsorbed protein layer was 1.20 g/cm³ [231]. All modelled “layer 1” parameters were set as constant parameters, then “layer 2” was included and the properties of the AuNP layer were modelled. The thickness, *i.e.*, the diameter (22 nm) of AuNPs, was set as a constant parameter of the modelled AuNP layer. For the evaluation of the thickness of the enzymatic layer adsorbed on AuNPs, similarly as in the previous modelling analysis, the fitted viscoelastic properties and thickness of the PLL-*ThLc*-AuNP layer were used for modelling as fixed parameters. Note that for the „background“ modelling of the adsorbed PLL-*ThLc*-AuNP layer the thickness was arbitrarily chosen and was assumed to be a constant. However, as demonstrated by Larsson *et al* [232], the adsorbed layer thickness primarily affects the density value of the adsorbed layer and not the adsorbed mass, or shear modulus and shear viscosity. Thereby, the fitted viscoelastic properties of the structure Au_{QCM-D}-PLL-*ThLc*-AuNPs could be assumed as fixed parameters to estimate the correct mass of AuNP bound layer of *ThLc*.

The best fit between the Voigt model and the experimental data for all the overtones was obtained considering the minimum value of the error function χ^2 . The mass (g cm⁻²) was obtained after multiplying the modelled values of density and thickness.

The experimental number of adsorbed AuNPs and *ThLc* molecules per geometric area was estimated by dividing the sensed mass by the mass of one AuNP or the mass of *Lc* molecule, respectively. The mass of one AuNP was obtained by calculating the mass of a sphere with a diameter of 22 nm and density of 19.3 g/cm³.

After each adsorption step, *i.e.*, for QCM-D electrode structure denoted as Au_{QCM-D}-PLL-*ThLc*, Au_{QCM-D}-PLL-*ThLc*-AuNPs, and Au_{QCM-D}-PLL-*ThLc*-AuNPs-*ThLc*, the electrode was assessed by linear sweep voltammetry (LSV)

at 1 mV/s potential scan rate using compactstat from IVIUM (Eindhoven, Netherlands). Ag/AgCl/3 M KCl inserted into the outlet of the QCM-D flow cell served as a reference and a sputtered ring of platinum on the glass window of the cell as a counter electrode, respectively. The volume above the sensor was about 100 μ l. LSVs were recorded under the flow (100 μ L/min) of the buffer solution in the QCM-D cell.

2.3.11. Evaluation of kinetic constants characterising bioelectrocatalytic reduction of O₂ at laccase modified AuNPs

The kinetic currents, i_{DET} and i_{bio} , given by Eqs. 26-27 were described based on the kinetic scheme presented in Fig. 54, *i.e.*, adopting the approach elaborated by Climent *et al* [233]. Following this work the maximal bioelectrocatalytic current of oxygen reduction as well as current dependence on the applied potential is described by the following equations:

$$i_{\text{max}} = nFA\Gamma k_5 = nFA\Gamma \frac{k_{\text{cat}}[O_2]}{K_M + [O_2]} \quad (26)$$

$$k_5 = \frac{k_{\text{cat}}[O_2]}{K_M + [O_2]} \quad (27)$$

$$i = \frac{i_{\text{max}}}{1 + \exp\left[\frac{F}{RT}(E - E_{T1}^{0'})\right] + \frac{k_5}{k_0} \exp\left[\frac{\alpha F}{RT}(E - E_{T1}^{0'})\right]} \quad (28)$$

These equations were fitted to the experimentally recorded current dependence on the applied potential measured by LSV measurements (as exemplified by Fig. 59). For the fitting Mathcad version 15.0 was used. The parameters used for the fitting and the results are summarised in the text of chapter 3.4.3., Table 7.

3. RESULTS AND DISCUSSION

3.1. Enzymatic polymerisation of polythiophene by immobilised glucose oxidase

In this study a self-encapsulation of glucose oxidase (GOx) from *Aspergillus niger* within polythiophene (PTP) layer was investigated. The polymerisation of thiophene was initiated by hydrogen peroxide (H_2O_2) produced in GOx catalysed glucose oxidation reaction. H_2O_2 acted as an oxidiser generating free radicals, which initiated the polymerisation reaction (See chapter 1.2.3.2.). The influence of PTP layer on GOx bioelectrocatalytic activity and stability was determined by the evaluation of amperometric signal. The formation of enzymatically induced formation of the PTP layer over GOx modified graphite rod electrode (GRE) was confirmed by attenuated total reflectance – Fourier transform infrared (ATR-FTIR) spectroscopy based investigation.

3.1.1. Dependence of $K_{m(app)}$ and I_{max} values of GRE/GOx/PTP-modified electrodes on the duration of PTP polymerisation

The GOx was immobilised on a GRE as described in chapter 2.3.8.2. and the amperometric signal was registered gradually increasing glucose concentration from 0.25 to 100 mM. This experiment was conducted in order to verify the quality of the freshly prepared GRE/GOx-modified electrode, which was later used for PTP polymerisation. Afterwards, the GRE/GOx-modified electrode was rinsed with UHQ water and then immersed for a certain period of time into the 50 mM A-PBS, pH 6.0, containing 200 mM of thiophene and 50 mM of glucose (polymerisation solution). Lastly, the GRE/GOx/PTP-modified electrode was washed with UHQ water and the current response to different glucose concentrations in an electrochemical cell was measured. This route was repeated at certain time intervals as long as completely vanishing anodic currents were observed (Fig. 34a).

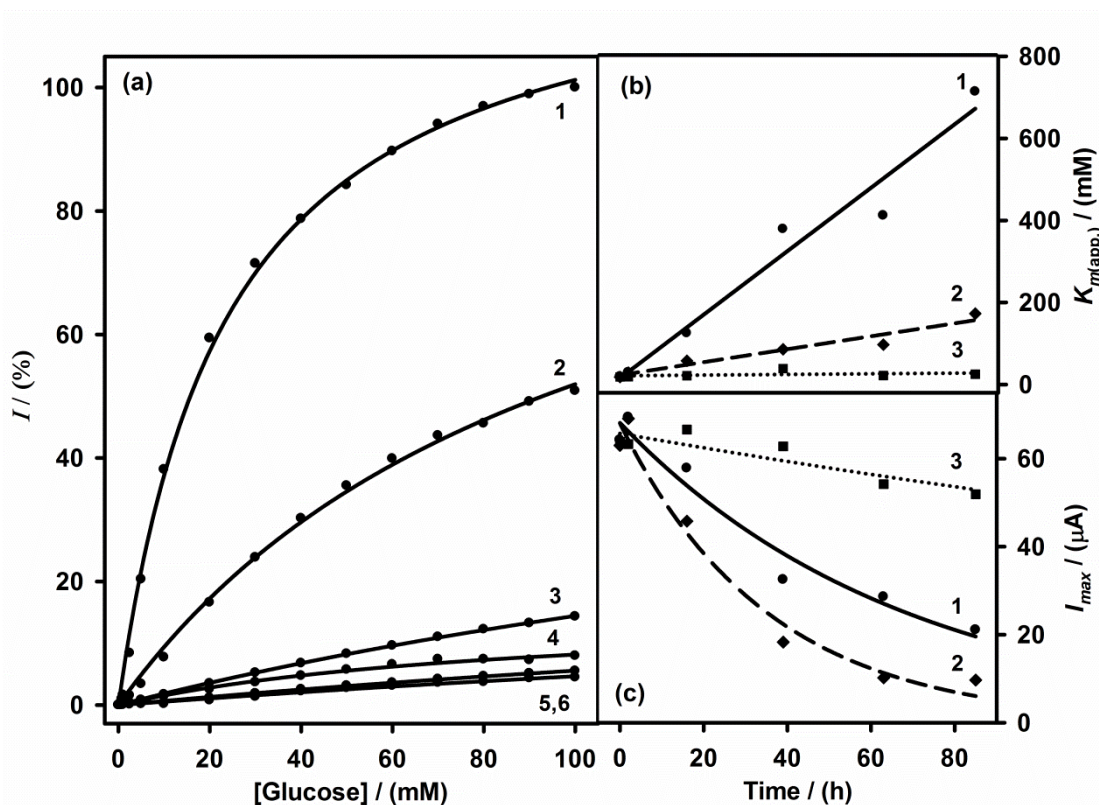


Figure 34. (a) Amperometric glucose calibration curves obtained with GOx modified GRE before (curve 1) and after immersing into the A-PBS, pH 6, containing 200 mM thiophene and 50 mM glucose (polymerisation solution) at room temperature (curve 2 - 2 h, 3 - 16 h, 4 - 39 h, 5 - 63 h, and 6 - 85 h). Amperometric measurements were performed at 300 mV vs. Ag/AgCl/3 M KCl in A-PBS, pH 6.0, containing 2 mM of PMS, continuously stirring at room temperature. Estimated $K_{m(app.)}$ (b) and I_{max} (c) values for glucose vs. duration of incubation in polymerisation solution (curve 1) as well as in control solution I^c (curve 2) and control solution II^c (curve 3) at room temperature

It was estimated that for GRE/GOx-modified electrode (before its covering by PTP) I_{max} was equal to $64.2 \pm 2.0 \mu A$ and $K_{m(app.)}$ accordingly to 18.9 ± 2.0 mM (Fig. 34a, curve 1; Table 5). While after keeping this electrode in polymerisation solution for 85 h, the values of I_{max} and $K_{m(app.)}$ changed to $21.1 \pm 12.1 \mu A$ and 714.0 ± 38.2 mM (Fig. 34a, curve 6; Table 5), respectively. Hence, after 85 h of polymerisation, the I_{max} decreased three times, while the $K_{m(app.)}$ increased approximately 37 times when comparing to the values determined for GRE/GOx-modified electrode. Due to these changes it is evident that the GRE/GOx/PTP-modified electrode operated in diffusion-limited mode, whereas GRE/GOx-modified electrode before its coverage with PTP layer operated in kinetic-limited mode. It is important to mention that the higher

$K_{m(app.)}$ value, thereby, extended linear concentration range for glucose detection using GRE/GOx/PTP-modified electrodes might be advantageous for designing glucose biosensors working in media with high glucose concentrations, e.g., food or beverage products.

Table 5. $K_{m(app.)}$ and I_{max} kinetic constants calculated for GRE/GOx/PTP-modified electrode vs control electrodes I and II incubated in "control solution I" and "control solution II", respectively.

Time (h)	GOx/PTP electrode		Control electrode I		Control electrode II	
	$K_{m(app.)}$, mM	I_{max} , μ A	$K_{m(app.)}$, mM	I_{max} , μ A	$K_{m(app.)}$, mM	I_{max} , μ A
0	18.9 \pm 2.0	64.2 \pm 2.0	18.2 \pm 2.0	63.0 \pm 2.0	18.5 \pm 2.0	63.8 \pm 2.0
2	29.2 \pm 2.3	69.4 \pm 2.1	29.1 \pm 2.5	69.1 \pm 1.8	18.9 \pm 2.0	63.3 \pm 2.2
16	125 \pm 13	57.8 \pm 4.7	57.8 \pm 4.1	45.8 \pm 1.3	21.5 \pm 2.0	66.6 \pm 2.2
39	379 \pm 28	32.5 \pm 2.3	86.0 \pm 6.6	18.3 \pm 0.7	38.7 \pm 7.5	62.8 \pm 5.5
63	412 \pm 39	28.6 \pm 6.8	97.1 \pm 4.1	10.2 \pm 0.22	21.9 \pm 3.6	54.2 \pm 2.9
85	714 \pm 382	21.1 \pm 12.1	173 \pm 23	9.69 \pm 0.81	25.2 \pm 3.4	51.9 \pm 2.5

In order to determine whether the significant increase in $K_{m(app.)}$ was caused by a diffusional barrier formed by the polymer layer or because of some other effects, e.g., GOx inactivation or detachment from the surface of an electrode, etc., control measurements were performed. During the preparation of control electrodes the same approach was applied as discussed before, the only one difference was the composition of incubation solution. Two different control solutions were prepared: one without thiophene and another one without glucose. Any polymer layer was formed on the electrode surface in both cases due to the absence of one of the components essential for the polymerization reaction (Fig. 9).

For this purpose, the first control measurement was performed with the GRE/GOx-modified electrode, which was incubated in 'control solution I' (A-PBS, pH 6.0, containing glucose only) by the same time periods as it was done in the case of polymerisation. It was found that before the electrode incubation in 'control solution I' the estimated I_{max} was 63.0 \pm 2.0 μ A and $K_{m(app.)}$ was 18.2 \pm 2.0 mM, and after 85 h of incubation the I_{max} decreased approximately by 6.5 folds to 9.69 \pm 0.81 μ A, while the $K_{m(app.)}$ increased approximately by 9 folds to 173.0 \pm 23.0 mM (Table 5; curve 2 in Figs. 34b and 34c). $K_{m(app.)}$ evaluated

for the GRE/GOx-modified electrode after its incubation in ‘control solution I’ for 85 h was more than 5 times higher, while I_{max} was almost twice lower when comparing to those parameters obtained with GRE/GOx-modified electrode incubated for the same period of time in polymerisation solution (GRE/GOx/PTP-modified electrode). Changes of both kinetic parameters of the GRE/GOx/PTP-modified electrode clearly indicated that: (i) the deposited PTP layer increased diffusional hindrances for GOx substrates (glucose and/or PMS) and (ii) at the same time formation of PTP layer did not influence the enzymatic activity of GOx, i.e., the estimated I_{max} retained relatively high even if the $K_{m(app.)}$ value decreased significantly; this was not in the case when GOx-modified electrode was incubated in ‘control solution I’. Whereas the GRE/GOx-modified electrode after its incubation for 85 h in ‘control solution II’ (A-PBS, pH 6.0, containing thiophene only) was characterised by the values of I_{max} and $K_{m(app.)}$ corresponding to $51.9 \pm 2.5 \mu\text{A}$ and $25.2 \pm 3.4 \text{ mM}$. During the 85 h period the value of I_{max} decreased by 1.2 times, while the $K_{m(app.)}$ increased by 1.3 times (Table 5; curve 3 in Figs. 34b and 34c). It is evident that there was no significant increase of the $K_{m(app.)}$ during 85 h period, compared to that case when the GOx was covered by the PTP layer. Therefore, the formed PTP layer is main factor that caused the changes of both considered kinetic parameters.

3.1.2. ATR-FTIR evaluation of PTP formed by GOx and H₂O₂ induced polymerisation

In order to evaluate PTP formed by GOx induced polymerisation two samples of PTP were investigated: (i) PTP enzymatically formed by GOx (Fig. 35, spectra 1) and (ii) PTP chemically formed by H₂O₂ (Fig. 35, spectra 2) induced polymerization. The obtained ATR-FTIR spectra of polymerized PTP were comparable with IR spectra observed for chemically formed PTP [234] and PTP derivatives [235, 236] evaluated by other authors. The spectra of not polymerized thiophene treated in the same way as other two aliquots did not show any features that are characteristic of the PTP and are present in the ranges of $1400\text{-}1500 \text{ cm}^{-1}$ and $2600\text{-}2900 \text{ cm}^{-1}$ (Fig. 35, spectra 3). Moreover, ATR-FTIR spectra of PTP formed by both GOx and H₂O₂ induced

polymerisation seemed very similar, because in both cases the H_2O_2 performed the role of the initiator of polymerisation reaction. The only difference was that, in the case of application of GOx, the H_2O_2 was produced in enzymatic reaction while in another case H_2O_2 was directly added to polymerisation solution.

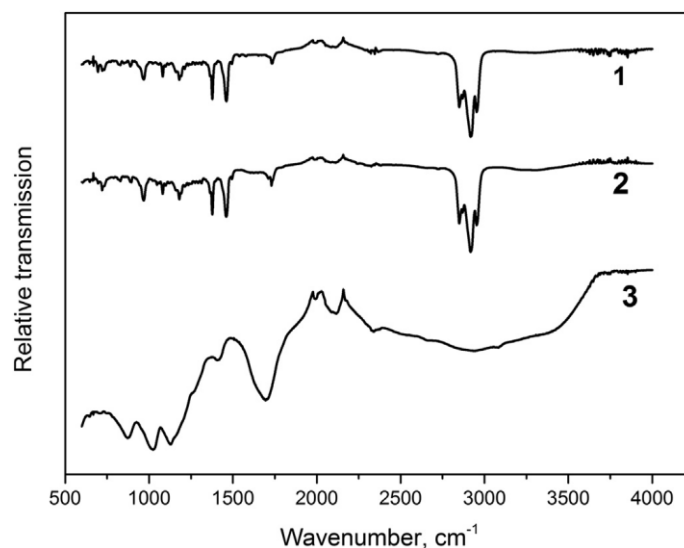


Figure 35. ATR-FTIR spectra of: (1) polythiophene synthesised by GOx induced polymerisation; (2) PTP synthesised by H_2O_2 induced polymerisation; (3) not polymerised thiophene treated and lyophilised in the same way as samples 1 and 2.

3.1.3. Stability of GRE/GOx/PTP-modified electrodes

As presented in Table 5, the $K_{m(app.)}$ value of GRE/GOx/PTP-modified electrode increased tenfold after the incubation of GRE/GOx-modified electrode in polymerisation solution for 16 h. Therefore, GRE/GOx-modified electrodes modified with PTP layer by 20 h lasting polymerisation were chosen for following stability measurements since it was a sufficient period of time to form a thick enough polymer layer on the GRE/GOx-modified electrode surface. The measurements of stability of GRE/GOx/PTP-modified electrode generated current were performed within 624 h (Table 6; Fig. 36). Between measurements the electrodes were stored at $+4\text{ }^\circ\text{C}$ in a closed vessel above a drop of 50 mM A-PBS, pH 6.0.

The values of $K_{m(app.)}$ and I_{max} of GRE/GOx-modified electrode before its modification by PTP were estimated to be $19.0\pm 2.0\text{ mM}$ and $63.2\pm 2.0\text{ }\mu\text{A}$,

respectively. While after the electrode incubation in polymerisation solution for 20 h and the formation of PTP layer, the $K_{m(app.)}$ value increased to 100 ± 6.0 mM and I_{max} decreased to 38.0 ± 1.4 μ A (Table 6). Afterwards, within 624 h the $K_{m(app.)}$ varied relatively insignificantly up to 1.3 times, while a consistent decrease in I_{max} was observed, and at the end of the experiment it decreased fourfold.

Table 6. K_m and I_{max} constants calculated for GOx/PTP-modified electrode, ‘control electrode I’ and ‘control electrode II’ during stability measurements.

Time (h)	GOx/PTP electrode		Control electrode I		Control electrode II	
	$K_{m(app.)}$, mM	I_{max} , μ A	$K_{m(app.)}$, mM	I_{max} , μ A	$K_{m(app.)}$, mM	I_{max} , μ A
-*	19 \pm 2	63.2 \pm 2.0	18.8 \pm 2.0	61 \pm 2.0	19.2 \pm 2.0	65 \pm 2.0
0**	100 \pm 6	38.0 \pm 1.4	133 \pm 8	27.5 \pm 1.2	14.6 \pm 1.5	46.5 \pm 1.2
24	102 \pm 7	30.4 \pm 1.1	119 \pm 7	22.2 \pm 0.7	16.6 \pm 1.8	42.7 \pm 1.3
48	131 \pm 12	29.2 \pm 1.7	115 \pm 6	17.8 \pm 0.6	13.8 \pm 1.5	43.6 \pm 1.2
96	132 \pm 7	22.7 \pm 0.9	129 \pm 5	15.1 \pm 0.4	14.2 \pm 1.7	43.7 \pm 1.4
168	141 \pm 10	23.6 \pm 1.1	141 \pm 5	13.7 \pm 0.3	17.0 \pm 1.4	34.4 \pm 0.8
312	164 \pm 14	18.0 \pm 1.1	139 \pm 3	13.7 \pm 0.2	20.7 \pm 1.5	29.5 \pm 0.7
432	138 \pm 8	15.5 \pm 0.6	166 \pm 6	15.8 \pm 0.4	27.8 \pm 1.7	32.3 \pm 0.7
624	124 \pm 5	9.35 \pm 0.26	132 \pm 5	9.61 \pm 0.23	25.6 \pm 2.4	24.6 \pm 0.8

*Freshly prepared GOx electrodes.

** GOx electrodes after their incubation for 20 h in particular solution (polymerisation solution or control solution I and II).

Control electrodes were prepared for stability experiments as well. For the ‘control electrode I’, which before stability measurement was incubated in ‘control solution I’ for 20 h, the kinetic parameters were as follows: $K_{m(app.)}$ =133.0 \pm 8.0 mM, I_{max} =27.5 \pm 1.0 μ A. While at the end of stability experiment, i.e., after 624 h period, the parameters changed accordingly to $K_{m(app.)}$ =132.0 \pm 5.0 mM, I_{max} =9.61 \pm 0.23 μ A. The maximal generated current decreased approximately by 3 times, therefore GOx stability after incubation in ‘control solution I’ was not high (Curve 2 in Figs. 36b and 36c).

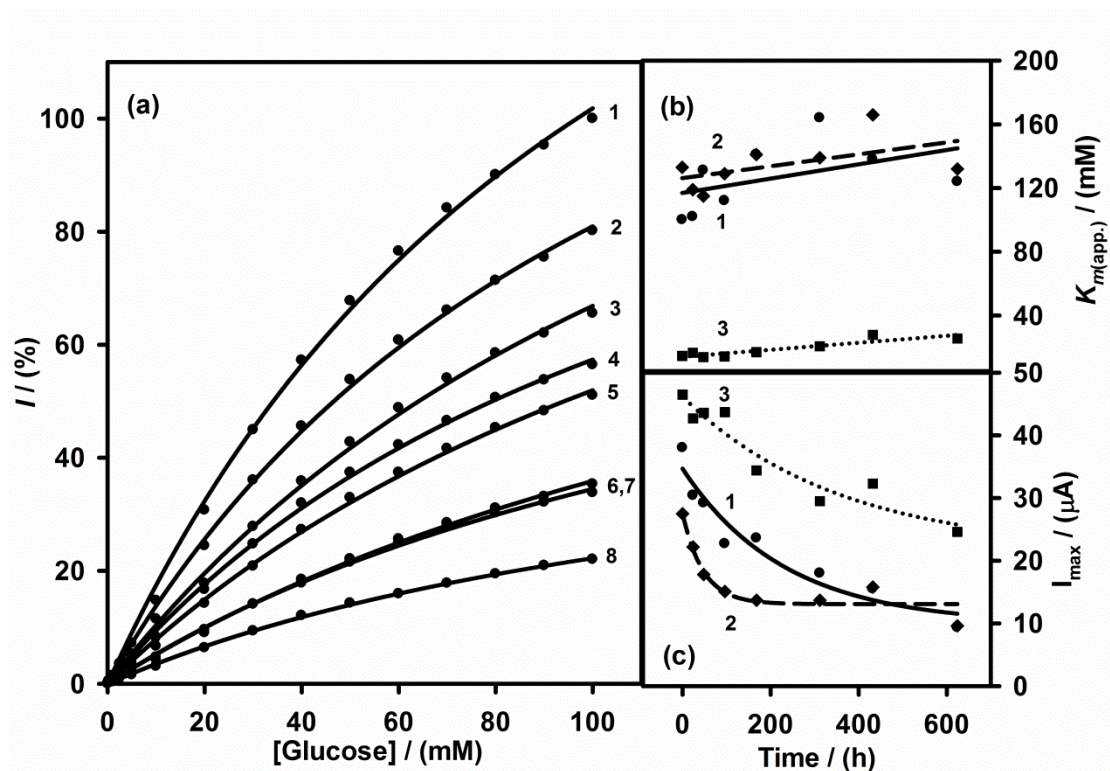


Figure 36. (a) Glucose calibration curves vs. time obtained with the GOx/PTP modified GRE. The GRE/GOx electrode was covered by PTP layer while incubating into the A-PBS, pH 6, containing 200 mM thiophene and 50 mM glucose (polymerisation solution) at room temperature for 20 h. The numbers show time intervals between stability measurements (curve 1 – 0 h, 2 – 24 h, 3 – 48 h, 4 – 96 h, 5 – 168 h, 6 – 312 h, 7 – 432, 8 – 624 h) which were performed at +300mV vs. Ag/AgCl/3M KCl in A-PBS, pH 6.0, containing 2 mM of PMS, continuously stirring at room temperature. Calculated $K_{m(app.)}$ (b) and I_{max} (c) values vs. time for GRE/GOx electrodes before stability measurements incubated in polymerisation solution (curve 1) as well as in ‘control solution I’ (curve 2) and ‘control solution II’ (curve 3), respectively, for 20 h at room temperature.

For the control electrode II, i.e., GRE/GOx-modified electrode incubated in ‘control solution II’ for 20 h, the evaluated $K_{m(app.)}$ and I_{max} corresponded to 14.6 ± 1.5 mM and 46.5 ± 1.2 μA , respectively, while after 624 h the parameters changed to $K_{m(app.)} = 25.6 \pm 2.4$ mM, $I_{max} = 24.6 \pm 0.8$ μA . The generated current decreased approximately by 2.15 times within 624 h (Table 6; curve 3 in Fig. 36b and 36b). The data show good stability of the control electrode II. One of the reasons for this exceptional stability might be the absence of glucose in the ‘control solution II’. Glucose is one of the best growth stimulating components for bacteria; therefore, this solution very likely has the lowest risk to be invaded by microorganisms. Furthermore, thiophene is an undesirable medium component for many bacteria, which prevents their growth and further

increases the stability of the electrode after being immersed in that solution. Moreover, in the presence of glucose the GOx was always in catalytic-action and significant amount of H₂O₂ was produced in incubation vessel; the H₂O₂ was forming free radicals, which in long term are highly likely to damage the GOx and in this way to reduce their enzymatic activity [237]. However, if thiophene is present in the same solution (polymerisation solution) then the concentration of H₂O₂ is reduced by involvement of this compound in polymerisation reaction of thiophene

3.2 Evaluation of 1,10-phenanthroline derivatives as ET mediators for anodic biocatalyst glucose oxidase

This study was focused on possible application of some 1,10-phenanthroline derivatives (PDs) as partly insoluble EP mediators in the development of glucose biosensors and EBFCs. Differently from some other studies, the PDs that were not involved into structures of metal complexes were investigated. Five PDs [1,10-phenanthroline monohydrate (PMH); 5-nitro-1,10-phenanthroline (5NP); 5-amino-1,10-phenanthroline (5AP), 5-amino,6-nitro-1,10-phenanthroline (5A6NP) and 5,6-diamino-1,10-phenanthroline (56DAP)] were selected for this study (Table 3). These PDs as a ligand form were investigated amperometrically and potentiometrically with respect to their ability to act as EP mediators for GOx.

3.2.1. Amperometric studies

In this study the cross-linking method for the immobilisation of PDs/GOx on the GRE surfaces has been chosen and the cross-linking was performed in the vapor over the media of 5 % glutaraldehyde (Chapter 2.3.8.3). The effect of pH is based on one of the several factors: (1) the effect of pH on electrocatalytic properties of EP mediator, and (2) the effect of pH on the activity of enzyme. During pH optimisation it was found that optimal pH for this system is around pH 6.0. Thus, the redox behavior of GOx- and PDs/GOx-modified GREs at different glucose concentrations were investigated amperometrically in A-PBS, pH 6 (Fig. 37).

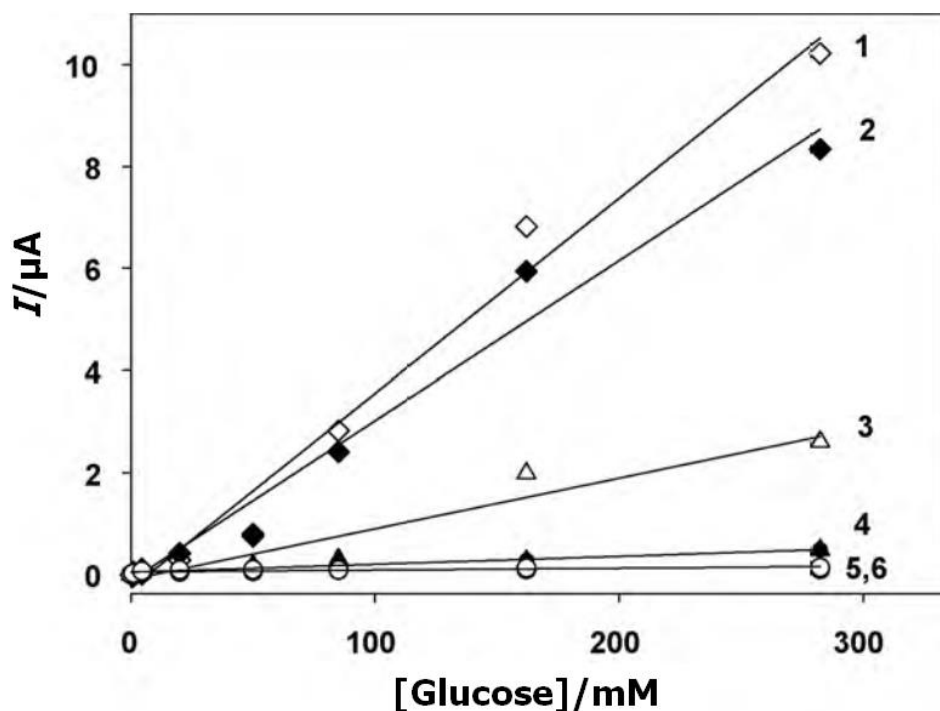


Figure 37. Amperometric responses of GRE/GOx and GRE/PDs/GOx electrodes vs. glucose concentration: (1) GRE/5AP/GOx, (2) GRE/56DAP/GOx, (3) GRE/5NP/GOx, (4) GRE/5A6NP/GOx, (5) GRE/PMH/GOx, and (6) GRE/GOx; differently modified GRE were tested at +0.6V vs. Ag/AgC_{sat.} (197 mV vs. NHE) upon successive addition of glucose.

Well-defined amperometrical signals vs. increasing glucose concentration were registered for the GRE/5AP/GOx, GRE/56DAP/GOx, and GRE/5NP/GOx electrodes (Fig. 37, curves 1-3, correspondingly). While 5A6NF and PMH showed miserable ET-mediating properties (Fig. 37, curves 4 and 5, correspondingly), and amperometrical signals were similar to that obtained with GRE/GO_x electrode (Fig. 37, curve 6) in the same conditions. The results of amperometrical measurements (Fig. 37, curves 1-3) illustrate that some PDs could be applied as ET mediators to shuttle the electrons between GOx and the GRE surface. The ET-mediating activity differs from one derivative to another, and this effect relies on the presence of different functional groups in the PDs structure. Achieving the DET from/to redox enzymes, which contain the redox centre embedded deep within the shell is a challenge [238]. To prove this fact GOx-modified GREs were prepared and investigated amperometrically in the presence of different glucose

concentrations. The current changes by GRE/GOx electrode were negligible (Fig. 37, curve 6). The bare GRE surface is not involved in ET from redox center of GOx. Thereby, electrode interfaces for GOx need to be modified by establishing an efficient ET pathway. Particularly in this case the surface of GRE is covered with a multi-layer of PDs molecules that are at some extent soluble in water [239, 240]. Positive potential applied to the electrode (+0.6V vs. Ag/AgCl_{sat.}) leads to the formation of interface containing high surface-concentration of oxidised and/or semi-oxidised PD molecules. The PD molecules are in close proximity with the conducting GRE surface. The redox-mediating activity of 56DAP and 5AP is positively influenced by inductive activity of -NH₂ (amino) groups, which increase electron density in the aromatic structure of PMH. Higher redox-mediating activity was achieved in the case of 5AP, which contains a single -NH₂ group, with the highest probability that the second -NH₂ group adds a negative steric-effect to 56DAP. Thus, 56DAP seems less sterically efficient when compared with 5AP. Due to increased electro-negativity, both 56DAP and 5AP seem relatively efficient for re-oxidation of the FAD-cofactor, which is reduced during catalytic action of GOx (Eq. 10). Significantly lower ET mediating activity was obtained with the GRE/5NP/GOx electrode because nitro groups exhibit negative induction effect and extract the electrons from the aromatic structure of PMH, which makes such compound less attractive for reduced form of GOx. Yet this effect theoretically renders the compound more easily oxidisable on the surface of an electrode. For this reason this compound shows relatively good redox-mediating properties. The 5A6NP contains -NO₂ and -NH₂ groups in its structure, these two groups exhibit very different induction effects: the -NH₂ delivers electrons towards the aromatic structure of PMH and the -NO₂ extracts electrons from the PMH. These two opposite induction effects at least partially compensate each other. The electron density in an aromatic structure of 5A6NP is similar to that in PMH. The absence of clear oxidative or reductive potentials makes these compounds electrochemically less active [241] and may be for these reasons the 5A6NP-based electrodes (GRE/5A6NP/GOx) were

completely inactive as well as GRE/GOx electrodes. The results illustrate that mediating characteristics of PDs mainly depend on electron accepting and/or electron-donating properties of substituting ligands.

3.2.2. Potentiometric studies

In order to demonstrate applicability of PDs for the design of EBFCs, the potentiometric measurements with PDs-modified GRE/GOx electrodes and PDs non-modified GREs were performed. The dependence of potentiometrical signal on glucose concentration is presented in corresponding plots (Fig. 38).

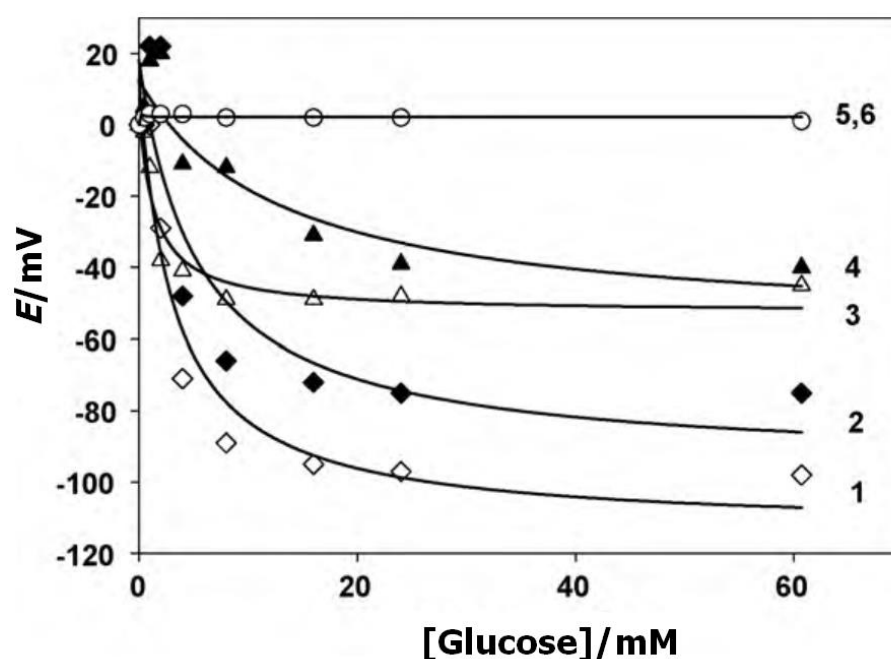


Figure 38. Potentiometric response of differently modified GRE: (1) GRE/5AF/GOx, (2) GRE/56DAP/GOx, (3) GRE/5NP/GOx, (4) GRE/5A6NP/GOx, (5) GRE/PMH/GOx and (6) GRE/GOx, at open circuit upon successive addition of glucose.

The best potentiometric response was registered with 5AP-based electrode. Slightly lower potentiometric response was monitored using the electrode modified with 56DAF, and some potential differences were obtained using the electrodes modified with 5NP and 5A6NP. Due to significant current density and ability to generate efficient potential, the electrodes based on 5AP and 56DAP could be applied in the development of GOx-based biosensors and/or of anodes of EBFCs.

3.3. Development and characterisation of glucose powered EBFCs

The whole chapter is focused on the development and studies of both MET (Chapter 3.3.1.) and DET (Chapter 3.3.2.) based glucose powered EBFCs including their separate electrode characterisation in order to evaluate the limiting factors of an overall EBFC performance.

3.3.1. Mediated glucose-powered EBFC based on anode and cathode modified by GOx

A single compartment EBFC based on an anode and a cathode powered by the same fuel glucose was designed and studied. GOx from *Aspergillus niger* was applied as a glucose consuming biocatalyst for both anode and cathode of the EFC. The 5-amino-1,10-phenanthroline (5AP) modified graphite rod electrode (GRE) with cross-linked GOx was used as the bioanode, and the GRE with co-immobilised horseradish peroxidase (HRP) and GOx was exploited as the biocathode of the EBFC (Fig. 39).

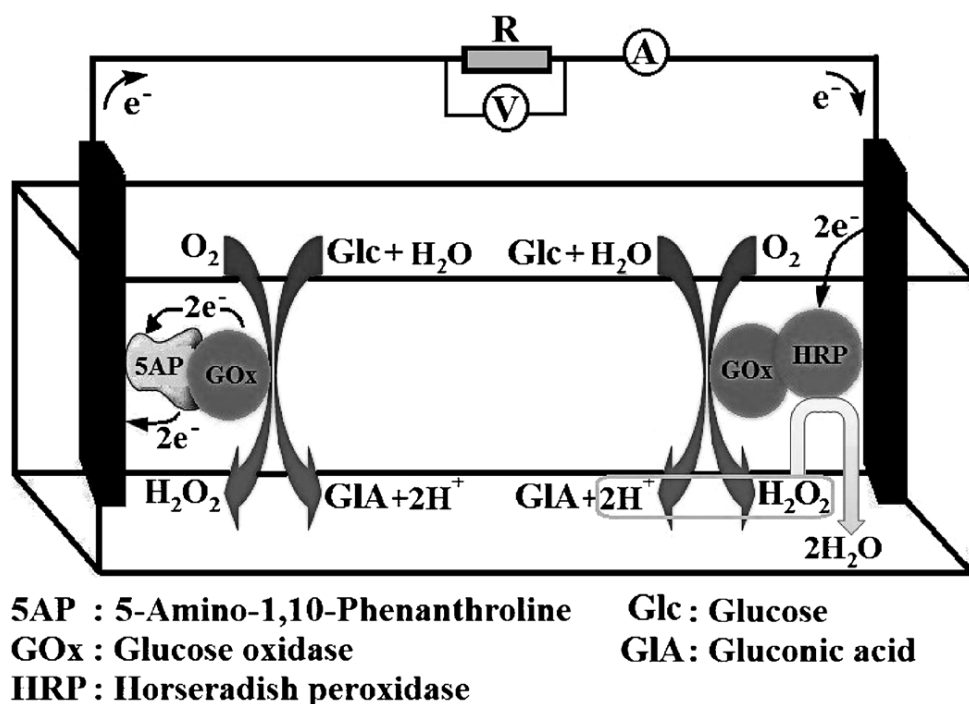


Figure 39. Representation of the EBFC configuration based on the GRE/5AP/GOx anode and GRE/HRP/GOx cathode.

3.3.1.1. Individual electrode characterisation

The functionality of the GRE/5AP/GOx bioanode (Fig. 40a) and GRE/HRP/GOx biocathode (Fig. 40b) were individually evaluated by means of cyclic voltammetry (CV) in air saturated A-PBS with (solid black cycles) or without 100 mM glucose (solid grey cycles). In the absence of glucose no biocatalytic activity for both bioelectrodes was observed. When glucose was added to the A-PBS, well defined bioelectrocatalytic currents were observed for both the bioanode and biocathode. The bioanodic electrode was observed to have the onset potential at around 0 V, while the biocathodic electrode at +0.5 V vs. Ag/AgCl/KCl_{sat}, respectively, which is comparable to the onset potential of the HRP/GOx bienzyme system adsorbed on GRE additionally pre-treated with carbon nanotubes and carbon microfibers [137].

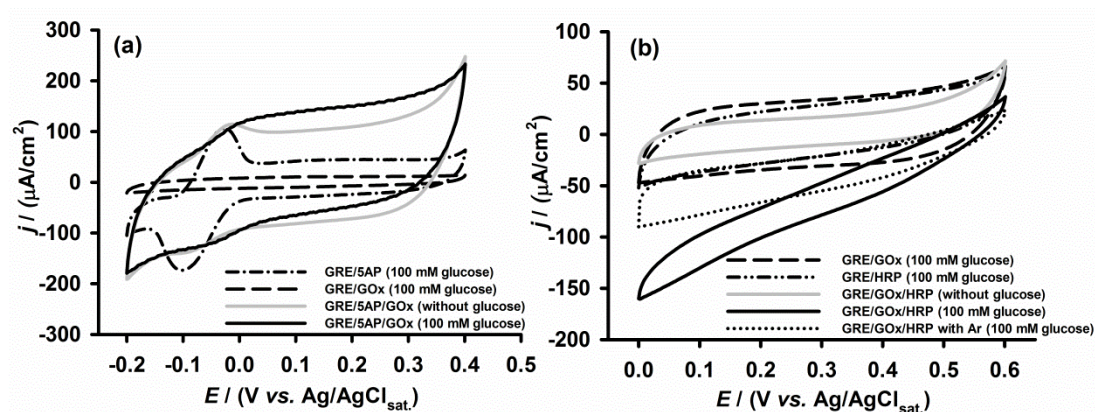


Figure 40. Cyclic voltammograms of differently modified electrodes performed in the potential range of bioanode (A) and biocathode (B). Cyclic voltammograms were carried out in quiescent A-PBS containing 100 mM KCl, pH 6.0, at ambient temperature (25 °C) with a scan rate of 10 mV/s.

Significant attenuation of the GRE/HRP/GOx cathode generated bioelectrocatalytic current was achieved under anaerobic conditions (Fig. 40b, dotted cycle), since the lack of O₂ in the solution hampers the formation of H₂O₂ during glucose bioelectrocatalysis by GOx (Chapter 1.2.4.1., Eq. 11). Additionally, as a control study for the bioanodic electrode, CV measurements were conducted in air saturated 100 mM glucose containing A-PBS using GREs modified only with GOx or 5AP (Fig. 40a, dashed and dashed-dotted cycles, respectively). No bioelectrocatalytic glucose oxidation current was

observed on the GRE/GOx-modified electrode, confirming that the DET between GOx and unmodified GRE (Fig. 40a, dashed cycle) cannot be achieved as it was concluded in previous studies [242]. While testing the 5AP-modified GRE, only significant peaks characterising the 5AP redox reactions were registered (Fig. 40a, dashed-dotted cycle). The same testing experiments were performed for the biocathode, using GREs modified either with HRP or GOx (Fig. 40b, dashed-dotted-dotted and dashed cycles). Only relatively high charging currents were observed at this potential range coinciding with that ones on GRE/HRP/GOx-modified electrodes in the absence of glucose or in the case if O₂ was removed.

3.1.1.2. Evaluation of the complete EBFC performance

The glucose EBFC was designed and characterised by combining the GRE/5AP/GOx based anode and GRE/HRP/GOx based cathode in a one compartment. The schematic depiction of the prepared EBFC is presented in Fig. 39.

The maximal registered open-circuit voltage of the EBFC exceeded 0.45 V at glucose concentration 16 mM or higher. Fig. 41a shows the dependence of the cell voltage vs. the power (a) and current (b) densities of the designed EBFC. In a quiescent A-PBS containing 16 mM glucose the maximum power density was 3.5 $\mu\text{W cm}^{-2}$ at 0.3 V of the cell voltage. With increasing glucose concentration, the power output achieved its maximal value equal to 16.3 $\mu\text{W cm}^{-2}$ at 150 mM glucose concentration (Fig. 41b). The previously reported studies show that the major parameters of glucose powered EBFCs vary in a broad range, e.g., the power output ranges from 2.8 $\mu\text{W cm}^{-2}$ [8] up to 1300 $\mu\text{W cm}^{-2}$ [5], and open-circuit voltage from 0.12 V [243] up to 0.95 V [5].

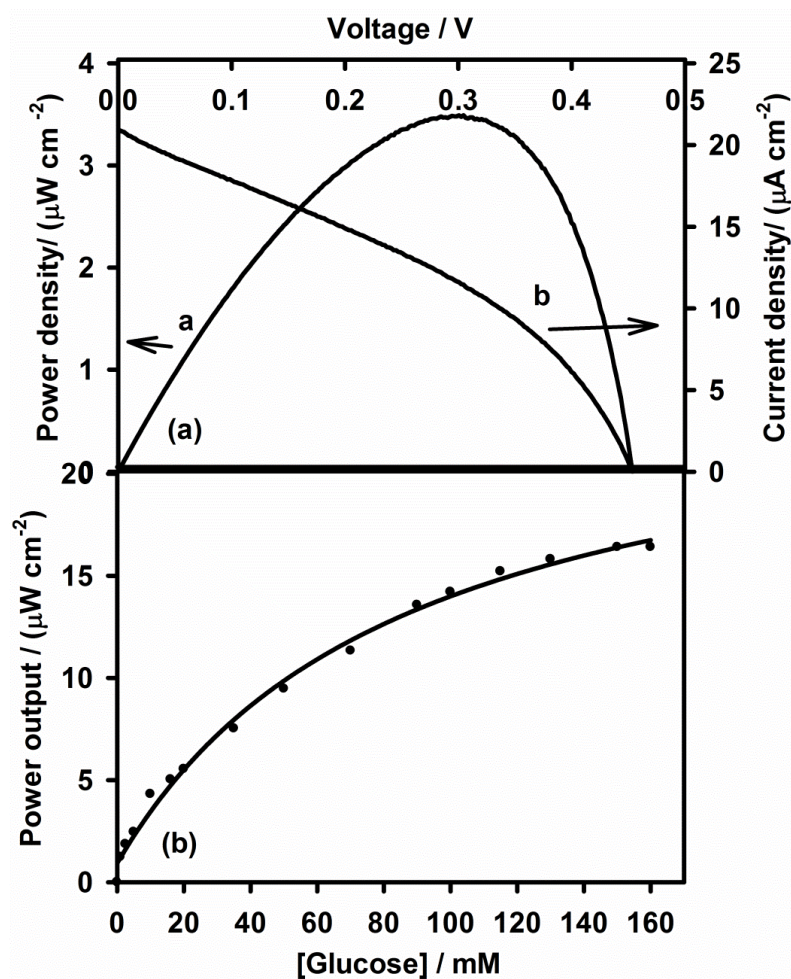


Figure 41. (a) Typical dependence of power (a) and current (b) densities on an operating voltage of the EBFC in quiescent A-PBS, pH 6, containing 16 mM glucose under aerobic conditions. Linear sweep voltammograms were recorded with a potential scan rate of 0.1 mV s^{-1} . (b) Dependence of power output on glucose concentration measured in chronoamperometric mode at a potential corresponding to the potential of the EFC at its maximal power density.

According to the maximal power generated by EBFC designed in this research it can be concluded that some improvement is still needed because it is in the range of $3.5 \mu\text{W cm}^{-2}$. However, it should be noted that the generated power strongly depends on the activity of applied enzymes and their immobilisation efficiency. These issues were not optimised in this research, therefore, there is still a lot of space for improvement of the EBFC performance. The maximal voltage of the designed EBFC was in the range of 0.45 V, which is relatively good in comparison to some other research [138, 243-246].

The stability of the OCV of the EBFC on 1st, 2nd, 3rd, 5th, and 11th days was examined (Fig. 42a).

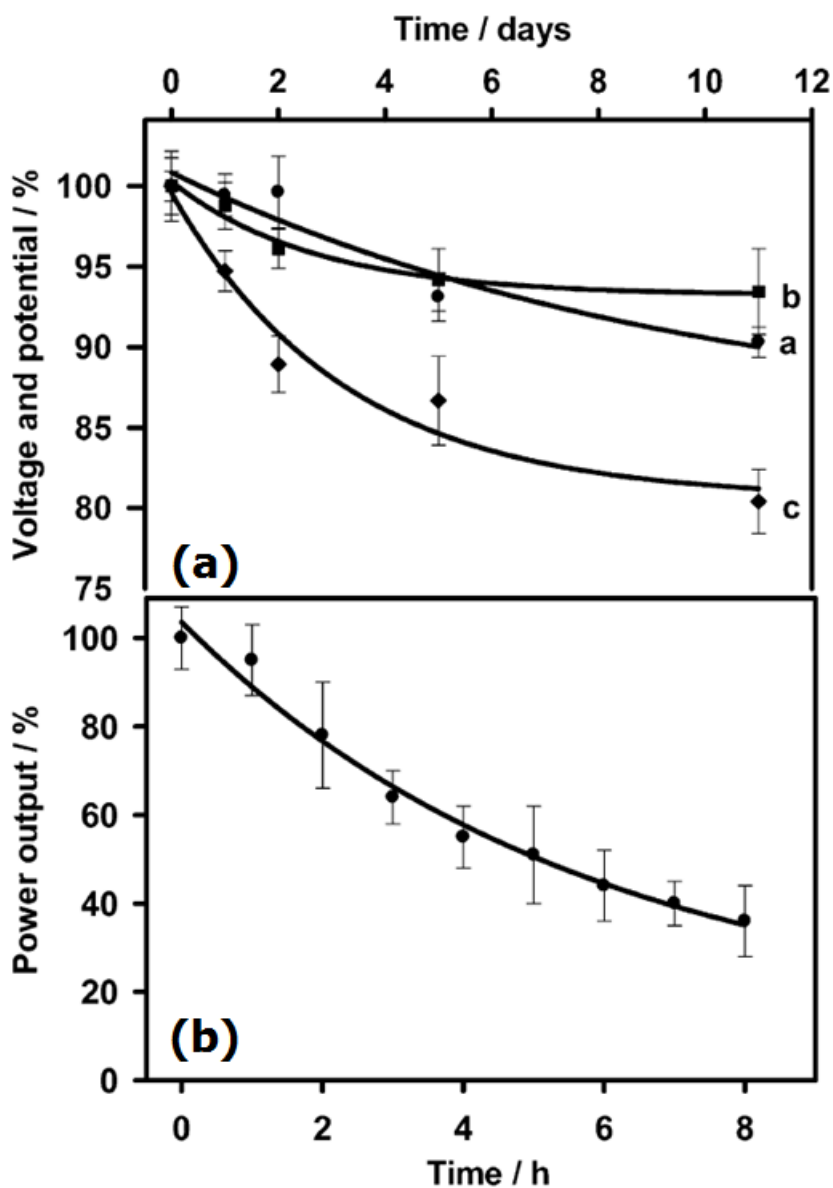


Figure 42. (A) Stability of the open circuit voltage generated by the complete EBFC in A-PBS containing 16 mM glucose (a); variation of the open circuit potentials within the time of individual GRE/HRP/GOx (b) and GRE/HRP (c) biocathodes in A-PBS (pH 6.0, with 100 mM KCl) containing 16 mM of glucose and 0.25 mM of hydrogen peroxide, respectively. (B) Time dependence of power output of the EFC submerged into 16 mM glucose containing A-PBS. All stability experiments were performed in quiescent A-PBS (pH 6.0, 100 mM KCl), under aerobic conditions.

Potentiometric stability tests of the complete EBFC showed that approximately only 10 % of the OCV of the EBFC was lost within 11 days (Fig. 42a, data a). The stability of open-circuit potential generated by

GRE/HRP/GOx (Fig. 42a, data b) and GRE/HRP (Fig. 42a, data c) cathodes was also examined. It was found that after 11 days the stability of the GRE/HRP/GOx electrode decreased by 7% and the GRE/HRP electrode by 19%. The higher stability of the GRE/HRP/GOx cathode in comparison with the GRE/HRP electrode could be associated with the additional GOx layer surrounding HRP, which was deposited on the electrode surface. This layer might decrease the chances of HRP molecules to diffuse away from the electrode surface. Consequently, we can predict that the limited stability of the EBFC was mostly influenced by the instability of HRP present in the GRE/HRP/GOx-based cathode design. On the other hand, the GRE/HRP/GOx cathode generated significantly higher open-circuit potential if compared to that registered for GRE/Microperoxidase-8/GOx cathode [138, 245]. This observation is in line with other research based on the evaluation of HRP/GOx based cathodes [137].

Operational stability of the EBFC was characterised in chronoamperometric mode at a potential corresponding to the potential of the BFC at its maximal power density. The half-life time of its power output was estimated to be at least 5 h in 16 mM glucose containing A-PBS.

3.3.2. Mediator-less carbohydrate/O₂ EBFCs with improved CDH based bioanode

According to the previous studies developing *CtCDH-MvBOx* based EBFCs it can be concluded that the bioelectrocatalytic current generated by the biocathode of the studied EBFCs was much higher compared to the current demonstrated by the bioanode, thus, the bioanode being limiting electrode for the EBFC performance *in vitro*. Moreover, the DET based coupling of *CtCDH* was complicated and required modification of the AuNP surface with a SAM consisted of two thiols followed by cross-linking with glutaraldehyde [8, 29]. Thereby, the main purpose of this study was to address the above mentioned problems and challenges. Specifically, (i) to simplify the preparation of CDH based bioanode, (ii) to improve the DET based performance of AuNP/CDH bioanode, and (iii) finally, by combining the AuNP/MHP/CDH based bioanode

and AuNP/MvBOx based biocathode in one compartment, to design a membrane- and mediatorless carbohydrate/O₂ EBFC (Fig. 43).

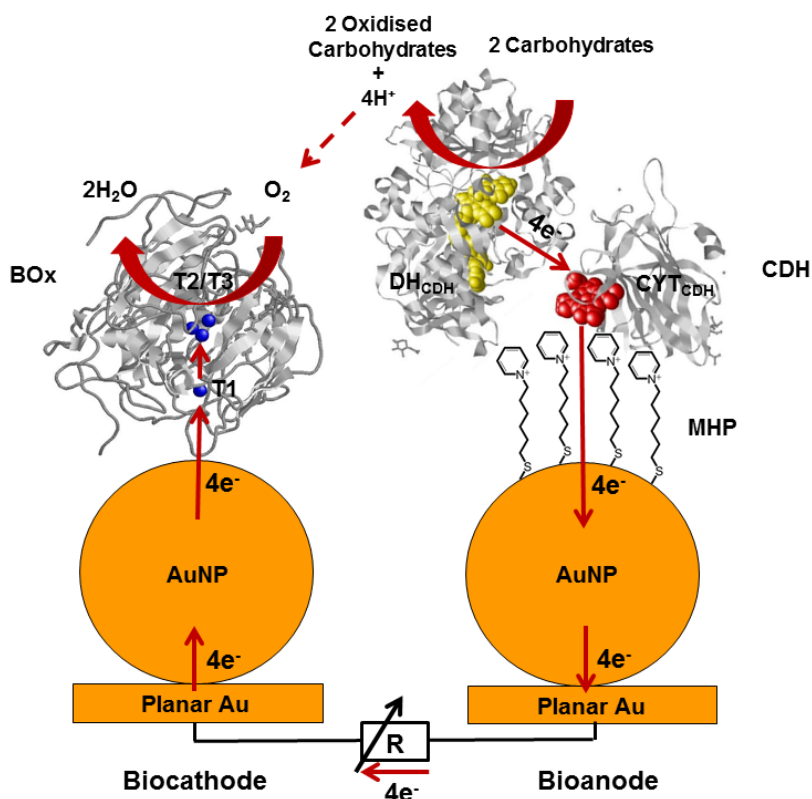


Figure 43. Schematic representation of the EBFC based on the Au/AuNP/MHP/CDH bioanode and the Au/AuNP/BOx biocathode. The three-dimensional structure of BOx is a model based on the structure of *M. verrucaria* BOx (PDB 3ABG). The schematic structure of CDH is a model constructed from the structures of the dehydrogenase (PDB 1NAA) and cytochrome (PDB 1D7C) domains of *P. chrysosporium* CDH. The proteins are shown as grey ribbons and the carbohydrates are shown as grey sticks. The T1 copper site and the T2/T3 copper cluster of BOx are shown as blue spheres, the FAD in CDH as yellow spheres, and the heme as red spheres, respectively.

3.3.2.1. Characterisation Au/AuNP/MHP/CDH bioanodes

*Hi*CDH or *Ct*CDH were immobilised on 3D Au/AuNP electrodes and DET based bioelectrocatalytic oxidation of two carbohydrates, *viz.*, glucose and lactose, was compared. To enable simple and improved DET based wiring of CDH enzymes on an electrode, for the first time a positively charged thiol, N-(6-mercapto) hexylpyridinium (MHP), was used. Before making appreciation of the results it should be kept in mind that DET based bioelectrocatalysis using *Ct*CDH has been realised on several types of electrodes including bare graphite [247], single-walled carbon nanotube modified graphite [248], thiol

modified Au/AuNP electrodes [8, 29], etc. Recently published results have indicated that *Ct*CDH is one of the best enzymes for realising efficient DET based bioelectrooxidation of carbohydrates [35]. In contrast, only negligible DET based bioelectrocatalysis using *Hi*CDH was demonstrated at graphite and thiol modified gold electrodes [101].

Bioelectrocatalytic oxidation of carbohydrates at CDH modified electrodes was investigated by cyclic voltammetry (CV). Fig. 44 summarises the data of CV measurements recorded using *Ct*CDH (a, c) and *Hi*CDH (b, d) modified Au/AuNP/MHP electrodes in PBS solution with or without 5 mM glucose (a, b) and 10 mM lactose (c, d), respectively.

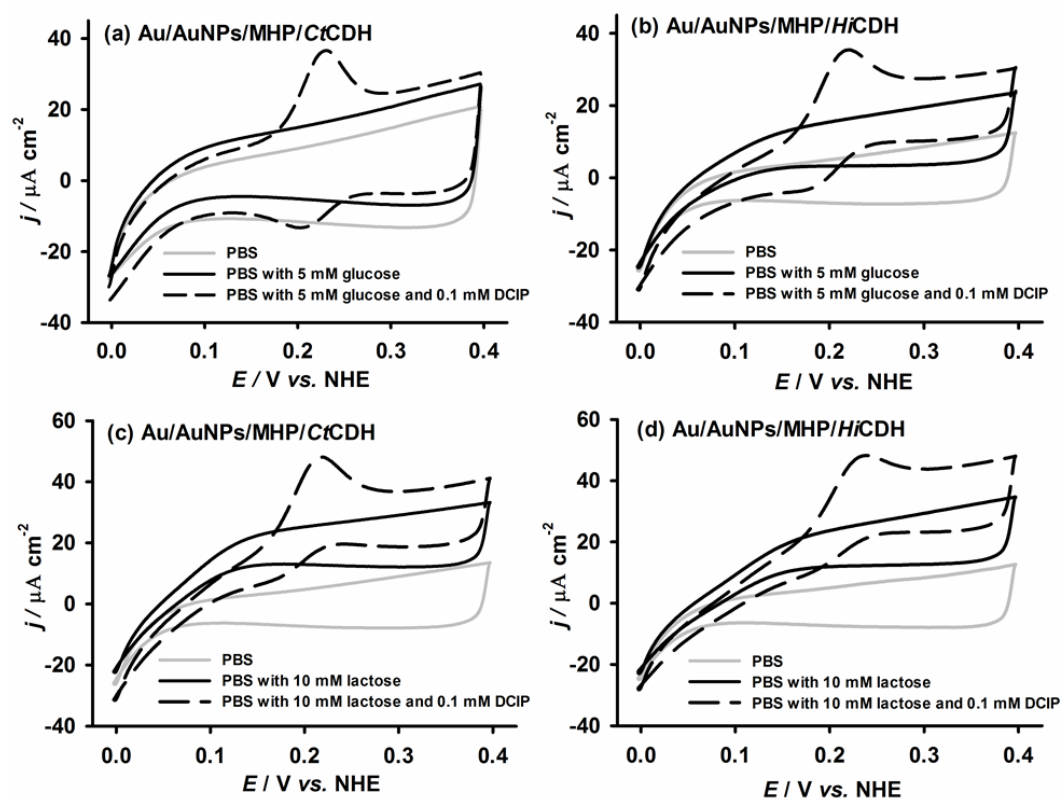


Figure 44. Cyclic voltammograms of (a, c) *Ct*CDH and (b, d) *Hi*CDH modified Au/AuNP/MHP electrodes. Conditions: (a, b) glucose; (c, d) lactose; (solid grey lines) air saturated quiescent 50 mM PBS, pH 7.4, containing 100 mM KCl; (solid black lines) PBS with carbohydrates; and (dashed black lines) PBS with carbohydrate and DCIP. Scan rate: 2 mV s⁻¹.

In the absence of carbohydrates the voltammograms (Fig. 44, grey solid lines) were featureless and reflected relatively high charging current of the electrodes. High charging current usually masks the current of electrochemical

redox conversion of CDH bound heme cofactor, *i.e.*, the non-turnover signals [249]. When glucose or lactose was present in the buffer solutions, well-defined bioelectrocatalytic oxidation currents (Fig. 44, dark solid lines) were observed at the electrodes modified with either enzyme. As can be seen the bioelectrochemical oxidation started at *ca.* 0.05 V *vs.* NHE. This potential is close to the formal potential of heme in CDH enzymes, *e.g.*, in case of *Ct*CDH the formal potential of the heme is equal to 0.075 V [8]. The described features of the voltammograms are in agreement with the current understanding of DET based bioelectrocatalysis at CDH modified electrodes; carbohydrates are oxidised by the FAD subunit of the CDH enzyme, then the electrons from the FAD are transferred to the heme subunit, which finally delivers the electrons to the electrode, as depicted in Fig. 43.

The results prove that the electrode modification with MHP is important since no bioelectrooxidation of lactose was observed, if the enzyme was immobilised directly on Au or Au/AuNP (Fig. 45). This observation is in agreement with previous studies showing that proteins tend to denature or adsorb in an unfavourable orientation for DET reactions at bare Au surfaces [170]. It should be pointed out that direct electrochemical oxidation of carbohydrates is possible at bare Au/AuNP, *i.e.* electrodes which neither modified with the enzyme nor thiol. This was confirmed by a control study, where lactose was efficiently electrooxidised on the Au/AuNP electrode at 0.32 V (Fig. 45). However, the adsorbed MHP or the CDH enzyme blocks the electrocatalytic properties of AuNPs, which is in agreement with previous studies [250].

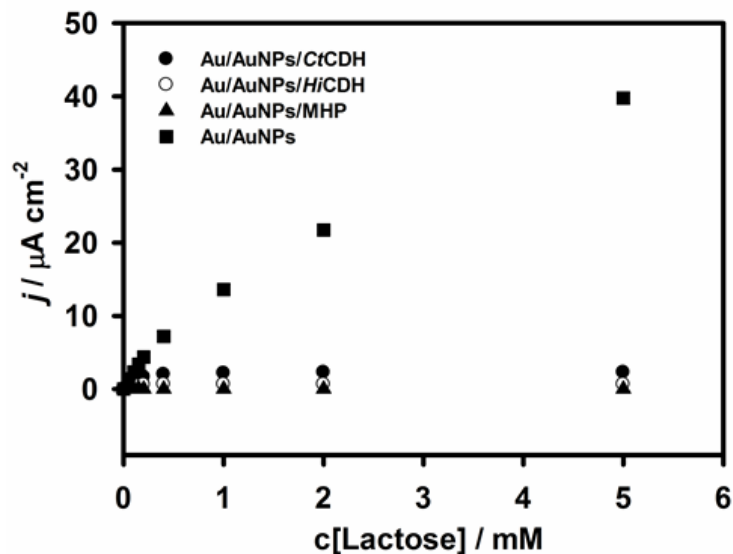


Figure 45. Dependence of current density on lactose concentration recorded using (■) an unmodified Au/AuNP electrode, and Au/AuNP electrodes modified with (▲) MHP, (●) *CtCDH* or (○) *HiCDH* only. The chronoamperometric measurements were performed at 0.32 V vs. NHE, while stirring 50 mM PBS, pH 7.4, containing 0-5 mM lactose.

Experimental results presented in Fig. 44 prove that both *CtCDH* and *HiCDH* can catalyse DET based bioelectrochemical oxidation of carbohydrates at Au/AuNP/MHP electrodes. To compare *CtCDH* vs. *HiCDH* modified electrodes, DET based bioelectrooxidation of lactose and glucose have been studied by chronoamperometry. Amperometric responses at different lactose concentrations are presented in Figs. 46a and 46b. It can be concluded that immobilised *CtCDH* demonstrated a maximal activity at 2 mM lactose which, unfortunately, was inhibited at higher lactose concentrations (Fig. 46a). In contrast, adsorbed *HiCDH* reached close to a maximal activity at *ca.* 10 times higher lactose concentration, *i.e.*, 20 mM, with no inhibition at the concentration up to 50 mM (Fig. 46b). The absence of the lactose inhibition of *HiCDH* is definitively an advantage for designing EBFC working in the media with high lactose concentrations, *e.g.*, milk or milk products containing up to 150 mM of the carbohydrate [251]. In the presence of 5 mM lactose both CDH modified Au/AuNP/MHP electrodes generated similar current densities of approximately $20 \mu\text{A cm}^{-2}$ (Fig. 46a and 46b).

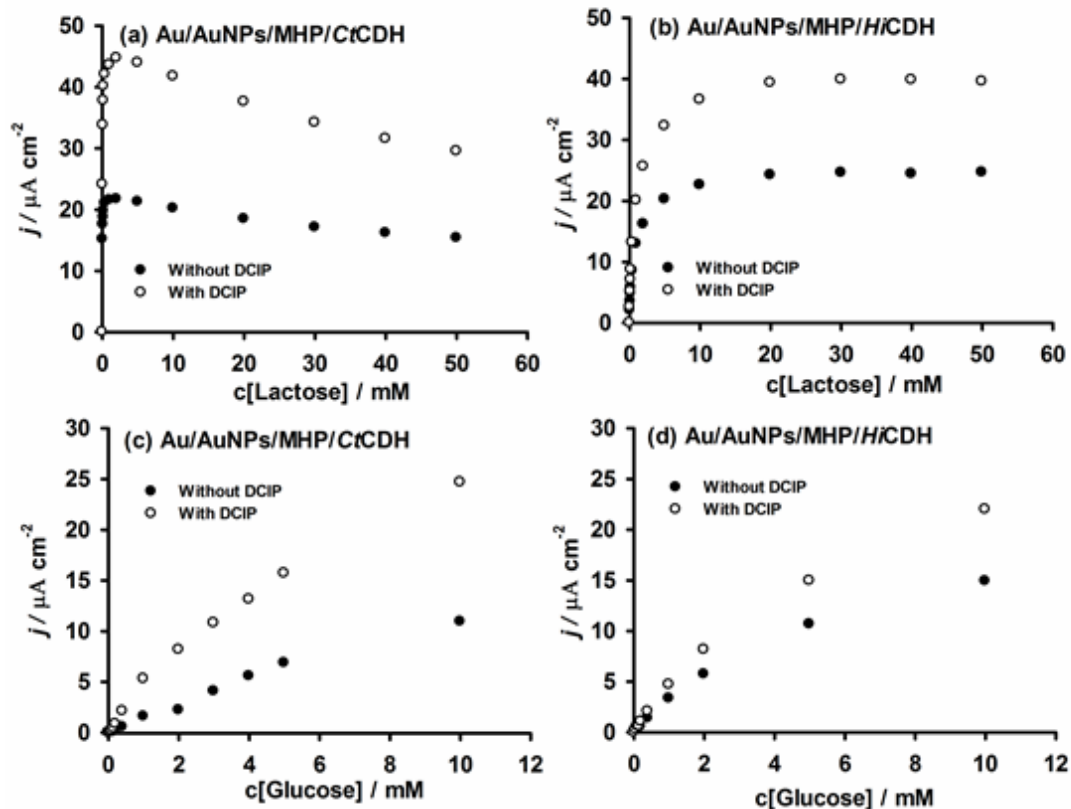


Figure 46. Dependence of current density on (a, b) lactose or (c, d) glucose concentration recorded using Au/AuNP/MHP electrode modified with (a, c) *CtCDH* or (b, d) *HiCDH*. The measurements were performed (\circ) with and (\bullet) without 0.1 mM 2, 6-dichlorindophenol sodium salt hydrate (DCIP) as a mediator under the same conditions as in Figure 45.

The obtained current densities are half of those previously reported for *CtCDH* modified electrodes, where the enzyme was adsorbed on Au/AuNP electrodes modified with the mixture of two-thiols and additionally cross-linked with glutaraldehyde [8]. Nevertheless, the presented amperometric results show a considerable improvement in preparation of CDH modified electrodes. This is supported by the facts that (i) comparable bioelectrocatalytic currents can be obtained by using a single thiol, *i.e.*, MHP, for DET coupling of the CDH enzymes and that (ii) the current at *HiCDH* modified electrodes is not decreased at high lactose concentrations.

Contrary to the above discussed differences (particularly inhibition effect) of amperometric responses of *CtCDH* and *HiCDH* modified Au/AuNP/MHP electrodes to different lactose concentrations, a very similar, monotonically increasing response was observed for both electrodes while increasing glucose

concentration (Figs. 46c and 46d). The electrodes were assessed at glucose concentration in the range of 0-10 mM. The current density at 5 mM glucose generated by the Au/AuNP/MHP/*Hi*CDH electrode was equal to $11 \mu\text{A cm}^{-2}$, being higher than $7 \mu\text{A cm}^{-2}$ obtained with Au/AuNP/MHP/*Ct*CDH electrode. The amperometric response of *Ct*CDH modified electrode is comparable to previously reported results [8], while the current generated by Au/AuNP/MHP/*Hi*CDH electrodes is approximately 1.5 times higher. Higher amperometric response of *Hi*CDH modified electrodes to glucose and the absence of lactose inhibition point to the fact that *Hi*CDH might become an important enzyme for the future development of EBFCs.

The efficiency of DET reactions between CDH and AuNP/MHP modified Au electrodes was assessed by comparing the CV measurements recorded with electrodes in carbohydrate solution in the absence and in the presence of soluble redox mediator. Dichloroindophenol (DCIP) was used as a mediator since it is stable in the presence of O_2 at pH lower than 7.5 [252]. As can be seen from Fig. 44 (dashed lines) the bioelectrocatalytic current in the presence of DCIP was higher, when both glucose and lactose were used as enzyme substrates. The increased current of the electrodes in the presence of DCIP was also registered by chronoamperometry (Fig. 46). The increase of the electrode current in the presence of DCIP shows that additional improvement of DET based wiring of *Ct*CDH and *Hi*CDH is possible; it could be that a certain population of the adsorbed CDH enzymes is not in DET contact with the Au electrodes. Nevertheless, the results discussed above undoubtedly point to the efficient DET coupling of *Hi*CDH to AuNPs. This provides a basis for making *Hi*CDH modified electrodes which, in some cases, generate a higher current (in glucose solution, at high concentration of lactose) than to date reported the best *Ct*CDH modified electrodes.

Additional measurements with rotating disk electrodes (RDEs) revealed that the observed current of the *Hi*CDH modified electrodes was almost independent on the electrode rotation rate (Fig. 47). This shows that the bioelectrocatalysis was not limited by the diffusion of the carbohydrates to the

electrode surface. Moreover, the bioelectrocatalytic current was almost independent on the applied potential at higher than 0.1 V over the formal potential of heme in CDH. All these results indicate that the bioelectrocatalytic process at CDH modified Au/AuNP/MHP electrodes was limited by the enzyme kinetics at FAD subunit or intermolecular ET between the FAD and the heme domains.

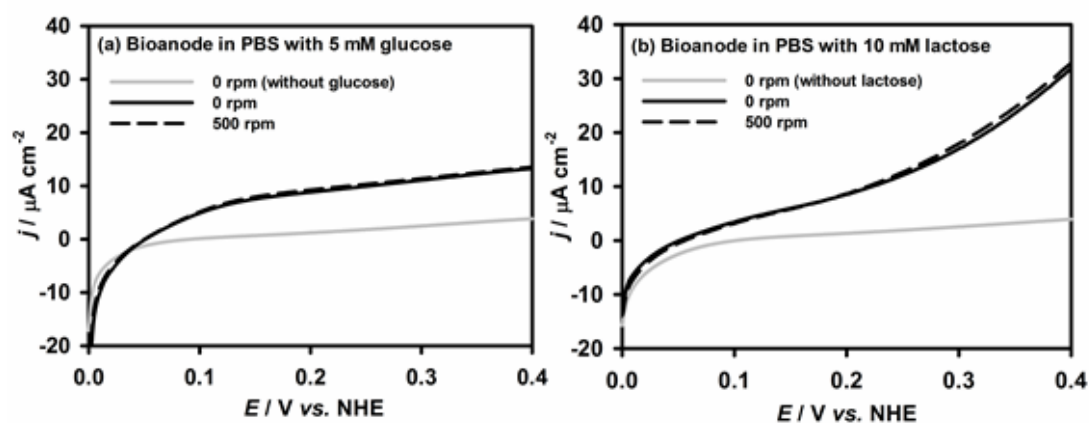


Figure 47. Current densities obtained using Au/AuNP/MHP/*Hi*CDH modified RDE in air saturated 50 mM PBS (pH 7.4) containing (a) 5 mM glucose or (b) 10 mM lactose. LSV measurements were performed (solid black lines) without and (dashed black lines) with rotation of 500 rpm in the presence of carbohydrates, as well as (solid grey lines) without rotation in absence of carbohydrates using a scan rate of 0.1 mV s⁻¹.

Keeping in mind the previously suggested mechanism of CDH function [95] and the fact that DET based bioelectrocatalytic current decreases at lower pH for *Hi*CDH modified electrodes (Fig. 48) it could be concluded that intramolecular ET (IET) between the FAD and the heme subunits of *Hi*CDH most probably is a rate limiting step of the bioelectrocatalysis at Au/AuNP/MHP/*Hi*CDH electrode.

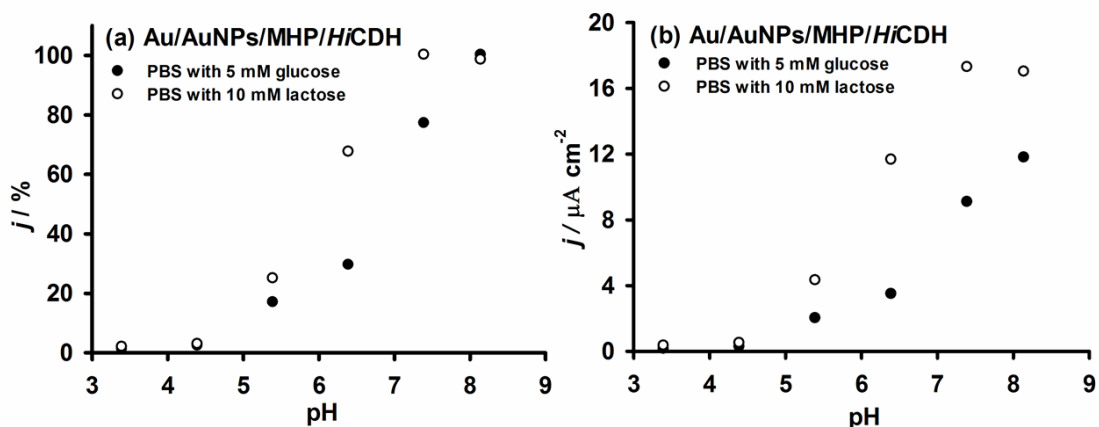


Figure 48. The pH dependencies of the current density of (a, b) Au/AuNP/MHP/HiCDH electrode registered at 0.32 V vs. NHE in air-saturated buffer solutions containing (●) 5 mM glucose or (○) 10 mM lactose.

3.3.2.2. Characterisation of the Au/AuNP/MvBOx biocathode

Biocathodes were prepared by adsorption of *MvBOx* on 3D Au/AuNP electrodes (see Chapter 2.3.8.4.). Fig. 49 shows data from CV measurements using AuNP modified cathodes under anaerobic and aerobic conditions. Well-pronounced bioelectrocatalytic reduction of O_2 at Au/AuNP/*MvBOx* electrodes submerged into air saturated PBS, pH 7.4, was obtained (Fig. 49, black solid line). The onset and half-wave potentials were 0.72 and 0.69 V vs. NHE, respectively, coinciding with the redox potential of the T1 site of the enzyme [253, 254]. Addition of 5 mM glucose or 10 mM lactose did not change the biocathode performance (Fig. 49, black dotted and dashed lines). No current was observed under anaerobic conditions at *MvBOx* modified electrodes (Fig. 49, inset, black line) or in the presence of O_2 without *MvBOx* modification (Fig. 49, inset, grey line) of Au/AuNP electrodes. All these experiments prove that observed electroreduction of O_2 was due to DET between the T1 copper centre of *MvBOx* and the electrode [114, 254], as illustrated in Fig. 44.

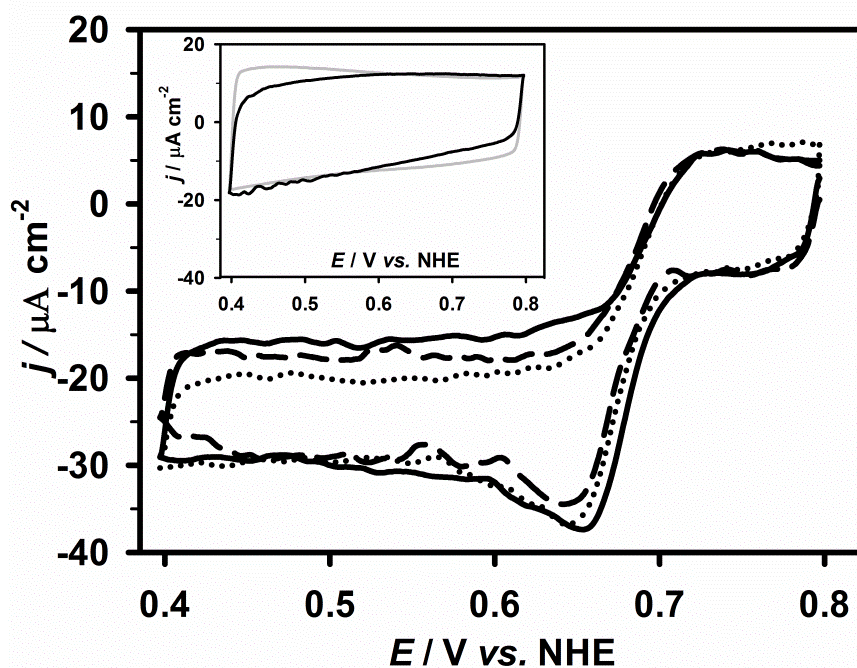


Figure 49. Cyclic voltammograms of Au/AuNP/*MvBOx* electrodes in 0.05 M PBS, pH 7.4. Conditions: (solid line) air saturated quiescent 50 mM PBS, pH 7.4, containing 100 mM KCl; (dotted line) 5 mM glucose containing PBS; and (dashed line) 10 mM lactose containing PBS. Scan rate: 2 mV s⁻¹. Inset: control experiments with (grey line) Au/AuNP electrode in air saturated PBS and with (black line) Au/AuNP/*MvBOx* electrode in N₂ saturated PBS.

Amperometric measurements employing rotating Au/AuNP/*MvBOx* electrodes revealed that the observed bioelectrocatalytic current was limited by O₂ diffusion to the electrode; the current considerably increased with the increasing rotation velocity. The condition of electrode limitation by *MvBOx* kinetics was achieved at 1000 rpm generating the current density of 180 μA cm⁻², which was five times higher than the current density registered without rotation (Fig. 50).

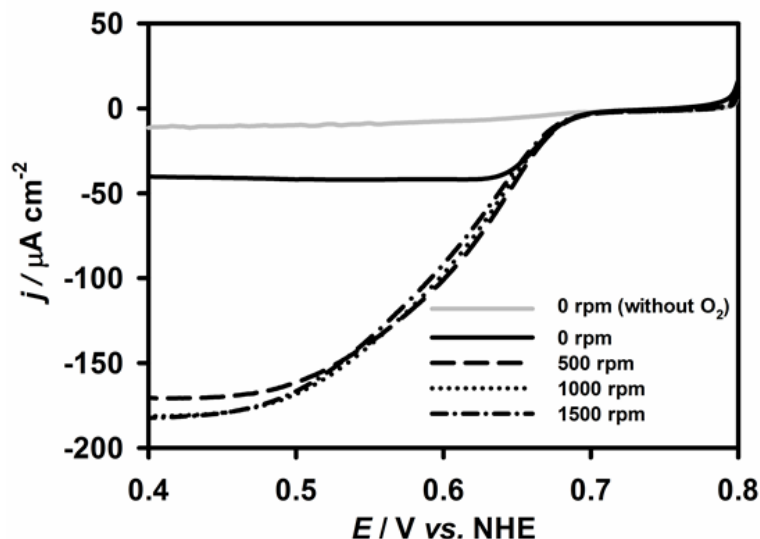


Figure 50. Current densities obtained using Au/AuNP/MvBOx modified RDEs in air saturated 50 mM PBS, pH 7.4. LSVs were recorded with a potential scan rate of 0.1 mV s^{-1} . The Au/AuNP/MvBOx system was evaluated (solid black line) without rotation, (dashed black line) at 500 rpm, (dotted black line) 1000 rpm and (dash-dotted black line) 1500 rpm. The solid grey line represents the LSV of Au/AuNP/MvBOx modified RDE in N_2 saturated PBS (O_2 removed by purified N_2 bubbling for 20 minutes).

Figs 51a and 51b show pH dependencies of bioelectrocatalytic currents obtained using Au/AuNP/MvBOx electrodes. The maximal currents were obtained at pH 6.4.

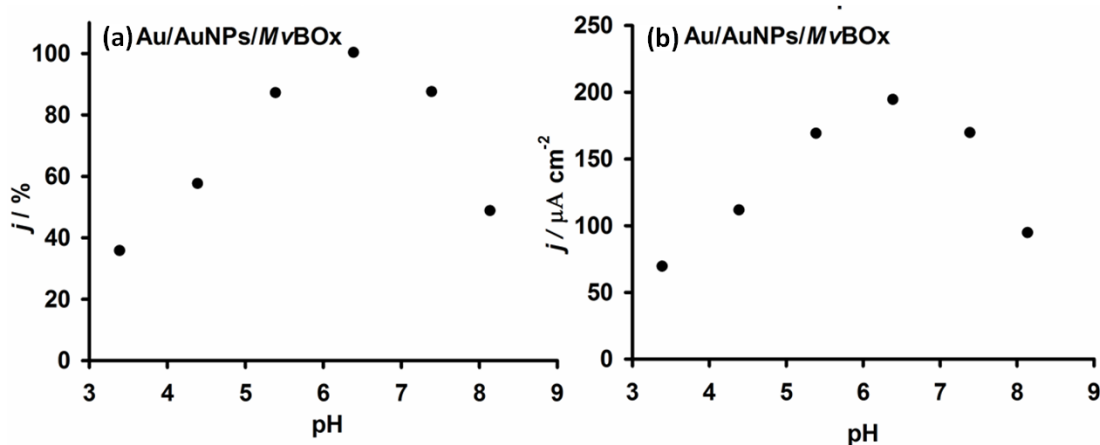


Figure 51. The pH dependencies of the current density of (c, d) Au/AuNP/MvBOx electrode at 0.45 V vs. NHE in air saturated buffer solutions. Rotation speed was set to 1000 rpm in order to eliminate possible diffusion limitations. Measurements were performed in air saturated 50 mM citrate-phosphate (pH 3.4-5.4) and phosphate (pH 6.4-8.2) buffers containing 100 mM KCl.

To conclude, it can be stated that the bioelectrocatalytic reduction current at *MvBOx* modified Au/AuNP electrodes was significantly higher than the bioelectrocatalytic oxidation current generated at *HiCDH* modified electrodes (Figs. 47 and 50). It could be mentioned that biocathodes delivering current densities up to 5 mA cm^{-2} on 3D AuNP structures [14] and up to 10 mA cm^{-2} on carbon materials [255] in saturated oxygen solutions have been reported confirming that the biocathode is usually not the limiting electrode in the performance of EBFC.

3.3.2.3. Evaluation of the complete EBFC performance

By combining the Au/AuNP/MHP/*HiCDH* bioanode and Au/AuNP/*MvBOx* biocathode in one compartment, an EBFC operating in different biofuels, *viz.*, lactose and glucose, was constructed (Fig. 52). The following parameters for the complete EBFC were obtained in quiescent air saturated PBS, pH 7.4, containing: (i) 5 mM glucose - open-circuit voltage (OCV) of $0.65 \pm 0.011 \text{ V}$ and the maximal power density of $4.77 \pm 1.34 \text{ } \mu\text{W cm}^{-2}$ at operating voltage of 0.50 V; or (ii) 10 mM lactose - OCV of $0.67 \pm 0.006 \text{ V}$ and the maximal power density of $8.64 \pm 1.91 \text{ } \mu\text{W cm}^{-2}$ at operating voltage of 0.50 V (Fig. 52).

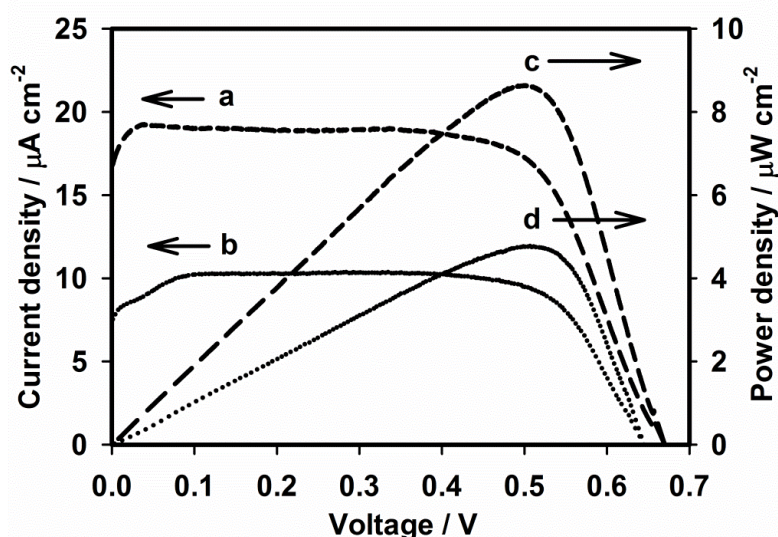


Figure 52. Typical dependences of current and power densities on operating voltage of the *HiCDH-MvBOx* based FCs in air saturated carbohydrate containing 50 mM PBS, pH 7.4. Conditions: PBS containing (a and c) 10 mM lactose and (b and d) 5 mM glucose. LSVs were recorded with a potential scan rate of 0.1 mV s^{-1} .

Comparing with previously reported results, the present EBFC configuration demonstrated the maximal power density approximately 1.5 times higher if compared to *CtCDH-MvBOx* based FC immobilised on spectrographic pyrolytic graphite (SPG) [247] and AuNP electrodes [8]. The improved power output was achieved for *HiCDH-MvBOx* based FC with glucose as a biofuel, specifically, in PBS, pH 7.4, containing 5 mM glucose. The open circuit voltage of the *HiCDH-MvBOx* based FC was practically the same as those reported for *CtCDH-MvBOx* based FCs, *i.e.*, in the range of 0.62-0.68 V. However, much higher power densities can be achieved for those EBFCs where enzymes of high biocatalytic activity, such PQQ-dependent glucose dehydrogenase or glucose oxidase, are employed as anodic biocatalysts. For example, PQQ glucose dehydrogenase (PQQ-GDH)/BOx based EBFCs, when adsorbed at carbon nanotube modified gold electrodes in 20 mM glucose solution, pH 6.5, generated an OCV of 0.60 V and demonstrated a power density up to 23 $\mu\text{W cm}^2$ [256]. Nevertheless, the immobilisation procedure of PQQ-GDH bioanode is quite complicated, *i.e.*, time- and reagent-consuming, as well as the enzyme lose approximately 50 % of its bioelectrocatalytic activity when operating at pH 7.5 [256]. Very exciting performance parameters were registered for GOx/laccase based EFC where the enzymes were incorporated in carbon nanotube disks by mechanical compression. The EFC delivered a power density up to 1.3 mW cm^{-2} and an OCV of 0.95 V in physiological conditions [5]. However, there is still an ongoing debate whether the true DET mechanism is realised or the bioelectrocatalytic current is observed due to naturally mediated glucose oxidation by free FAD, which has diffused out from the active centres of some partly denatured enzyme molecules. Moreover, an additional problem with using GOx in implantable conditions is the fact that O_2 is the natural electron acceptor, and the enzyme produces hydrogen peroxide in the presence of O_2 , which is toxic, and hence requires additional modifications for their operation *in vivo*, *e.g.*, co-immobilisation of catalase, which makes the bioelectrode design much more complicated.

According to the maximal power generated by a EFC designed in this research in glucose containing solutions it can be concluded that a weakness of utilising CDH enzyme is the fact that glucose is not the natural substrate of the enzyme. Thus, the catalytic efficiency is significantly lower compared to GOx based biodevices. Thereby, there is still a lot of space for improvement of the *HiCDH-MvBOx* EFC performance by improving the kinetics at FAD subunit or/and intermolecular ET between the FAD and the heme domains of the *HiCDH* enzyme which might be done employing genetic engineering manipulations.

With lactose as a biofuel (10 mM lactose in PBS), the *HiCDH-MvBOx* based FC showed 1.7 times lower power output. Increased power density can be achieved by using higher concentration of lactose since *HiCDH* bioanode is not inhibited by high lactose concentrations, while the inhibition of *CtCDH* based bioanode already starts at 2 mM lactose concentration [8]. Keeping in mind that milk and its products might contain up to 150 mM lactose the *HiCDH-MvBOx* based FC might be advantageous in some real applications.

Operational stabilities of *HiCDH-MvBOx* FCs were characterised by half-life times of their power outputs (at 1 M Ω external resistance load) of at least 13 h and 44 h in glucose and lactose containing PBS, respectively. In the non-loaded situation, *i.e.*, when OCV was monitored, only a 20 % drop in voltage of the biodevice was registered after 100 h in PBS containing 5 mM glucose (Fig. 53). In our previously published reports on *CtCDH-MvBOx* based FCs in glucose containing solutions half-times of 6 h and 30 h are stated [8, 247]. The 30 h half-time was achieved by crosslinking the bioanode enzyme with glutaraldehyde. The BFC in the current work had a half-time of 13 h, indicating that the stability of the design could be further improved, *e.g.*, by cross-linking of the adsorbed enzyme, which slows down gradual desorption and deactivation of the surface bound enzyme molecules.

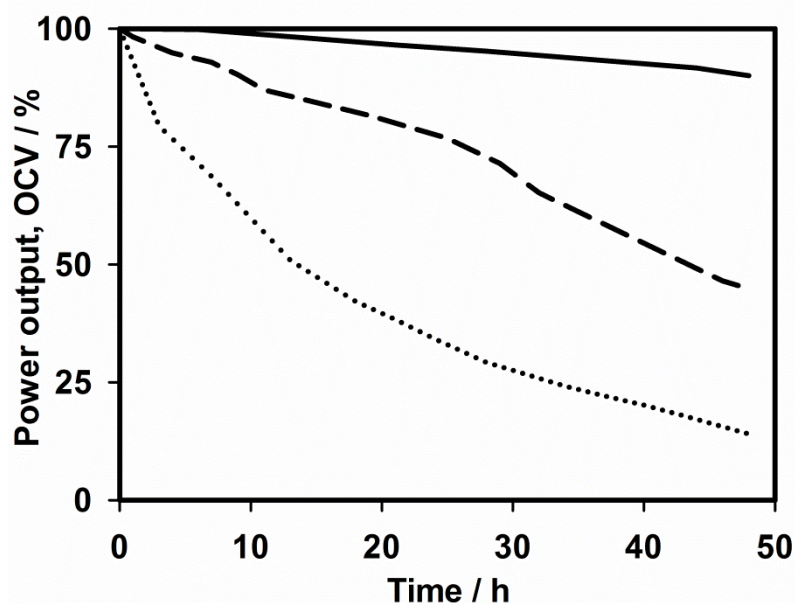


Figure 53. Time dependent decrease (in %) of power outputs and open circuit voltages of the *HiCDH-MvBOx* based FCs in air saturated quiescent PBS, pH 7.4: (solid line) OCV of the biodevice in 5 mM glucose containing PBS; (broken line) power output of the biodevice in 5 mM glucose containing PBS; and (dotted line) power output of the biodevice in 10 mM lactose containing PBS.

3.4. Bioelectrocatalytic reduction of O_2 by laccase at AuNP monolayers

Being aware that if designed properly, stable and high current density providing 3D biocathodes might be assembled by using Lc and AuNP building blocks, the DET studies of the Lc from *Trametes hirsuta* (*ThLc*) at AuNP-modified surfaces have been performed to understand the limitations and improvement possibilities of bioelectrocatalysis at the AuNP-*ThLc* assemblies. For this purpose the following questions were addressed in this chapter: (i) How many *ThLc* molecules adsorb at a single AuNP? (ii) What is an approximate current magnitude of O_2 bioelectroreduction at a single AuNP modified with *ThLc*? (iii) How do these characteristics correlate with the density of AuNP monolayer? (iv) What is the rate of the limiting reaction which defines oxygen bioelectroreduction at the AuNP-*ThLc* structure (Fig. 54)?

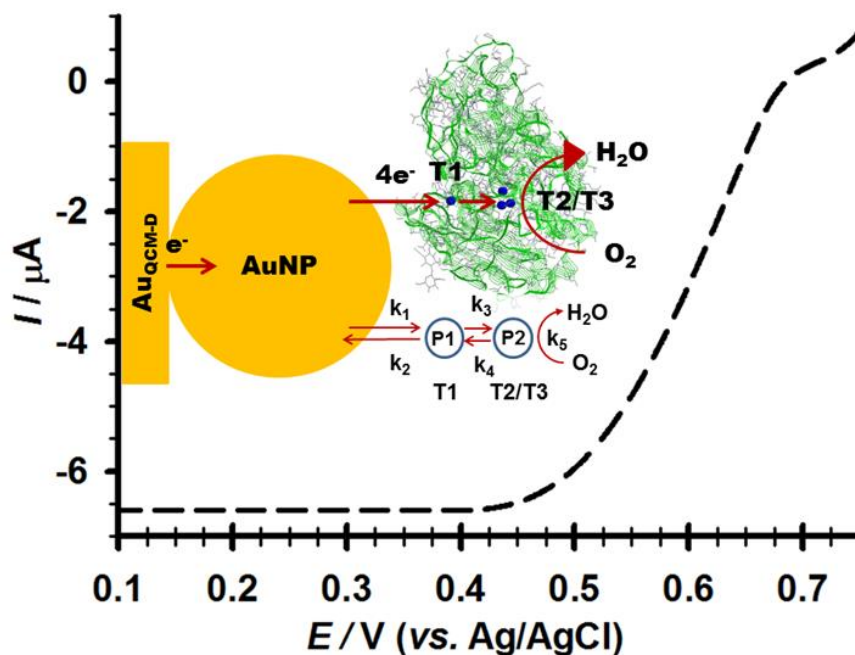


Figure 54. The schematic representation of DET between a Lc molecule (green ribbons) and the AuNP modified planar gold electrode. The T1 copper site and the T2/T3 copper cluster in Lc are presented as blue dots. Red arrows represent the direction of ET and the reaction of oxygen reduction to water at the applied potential below 0.65 V (vs. Ag/AgCl/3M KCl). The scheme represents a sketch summarising the mechanism of bioelectroreduction of oxygen at the electrode as described by Eqs. 32-36.

To quantify the total amount of the AuNPs attached to the surface of a gold electrode ($\text{Au}_{\text{QCM-D}}$), assess the number of *ThLc* molecules adsorbed on the surface of AuNPs, as well as evaluate the bioelectroreduction of O_2 at AuNP-*ThLc* layer, electrochemical methods combined with the quartz crystal microbalance with dissipation (QCM-D) technique were employed. The density of the monolayers of AuNPs was varied by changing the ionic strength of AuNP dispersion.

The mass was monitored for surface structures obtained by the following adsorption sequence: $\text{Au}_{\text{QCM-D}}\text{-PLL}$ (PLL adsorbed on the QCM-D sensor surface), $\text{Au}_{\text{QCM-D}}\text{-PLL-}ThLc$ (PLL adsorption was followed by *ThLc* adsorption), $\text{Au}_{\text{QCM-D}}\text{-PLL-}ThLc\text{-AuNPs}$ (AuNPs were adsorbed on PLL-*ThLc* treated QCM-D sensor surface), and $\text{Au}_{\text{QCM-D}}\text{-PLL-}ThLc\text{-AuNPs-}ThLc$ (*ThLc* was adsorbed on surface modified by PLL-*ThLc*-AuNPs). We should mention that notations of surface structures, e.g., $\text{Au}_{\text{QCM-D}}\text{-PLL-}ThLc\text{-AuNPs-}ThLc$,

reflect rather the sequence of the surface modification than the real layer structure, which is much less ordered (Fig. 55).

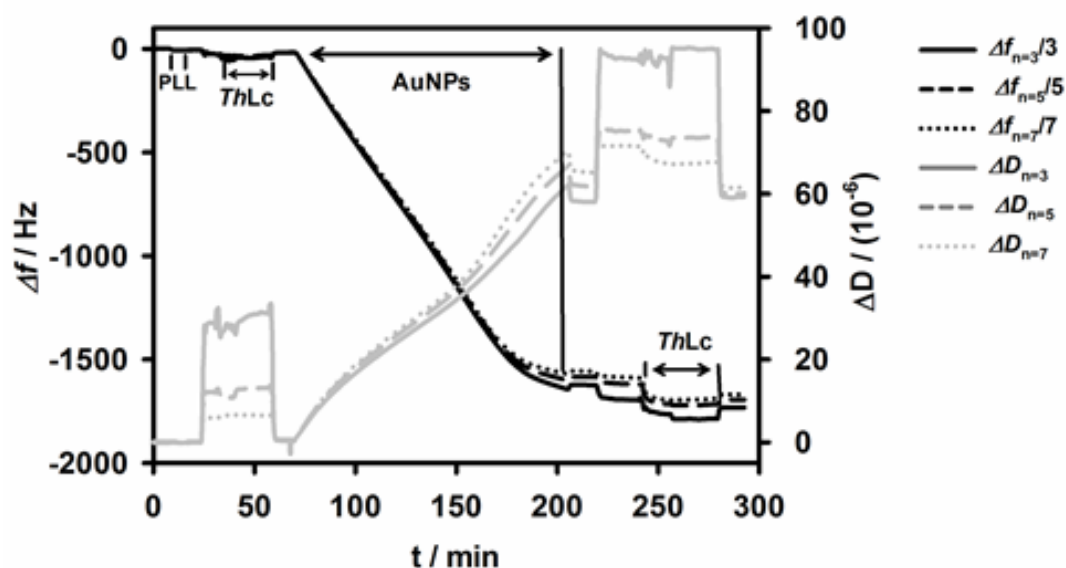


Figure 55. The dependence of change in frequency (Δf) and dissipation (ΔD) vs. time during the adsorption of poly-L-lysine (PLL), laccase (Lc), gold nanoparticles (AuNPs) and laccase (Lc) on the surface of QCM-D gold sensor. The data are recorded by QCM-D instrument when AuNPs assembly was carried at 20 mM NaCl. Time intervals when appropriate compound solution was pumped through the QCM-D gold sensor are indicated by PLL, *ThLc*, AuNP, and *ThLc*. In between these intervals the sensor was washed with water or/and buffer as specified in the text below.

It was experimentally found that AuNPs did not adsorb on the *ThLc* modified planar Au_{QCM-D} electrode if the modification with PLL was omitted. These experiments revealed that AuNP assembly is due to the AuNP interaction with PLL layer. The PLL-AuNP interaction was also negligibly affected by the *ThLc* layer adsorbed on Au_{QCM-D}-PLL surface structure since there was no noticeable difference in the amount of adsorbed AuNPs on Au_{QCM-D}-PLL and Au_{QCM-D}-PLL-*ThLc* surface. This indicates that the majority of *ThLc* molecules adsorb on PLL non-covered planar Au_{QCM-D} sensor surface. Due to the importance of PLL for the assembly of the AuNP-*ThLc* layer, PLL adsorption is discussed as well.

3.4.1. Adsorption of PLL

The measurement of PLL adsorption onto a gold coated quartz crystal by QCM-D showed very small changes in f and hardly any observable variation in D . The average ratio of $\Delta D/\Delta f$ at 3rd overtone was equal to 0.001, which

indicated the formation of a very rigid PLL film [257], justifying the Sauerbrey formula based calculation of the adsorbed mass [229]. The adsorbed PLL mass, calculated using the Sauerbrey formula was $93 \pm 22 \text{ ng cm}^{-2}$ ($0.8 \pm 0.2 \text{ pmol cm}^{-2}$ assuming that with the molecular weight of 70-150 kDa has an average MW of 110 kDa). This amount is less than ellipsometrically determined surface concentrations ($120\text{-}400 \text{ ng cm}^{-2}$) of a monolayer of average size proteins on gold [258], or PLL on methacrylate (400 ng cm^{-2}), and on polyvinylchloride (170 ng cm^{-2}) surfaces [259]. It could be stated that the dry mass of the adsorbed PLL practically must be less than 100 ng cm^{-2} , if we take into account that the mass measured by QCM-D also accounts for 50-80% of water coupled to the layer [260]. A low surface concentration and very small $\Delta D/\Delta f$ ratio indicate that PLL molecules adsorb in a flat, rod-like conformation. Such a PLL structure in the film can be explained by a strong PLL interaction with the gold surface and high electrostatic repulsion between the positively charged lysine monomers in PLL, particularly because PLL was adsorbed from water.

3.4.2. Sequential adsorption of Lc, AuNPs, and Lc

After the PLL layer was adsorbed on $\text{Au}_{\text{QCM-D}}$ sensor and rinsed with water the *ThLc* solution was pumped through the QCM-D flow cell. QCM-D measurements revealed that *ThLc* adsorbed on top of PLL and probably directly on the PLL unoccupied gold surface. The surface concentration of the enzyme calculated using the Voigt model was equal to $3.5 \pm 0.8 \text{ pmol cm}^{-2}$ which was much higher than the concentration of adsorbed PLL ($0.8 \pm 0.2 \text{ pmol cm}^{-2}$, see chapter 3.5.1.). Higher adsorption of the enzyme is reasonable because *ThLc* is a globular protein compared to the coil-shaped PLL. *ThLc* is slightly net positively charged ($\text{pI} = 4.2$) at pH 4 (in the adsorption conditions). Though the electrostatic PLL-*ThLc* interaction might not be expected at this pH, locally, it still might take place between negatively charged areas of the protein and PLL, especially, at higher ionic strength. The concentration of adsorbed *ThLc* is comparable to the surface concentration ($\sim 2.6 \text{ pmol cm}^{-2}$) of

BSA (a globular protein of similar MW) on gold surfaces as previously measured by ellipsometry [258].

After the Au_{QCM-D} sensor surface was pre-treated with PLL and *ThLc*, the layer of AuNPs was assembled on the sensor surface. The adsorption sequence is denoted by abbreviation Au_{QCM-D}-PLL-*ThLc*-AuNPs. Experimental conditions were chosen to assemble the AuNP layer with NP packing density lower than monolayer, *i.e.*, diluted monolayer. This was done by adsorbing AuNPs from NP dispersion with the same NP concentration, but with a different NaCl concentration. Our experiments showed (Fig. 56) that the degree of monolayer coverage, θ (Eq. 29), depended on the NaCl concentration present in the AuNP dispersion. θ is defined as the ratio of experimentally determined surface concentration of NPs, C_a , to their surface concentration maximally possible by hexagonal packing, $C_{a,max}$. For 22 nm diameter AuNPs $C_{a,max}$ is estimated to be equal to 0.396 pmol cm⁻².

$$\theta = \frac{C_a}{C_{a,max}} \quad (29)$$

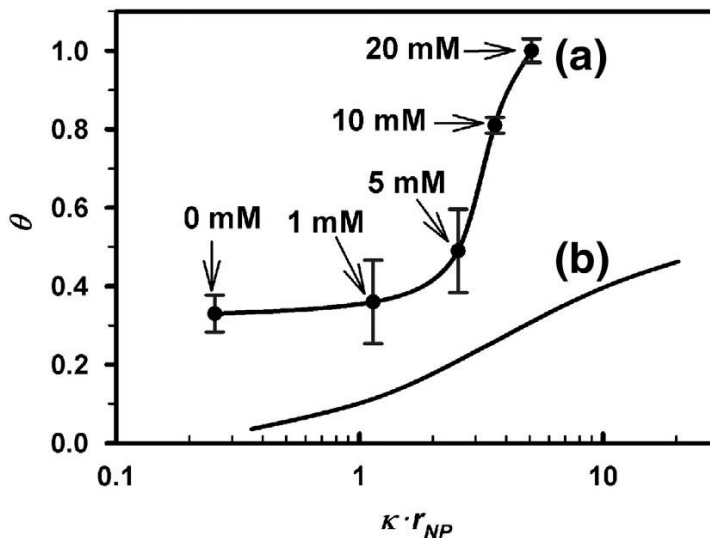


Figure 56. The degree of monolayer coverage (θ) by 22 nm diameter AuNPs: (a) experimental and (b) theoretical θ dependencies vs. the product of the Debye screening length (κ^{-1}) and NP radius (r_{NP}). $\theta = 1$ corresponds to complete 2D hexagonal packing. Theoretical dependence (b) is calculated for random sequential adsorption model, Eq. 30. λ values are presented in Table S1, supplementary materials. Arrows mark the concentration of NaCl in AuNP dispersion used during AuNP assembly.

It is hard to believe that the adsorption sequence PLL-*Th*Lc-AuNPs results into an idealised layered structure as can be interpreted from the abbreviation Au_{QCM-D}-PLL-*Th*Lc-AuNPs. However, the appraisal of the Au_{QCM-D}-PLL-*Th*Lc-AuNP surface structure is very important for later interpretation of bioelectrocatalysis down to a single AuNP level. This is why we analysed the dependence of θ on the concentration of NaCl (Fig. 56) in the light of idealised AuNP adsorption model which considers electrostatic repulsion between the AuNPs as the major factors determining surface density of NPs [206]. It should be noted that more comprehensive theoretical models, additionally accounting for van der Waals inter-particle interactions [261] or double layer effect of planar surface [209], were not used in the rationalisation of our data because the evaluation of these interactions is beyond the scope of this study.

The dependence θ vs. dimensionless multiple of κr_{NP} shown in Fig. 56 can be modelled by Eq. 30 (Fig. 56, curve b), where r_{NP} is a geometric (“hard”) radius of NPs and κ is a reciprocal of Debye length (Eq. 31).

$$\theta = \theta_{jam} \left(\frac{r_{NP}}{r_{NP,eff}} \right)^2 = \theta_{jam} \left(\frac{r_{NP} \cdot \kappa}{r_{NP} \cdot \kappa + \lambda} \right)^2 = \theta_{jam} \left(\frac{r_{NP}}{r_{NP} + \lambda \cdot \kappa^{-1}} \right)^2 \quad (30)$$

$$\kappa = \sqrt{\frac{2F^2 z_i^2 c_i}{\varepsilon \varepsilon_0 RT}} \quad (31)$$

F and R denote Faraday and Molar gas constants, respectively; z_i and c_i denote the valency and the concentration of electrolyte ions; ε and ε_0 denote the dielectric constant of the solution and vacuum, respectively; and T stands for absolute temperature.

In Eq. 30 θ_{jam} is a jamming limit of θ for a random sequential adsorption of NPs experimentally determined to be equal to 0.547, *i.e.*, $\theta_{jam} = 0.547$ [206]. Effective (“soft”) radius, $r_{NP,eff}$, of nanoparticles (Eq. 30) accounts for the repulsive forces between the NPs resulting into a diluted NP monolayer coverage, *i.e.*, for $\theta < \theta_{jam}$. In case of electrostatic repulsion of NPs the effective radius can be estimated as a multiple of Debye screening length, κ^{-1}

(Eq. 30). Parameter λ , to the highest degree, accounts for the effect of electrical surface potential of NPs on θ [262]. However, λ depends also on κ and r_{NP} [209] and obviously includes all interactions that are included into theoretical modelling of inter-particle interaction potential at the interface. Kooij [212], however, demonstrated that accounting only for particle-particle electrostatic repulsion satisfactory describes θ for diluted NP monolayer. Following mathematical formalism justified by Kooij [212] λ values were calculated to increase from $\lambda = 1.05$ (at 0.1 mM NaCl) to $\lambda = 1.68$ (at 20 mM NaCl) for 22 nm diameter NPs ($r_{NP} = 11$ nm) with the surface potential of 0.05 V. Mathematical formulas used in the calculation are summarised in the supplementary materials including full set of λ values. By substituting these λ values in Eq. 30 a theoretical θ vs. κr_{NP} dependence is drawn in Fig. 56 (curve b).

From Fig. 56 it can be seen that AuNP assembly from dispersion dialyzed against water (concentration of NaCl is 0 mM) results in a surface concentration corresponding to $\theta = 0.33$. Increasing NaCl concentration in AuNP dispersion up to 20 mM obviously diminishes the repulsion between AuNPs allowing higher AuNP packing density on the surface. A nearly complete, *i.e.*, $\theta = 0.8$, AuNP monolayer coverage was reached using the AuNP dispersion containing 10 mM NaCl. While in the presence of 20 mM NaCl the estimated surface coverage approached $\theta = 1$ (Fig. 56). It should be noted that AuNP dispersion containing 20 mM NaCl was not stable for longer than 30 min and hence the onset of multilayer formation might be expected. In SEM images it can also be seen that the surface coverage was increased with ionic strength to almost full coverage already at 10 mM as presented in Fig. 57b. Imaging was conducted on the same quartz crystal sensor as used in the QCM-D experiments. It is important to note that after each finished QCM-D experiment the sensors were rinsed with UHQ water for 20 min before they were removed from the QCM-D module and dried with N_2 . Then they were glued and prepared for the SEM experiments.

From Fig. 56 it can be seen that the theoretical dependence of θ on the dimensionless product κr_{NP} (Fig. 56, curve b) describes the experimental points rather poorly. This indicates that the model of random sequential adsorption with jamming of NPs does not explain AuNP adsorption on the PLL treated surface. The model of random adsorption with jamming of NPs seems to suit relatively well for the surfaces modified with the compounds of small molecular weight, *e.g.*, silanes [209, 212] or thiols [263].

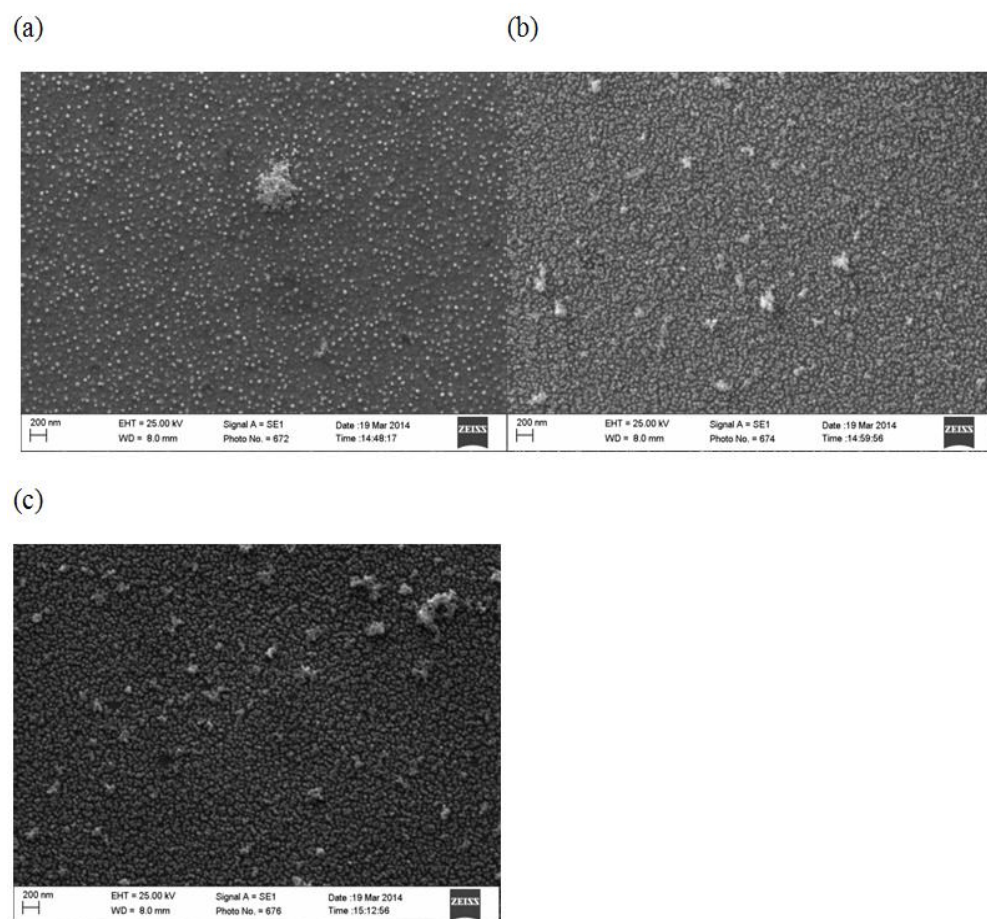


Figure 57. SEM images of monolayers of AuNPs adsorbed on Au/ PLL/Lc (a) from 0 mM NaCl, (b) from 10 mM NaCl and (c) from 20 mM NaCl solution. An additional layer of Lc is adsorbed on the AuNPs deposited on PLL. However, this does not affect the packing density during the adsorption of AuNPs but might rather affect the resolution of the SEM image.

However, it does not explain AuNP adsorption on PLL modified surfaces. Similar conclusion was drawn in an earlier study of ferritin

adsorption on PLL modified polystyrene [206]. The authors found more than monolayer coverage of ferritin on the PLL treated surface. Taking into account previously published results and our data presented in Fig. 56 we can assume that certain parts of long PLL molecules probably detach from the planar gold surface and wrap AuNPs. This phenomenon is highly likely to enable the higher surface density of AuNP as it is allowed by random sequential adsorption model. Pointing that PLL can wrap AuNPs becomes important when the explanation of bioelectrocatalysis per single AuNP modified with *ThLc* is discussed below.

Assembly of bioelectrocatalytic multi-component system was completed by adsorbing the second layer of *ThLc*. The final structure is denoted as $\text{Au}_{\text{QCM-D}}\text{-PLL-}ThLc\text{-AuNPs-}ThLc$. The surface concentration of the last *ThLc* layer was dependent on the coverage of AuNPs. Specifically, the estimated surface concentrations were 9 ± 1 , 8.9 ± 1.9 , 9.9 ± 1.6 , 14 ± 4 , and 24 ± 5 pmol/cm² (geometric sensor area, *i.e.*, $\text{Au}_{\text{QCM-D}}$) at AuNP coverage θ of 0.33, 0.35, 0.49, 0.81, and 1, respectively. It can be noted that adsorption of *ThLc* bound on the AuNP surface (at AuNP θ of 1) was approximately 7 times higher if compared to the first *ThLc* layer adsorbed on $\text{Au}_{\text{QCM-D}}\text{-PLL}$ surface (3.5 ± 0.8 pmol cm⁻²). It is important to emphasize that a part of the mass accounted for *ThLc* can come from the mass of coupled water sensed by QCM-D. A typical part of coupled water for different proteins can vary from 30% to 90% [264]. We have neglected the mass of coupled water (taken as 0%) when assessing the number of *ThLc* molecules adsorbed per single AuNP (Fig. 58). From Fig. 58, especially at $\theta > 0.4$, it can be concluded that experimentally found number of *ThLc* molecules adsorbed per single AuNP is close to the theoretical estimate of 44 laccase molecules per 22 nm diameter NP. Reasonably, this number is practically independent on AuNP monolayer coverage. The theoretical *ThLc* number per AuNP was calculated assuming that each *ThLc* molecule (PDB database: 3FPX) occupies a 6.4×5.4 nm² rectangle.

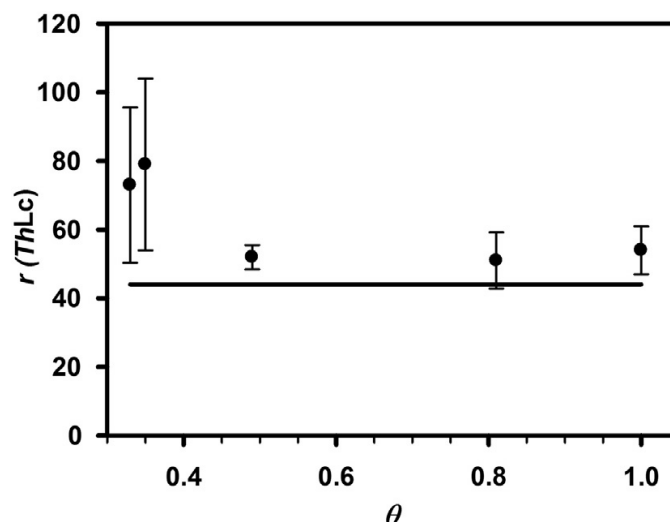


Figure 58. The number of *ThLc* molecules $r(\text{ThLc})$ adsorbed per one AuNP at a different AuNP monolayer coverage. The solid line shows 44 theoretically expected *ThLc* molecules per one AuNP.

3.4.3. Evaluation of kinetic constants of bioelectrocatalytic reduction of O_2 at Lc modified AuNPs

DET characteristics of *ThLc* enzyme at AuNPs were investigated by running LSVs after each modification step of $\text{Au}_{\text{QCM-D}}$ electrode. Fig. 59 shows LSVs recorded for the case of the AuNP layer with $\theta = 1$, *i.e.*, the electrode which generated the highest current of bioelectrocatalytic oxygen reduction.

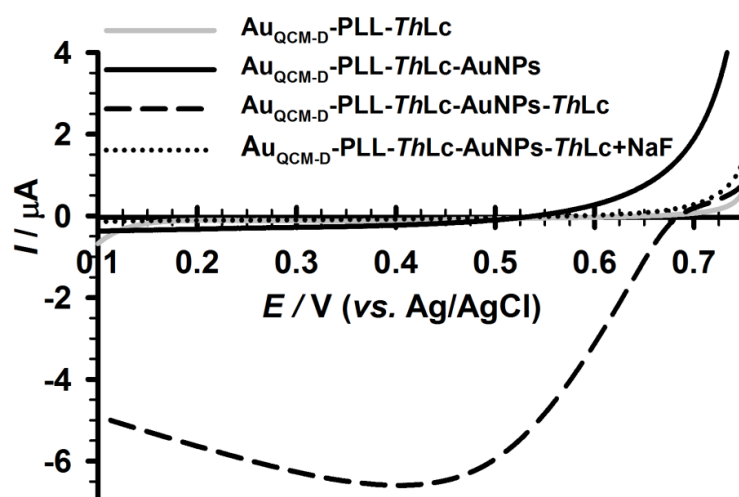


Figure 59. LSVs obtained using the $\text{Au}_{\text{QCM-D}}$ electrode modified with the PLL-*ThLc*-AuNP-*ThLc* biocatalytic structure. The assembly of AuNP was made from 20 mM NaCl (resulting $\theta = 1$). Potential scan rate: 1 mV s^{-1} ; flow rate: $100 \mu\text{L min}^{-1}$; 50 mM citrate - phosphate buffer, pH 4.0.

From Fig. 59 it can be seen that decreasing the applied potential causes the increase of the reduction current starting at approximately 0.65 V and reaching the maximum at 0.40 V. It is well established that the current is due to the bioelectrocatalytic reduction of oxygen at the *ThLc*-AuNP modified electrode [183]. Inhibition of laccase by NaF (Fig. 59, dotted curve) entirely diminishes the current. Practically, no bioelectrocatalytic current was observed, if the electrode had been modified only by *ThLc* (structure Au_{QCM-D}-PLL-*ThLc*, Fig. 59, grey curve) or AuNPs (structure Au_{QCM-D}-PLL-*ThLc*-AuNPs, Fig. 59, solid curve). The bioelectroreduction current was higher at a higher AuNP monolayer coverage (Fig. 60) as expected due to a higher amount of AuNPs modified with *ThLc* molecules at the electrode.

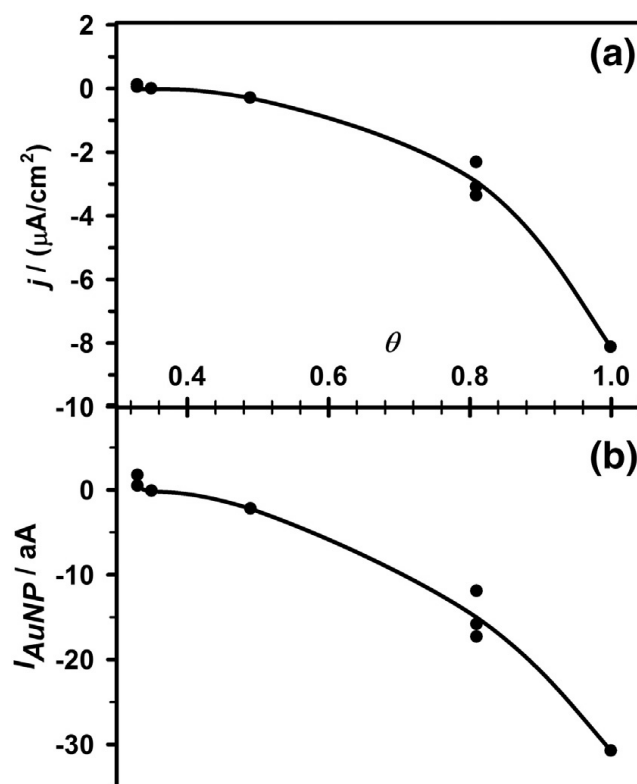


Figure 60. The dependence of bioelectroreduction of oxygen on AuNP monolayer coverage (θ): (a) current density per geometric electrode area (Au_{QCM-D}); (b) the absolute current at a single AuNP. The values of the bioelectrocatalytic current are taken at $E = 0.4$ V vs. Ag/AgCl using the data of LSV experiments (See Fig. 59 for $\theta = 1$). The geometric electrode area was 0.785 cm². Current per NP was evaluated dividing the measured current density by the AuNP number at cm² estimated by QCM-D measurements

Dividing current density (Fig. 60a) by a known amount of AuNPs at the electrode, the bioelectroreduction current at a single AuNP was calculated

(Fig. 60b) which reached the maximum of $31 \cdot 10^{-18}$ A. Surprisingly, the current per AuNP modified with *ThLc* molecules depended on the NP density, or θ , on the electrode surface. To explain this dependence (Fig. 60b) we considered three limiting steps of bioelectrocatalysis, which determine the bioelectrocatalytic current, i , at the electrode:

$$\frac{1}{i} = \frac{1}{i_{DET}} + \frac{1}{i_{bio}} + \frac{1}{i_{mt}} \quad (32)$$

where i_{DET} , i_{bio} , and i_{mt} , are electrode current which is limited by DET between the *ThLc* and AuNP, catalytic activity of *ThLc*, and mass transfer of oxygen, respectively. The limitation of the electrode current by the diffusion of oxygen (i_{mt}) can be easily excluded from the consideration as experimentally increasing the rate of solution flow at the electrode has not increased the electrode current. The kinetic currents, i_{DET} and i_{bio} , were described based on the kinetic scheme presented in Fig. 54, *i.e.*, adopting the approach elaborated by Climent et al [233]. The equations defining the currents are provided below and the final formulas used for fitting the experimental results are presented in the supplementary information.

$$i_{DET} = FA\Gamma[k_1(1-P_1) - k_2P_1] \quad (33)$$

$$k_1 = k_0 \exp\left[-\alpha \frac{F}{RT} (E - E_{T1}^{0'})\right] \quad (34)$$

$$k_2 = k_0 \exp\left[(1-\alpha) \frac{F}{RT} (E - E_{T1}^{0'})\right] \quad (35)$$

$$i_{bio} = nFA\Gamma k_5 = nFA\Gamma \frac{k_{cat}[O_2]}{K_M + [O_2]} \quad (36)$$

In Eqs. 33-36 F is Faraday constant, A is a geometric area of the electrode, Γ is surface concentration of AuNP-bound *ThLc* molecules, k_1 and k_2 are potential dependent DET rate constants defined by the Butler-Volmer formalism (Eqs. 34 and 35). P_1 represents a fraction of NP-bound *ThLc* molecules with the reduced, Cu(I), T1 copper centre. k_0 is the standard heterogeneous ET rate constant, R is the gas constant, T is temperature, E is applied potential, $E_{T1}^{0'}$ is

the formal redox potential of the T1 copper centre, α is the transfer coefficient. $n=4$ is a number of electrons of the reaction (see Fig. 54), k_{cat} is a homogeneous catalytic rate constant (turnover) of the enzyme, $[O_2]$ is oxygen concentration (substrate) at the electrode surface and K_m is a Michaelis-Menten constant.

Fitting the experimental bioelectrocatalytic currents obtained at the electrodes characterised by different θ of AuNPs (*e.g.*, Fig. 59 for $\theta = 1$) to the Eqs. 33-36 k_{cat} and k_0 constants were assessed. The calculation results are presented in Table 7.

Table 7. Kinetic constants, k_{cat} and k_0 , characterising bioelectrocatalytic reduction of O_2 at electrodes modified with *ThLc* and AuNPs. The constants were calculated using Eqs. 33-36. Parameters $\alpha = 0.5$; $K_m = 100 \mu\text{M}$; and $[O_2] = 250 \mu\text{M}$ were fixed. Columns summarise the following: $[\text{NaCl}]$ - sodium chloride concentration in water during the assembly of AuNPs, θ - degree of monolayer coverage by AuNPs, Γ - surface concentration of *ThLc* on AuNPs, $E_{T1}^{0'}$ - the formal potential of the T1 copper site estimated by fitting procedure (supplementary materials).

$[\text{NaCl}]$, mM	θ	Γ , pmol/cm ²	k_{cat} , s ⁻¹	k_0 , s ⁻¹	$E_{T1}^{0'}$ vs. Ag/AgCl, V
0	0.33	2.37	1.40	0.38	0.63
1	0.35	1.4	1.41	0.39	0.64
5	0.49	0.99	2.75	0.55	0.66
10	0.81	0.89	9.10	4.2	0.66
20	1	0.91	13.0	6.1	0.66

As can be seen from Table 7, k_{cat} and k_0 increase by approximately 10 and 16 times when θ increases from 0.33 to 1. This apparently means that the enzyme becomes more active at higher θ as well as DET coupling improves considerably when the AuNP density on the surface increases. The dependence of the constants on θ cannot be explained considering that *ThLc*-AuNP interaction remains the same at a different AuNP density on the electrode surface. For reasoning the dependence of the constants on θ , we can put forward several hypotheses. The first, yet hardly probable, is that an unknown impurity occupies the surface of AuNPs, when NP density on the surface is

low. The second hypothesis is that PLL probably partly lifts from the planar Au_{QCM-D} surface and wraps up the surface of AuNPs impairing proper orientation of *ThLc* on AuNPs. PLL acts as an “impurity” limiting the DET coupling between the enzyme and AuNP as well as the amount of *ThLc* in DET contact, though similar *ThLc* amount adsorbs per AuNP at different θ (Fig. 58). This explanation is also in line with the observation of much higher AuNP coverage than jamming limit, which is practically possible if PLL partly wraps AuNPs bound at the planar Au_{QCM-D}-PLL surface. As can be seen from Table 1 the maximal values of $k_{\text{cat}} = 13 \text{ s}^{-1}$ and $k_0 = 6.1 \text{ s}^{-1}$ were obtained in conditions when AuNP assembly was carried out from the NP dispersion containing 20 mM NaCl ($\theta = 1$). The constants can probably be underestimated since the mass of coupled water measured by QCM-D cannot be excluded from the determined mass of the *ThLc* layer. If we accept that about 50% of the mass in the *ThLc* layer comes from the coupled water, then the estimated k_{cat} could be twice as high. Nevertheless, comparing this to the k_{cat} (190 s^{-1}) known from the homogeneous activity assays, it can be concluded that DET coupling of *ThLc* to AuNP by simple adsorption still could be improved. To deeper understand DET of laccases at AuNPs we continue with the measurements of the dependence of oxygen bioelectrocatalysis on the size (radius) of AuNPs.

3.5. Evaluation of physicochemical properties of mono-and multi-layers of AuNPs

In the studies described in this chapter the assembly of mono (2D)- and multi (3D)-layers of AuNPs formed on a planar gold surface was performed using layer-by-layer (LbL) deposition method. Negatively charged citrate-coated AuNPs of an average diameter of 22 nm were (inter)linked on the surface *via* positively charged high- or low- molecular weight (inter)linkers, i.e., poly-L-lysine (PLL) or 1-(6- mercaptohexyl) pyridinium (MHP), respectively. Additionally, AuNP adsorption on PLL-*ThLc* bi-layer, used to attach AuNP monolayer on a gold electrode for the studies carried out in chapter 3.4., is mainly discussed in the context of rheological properties. Physicochemical

characteristics, such as a surface concentration and structural properties, of resulting AuNP structures, were evaluated using raw data obtained from QCM-D measurements while adsorbing AuNPs from dispersions of different ionic strength and, thus, varying the surface coverage of AuNPs. The use of AuNPs as building elements in 3D structures provides an advantage of being a well-defined object to obtain direct rheological information about the linker-NP interface, since the size AuNP is known, and they have a spherical form which is not expected to deform upon adsorption.

3.5.1. MHP and PLL adsorption

The adsorption of two different compounds, i.e., a small MHP compound of low MW assembling to a SAM and a long linear PLL macromolecule of high MW forming a homogenous film with flexible chains, was used to attach AuNP on a planar gold surface or interlink AuNP layers into 3D structure. The characterisation of these structures is briefly discussed. Their adsorption features are compared with the adsorption characteristics of PLL-*ThLc* bi-layer previously used for the formation 2D AuNP structure (Chapter 3.4.) which is consisted of long flexible PLL molecules and globular *ThLc* proteins. Some *ThLc* molecules (or most of them) are suspected to attach directly to a gold surface unoccupied by PLL.

The normalised frequency change (Δf) and the energy dissipation change (ΔD) associated with the adsorption of MHP (0.1 mM solution), PLL (0.002 wt % solution) and *ThLc* (0.7 mg ml⁻¹) was recorded at 7 overtones and analysed in order to determine the mass of the adsorbed films. The adsorption process was rapid for all investigated compounds, though slightly faster for MHP molecules.

The finite Δf for MHP, PLL, and PLL-*ThLc* bi-layer (*ThLc* adsorbed on PLL), after rinsing of loosely attached molecules, were following: -2.5±0.9 Hz, -1.1±0.4, and -12.8±3.8 Hz, respectively. Considering the small dissipation change (< 0.2·10⁻⁶ per 5 MHz for MHP and PLL, and ~ 0.6·10⁻⁶ per 5 MHz for PLL-*ThLc*) for all pre-adsorbed films the adsorbed masses presented in Table 8

were calculated according to the Sauerbrey equation (using the values of MW presented above). The estimated area occupied by an adsorbed MHP molecule (Table 8) can be compared to the area captured by an alkane chain of diameter of 0.45 nm [265] occupying an area of 0.15 nm² in a SAM [266]. Comparing with the values presented in other studies of alkanes, the area (0.68 nm²) occupied by a MHP molecule is reasonable since the presence of a charged pyridine ring destabilised the layer yielding a less ordered non-crystalline SAM. From ellipsometry measurements the dry mass and thickness of MHP was estimated to be 120 ng cm⁻² and 1.5 ± 0.1 nm, respectively, as reported elsewhere [267]. The calculated density of 0.80 g cm⁻³ is in the range of 0.75-1.050 g cm⁻³ typical for oils. PLL and *ThLc* occupy a much larger space as expected since the molecules are larger. For the *ThLc* the occupied area is in good agreement what is expected for the molecule dimensions (53x76x129 Å): <http://www.rcsb.org/pdb/explore/explore.do?structureId=3PXL>).

Table 8. The mass and calculated area per molecule as measured with QCM-D for monolayer of MHP, PLL and *ThLc* adsorbed on Au. *ThLc* is adsorbed on a pre-adsorbed layer of PLL, however, the presented mass and area is solely for *ThLc*. The mass of the adsorbed films are mean values of at least 3 separate experiments.

	Mass (ng cm ⁻²)	nm ² per molecule	Density (g cm ⁻³)
MHP	47.8 ± 0.2	0.68	0.8
PLL	18.8 ± 6.3	972	-
<i>ThLc</i>	226.7±66.5	51.3	-

3.5.2. Self-assembly of AuNP monolayers

Analysis of $\Delta D/\Delta f$ -plots reveals the information about structural changes of an adsorbed layer since during adsorption time independent correlation between ΔD and Δf is studied. In a typical homogeneous film the ΔD is expected to linearly increase with the thickness/mass, i.e., with grow of the absolute value of Δf .

BSM (mucin type I-S from bovine submaxillary gland, BSM, prod. No. 3895, Sigma) adsorption on Au_{QCM-D} sensor was carried out from a 100 mM acetate buffer, pH 7, and the overtones for n= 3, 5, and 7 are presented. Typical BSM adsorption shows a linearity of increasing dissipation with decreasing Δf and overlapping overtones that is typical for homogenous film in absence of structural changes during adsorption. The adsorption pattern of AuNPs on MHP, PLL, and PLL-*Th*Lc pretreated Au_{QCM-D} in the presence of 1 mM of NaCl was pretty similar in all the cases demonstrating the decrease in slope of ΔD with increasing mass load (decrease in Δf).

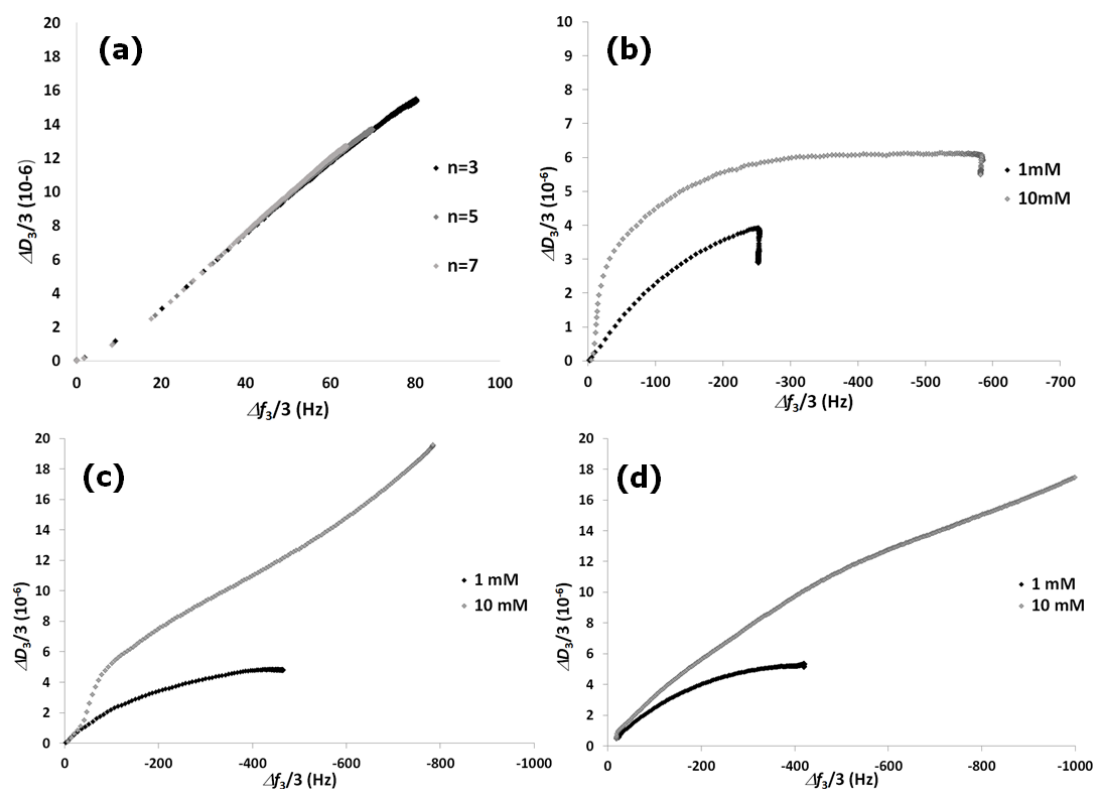


Figure 61. $\Delta D/\Delta f$ -plots for the adsorption of a model protein BSM forming homogeneous layer (a), AuNPs on MHP (b), AuNPs on PLL (c), and AuNPs on PLL-Lac (d) in the presence of 1 or 10 mM of NaCl.

This tendency indicates the limitation of AuNP movement at the NP-surface interface as the number of particles adsorbed per surface area increased. At higher ionic strength, i.e., in the presence of 10 mM NaCl, the $\Delta D/\Delta f$ -plots for the adsorption of AuNPs on PLL shows a trend of increasing

slope with decreasing frequency meaning that the system becomes more dissipative as the mass increases. This might be an effect of the flexibility of the PLL chain that gives the AuNPs a higher rate of movement in the AuNP-PLL interface. The increase was not seen at 10 mM for PLL-*ThLc* and might be absent due to interaction between PLL-*ThLc* that limits the flexibility of the PLL chain.

In order to further characterise the structure of the adsorbed film the behaviour of f and D changes as $\Delta D/\Delta f$ vs Δf plots can be analysed while as L-b-L deposition is monitored in order to elucidate information about the uniformity of the film. In Figure 62 the adsorption of AuNPs is illustrated and compared to that of BSM and how it is affected with regard to the structure of a linker.

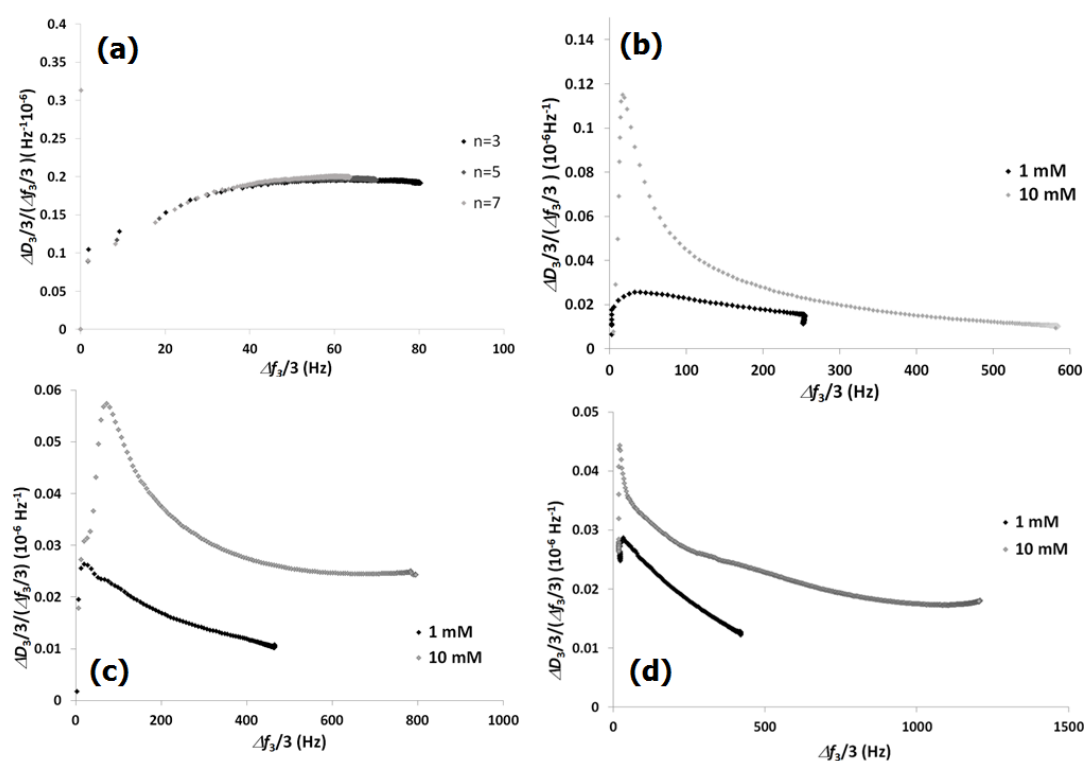


Figure 62. $\Delta D/\Delta f$ vs. Δf - plots for the adsorption of a model protein BSM forming homogeneous layer (a), AuNPs on MHP (b), AuNPs on PLL (c), and AuNPs on PLL-Lac (d) in the presence of 1 or 10 mM of NaCl.

In homogenous film the $\Delta D/\Delta f$ ratio is expected to increase, or be constant, with decreasing Δf , i.e., with increasing mass as illustrated for BSM. However, the ratio for the adsorption of AuNPs on MHP, PLL and PLL-*ThLc*

shows a different trend. At low ionic strength a distinct decrease in $\Delta D/\Delta f$ with increasing Δf demonstrates a build-up of heterogeneous layer. At higher ionic strengths the influence of closer packing and higher surface coverage was believed to transform the QCM-D response from heterogeneous to homogenous signal. However, only a negligible tendency to reach a constant $\Delta D/\Delta f$ change vs Δf was observed for AuNP adsorption on PLL and PLL-*ThLc*. The plots presented in Fig. 62 can be used to estimate surface concentration of NPs by so called model independent analysis [REF]. Full explanation of this calculation is beyond the scope of this thesis. However, the preliminary results (Table 2) are included in this thesis for comparison with a surface confined NP mass calculated by Sauerbrey equation and Voight model.

Table 9. Total mass of AuNPs adsorbed on MHP, PLL, and PLL-*ThLc* at different ionic strengths calculated with the Sauerbrey equation, the Voigt model and model-independent analysis (MIA). In MIA mass determination all data point or just a linear part of $\Delta D/\Delta f$ vs. Δf was used for making linear regression and intercept (on Δf axis) calculation. Masses in MIA is calculated as the average of liner regression from three overtones (n= 3, 5, and 7).

	NaCl (mM)	Sauerbrey (mg m ⁻²)	Voigt (mg m ⁻²)	Difference Sauerbrey vs. Voigt (%)	MIA (mg/m ²)	MIA linear (mg m ⁻²)
MHP-AuNPs	0	43.0	49.7	13.5	98.8	98.8
	1	43.9	48.9	10.2	98.3	98.3
	5	64.4	68.2	5.6	109.1	111.5
	10	104.2	106.3	2.0	120.8	97.8
	20	98.2	103.2	4.8	164.8	107.6
PLL-AuNP	0	45.3	52.7	14.0	74.5	74.5
	1	70.9	86.4	17.9	104.4	94.2
	10	138.6	155.2	10.7	259.0	104.6
PLL-<i>ThLc</i>-AuNPs	0	95.0	102.0	6.9	145.7	116.4
	1	70.1	76.5	8.4	125.7	121.7
	5	142.4	150.0	5.1	227.4	131.9
	10	210.1	222.3	5.5	493.8	205.3
	20	284.1	303.2	6.3	1034.2	289.1
PLL-AuNPs+<i>ThLc</i>	20	42.8	52.7	18.8	-	-

As can be seen, Table 9, the adsorption of AuNPs on MHP and PLL three trends are revealed: (1) the Δf intercept increase with ionic strength, (2) the $\Delta D/\Delta f$ values were in the same range when adsorbed on both MHP and PLL

and (3) the Δf intercept was larger for AuNPs adsorbed on PLL than on MHP. In a previous study it was shown that the $\Delta D/\Delta f$ ratio decreases with particle size [218] and stiffness of the particle-surface linker[217]. Putting that in context of the observations made in Fig. 62 the following conclusions can be made for the adsorption of AuNPs on MHP and PLL: (1) the electrostatic attraction between the MHP-AuNP/PLL-AuNP is decreased with increased ionic strength giving the particle more freedom to slip on the surface hence the higher dissipation, (2) the attractive electrostatic interactions between MHP and AuNPs are stronger or more specific than those between PLL and AuNPs since the intercept is smaller indicating a stiffer interaction in the particle-surface interface.

Additionally, comparing the masses obtained with the Sauerbrey equation and the Voigt model an increase in mass with increasing ionic strength is observed for all pre-adsorbents. However the trend is more pronounced for AuNPs adsorbing on MHP and PLL than on PLL-*ThLc*. The mass difference between Sauerbrey and Voigt mass is decreasing with increasing ionic strength for AuNPs adsorbed on both MHP and PLL whereas when adsorbed on PLL-*ThLc* no distinct difference is observed. When AuNPs adsorb on PLL-*ThLc* the formed film is likely to be more homogenous already from the beginning than for MHP-AuNP and PLL-AuNP, since the underestimation of the mass using the Sauerbrey equation is similar at all ionic strengths. This might suggest that adsorption of an interlayer of smaller globular molecules fills up the interspace between the particles and thus work as a steric barrier for interparticle interaction. This observation is important in explaining bioelectrochemical reactions in multilayer systems as discussed below.

3.5.3. Self-assembly of AuNP multilayers

In Fig. 63 $\Delta D/\Delta f$ vs. Δf plots for the L-b-L assembly of AuNPs from the dispersion of AuNPs containing 1 and 10 mM of NaCl, respectively, using MHP (a) and PLL (b) as an (inter)linker at 1 and 10 mM is presented. It can be seen that varying changes of the $\Delta D/\Delta f$ ratio with increasing layer number was

observed in the presence of 1 and 10 mM of NaCl, respectively. The observed results indicate that the behaviour of the AuNP multilayers changes from heterogeneous, i.e., from a discrete adsorbed film to behave more as a homogenous film. This means that the analysis of the adsorbed film can be conducted in different ways. For the first layer the mass of the adsorbed entities and, thereby, the surface coverage can be calculated using the Sauerbrey equation. With increasing ionic strength and layer number that is, when the 2nd linker-AuNP layer is deposited, the Voigt model can be used to calculate mass and viscoelastic properties of the adsorbed multilayer film.

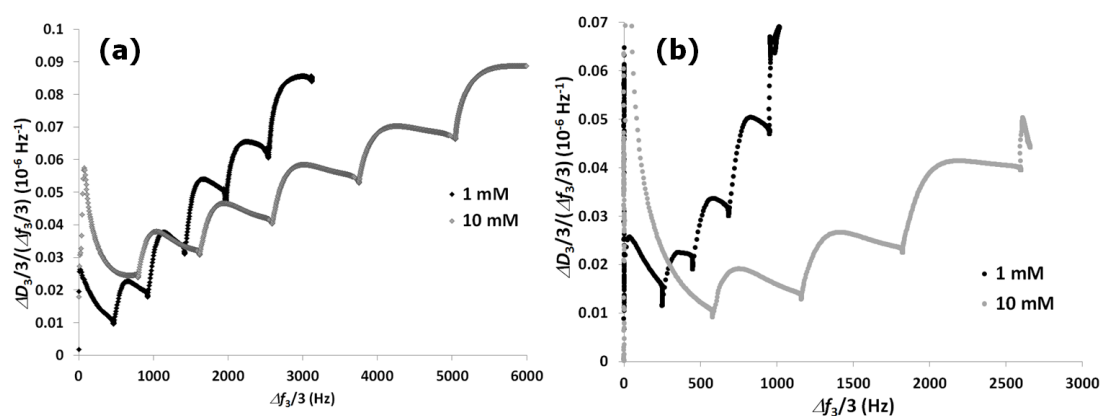


Figure 63. $\Delta D/\Delta f$ vs. Δf plots for the adsorption of multilayers of AuNPs on MHP (a) and PLL (b) pretreated electrode in the presence 1 and 10 mM mM of NaCl.

3.6. Bioelectrocatalytic reduction of O₂ by laccase differently incorporated into AuNP multilayers

In the last part of the research two different approaches of the assembly of AuNPs and *TaLc* enzymes into multilayer (3D) bionanostructures were studied seeking to prepare optimally functioning bioelectrocatalytic AuNP-*TaLc* structures; specifically, to attain the bioelectroreduction of O₂ in the entire volume of 3D electrodes. For this purpose, the incorporation of *TaLc* into 3D (4 layers) AuNP nanostructures was done by: making a (Fig. 64a) 3D AuNP nanostructure first, and then loading this structure with the *TaLc*, or (Fig. 64b) assembling AuNP-*TaLc* conjugates into a 3D nanobiostructure. The multilayer assembly was performed using the AuNPs of an average size of 20 nm by L-b-L method (Chapter 1.6.3.) while utilising PLL as an (inter)linker.

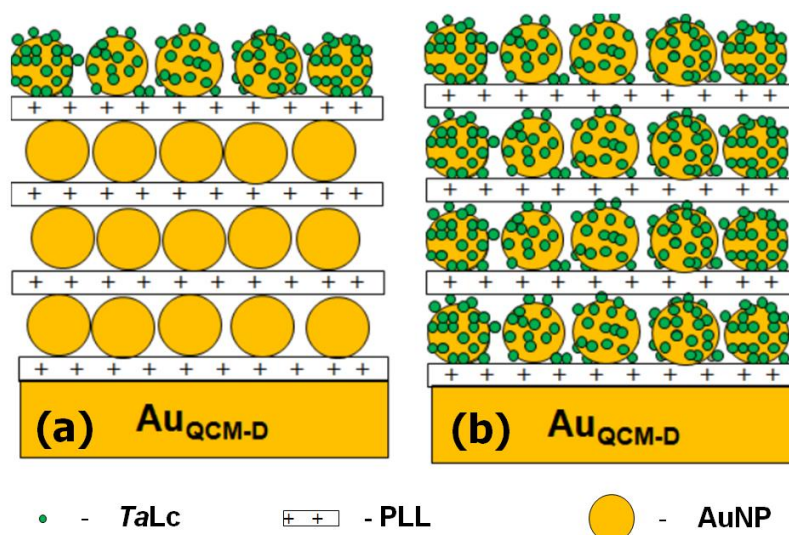


Figure 64. Two approaches of AuNP and *TaLc* assembly into 3D AuNP-*TaLc* bionanostructures.

Additionally, the bioelectroreduction of O_2 was investigated when *TaLc* was adsorbed on a monolayer (2D structure) of AuNPs in order to compare the bioelectroreduction of O_2 in 2D and 3D format.

More effective AuNP assembly and, at the same, the significant O_2 bioelectroreduction was observed for the 3D AuNP-*TaLc* nanostructure which was build using the AuNP dispersion free of the enzyme (Figs. 65a, 66a). When comparing the quantity of AuNPs adsorbed on the surface in each particular case, it can be summarised that in the case of Lc-free AuNP multilayer formation, the surface concentration of AuNP multilayer was three times as high as the one prepared using AuNP-Lc conjugates. The surface concentration of *TaLc* adsorbed on the PLL/AuNP structure was twice higher when comparing with the quantity of *TaLc* deposited on the PLL/AuNP-*TaLc* bionanostructure.

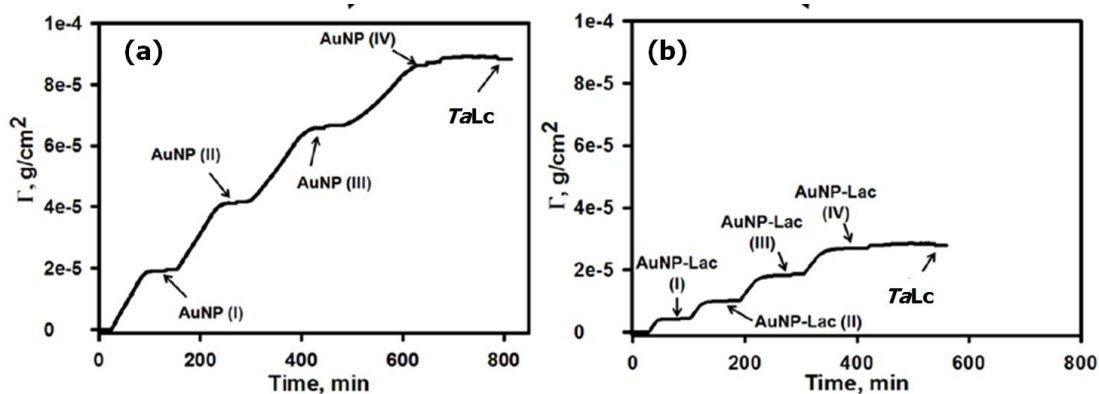


Figure 65. Monitoring of adsorption kinetic of the 3D nanostructures consisted of PLL, AuNP, and *TaLc*. The assembly of AuNP or AuNP-*TaLc* was made from 20 mM NaCl solution. The mixture of AuNPs and *TaLc* was prepared 15 min before the QCM-D experiment.

A very negligible and potential-dependent bioelectrocatalytic current for the electrode prepared using AuNP-*TaLc* conjugates shows that 3D structure assembled from AuNP-enzyme building elements hampers the DET of *TaLc* adsorbed on top of the structure.

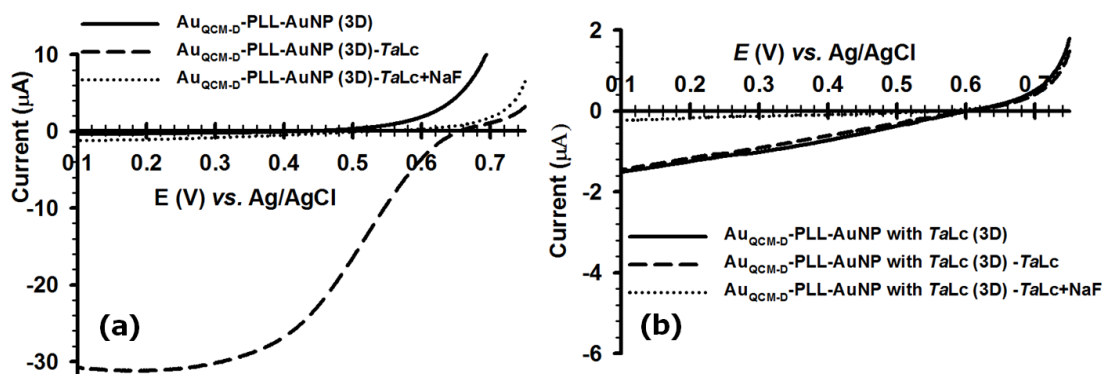


Figure 66. *TaLc* assisted bioelectrocatalytic reduction of oxygen in differently prepared 3D AuNP structures. The assembly of AuNP or AuNP-*TaLc* was made from 20 mM NaCl solution. Potential scan rate: 1 mV s⁻¹; flow rate: 100 μL min⁻¹; 50 mM citrate-phosphate buffer, pH 4.0.

It is important to emphasise the fact that, when *TaLc* was adsorbed on top of the PLL/Lc free-AuNP multilayer, PLL interlayers did not affect the conductivity of the AuNP nanostructure since in this case a very high bioelectrocatalytic current was registered. The current was approximately 5

times higher comparing with the one obtained when *TaLc* was adsorbed on AuNP monolayer (Fig 67).

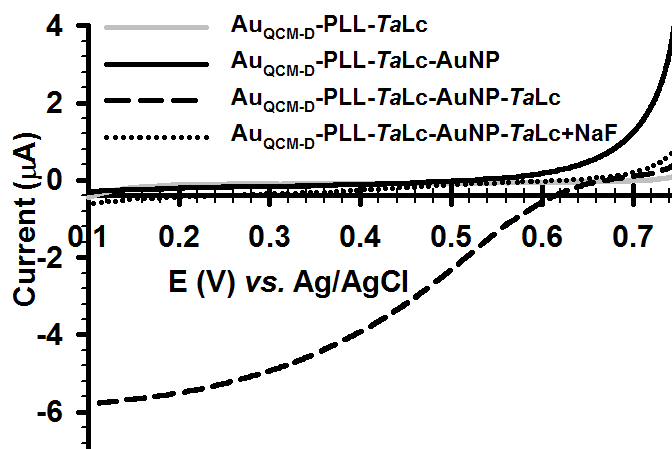


Figure 67. LSVs obtained with AuQCM-D electrode modified with the PLL-*ThLc*-AuNP(monolayer)-*ThLc* bionanostructure. The assembly of AuNP was made from 20 mM NaCl. Potential scan rate: 1 mV s⁻¹; flow rate: 100 µL min⁻¹; 50 mM citrate - phosphate buffer, pH 4.0.

Nevertheless, comparing the quantity of *TaLc* incorporated into the 2D and 3D AuNP structures it can be concluded that no significant penetration of *TaLc* was observed when the attempt was made to impregnate 3D AuNP structure with the enzyme. Nevertheless, the 3D PLL/AuNP nanostructure is an advantageous scaffold for the DET based coupling of *TaLc* enzyme, though it does not allow the *TaLc* molecules effectively penetrate into the entire structure.

To explain poor assembly of AuNP-*TaLc* conjugates into 3D structures zeta potential of AuNP-*TaLc* was measured and was found to be approximately -20 mV. This value is almost the same as for not modified AuNPs and, thus, should have been sufficient for electrostatically driven 3D assembly of AuNP- *TaLc*/PLL structure. Poor assembly, however, could be prevented if *TaLc* molecules on AuNP impose steric hindrance for AuNP and PLL interaction. This steric hindrance is probably the reason for poor assembly and bioelectrochemical performance of the structure made from AuNPs modified with Lac molecules.

CONCLUSIONS

1. GOx enabled the enzymatic polymerisation of polythiophene (PTP) *via* its catalytic cycle during glucose oxidation. PTP coated GOx enzyme demonstrated improved stability characteristics;
2. The best ET mediators for GOx enzyme have been found the PDs containing amino groups: 5-amino-1,10-phenanthroline (5AP) and 5,6-diamino-1,10-phenanthroline. While 5-amino,6-nitro-1,10-phenanthroline and [1,10-phenanthroline monohydrate showed miserable redox-mediating properties;
3. 5AP compound cross-linked with GOx enzyme on a graphite rod electrode (GRE) was employed as an anode while GRE with co-immobilised horseradish peroxidase (HRP) and GOx was exploited as a cathode in order to design a glucose powered EBFC;
4. A positively charged bi-functional thiol, N-(6-mercapto) hexylpyridinium (MHP), enabled DET based coupling of CDH enzymes from *Corynascus thermophilus* (CtCDH) and *Humicola insolens* (HiCDH) to the AuNP surface. HiCDH enzyme, demonstrating the resistance to substrate inhibition by lactose, was employed as an anodic biocatalyst in the designing of a mediatorless carbohydrate (glucose or lactose)/O₂ EBFC. The biocathode of the EBFC was based on bilirubin oxidase from *Myrothecium verrucaria* directly immobilised on the surface of AuNPs. This EBFC configuration is advantageous for the designing EBFC working in the media with high lactose concentrations, *e.g.*, milk or milk products;
5. When separate electrodes of the designed EBFCs were studied, it was estimated that the anodes were the limiting electrodes of the performance of both mediated and direct ET based EBFCs;
6. Assembling the monolayers of AuNPs with different degree a AuNP-monolayer coverage, θ ranged from 0.33 to 1. In every case of θ close to theoretically possible 44 ThLc molecules adsorbed at 22 nm diameter AuNP. The maximum current reached at a single AuNP was $31 \cdot 10^{-18}$ A

which corresponds to the enzyme turnover (k_{cat}) 13 s^{-1} . This rate is lower than the homogeneous *ThLc* turnover (190 s^{-1}) suggesting partial denaturation of *ThLc* upon adsorption or that some *ThLc* are not in DET contact with the electrode;

7. Measurements of energy dissipation at AuNP monolayer (2D) and multilayer (3D) structures showed that viscoelastic properties of entire layer changes during the adsorption of NPs, i.e., the viscoelastic properties change with growing of the 2D or 3D AuNP structure. This was compared with the adsorption of mucin, which gives a surface confined protein layer of constant viscoelasticity during the entire growth of the protein film;
8. PLL/AuNP based multilayer (four layers) is a highly conductive nanostructure suitable for DET based immobilisation of Lc enzyme, though it does not allow the *ThLc* molecules effectively penetrate into the entire structure.

LIST OF PUBLICATIONS AND CONFERENCE CONTRIBUTION

Publications included in the thesis:

1. Oztekin, Y., **Krikstolaityte, V.**, Ramanaviciene, A., Yazicigil, Z., Ramanavicius A. 1,10-Phenanthroline derivatives as mediators for glucose oxidase. *Biosensors and Bioelectronics*, 2010, 26 (1), 267-270;
2. Ramanavicius, A., Oztekin, Y., Balevicius, Z., Kausaite-Minkstimiene, A., **Krikstolaityte, V.**, Baleviciute, I., Ratautaite, V., Ramanaviciene, A. Conducting and electrochemically generated polymers in sensor design (Mini Review). *Procedia Engineering*, 2012, 47, 825 – 828;
3. **Krikstolaityte, V.**, Oztekin, Y., Kuliesius, J., Ramanaviciene, A., Yazicigil, Z., Ersoz, M., Okumus, A., Kausaite-Minkstimiene, A., Kilic, Z., Osman Solak, A., Makaraviciute, A., Ramanavicius, A. Biofuel cell based on anode and cathode modified by glucose oxidase. *Electroanalysis*, 2013, 25, 2677-2683.
4. **Krikstolaityte, V.**, Barrantes, A., Ramanavicius, A., Arnebrant, T., Shleev, S., Ruzgas., T. Bioelectrocatalytic reduction of oxygen at gold nanoparticles modified with laccase. *Bioelectrochemistry*, 2014, 95, 1-6.
5. **Krikstolaityte, V.**, Kuliesius, J., Ramanaviciene, A., Mikoliunaite, L., Kausaite-Minkstimiene, A., Oztekin., Y., Ramanavicius, A. Enzymatic polymerization of polythiophene by immobilized glucose oxidase. *Polymer*, 2014, 7, 1613-1620.
6. **Krikstolaityte, V.**, Lamberg, P., Toscano, M. D., Silow, M., Eicher-Lorka, O., Ramanavicius, A., Niaura, G., Abariute, L., Ruzgas, T., Shleev S. Mediatorless carbohydrate/oxygen biofuel cells with improved cellobiose dehydrogenase based bioanode. *Fuel Cells*, 2014 (Accepted).

Conference contribution:

1. **Krikstolaityte, V.**, Lamberg, P., Toscano, M. D., Silow, M., Eicher-Lorka, O., Ramanavicius, A., Niaura, G., Abariute, L., Ruzgas, T., Shleev, S. Mediatorless carbohydrate/oxygen biofuel cells with improved cellobiose dehydrogenase based bioanode. The 15th International Conference on Electroanalysis (ESEAC), Malmö, Sweden, June 11-15, 2014;
2. **Krikstolaityte, V.**, Lamberg, P., Toscano, M. D., Silow, M., Eicher-Lorka, O., Ramanavicius, A., Niaura, G., Abariute, L., Ruzgas, T., Shleev, S. Mediatorless carbohydrate/oxygen biofuel cell based on *Humicola insolens* cellobiose dehydrogenase as anodic biocatalyst. The 14th European Student Colloid Conference, Potsdam, Germany, June 10-13, 2013;
3. **Krikstolaityte, V.** Mediatorless carbohydrate/oxygen biofuel cells. The 7th Nanoschool “Novel nanomaterials and their application in bioanalysis”, Vilnius, Lithuania, May 8-10, 2013;
4. **Krikstolaityte, V.**, Toscano, M. D., Silow, M., Eicher-Lorka, O., Ramanavicius, A., Ruzgas T., Shleev S. Sugar/oxygen biofuel cells based on redox enzymes adsorbed on gold nanoparticle multilayers. The 8th Annual Biofilms Workshop - Research Center of Biointerfaces “Hydration of Biomolecules and Biointerfaces”, Malmö, Sweden, October 4-5, 2012;
5. Ramanaviciene, A., **Krikstolaityte, V.**, Oztekin, Y., German, N., Kausaite-Minkstimiene, A., Kuliesius, J., Baniukevic, J., Mazeiko V., Voronovic, J., Ramanavicius, A. Some aspects in conducting polymers synthesis. The 26th Conference of the

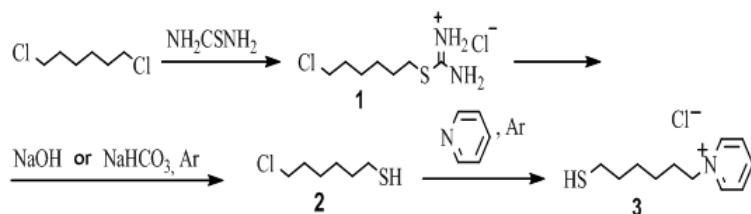
- European Colloid and Interface Society, Malmö, Sweden, September 2-7, 2012;
6. Ramanaviciene, A., **Krikstolaityte, V.**, Oztekin, Y., German, N., Kausaite-Minkstimiene, A., Kuliesius, J., Baniukevic, J., Mazeiko V., Voronovic, J., Ramanavicius, A. Enzymatic synthesis of conducting polymers. The 26th Conference of the European Colloid and Interface Society, Malmö, Sweden, September 2-7, 2012;
 7. **Krikstolaityte, V.**, Hamit-Eminovski, J., Barrantes, A., Ramanavicius, A., Abariute, L., Niaura, G., Arnebrant, T., Ruzgas, T. Investigation of viscoelastic properties of assembled gold nanoparticle mono- and multi-layer structures using quartz crystal microbalance with dissipation. The 26th Conference of the European Colloid and Interface Society, Malmö, Sweden, September 2-7, 2012;
 8. **Krikstolaityte, V.**, Barrantes, A., Arnebrant, T., Ramanavicius, A., Shleev, S., Ruzgas, T. Direct electron transfer of laccase incorporated in 2D and 3D gold nanoparticle nanostructures. The 14th International Conference of Electroanalysis (ESEAC), Portorož, Slovenia, June 3-7, 2012;
 9. **Krikstolaityte, V.**, Barrantes, A., Sotres, J., Arnebrant, T., Ramanavicius, A., Ruzgas, T. Physicochemical properties of gold nanoparticle multilayers. The 7th Annual Biofilms Workshop - Research Center of Biointerfaces "Non-Invasive Biomedical Monitoring and Devices", Malmö, Sweden, October 24-25, 2011;
 10. **Krikstolaityte, V.**, Barrantes, A., Sotres, J., Arnebrant, T., Ramanavicius, A., Ruzgas, T. Influence of ionic strength on physicochemical properties of gold nanoparticle multilayer

- structures. The 13th International Conference-School „Advanced Materials and Technologies“, Palanga, Lithuania, August 27-31, 2011;
11. **Krikstolaityte, V.**, Ramanavicius, A., Arnebrant, T., Shleev, S., Ruzgas, T. Control of laccase-gold nanoparticle assembly for reduction of oxygen to water. The XXI International Symposium on Bioelectrochemistry and Bioenergetics, Cracow, Poland, May 8-12, 2011;
 12. **Krikstolaityte, V.**, Dagys, M., Kulys, J., Ramanavicius, A., Arnebrant, T., Shleev, S., Ruzgas, T. Reduction of oxygen at laccase modified gold nanoparticles. The 61st Annual Meeting of the International Society of Electrochemistry, Nice, France, September 26 - October 1, 2010;
 13. Ramanavicius, A., Oztekin, Y., **Krikstolaityte, V.**, Kausaite, A., German, N., Voronovic, J., Ramanaviciene, A. Development of enzymatic biofuel cells. The 24th Conference of the European Colloid and Interface Society, Prague, Czech Republic, September 5-10, 2010
 14. **Krikstolaityte, V.**, Ramanavicius, A., Arnebrant, T., Ruzgas, T. Evaluation of gold nanoparticle assembly by electrochemical and QCM-D methods. The 15th Annual International Research Conference for Students and Young Researchers "Chemistry and Chemical Technology", Vilnius, Lithuania, May 7, 2010;
 15. Oztekin, Y., **Krikstolaityte, V.**, Voronovic, J., Ramanaviciene, A., Ramanavicius, A. New electron transfer mediators for redox enzymes. PITTCON 2010, Orlando, The USA, March 2, 2010

SUPPLEMENTARY INFORMATION

1. Synthesis and Characterization of N-(6-mercapto)hexylpyridinium (MHP)

MHP was synthesized as shown in Supplementary Figure S1.



Supplementary Figure S1. Synthesis scheme of N-(6-mercapto)hexylpyridinium (MHP) chloride (compound 3).

1.1. General procedures

Acetonitrile (HPLC grade) was purchased from Sigma Aldrich. Chloroform, 1,6-dichlorohexane, pyridine, 2-propanol, thiourea, and NaOH were obtained from Across Organics. Ethyl ether and acetone was purchased from Spolchim. Millipore purified water (18.2 M Ω cm) was used through the work. ^1H and ^{13}C NMR spectra were recorded in CDCl_3 , $\text{DMSO-}d_6$ and CD_3OD on Bruker Avance III 400 NMR spectrometer (δ in ppm, J in Hz) at ^1H operating frequencies of 400.13 MHz and 100.61 MHz for ^{13}C ; spectra were referenced using the solvent or TMS signal as internal standard. Elemental analyses were carried out on a Perkin-Elmer 2400-B microanalyser.

1.2. Synthesis of 2-(6-chlorohexyl)isothiuronium chloride (compound 1)

93 g (0.6 M) of 1,6-dichlorohexane and 11.4 g (0.15 M) of thiourea were added to the 1 L of 2-propanole and the mixture was boiled for ~20 h. After that the reaction mixture was cooled and the formed crystals were collected by filtration. Then the solvent and excess of 1,6-dichlorohexane was distilled off; the residue was infused with 200 mL of acetone and boiled. After cooling the formed crystal was filtered off and after re-crystallisation from dry acetonitrile, compound 1 was collected as white solid (29 g, 71%). Mp. 98–100°C; ^1H NMR (CD_3OD): 1.46–1.51 (4H, m, $\text{ClCH}_2\text{CH}_2\text{CH}_2\text{CH}_2$), 1.68–1.82 (4H, m, $\text{ClCH}_2\text{CH}_2\text{CH}_2\text{CH}_2\text{CH}_2$), 3.16 (2H, t, J 7.16, SCH_2), 3.56 (2H, t, J 6.34,

ClCH_2). ^{13}C (DMSO- d_6): 25.01 (SCH_2), 27.35 (SCH_2CH_2), 28.97 ($\text{ClCH}_2\text{CH}_2\text{CH}_2$), 29.52 ($\text{SCH}_2\text{CH}_2\text{CH}_2$), 31.94 (ClCH_2CH_2), 45.33 (ClCH_2). Elemental analyses (%). Found: C, 81.25; H, 7.25; Cl, 30.57; N, 12.05; S, 13.75. Calc. for $\text{C}_7\text{H}_{16}\text{Cl}_2\text{N}_2\text{S}$ (231.19): C, 81.39; H, 7.19; Cl, 30.67; N, 12.12; S, 13.87.

1.3. Synthesis of 6-chlorohexane-1-thiol (compound 2)

23.1 g (100 mM) of compound **1** was dissolved in 150 mL of water. Under the protection of argon at room temperature, a solution of 4.4 g (110 mM) of NaOH in 100 mL of water was added dropwise to the reaction mixture during an hour. Then the reaction mixture was stirred for another 8–10 h at 60 °C. The reaction mixture was cooled down to room temperature, acidified with HCl to pH \approx 7, and the product was extracted with chloroform (3x100 mL), washed with water to neutral pH and dried over anhydrous MgSO_4 . After that the solvent was distilled in argon atmosphere the product was distilled in vacuum to give compound **1** as colorless liquid (10 g, 65%). Bp. 82–83°C/5 mm, n_D^{20} 1.4842; ^1H NMR (CDCl_3 , TMS): 1.29 (1H, t, J 7.75, SH), 1.36–1.42 (4H, m, $\text{HSCH}_2\text{CH}_2\text{CH}_2\text{CH}_2$), 1.57 (2H, q, J 7.30, SCH_2CH_2), 1.73 (2H, q, J 7.53, ClCH_2CH_2), 2.44–2.51 (2H, td, HSCH_2), 3.48 (2H, t, J 6.60, ClCH_2). ^{13}C (CDCl_3): 24.40 ($\text{ClCH}_2\text{CH}_2\text{CH}_2$), 26.23 ($\text{SCH}_2\text{CH}_2\text{CH}_2$), 27.48 (SCH_2CH_2), 32.35 (SCH_2), 33.67 (ClCH_2CH_2), 44.89 (ClCH_2). Elemental analyses (%). Found: C, 47.11; H, 8.67; Cl, 23.17; S, 21.15. Calc. for $\text{C}_6\text{H}_{13}\text{ClS}$ (152.69): C, 47.20; H, 8.58; Cl, 23.22; S, 21.00.

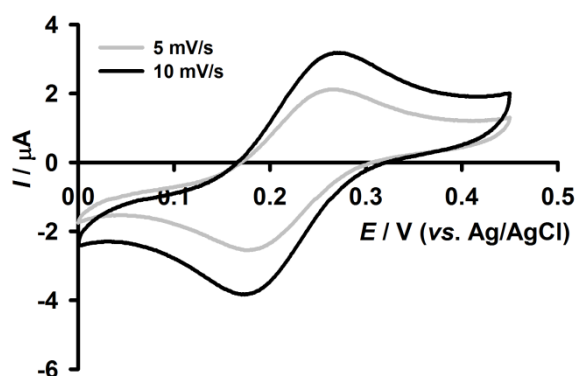
1.4. Synthesis of N-(6-mercapto)hexylpyridinium chloride (compound 3)

The mixture of 3.95 g (50 mM) of dry pyridine and 1.53 g (10 mM) of compound **2** at argon atmosphere was refluxed (115 °C) 20 min under the assistance of microwave irradiation (450W). The excess of pyridine was distilled off in vacuum at the argon atmosphere. The residue was recrystallized from dry acetonitrile and dry ethyl ether 1:10 and compound **3** was collected as white solid (8 g, 80%). Mp. 115–116°C; ^1H NMR (CDCl_3 , TMS): 1.42 (1H, t, J 7.89, SH), 1.30–1.51 (4H, m, $\text{HSCH}_2\text{CH}_2\text{CH}_2\text{CH}_2$), 1.59 (2H, q,

J 6.88, SCH_2CH_2), 2.09 (2H, q, J 7.46, $\text{N}^+\text{CH}_2\text{CH}_2$), 2.47–2.54 (2H, td, HSCH_2), 5.08 (2H, t, J 7.75, NCH_2), 8.13–8.18 (2H, m, Py-3,5), 8.49–8.54 (2H, m, Py-4), 9.71–9.73 (2H, m, Py-2,6). ^{13}C (CDCl_3): 24.40 ($\text{NCH}_2\text{CH}_2\text{CH}_2$), 25.40 ($\text{SCH}_2\text{CH}_2\text{CH}_2$), 27.51 (SCH_2CH_2), 31.94 (SCH_2), 33.38 (NCH_2CH_2), 61.72 (NCH_2), 128.37 (Py-3,5), 144.85 (Py-2,6), 145.39 (Py-4). Elemental analyses (%). Found: C, 56.79; H, 7.92; Cl, 15.12; N, 5.87; S, 13.90. Calc. for $\text{C}_{11}\text{H}_{18}\text{ClNS}$ (231.79): C, 57.00; H, 7.83; Cl, 15.30; N, 6.04; S, 13.83.

2. Evaluation of the QCM-D electrode working area by cyclic voltammetry

The working area of the QCM-D gold electrode has been measured by cyclic voltammetry (CV). Electrochemical QCM-D cell was filled with 40 μM of ferricyanide solution in 50 mM phosphate buffer (pH 4.0) containing 0.1 M Na_2SO_4 (adjusted by citric acid). CVs were run at 5 and 10 mV/s sweep rate of applied potential. The examples of CVs are presented in Fig. S2. Working area of the electrode was calculated by using Randles-Sevcik equation. The experimentally obtained value for the electrode area was $0.84 \pm 0.06 \text{ cm}^2$, presented as a mean value \pm standard deviation of four measurements. The experimentally obtained area of the electrode is very close to its geometric area of 0.785 cm^2 .



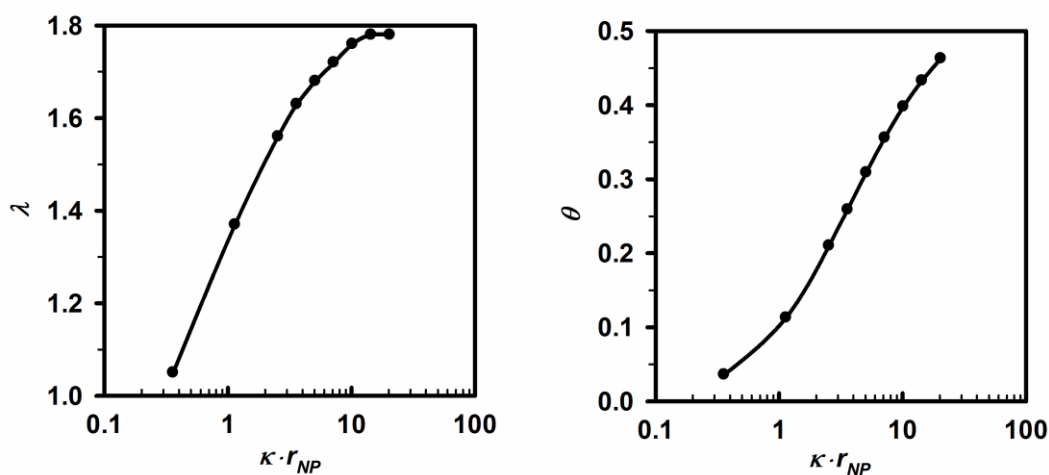
Supplementary Figure S2. Cyclic voltammograms of ferricyanide recorded with QCM-D gold electrode in QCM-D electrochemical cell at 5 and 10 mV/s sweep rate of applied potential. The QCM-D electrode was modified with monolayer of AuNPs assembled from 10 mM NaCl solution (for modification details see the main text of the article). Concentration of ferricyanide was 40 μM in 50 mM phosphate buffer (pH 4.0) containing 0.1 M Na_2SO_4 .

3. Surface concentration of nanoparticles: parameter λ

Using Eqs. 19-22 λ and θ values were calculated numerically at condition where $U_{pp}^{dl} = kT$, taking surface potential of NPs equal to $\psi_p = -0.05$ V and $r_{NP} = 11 \cdot 10^{-9}$ m. The values are summarised in Table S1 and presented in Fig. S3 as λ and θ vs. κr_{NP} .

Supplementary Table S1. Debye screening length (κ^{-1}), κr_{NP} , λ , and θ values calculated at experimentally relevant concentration of NaCl in AuNP dispersion. NP diameter is 22 nm ($r_{NP} = 11 \cdot 10^{-9}$ m) and surface potential was assumed to be equal to -0.05 V ($\psi_p = -0.05$ V). Calculations are based on Eqs. S1-S5.

C, M	κ^{-1} , nm	$r_{NP} \cdot \kappa$	λ	θ
0,0001	30,58	0,36	1,05	0,036
0,001	9,67	1,14	1,37	0,113
0,005	4,33	2,54	1,56	0,210
0,01	3,06	3,60	1,63	0,259
0,02	2,16	5,09	1,68	0,309
0,04	1,53	7,19	1,72	0,356
0,08	1,08	10,17	1,76	0,398
0,16	0,76	14,39	1,78	0,433
0,32	0,54	20,34	1,78	0,463

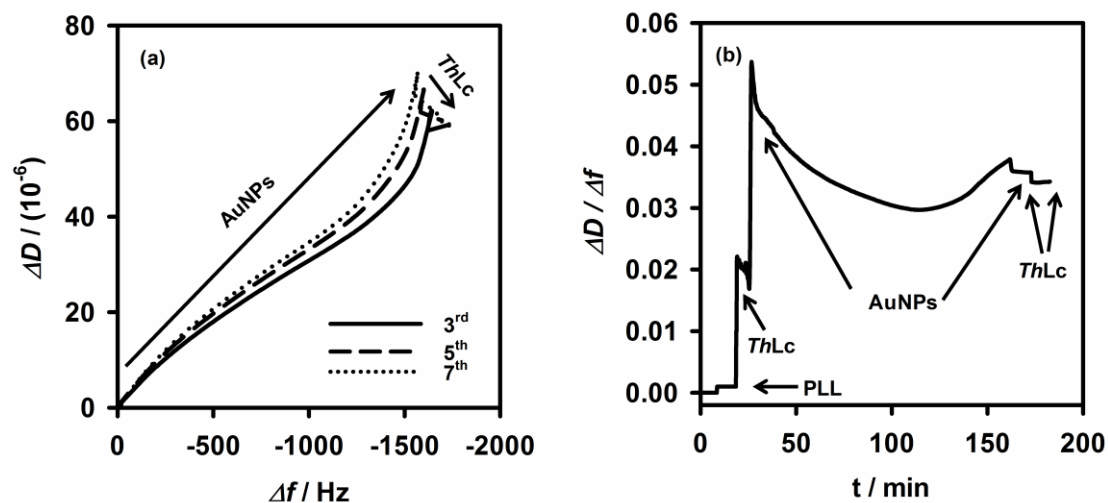


Supplementary Figure S3. Theoretical dependence of λ and θ vs. κr_{NP} constructed from data summarised in Table S1.

From Table S1 and Fig. S3 it can be concluded that parameter λ varies less than two times in the chosen concentration range of NaCl in solution. It is interesting to compare (Table S1) that at the same conditions Debye screening length,

dimensionless product $\kappa \cdot r_{\text{NP}}$, and even θ show much stronger dependence on NaCl concentration in NP dispersion.

4. Δf - ΔD plot for the PLL-*ThLc*-AuNPs-*ThLc* film



Supplementary Figure S4. (a) The Δf - ΔD plot for the PLL-*ThLc*-AuNPs-*ThLc* film when AuNP assembly was carried at 20 mM NaCl. The behaviour of the 3rd, 5th and 7th harmonics is shown; (b) the $\Delta D / \Delta f$ ratio of the 3rd overtone during the adsorption of the entire structure. To avoid a bulk effect of the buffer on the experimental data, $\Delta f / \Delta D$ changes during washing steps are not shown.

REFERENCES

- [1] J.A. Cracknell, K.A. Vincent, F.A. Armstrong, Enzymes as working or inspirational electrocatalysts for fuel cells and electrolysis, *Chem. Rev.* 108 (2008) 2439-2461.
- [2] E. Katz, K. MacVittie, Implanted biofuel cells operating in vivo - methods, applications and perspectives - feature article, *Energ. Environ. Sci.* 6 (2013) 2791-2803.
- [3] S.C. Barton, J. Gallaway, P. Atanassov, Enzymatic biofuel cells for implantable and microscale devices, *Chem. Rev.* 104 (2004) 4867-4886.
- [4] J. Larminie, A. Dicks, *Fuel Cell Systems Explained*, 2nd ed., John Wiley & Sons Ltd, Chichester, 2003.
- [5] A. Zebda, C. Gondran, A. Le Goff, M. Holzinger, P. Cinquin, S. Cosnier, Mediatorless high-power glucose biofuel cells based on compressed carbon nanotube-enzyme electrodes, *Nat. Commun.* 2 (2011) 370.
- [6] Z. Zhu, T. Kin Tam, F. Sun, C. You, Y.H. Percival Zhang, A high-energy-density sugar biobattery based on a synthetic enzymatic pathway, *Nat. Commun.* 5 (2014).
- [7] C.F. Blanford, R.S. Heath, F.A. Armstrong, A stable electrode for high-potential, electrocatalytic O₂ reduction based on rational attachment of a blue copper oxidase to a graphite surface., *Chem. Commun.* 17 (2007) 170-1712.
- [8] X.J. Wang, M. Falk, R. Ortiz, H. Matsumura, J. Bobacka, R. Ludwig, M. Bergelin, L. Gorton, S. Shleev, Mediatorless sugar/oxygen enzymatic fuel cells based on gold nanoparticle-modified electrodes, *Biosens. Bioelectron.* 31 (2012) 219-225.
- [9] A.T. Yahiro, S.M. Lee, D.O. Kimble, Bioelectrochemistry: I. Enzyme utilizing bio-fuel cell studies, *Biochim. Biophys. Acta* 88 (1964) 375-383.
- [10] J.H. Pazur, K. Kleppe, The oxidation of glucose and related compounds by glucose oxidase from *Aspergillus niger**, *Biochemistry* 3 (1964) 578-583.
- [11] H.J. Hecht, H.M. Kalisz, J. Hendle, R.D. Schmid, D. Schomburg, Crystal structure of glucose oxidase from *Aspergillus niger* refined at 2.3 Å resolution, *J. Mol. Biol.* 229 (1993) 153-172.
- [12] B.A. Gregg, A. Heller, Cross-linked redox gels containing glucose oxidase for amperometric biosensor applications, *Anal. Chem.* 62 (1990) 258-263.

- [13] W. Schuhmann, T.J. Ohara, H.L. Schmidt, A. Heller, Electron transfer between glucose oxidase and electrodes via redox mediators bound with flexible chains to the enzyme surface, *J. Am. Chem. Soc.* 113 (1991) 1394-1397.
- [14] K. Murata, K. Kajiya, N. Nakamura, H. Ohno, Direct electrochemistry of bilirubin oxidase on three-dimensional gold nanoparticle electrodes and its application in a biofuel cell, *Energ. Environ. Sci.* 2 (2009) 1280–1285.
- [15] G.T.R. Palmore, Biofuel Cells, in: *Bioelectrochemistry*, John Wiley & Sons, Ltd, Chichester, 2008, pp. 359-375.
- [16] U. Schröder, J. Nießen, F. Scholz, A generation of microbial fuel cells with current outputs boosted by more than one order of magnitude, *Angew. Chem. Inter. Ed.* 42 (2003) 2880-2883.
- [17] D. Bhatnagar, S. Xu, C. Fischer, R.L. Arechederra, S.D. Minteer, Mitochondrial biofuel cells: Expanding fuel diversity to amino acids, *Phys. Chem. Chem. Phys.* 13 (2011) 86-92.
- [18] F. Xu, Applications of oxidoreductases: Recent progress, *Industrial Biotechnology* 1 (2005) 38-50.
- [19] D.P. Hickey, F. Giroud, D.W. Schmidtke, D.T. Glatzhofer, S.D. Minteer, Enzyme cascade for catalyzing sucrose oxidation in a biofuel cell, *ACS Catalysis* 3 (2013) 2729-2737.
- [20] M. Falk, Z. Blum, S. Shleev, Direct electron transfer based enzymatic fuel cells, *Electrochim. Acta* 82 (2012) 191-202.
- [21] D. Leech, P. Kavanagh, W. Schuhmann, Enzymatic fuel cells: Recent progress, *Electrochim. Acta* 84 (2012) 223-234.
- [22] R.A. Bullen, T.C. Arnot, J.B. Lakeman, F.C. Walsh, Biofuel cells and their development, *Biosens. Bioelectron.* 21 (2006) 2015-2045.
- [23] M.T. Meredith, S.D. Minteer, Biofuel cells: Enhanced enzymatic bioelectrocatalysis, *Annu. Rev. Anal. Chem.* 5 (2012) 157-179.
- [24] A.J. Bard, L.R. Faulkner, Potentials and Thermodynamics of Cells, in: *Electrochemical Methods*, John Wiley & Sons, Inc., New York, 2001, pp. 44-87.
- [25] D.L. Johnson, J.L. Thompson, S.M. Brinkmann, K.A. Schuller, L.L. Martin, Electrochemical characterization of purified *Rhus vernicifera* laccase:

Voltammetric evidence for a sequential four-electron transfer, *Biochemistry* 42 (2003) 10229-10237.

[26] N. Mano, V. Soukharev, A. Heller, A laccase-wiring redox hydrogel for efficient catalysis of O₂ electroreduction, *J. Phys. Chem. B.* 110 (2006) 11180-11187.

[27] H. Sakai, T. Nakagawa, Y. Tokita, T. Hatazawa, T. Ikeda, S. Tsujimura, K. Kano, A high-power glucose/oxygen biofuel cell operating under quiescent conditions, *Energ. Environ. Sci.* 2 (2009) 133-138.

[28] Y. Tokita, T. Nakagawa, H. Sakai, T. Hatazawa, Sugar-powered electronics, in, RSC Publishing, http://www.rsc.org/Publishing/ChemTech/Volume/2008/11/sugar_powered_electronics.asp, 2008.

[29] M. Falk, V. Andoralov, Z. Blum, J. Sotres, D.B. Suyatin, T. Ruzgas, T. Arnebrant, S. Shleev, Biofuel cell as a power source for electronic contact lenses, *Biosens. Bioelectron.* 37 (2012) 38-45.

[30] V. Flexer, N. Mano, From dynamic measurements of photosynthesis in a living plant to sunlight transformation into electricity, *Anal. Chem.* 82 (2010) 1444-1449.

[31] L. Halamkova, J. Halamek, V. Bocharova, A. Szczupak, L. Alfonta, E. Katz, Implanted biofuel cell operating in a living snail, *J. Am. Chem. Soc.* 134 (2012) 5040-5043.

[32] J.A. Castorena-Gonzalez, C. Foote, K. MacVittie, J. Halánek, L. Halámková, L.A. Martinez-Lemus, E. Katz, Biofuel cell operating in vivo in rat, *Electroanalysis* 25 (2013) 1579-1584.

[33] M. Rasmussen, R.E. Ritzmann, I. Lee, A.J. Pollack, D. Scherson, An implantable biofuel cell for a live insect, *J. Am. Chem. Soc.* 134 (2012) 1458-1460.

[34] A. Szczupak, J. Halamek, L. Halamkova, V. Bocharova, L. Alfonta, E. Katz, Living battery - biofuel cells operating in vivo in clams, *Energ. Environ. Sci.* 5 (2012) 8891-8895.

[35] K. MacVittie, J. Halamek, L. Halamkova, M. Southcott, W.D. Jemison, R. Lobel, E. Katz, From "cyborg" lobsters to a pacemaker powered by implantable biofuel cells, *Energ. Environ. Sci.* 6 (2013) 81-86.

- [36] A. Heller, Electrical wiring of redox enzymes, *Accounts Chem. Res.* 23 (1990) 128-134.
- [37] D.L. Nelson, M.M. Cox., Enzymes, in: *Lehninger principles of biochemistry*, WH Freeman, New York, 2005, pp. 190-237.
- [38] E. Katz, I. Willner, A.B. Kotlyar, A non-compartmentalized glucose/O₂ biofuel cell by bioengineered electrode surfaces, *J. Electroan. Chem.* 479 (1999) 64-68.
- [39] A.C. Guyton, J.E. Hall, *Textbook of Medical Physiology*, 11 ed., Elsevier Saunders, Philadelphia, 2006.
- [40] C. Jurysta, N. Bulur, B. Oguzhan, I. Satman, T.M. Yilmaz, W.J. Malaisse, A. Sener, Salivary glucose concentration and excretion in normal and diabetic subjects, *J. Biomed. Biotechnol.* (2009).
- [41] C.R. Taormina, J.T. Baca, S.A. Asher, J.J. Grabowski, D.N. Finegold, Analysis of tear glucose concentration with electrospray ionization mass spectrometry, *J. Am. Soc. Mass. Spectrom.* 18 (2007) 332-336.
- [42] M.J. Cooney, V. Svoboda, C. Lau, G. Martin, S.D. Minter, Enzyme catalysed biofuel cells, *Energ. Environ. Sci.* 1 (2008) 320-337.
- [43] M.D. Toscano, K.J. Woycechowsky, D. Hilvert, Minimalist active-site redesign: Teaching old enzymes new tricks, *Angew. Chem. Int. Ed.* 46 (2007) 3212-3236.
- [44] A. Walcarius, S.D. Minter, J. Wang, Y. Lin, A. Merkoci, Nanomaterials for bio-functionalized electrodes: Recent trends, *J. Mater. Chem. B* 1 (2013) 4878-4908.
- [45] A. Illanes, Introduction, in: *Enzyme Biocatalysis*, Springer Netherlands, Valparaíso, 2008, pp. 1-56.
- [46] A.W. Munro, P. Taylor, M.D. Walkinshaw, Structures of redox enzymes, *Curr. Opin. Biotech.* 11 (2000) 369-376.
- [47] D.L. Nelson, M.M. Cox., Glycolysis, Gluconeogenesis, and the Pentose Phosphate Pathway, in: *Lehninger principles of biochemistry*, WH Freeman, New York, 2005, pp. 521-559.
- [48] R.C. Bean, W.Z. Hassid, Carbohydrate oxidase from a red alga, *iridophycus flaccidum*, *J. Biol. Chem.* 218 (1956) 425-436.

- [49] R.C. Bean, G.G. Porter, B.M. Steinberg, Carbohydrate metabolism of citrus fruits: II. Oxidation of sugars by an aerodehydrogenase from young orange fruits, *J. Biol. Chem.* 236 (1961) 1235-1240.
- [50] J.H. Dowling, H.B. Levine, Hexose oxidation by an enzyme system of *malleomyces-pseudomallei*, *J. Bacteriol.* 72 (1956) 555-560.
- [51] A.I. Schepartz, M.H. Subers, The glucose oxidase of honey I. Purification and some general properties of the enzyme, *Biochem. Biophys. Acta* 85 (1964) 228-237.
- [52] D.G. Hatzinikolaou, O.C. Hansen, B.J. Macris, A. Tingey, D. Kekos, P. Goodenough, P. Stougaard, A new glucose oxidase from *Aspergillus niger*: characterization and regulation studies of enzyme and gene, *App. Microbiol. Biotechnol.* 46 (1996) 371-381.
- [53] M. Kiess, H.-J. Hecht, H.M. Kalisz, Glucose oxidase from *Penicillium amagasakiense*, *Eur. J. Biochem.* 252 (1998) 90-99.
- [54] C. Wong, K. Wong, X. Chen, Glucose oxidase: natural occurrence, function, properties and industrial applications, *Appl. Microbiol. Biotechnol.* 78 (2008) 927-938.
- [55] P.H.S. Tse, D.A. Gough, Time-dependent inactivation of immobilized glucose oxidase and catalase, *Biotechnol. Bioeng.* 29 (1987) 705-713.
- [56] E.-H. Park, Y.-M. Shin, Y.-Y. Lim, T.-H. Kwon, D.-H. Kim, M.-S. Yang, Expression of glucose oxidase by using recombinant yeast, *J. Biotechnol.* 81 (2000) 35-44.
- [57] H. Tsuge, O. Natsuaki, K. Ohashi, Purification, properties, and molecular features of glucose oxidase from *Aspergillus niger*, *J. Biochem.* 78 (1975) 835-843.
- [58] K.R. Frederick, J. Tung, R.S. Emerick, F.R. Masiarz, S.H. Chamberlain, A. Vasavada, S. Rosenberg, S. Chakraborty, L.M. Schopfer, L.M. Schopfer, Glucose oxidase from *Aspergillus niger*. Cloning, gene sequence, secretion from *Saccharomyces cerevisiae* and kinetic analysis of a yeast-derived enzyme, *J. Biol. Chem.* 265 (1990) 3793-3802.
- [59] Q.H. Gibson, B.E.P. Swoboda, V. Massey, Kinetics and mechanism of action of glucose oxidase, *J. Biol. Chem.* 239 (1964) 3927-3934.

- [60] F. Barrière, P. Kavanagh, D. Leech, A laccase–glucose oxidase biofuel cell prototype operating in a physiological buffer, *Electrochim. Acta* 51 (2006) 5187-5192.
- [61] W. Schuhmann, Electron-transfer pathways in amperometric biosensors. Ferrocene-modified enzymes entrapped in conducting-polymer layers, *Biosens. Bioelectron.* 10 (1995) 181-193.
- [62] H.M. Kalisz, H.-J. Hecht, D. Schomburg, R.D. Schmid, Effects of carbohydrate depletion on the structure, stability and activity of glucose oxidase from *Aspergillus niger*, *Biochim. Biophys. Acta* 1080 (1991) 138-142.
- [63] B.E.P. Swoboda, V. Massey, Purification and Properties of the Glucose Oxidase from *Aspergillus niger*, *J. Biol. Chem.* 240 (1965) 2209-2215.
- [64] M.K. Weibel, H.J. Bright, The glucose oxidase mechanism: interpretation of the pH dependence, *J. Biol. Chem.* 246 (1971) 2734-2744.
- [65] G. Tourillon, F. Garnier, Structural effect on the electrochemical properties of polythiophene and derivatives, *J. Electroanal. Chem.* 161 (1984) 51-58.
- [66] F.M. Suarez-Herrera, J.M. Feliu, Electrochemical properties of thin films of polythiophene polymerized on basal plane platinum electrodes in nonaqueous media, *J. Phys. Chem.* 113 (2009) 1899-1905.
- [67] M. Sangermano, F. Sordo, A. Chiolerio, Y. Yagci, One-pot photoinduced synthesis of conductive polythiophene-epoxy network films, *Polymer* 54 (2013) 2077-2080.
- [68] Y.-C. Huang, T.-C. Lu, C.-I. Huang, Exploring the correlation between molecular conformation and UV–visible absorption spectra of two-dimensional thiophene-based conjugated polymers, *Polymer* 54 (2013) 6489-6499.
- [69] L.T. Strover, J. Malmström, O. Laita, J. Reynisson, N. Aydemir, M.K. Nieuwoudt, D.E. Williams, P.R. Dunbar, M.A. Brimble, J. Travas-Sejdic, A new precursor for conducting polymer-based brush interfaces with electroactivity in aqueous solution, *Polymer* 54 (2013) 1305-1317.
- [70] M. Vignali, R.A.H. Edwards, M. Serantoni, V.J. Cunnane, Electropolymerized polythiophene layer extracted from immiscible electrolyte solutions: current-time analysis, *J. Electroanal. Chem.* 591 (2006) 59-68.

- [71] S. Yigit, J. Hacaloglu, U. Akbulut, L. Toppare, Conducting polymer composites of polythiophene with natural and synthetic rubbers *Synthetic Met.* 79 (1996) 11-16.
- [72] F. Jonas, G. Heywang, W. Schmidtberg, J. Heinze, M. Dietrich, US Patent 5035926, (1991).
- [73] K. Leonavicius, A. Ramanaviciene, A. Ramanavicius, Model for hydrogen peroxide initiated synthesis of polypyrrole nanoparticles *Langmuir* 17 (2011) 10970-10976.
- [74] M.F. Abasiyanik, M. Senel, Immobilization of glucose oxidase on reagentless ferrocene-containing polythiophene derivative and its glucose sensing application, *J. Electroanal. Chem.* 639 (2010) 21-26.
- [75] T. Yamamoto, A. Morita, Y. Miyazaki, T.M.H. Zhou, Y. Nakamura, T. Kanbara, S. Sasaki, K. Kubota, Preparation of pi-conjugated poly(thiophene-2,5-diyl), poly(p-phenylene), and related polymers using zerovalent nickel complexes. Linear structure and properties of the pi-conjugated polymers, *Macromolecules* 25 (1992) 1214-1223.
- [76] M. Thiyagarajan, L.A. Samuelson, J. Kumar, A.L. Cholli, Helical conformational specificity of enzymatically synthesized water-soluble conducting polyaniline nanocomposites, *J. Am. Chem. Soc.* 125 (2003) 11502-11503.
- [77] Z. Jin, Y. Su, Y. Duan, A novel method for polyaniline synthesis with immobilized horseradish peroxidase enzyme, *Synthetic Met.* 122 (2001) 237-242.
- [78] M.R. Nabid, A.A. Entezami, A Novel method for synthesis of water-soluble polypyrrole with horseradish peroxidase enzyme, *J. App. Polym. Sci.* 94 (2004) 254-258.
- [79] S.S. Razola, B.L. Ruiz, N.M. Diez, H.B.M. Jr, J.-M. Kauffmann, Hydrogen peroxide sensitive amperometric biosensor based on horseradish peroxidase entrapped in a polypyrrole electrode, *Biosens. Bioelectron.* 17 (2002) 921-928.
- [80] A.Z. Guo, H. Ruegger, R. Kissner, T. Ishikawa, M. Willeke, P. Walde, Vesicles as soft templates for the enzymatic polymerization of aniline, *Langmuir* 25 (2009) 11390-11405.

- [81] I.S. Vasil'eva, O.V. Morozova, G.P. Shumakovich, S.V. Shleev, I.Y. Sakharov, A.I. Yaropov, Laccase catalyzed synthesis of optically active polyaniline, *Synthetic Met.* 157 (2007) 684-689.
- [82] A. Karamyshev, S. Shleev, O. Koroleva, A. Yaropolov, I. Sakharov, Laccase-catalyzed synthesis of conducting polyaniline, *Enzyme Microb. Tech.* 33 (2003) 556–564.
- [83] R. Cruz-Silva, J. Romero-Garci, J.L. Angulo-Sanchez, A. Ledezma-Perez, E. Arias-Marin, I. Moggio, E. Flores-Loyola, Template-free enzymatic synthesis of electrically conducting polyaniline using soybean peroxidase, *Eur. Polym. J.* 41 (2005) 1129-1135.
- [84] I.Y. Sakharov, I. Ouporov, A.K. Vorobiev, M.G. Roig, O.Y. Pletjushkina, Modeling and characterization of polyelectrolyte complex of polyaniline and sulfonated polystyrene produced by palm tree peroxidase, *Synthetic Met.* 142 (2004) 127-135.
- [85] A. Ramanavicius, A. Kausaite, A. Ramanaviciene, J. Acaite, A. Malinauskas, Redox enzyme – glucose oxidase – initiated synthesis of polypyrrole, *Synthetic Met.* 156 (2006) 409-413.
- [86] A. Kausaite-Minkstimiene, V. Mazeiko, A. Ramanaviciene, A. Ramanavicius, Enzymatically synthesized polyaniline layer for extension of linear detection region of amperometric glucose biosensor, *Biosens. Bioelectron.* 26 (2010) 790-797.
- [87] A. Kausaite-Minkstimiene, V. Mazeiko, A. Ramanaviciene, A. Ramanavicius, Evaluation of amperometric glucose biosensors based on glucose oxidase encapsulated within enzymatically synthesized polyaniline and polypyrrole, *Sens. Actuat. B-Chem* 158 (2011) 278–285.
- [88] A. Ramanavicius, A. Kausaite, A. Ramanaviciene, Self-encapsulation of oxidases as a basic approach to tune upper detection limit of amperometric biosensors, *Analyst* 133 (2008) 1083-1089.
- [89] A. Ramanaviciene, A. Kausaite-Minkstimiene, Y. Oztekin, G. Carac, J. Voronovic, N. German, A. Ramanavicius, Visualization of red-ox proteins on the gold surface using enzymatic polypyrrole formation, *Microchim. Acta* 175 (2011) 79-86.
- [90] A. Kausaite, A. Ramanaviciene, A. Ramanavicius, Polyaniline synthesis catalyzed by glucose oxidase, *Polymer* 50 (2009) 1846–1851.

- [91] W. Lu, A.G. Fadeev, B. Qi, E. Smela, B.R. Mattes, J. Ding, G.M. Spinks, L. Mazurkiewicz, D. Zhou, G.H. Wallace, D.R. MacFarlane, S.A. Forsyth, M. Forsyth, Use of ionic liquids for pi-conjugated polymer electrochemical devices, *Science* 297 (2002) 983-987.
- [92] M. Zamocky, R. Ludwig, C. Peterbauer, B.M. Hallberg, C. Divne, P. Nicholls, D. Haltrich, Cellobiose dehydrogenase--a flavocytochrome from wood-degrading, phytopathogenic and saprotropic fungi, *Curr. Protein. Pept. Sci.* 7 (2006) 255-280.
- [93] J.A. Langston, T. Shaghasi, E. Abbate, F. Xu, E. Vlasenko, M.D. Sweeney, Oxidoreductive cellulose depolymerization by the enzymes cellobiose dehydrogenase and glycoside hydrolase 61, *Appl. Environ. Microbiol.* 77 (2011) 7007-7015.
- [94] L. Žifčáková, P. Baldrian, Fungal polysaccharide monooxygenases: new players in the decomposition of cellulose, *Fungal Ecol.* 5 (2012) 481-489.
- [95] B.M. Hallberg, T. Bergfors, K. Bäckbro, G. Pettersson, G. Henriksson, C. Divne, A new scaffold for binding haem in the cytochrome domain of the extracellular flavocytochrome cellobiose dehydrogenase, *Structure* 8 (2000) 79-88.
- [96] B. Martin Hallberg, G. Henriksson, G. Pettersson, C. Divne, Crystal structure of the flavoprotein domain of the extracellular flavocytochrome cellobiose dehydrogenase, *J. Mol. Biol.* 315 (2002) 421-434.
- [97] R. Ludwig, R. Ortiz, C. Schulz, W. Harreither, C. Sygmund, L. Gorton, Cellobiose dehydrogenase modified electrodes: advances by materials science and biochemical engineering, *Anal. Bioanal. Chem.* 405 (2013) 3637-3658.
- [98] R. Ludwig, W. Harreither, F. Tasca, L. Gorton, Cellobiose dehydrogenase: A versatile catalyst for electrochemical applications, *Chem. Phys. Chem.* 11 (2010) 2674-2697.
- [99] W. Harreither, C. Sygmund, M. Augustin, M. Narciso, M.L. Rabinovich, L. Gorton, D. Haltrich, R. Ludwig, Catalytic properties and classification of cellobiose dehydrogenases from ascomycetes, *Appl. Environ. Microb.* 77 (2011) 1804-1815.
- [100] W. Harreither, P. Nicholls, C. Sygmund, L. Gorton, R. Ludwig, Investigation of the pH-dependent electron transfer mechanism of Ascomycetous class II cellobiose dehydrogenases on electrodes, *Langmuir* 28 (2012) 6714-6723.

- [101] A. Lindgren, L. Gorton, T. Ruzgas, U. Baminger, D. Haltrich, M. Schülein, Direct electron transfer of cellobiose dehydrogenase from various biological origins at gold and graphite electrodes, *J. Electroanal. Chem.* 496 (2001) 76-81.
- [102] F. Xu, E.J. Golightly, K.R. Duke, S.F. Lassen, B. Knusen, S. Christensen, K.M. Brown, S.H. Brown, M. Schülein, *Humicola insolens* cellobiose dehydrogenase: cloning, redox chemistry, and “logic gate”-like dual functionality, *Enzyme Microb. Tech.* 28 (2001) 744-753.
- [103] W. Harreither, A.K.G. Felice, R. Paukner, L. Gorton, R. Ludwig, C. Sygmund, Recombinantly produced cellobiose dehydrogenase from *Corynascus thermophilus* for glucose biosensors and biofuel cells, *Biotechnol. J.* 7 (2012) 1359-1366.
- [104] P. Baldrian, Fungal laccases – occurrence and properties, *FEMS Microbiol. Rev.* 30 (2006) 215-242.
- [105] H. Yoshida, LXIII.-Chemistry of lacquer (Urushi). Part I. Communication from the Chemical Society of Tokio, *J. Chem. Soc. Trans.* 43 (1883) 472-486.
- [106] I.V. Berezin, V.A. Bogdanovskaya, S.D. Varfolomeev, M.R. Tarasevich, A.I. Yaropolov, Bioelectrocatalysis. Equilibrium oxygen potential in the presence of laccase, *Dokl. Akad. Nauk SSSR* 240 (1978) 615-618.
- [107] P. Ranocha, M. Chabannes, S. Chamayou, S.d. Danoun, A. Jauneau, A.-M. Boudet, D. Goffner, Laccase down-regulation causes alterations in phenolic metabolism and cell wall structure in poplar, *Plant Physiol.* 129 (2002) 145-155.
- [108] C.F. Thurston, The structure and function of fungal laccases, *Microbiology* 140 (1994) 19-26.
- [109] K.J. Kramer, M.R. Kanost, T.L. Hopkins, H.B. Jiang, Y.C. Zhu, R.D. Xu, J.L. Kerwin, F. Turecek, Oxidative conjugation of catechols with proteins in insect skeletal systems, *Tetrahedron* 57 (2001) 385-392.
- [110] L.g.O. Martins, C.M. Soares, M.M. Pereira, M. Teixeira, T. Costa, G.H. Jones, A.O. Henriques, Molecular and biochemical characterization of a highly stable bacterial laccase that occurs as a structural component of the *Bacillus subtilis* endospore coat, *J. Biol. Chem.* 277 (2002) 18849-18859.

- [111] H. Claus, Laccases: structure, reactions, distribution, *Micron* 35 (2004) 93-96.
- [112] E.I. Solomon, A.J. Augustine, J. Yoon, O₂ reduction to H₂O by the multicopper oxidases, *Dalton T.* (2008) 3921-3932.
- [113] A. Kunamneni, F.J. Plou, A. Ballesteros, M. Alcalde, Laccases and their applications: A patent review, *Rec. Pat. Biotechnol.* 2 (2008) 10-24.
- [114] S. Shleev, J. Tkac, A. Christenson, T. Ruzgas, A.I. Yaropolov, J.W. Whittaker, L. Gorton, Direct electron transfer between copper-containing proteins and electrodes *Biosens. Bioelectron.* 20 (2005) 2517-2554.
- [115] A. Christenson, N. Dimcheva, E.E. Ferapontova, L. Gorton, T. Ruzgas, L. Stoica, S. Shleev, A.I. Yaropolov, D. Haltrich, R.N.F. Thorneley, S.D. Aust, Direct electron transfer between ligninolytic redox enzymes and electrodes, *Electroanalysis* 16 (2004) 1074-1092.
- [116] S. Shleev, A. Christenson, V. Serezhenkov, D. Burbaev, A. Yaropolov, L. Gorton, T. Ruzgas, Electrochemical redox transformations of T1 and T2 copper sites in native *Trametes hirsuta* laccase at gold electrode, *Anglais* 385 (2005) 745-754.
- [117] M. Fernández-Fernández, M.Á. Sanromán, D. Moldes, Recent developments and applications of immobilized laccase, *Biotechnol. Adv.* 31 (2013) 1808-1825.
- [118] S.V. Shleev, O. Morozova, O. Nikitina, E.S. Gorshina, T. Rusinova, V.A. Serezhenkov, D.S. Burbaev, I.G. Gazaryan, A.I. Yaropolov, Comparison of physico-chemical characteristics of four laccases from different basidiomycetes, *Biochimie* 86 (2004) 693-703.
- [119] K.-L. Min, Y.-H. Kim, Y.W. Kim, H.S. Jung, Y.C. Hah, Characterization of a novel laccase produced by the wood-rotting fungus *Phellinus ribis*, *Arch. Biochem. Biophys.* 392 (2001) 279-286.
- [120] W.A. Edens, T.Q. Goins, D. Dooley, J.M. Henson, Purification and characterization of a secreted laccase of *Gaeumannomyces graminis* var. *tritici*, *Appl. Environ. Microbiol.* 65 (1999) 3071-3074.
- [121] P.J. Strong, H. Claus, Laccase: A Review of its past and its future in bioremediation, *Cri. Rev. Env. Sci. Tec.* 41 (2011) 373-434.
- [122] E.I. Solomon, U.M. Sundaram, T.E. Machonkin, Multicopper oxidases and oxygenases, *Chem. Rev.* 96 (1996) 2563-2605.

- [123] F. Xu, W. Shin, S.H. Brown, J.A. Wahleithner, U.M. Sundaram, E.I. Solomon, A study of a series of recombinant fungal laccases and bilirubin oxidase that exhibit significant differences in redox potential, substrate specificity, and stability, *BBA-Protein. Struct. M.* 1292 (1996) 303-311.
- [124] F. Xu, Oxidation of phenols, anilines, and benzenethiols by fungal laccases: correlation between activity and redox potentials as well as halide inhibition†, *Biochemistry* 35 (1996) 7608-7614.
- [125] Y. Liu, S. Dong, A biofuel cell with enhanced power output by grape juice, *Electrochem. Commun.* 9 (2007) 1423-1427.
- [126] S. Murao, N. Tanaka, A new enzyme bilirubin oxidase produced by *Myrothecium verrucaria* MT-1, *Agric. Biol. Chem.* 45 (1981) 2383-2384.
- [127] S. Sakasegawa, H. Ishikawa, S. Imamura, H. Sakuraba, S. Goda, T. Ohshima, Bilirubin oxidase activity of *Bacillus subtilis* CotA, *Appl. Environ. Microbiol.* 72 (2006) 972-975.
- [128] N. Tanaka, S. Murao, Purification and some properties of bilirubin oxidase of *Myrothecium verrucaria* MT-1, *Agric. Biol. Chem.* 46 (1982) 2499-2503.
- [129] T. Sakurai, K. Kataoka, Basic and applied features of multicopper oxidases, CueO, bilirubin oxidase, and laccase, *Chem. Rec.* 7 (2007) 220-229.
- [130] J.A. Cracknell, T.P. McNamara, E.D. Lowe, C.F. Blanford, Bilirubin oxidase from *Myrothecium verrucaria*: X-ray determination of the complete crystal structure and a rational surface modification for enhanced electrocatalytic O₂ reduction, *Dalton T.* 40 (2011) 6668-6675.
- [131] N. Mano, Features and applications of bilirubin oxidases, *Appl. Microbiol. Biotechnol.* 96 (2012) 301-307.
- [132] A. Christenson, S. Shleev, N. Mano, A. Heller, L. Gorton, Redox potentials of the blue copper sites of bilirubin oxidases, *Biochim. Biophys. Acta* 1757 (2006) 1634-1641.
- [133] S. Tsujimura, H. Tatsumi, J. Ogawa, S. Shimizu, K. Kano, T. Ikeda, Bioelectrocatalytic reduction of dioxygen to water at neutral pH using bilirubin oxidase as an enzyme and 2,2'-azinobis (3-ethylbenzothiazolin-6-sulfonate) as an electron transfer mediator, *J. Electroanal. Chem.* 496 (2001) 69-75.
- [134] J. Wang, M. Ozsoz, A polishable amperometric biosensor for bilirubin, *Electroanalysis* 2 (1990) 647-650.

- [135] N. Mano, L. Edembe, Bilirubin oxidases in bioelectrochemistry: Features and recent findings, *Biosens. Bioelectron.* 50 (2013) 478-485.
- [136] D. Pankratov, J. Sotres, A. Barrantes, T. Arnebrant, S. Shleev, Interfacial behavior and activity of laccase and bilirubin oxidase on bare gold surfaces, *Langmuir* 30 (2014) 2943-2951.
- [137] W. Jia, C. Jin, W. Xia, M. Muhler, W. Schuhmann, L. Stoica, Glucose oxidase/horseradish peroxidase co-immobilized at a CNT-modified graphite electrode: towards potentially implantable biocathodes, *Chem. Eur. J.* 18 (2012) 2783-2786.
- [138] A. Ramanavicius, A. Kausaite, A. Ramanaviciene, Enzymatic biofuel cell based on anode and cathode powered by ethanol, *Biosens. Bioelectron.* 24 (2008) 761-766
- [139] A. Ramanavicius, A. Ramanaviciene, Hemoproteins in design of biofuel cells, *Fuel Cells* 9 (2009) 25-36.
- [140] N.C. Veitch, Horseradish peroxidase: a modern view of a classic enzyme, *Phytochemistry* 65 (2004) 249-259.
- [141] K.G. Welinder, Amino acid sequence studies of horseradish peroxidase, *Eur. J. Biochem.* 96 (1979) 483-502.
- [142] G.I. Berglund, G.H. Carlsson, A.T. Smith, H. Szoke, A. Henriksen, J. Hajdu, The catalytic pathway of horseradish peroxidase at high resolution, *Nature* 417 (2002) 463-468.
- [143] J.W. Tams, K.G. Welinder, Glycosylation and thermodynamic versus kinetic stability of horseradish peroxidase, *FEBS Lett.* 421 (1998) 234-236.
- [144] G. Bayramoğlu, M.Y. Arica, Enzymatic removal of phenol and p-chlorophenol in enzyme reactor: Horseradish peroxidase immobilized on magnetic beads, *J. Hazard. Mat.* 156 (2008) 148-155.
- [145] K. Chattopadhyay, S. Mazumdar, Structural and conformational stability of horseradish peroxidase: Effect of temperature and pH, *Biochemistry* 39 (1999) 263-270.
- [146] Y.J. Teng, S.H. Zuo, M.B. Lan, Direct electron transfer of Horseradish peroxidase on porous structure of screen-printed electrode, *Biosens. Bioelectron.* 24 (2009) 1353-1357.

- [147] R. Andreu, E.E. Ferapontova, L. Gorton, J.J. Calvente, Direct electron transfer kinetics in horseradish peroxidase electrocatalysis, *J. Phys. Chem. B* 111 (2006) 469-477.
- [148] G. Presnova, V. Grigorenko, A. Egorov, T. Ruzgas, A. Lindgren, L. Gorton, T. Borchers, Direct heterogeneous electron transfer of recombinant horseradish peroxidases on gold, *Faraday Discuss.* 116 (2000) 281-289.
- [149] A. Pizzariello, M. Stred'ansky, S. Miertuš, A glucose/hydrogen peroxide biofuel cell that uses oxidase and peroxidase as catalysts by composite bulk-modified bioelectrodes based on a solid binding matrix, *Bioelectrochemistry* 56 (2002) 99-105.
- [150] S. Aquino Neto, A.R. De Andrade, New energy sources: the enzymatic biofuel cell, *J. Braz. Chem. Soc.* 24 (2013) 1891-1912.
- [151] S. Ha, Y. Wee, J. Kim, Nanobiocatalysis for Enzymatic Biofuel Cells, *Top. Catal.* 55 (2012) 1181-1200.
- [152] E.E. Ferapontova, S. Shleev, T. Ruzgas, L. Stoica, A. Christenson, J. Tkac, A.I. Yaropolov, L. Gorton, Direct electrochemistry of proteins and enzymes, in: *Perspectives in Bioanalysis*, Elsevier, 2005, pp. 517-598.
- [153] P. Kavanagh, D. Leech, Mediated electron transfer in glucose oxidising enzyme electrodes for application to biofuel cells: recent progress and perspectives, *Phys. Chem. Chem. Phys.* 15 (2013) 4859-4869.
- [154] X.-Y. Yang, G. Tian, N. Jiang, B.-L. Su, Immobilization technology: a sustainable solution for biofuel cell design, *Energ. Environ. Sci.* 5 (2012) 5540-5563.
- [155] L.-H. Guo, H.A. Hill, O., Direct electrochemistry of proteins and enzymes, in: A.G. Sykes (Ed.) *Adv. Inorg. Chem.*, Academic Press, 1991, pp. 341-375.
- [156] O. Courjean, F. Gao, N. Mano, Deglycosylation of glucose oxidase for Direct and efficient glucose electrooxidation on a glassy carbon electrode, *Angew. Chem. Int. Ed.* 48 (2009) 5897-5899.
- [157] R.A. Marcus, N. Sutin, Electron transfers in chemistry and biology, *Biochim. Biophys. Acta* 811 (1985) 265-322.
- [158] C.C. Page, C.C. Moser, X. Chen, P.L. Dutton, Natural engineering principles of electron tunnelling in biological oxidation-reduction, *Nature* 402 (1999) 47-52.

- [159] J. Kim, H. Jia, P. Wang, Challenges in biocatalysis for enzyme-based biofuel cells, *Biotechnol. Adv.* 24 (2006) 296-308.
- [160] A. Bencini, V. Lippolis, 1,10-Phenanthroline: A versatile building block for the construction of ligands for various purposes, *Coordin. Chem. Rev.* 254 (2010) 2096-2180.
- [161] G.F. Smith, C.A. Getz, The improved synthesis of o-phenanthroline, *Chem. Rev.* 16 (1935) 113-120.
- [162] F.H. Case, Substituted 1,10-phenanthrolines. I. The synthesis of certain mono- and polymethyl-1,10-phenanthrolines, *J. Am. Chem. Soc.* 70 (1948) 3994-3996.
- [163] C.X. Zhang, T. Haruyama, E. Kobatake, M. Aizawa, Evaluation of substituted-1,10-phenanthroline complexes of osmium as mediator for glucose oxidase of *Aspergillus Niger*, *Anal. Chim. Acta* 408 (2000) 225-232.
- [164] T. Schilling, A. Okunola, J. Masa, W. Schuhmann, M. Bron, Carbon nanotubes modified with electrodeposited metal porphyrins and phenanthrolines for electrocatalytic applications, *Electrochim. Acta* 55 (2010) 7597-7602.
- [165] M.L. Lozano-Camargo, A. Rojas-Hernandez, M. Gomez-Hernandez, M.D. Pacheco-Hernandez, L. Galicia, M.T. Ramirez-Silva, UV-visible spectroscopic and electrochemical study of the complex formation between Fe(II) and 5-amino-1,10-phenanthroline (5-Aphen) in aqueous solution, *Talanta* 72 (2007) 1458-1468.
- [166] A.D. Ryabov, Y.N. Firsova, A.Y. Ershov, D.I. A., Spectrophotometric kinetic study and analytical implications of the glucose oxidase-catalyzed reduction of $[M^{III}(LL)_2Cl_2]^+$ complexes by D-glucose (M=Os and Ru, LL=2,2'-bipyridine and 1,10-phenanthroline type ligands), *J. Biol. Inorg. Chem.* 4 (1999) 175-182.
- [167] W. Zheng, Q. Li, L. Su, Y. Yan, J. Zhang, L. Mao, Direct electrochemistry of multi-copper oxidases at carbon nanotubes noncovalently functionalized with cellulose derivatives, *Electroanalysis* 18 (2006) 587-594.
- [168] R. Duma, S.D. Minteer, Bilirubin oxidase biocathodes for ethanol biofuel cells, *ECS Transactions* 5 (2007) 117-127.

- [169] D. Ivnitski, B. Branch, P. Atanassov, C. Apblett, Glucose oxidase anode for biofuel cell based on direct electron transfer, *Electrochem. Commun.* 8 (2006) 1204-1210.
- [170] M. Shimizu, K. Kobayashi, H. Morii, K. Mitsui, W. Knoll, T. Nagamune, Secondary structure analyses of protein films on gold surfaces by circular dichroism, *Biochem. Biop. Res. Co.* 310 (2003) 606-611.
- [171] J.C. Love, L.A. Estroff, J.K. Kriebel, R.G. Nuzzo, G.M. Whitesides, Self-assembled monolayers of thiolates on metals as a form of nanotechnology, *Chem. Rev.* 105 (2005) 1103-1170.
- [172] S. Andreescu, J. Njagi, C. Ispas, Chapter 7 - Nanostructured materials for enzyme immobilization and biosensors, in: V. Erokhin, M.K. Ram, O. Yavuz (Eds.) *The New Frontiers of Organic and Composite Nanotechnology*, Elsevier, Amsterdam, 2008, pp. 355-394.
- [173] J. Kim, J.W. Grate, P. Wang, Nanobiocatalysis and its potential applications, *Trends Biotechnol.* 26 (2008) 639-646.
- [174] G. Schmid, B. Corain, Nanoparticulated gold: Syntheses, structures, electronics, and reactivities, *Eur. J. Inorg. Chem.* 34 (2003) 3081-3098.
- [175] J.S. Bradley, G. Schmid, D.V. Talapin, E.V. Shevchenko, H. Weller, Syntheses and Characterizations: 3.2 Synthesis of Metal Nanoparticles, in: *Nanoparticles*, Wiley-VCH Verlag GmbH & Co. KGaA, 2005, pp. 185-238.
- [176] J. Turkevich, P. Stevenson, J. Hillier, A study of the nucleation and growth processes in the synthesis of colloidal gold, *Discuss. Faraday Soc.* 11 (1951) 55-75.
- [177] G. Frens, Controlled nucleation for regulation of particle-size in monodisperse gold suspension, *Nat. Phys. Sci.* 241 (1973) 20-22.
- [178] J.W. Slot, H.J. Geuze, A new method of preparing gold probes for multiple-labeling cytochemistry, *Eur. J. Cell. Biol.* 38 (1985) 87-93.
- [179] M. Brust, M. Walker, D. Bethell, D.J. Schiffrin, R. Whyman, Synthesis of thiol-derivatised gold nanoparticles in a two-phase Liquid-Liquid system, *J. Chem. Soc., Chem. Commun.* (1994) 801-802.
- [180] M.J. Hostetler, J.E. Wingate, C.-J. Zhong, J.E. Harris, R.W. Vachet, M.R. Clark, J.D. Londono, S.J. Green, J.J. Stokes, G.D. Wignall, G.L. Glish, M.D. Porter, N.D. Evans, R.W. Murray, Alkanethiolate gold cluster molecules

with core diameters from 1.5 to 5.2 nm: core and monolayer properties as a function of core size, *Langmuir* 14 (1998) 17-30.

[181] M. Zheng, X. Huang, Nanoparticles comprising a mixed monolayer for specific bindings with biomolecules†, *JACS* 126 (2004) 12047-12054.

[182] D.V. Pankratov, Y.S. Zeifman, A.V. Dudareva, G.K. Pankratova, M.E. Khlupova, Y.M. Parunova, D.N. Zajtsev, N.F. Bashirova, V.O. Popov, S.V. Shleev, Impact of surface modification with gold nanoparticles on the bioelectrocatalytic parameters of immobilized bilirubin oxidase, *Acta Naturae* 6 (2014) 102-106.

[183] M. Dagys, K. Haberska, S. Shleev, T. Arnebrant, J. Kulys, T. Ruzgas, Laccase–gold nanoparticle assisted bioelectrocatalytic reduction of oxygen, *Electrochem. Commun.* 12 (2010) 933–935.

[184] H. Matsumura, R. Ortiz, R. Ludwig, K. Igarashi, M. Samejima, L. Gorton, Direct electrochemistry of *Phanerochaete chrysosporium* cellobiose dehydrogenase covalently attached onto gold nanoparticle modified solid gold electrodes, *Langmuir* 28 (2012) 10925-10933.

[185] M. Zayats, E. Katz, R. Baron, I. Willner, Reconstitution of apo-glucose dehydrogenase on pyrroloquinoline quinone-functionalized Au nanoparticles yields an electrically contacted biocatalyst, *J. Am. Chem. Soc.* 127 (2005) 12400-12406.

[186] Y. Xiao, F. Patolsky, E. Katz, J.F. Hainfeld, I. Willner, "Plugging into enzymes": Nanowiring of redox enzymes by a gold nanoparticle, *Science* 299 (2003) 1877-1881.

[187] B. Willner, E. Katz, I. Willner, Electrical contacting of redox proteins by nanotechnological means, *Curr. Opin. Biotech.* 17 (2006) 589-596

[188] K. Habermüller, M. Mosbach, W. Schuhmann, Electron-transfer mechanisms in amperometric biosensors, *Fresen. J. Anal. Chem.* 366 (2000) 560-568.

[189] C. Gutiérrez-Sánchez, M. Pita, C. Vaz-Domínguez, S. Shleev, A.L. De Lacey, Gold nanoparticles as electronic bridges for laccase-based biocathodes, *J. Am. Chem. Soc.* 134 (2012) 17212-17220.

[190] M. Suzuki, K. Murata, N. Nakamura, H. Ohno, The effect of particle size on the direct electron transfer reactions of metalloproteins using Au nanoparticle-modified electrodes, *Electrochemistry* 80 (2012) 337-339.

- [191] M. Dagys, P. Lamberg, S. Shleev, G. Niaura, I. Bachmatova, L. Marcinkeviciene, R. Meskys, J. Kulys, T. Arnebrant, T. Ruzgas, Comparison of bioelectrocatalysis at *Trichaptum abietinum* and *Trametes hirsuta* laccase modified electrodes, *Electrochim. Acta* 130 (2014) 141-147.
- [192] E.D. Kaufman, J. Belyea, M.C. Johnson, Z.M. Nicholson, J.L. Ricks, P.K. Shah, M. Bayless, T. Pettersson, Z. Feldotö, E. Blomberg, P. Claesson, S. Franzen, Probing protein adsorption onto mercaptoundecanoic acid stabilized gold nanoparticles and surfaces by quartz crystal microbalance and zeta-potential measurements
Langmuir 23 (2007) 6053-6062.
- [193] P. Lamberg, S. Shleev, R. Ludwig, T. Arnebrant, T. Ruzgas, Performance of enzymatic fuel cell in cell culture, *Biosens. Bioelectron.* 55 (2014) 168-173.
- [194] L.H. Dubois, R.G. Nuzzo, Synthesis, structure, and properties of model organic surfaces, *Ann. Rev. Phys. Chem.* 43 (1992) 437-463.
- [195] V. Voiciuk, G. Valincius, R. Budvytytė, A. Matijoška, I. Matulaitienė, G. Niaura, Surface-enhanced Raman spectroscopy for detection of toxic amyloid β oligomers adsorbed on self-assembled monolayers, *Spectrochim. Acta A.* 95 (2012) 526-532.
- [196] I. Matulaitienė, J. Barkauskas, R. Trusovas, G. Račiukaitis, R. Mažeikienė, O. Eicher-Lorka, G. Niaura, Potential dependence of SERS spectra of reduced graphene oxide adsorbed on self-assembled monolayer at gold electrode, *Chem. Phys. Lett.* 590 (2013) 141-145.
- [197] I. Szilagyi, G. Trefalt, A. Tiraferri, P. Maroni, M. Borkovec, Polyelectrolyte adsorption, interparticle forces, and colloidal aggregation, *Soft Matter* 10 (2014) 2479-2502.
- [198] M.M. Ottakam Thotiyl, H. Basit, J.A. Sánchez, C. Goyer, L. Coche-Guerente, P. Dumy, S. Sampath, P. Labbé, J.-C. Moutet, Multilayer assemblies of polyelectrolyte–gold nanoparticles for the electrocatalytic oxidation and detection of arsenic(III), *J. Colloid Interf. Sci.* 383 (2012) 130-139.
- [199] T. Yoshida, T. Nagasawa, ϵ -Poly-l-lysine: microbial production, biodegradation and application potential, *Appl. Microbiol. Biotechnol.* 62 (2003) 21-26.

- [200] Z. Adamczyk, P. Weroński, Application of the DLVO theory for particle deposition problems, *Adv. Colloid Interfac.* 83 (1999) 137-226.
- [201] B. Derjaguin, L. Landau, Theory of the stability of strongly charged lyophobic sols and of the adhesion of strongly charged particles in solutions of electrolytes, *Prog. Surf. Sci.* 43 (1993) 30-59.
- [202] A. Zabet-Khosousi, A.-A. Dhirani, Charge transport in nanoparticle assemblies, *Chem. Rev.* 108 (2008) 4072-4124.
- [203] K. Murata, M. Suzuki, K. Kajiya, N. Nakamura, H. Ohno, High performance bioanode based on direct electron transfer of fructose dehydrogenase at gold nanoparticle-modified electrodes, *Electrochem. Commun.* 11 (2009) 668-671.
- [204] K. Murata, K. Kajiya, M. Nukaga, Y. Suga, T. Watanabe, N. Nakamura, H. Ohno, A Simple Fabrication Method for Three-Dimensional Gold Nanoparticle Electrodes and Their Application to the Study of the Direct Electrochemistry of Cytochrome c, *Electroanal.* 22 (2010) 185 – 190.
- [205] J. Feder, Random sequential adsorption, *J.Theor. Biol.* 87 (1980) 237-254.
- [206] J. Feder, I. Giaever, Adsorption of ferritin, *J. Colloid Interf. Sci.* 78 (1980) 144-154.
- [207] K.C. Grabar, P.C. Smith, M.D. Musick, J.A. Davis, D.G. Walter, M.A. Jackson, A.P. Guthrie, M.J. Natan, Kinetic control of interparticle spacing in Au colloid-based surfaces: rational nanometer-scale architecture, *J. Am. Chem. Soc.* 118 (1996) 1148-1153.
- [208] A. Lundgren, Self-organization of nanoparticles - implications for interface biology, Doctoral thesis (2012).
- [209] Z. Adamczyk, M. Zembala, B. Siwek, P. Warszyński, Structure and ordering in localized adsorption of particles, *J. Colloid Interf. Sci.* 140 (1990) 123-137.
- [210] J. Lyklema, Fundamentals of interfaces and colloidal science, Acad. Press, London, 2001.
- [211] Z. Adamczyk, M. Zembala, B. Siwek, P. Warszyński, Structure and ordering in localized adsorption of particles, *J. Colloid & Interface Sci.* 140 (1990) 123-137.

- [212] E.S. Kooij, E.A.M. Brouwer, H. Wormeester, B. Poelsema, Ionic strength mediated self-organisation of gold nanocrystals: an AFM study, *Langmuir* 18 (2002) 7677-7682.
- [213] G.Z. Sauerbrey, Use of quartz crystal vibrator for weighting thin films on a microbalance, *Z. Phys.* 155 (1959) 206-222.
- [214] M.V. Voinova, M. Rodahl, M. Jonson, B. Kasemo, Viscoelastic acoustic response of layered polymer films at fluid-solid interfaces: Continuum mechanics approach, *Phys Scripta* 59 (1999) 391-396.
- [215] I. Reviakine, D. Johannsmann, R.P. Richter, Hearing What You Cannot See and Visualizing What You Hear: Interpreting Quartz Crystal Microbalance Data from Solvated Interfaces, *Anal. Chem.* 83 (2011) 8838-8848.
- [216] P. Bingen, G. Wang, N.F. Steinmetz, M. Rodahl, R.P. Richter, Solvation Effects in the Quartz Crystal Microbalance with Dissipation Monitoring Response to Biomolecular Adsorption. A Phenomenological Approach, *Anal. Chem.* 80 (2008) 8880-8890.
- [217] D. Johannsmann, I. Reviakine, R.P. Richter, Dissipation in Films of Adsorbed Nanospheres Studied by Quartz Crystal Microbalance (QCM), *Anal. Chem.* 81 (2009) 8167-8176.
- [218] E. Tellechea, D. Johannsmann, N.F. Steinmetz, R.P. Richter, I. Reviakine, Model-Independent Analysis of QCM Data on Colloidal Particle Adsorption, *Langmuir* 25 (2009) 5177-5184.
- [219] A.L.J. Olsson, I.R. Quevedo, D.Q. He, M. Basnet, N. Tufenkji, Using the Quartz Crystal Microbalance with Dissipation Monitoring to Evaluate the Size of Nanoparticles Deposited on Surfaces, *Acs Nano* 7 (2013) 7833-7843.
- [220] D. Johannsmann, I. Reviakine, E. Rojas, M. Gallego, Effect of Sample Heterogeneity on the Interpretation of QCM(-D) Data: Comparison of Combined Quartz Crystal Microbalance/Atomic Force Microscopy Measurements with Finite Element Method Modeling, *Anal. Chem.* 80 (2008) 8891-8899.
- [221] W. Harreither, V. Coman, R. Ludwig, D. Haltrich, L. Gorton, Investigation of graphite electrodes modified with cellobiose dehydrogenase from the ascomycete *myriococcum thermophilum*, *Electroanal.* 19 (2007) 172-180.

- [222] F. Xu, W.S. Shin, S.H. Brown, J.A. Wahleithner, U.M. Sundaram, E.I. Solomon, A study of a series of recombinant fungal laccases and bilirubin oxidase that exhibit significant differences in redox potential, substrate specificity, and stability, *Biochim. Biophys. Acta* 1292 (1996) 303-311.
- [223] Y. Oztekin, Ph.D thesis, in: Department of Analytical Chemistry, Selcuk University, Konya, Turkey, 2008.
- [224] S. Kumar, K.S. Gandhi, R. Kumar, Modeling of formation of gold nanoparticles by citrate method, *Ind. Eng. Chem. Res.* 46 (2006) 3128-3136.
- [225] J. Turkevich, Colloidal gold. Part I, *Gold Bull* 18 (1985) 86-91.
- [226] W. Haiss, N.T.K. Thanh, J. Aveyard, D.G. Fernig, Determination of size and concentration of gold nanoparticles from UV–Vis spectra, *Anal. Chem.* 79 (2007) 4215-4221.
- [227] A. Ramanavicius, Amperometric biosensor for the determination of creatine, *Anal. Bioanal. Chem.* 387 (2007) 1988-1906.
- [228] M.C. Dixon, Quartz crystal microbalance with dissipation monitoring: enabling real-time characterization of biological materials and their interactions, *J. Biomol. Tech.* 19 (2008) 151–158.
- [229] G. Sauerbrey, Use of quartz crystal vibrator for weighing thin films on a microbalance., *Z. Phys.* 155 (1959) 206-222.
- [230] M.V. Voinova, M. Rodahl, M. Jonson, B. Kasemo, Viscoelastic acoustic response of layered polymer films at fluid-solid interfaces: continuum mechanics approach *Physica Scripta* 59 (1999) 391-396.
- [231] M. Rodahl, F. Höök, C. Fredriksson, C.A. Keller, A. Krozer, P. Brzezinski, M. Voinova, B. Kasemo, Simultaneous frequency and dissipation factor QCM measurements of biomolecular adsorption and cell adhesion, *Faraday Discussions* 107 (1997) 229-246.
- [232] C. Larsson, M. Rodahl, F. Höök, Characterization of DNA immobilization and subsequent hybridization on a 2D arrangement of streptavidin on a biotin-modified lipid bilayer supported on SiO₂, *Anal. Chem.* 75 (2003) 5080-5087.
- [233] V. Climent, J. Zhang, E.P. Friis, L.H. Ostergaard, J. Ulstrup, Voltammetry and single-molecule in situ scanning tunneling microscopy of laccase and bilirubin oxidase in electrocatalytic dioxygen reduction on Au(111) single-crystal electrodes, *J. Phys. Chem. C* 116 (2012) 1232-1243.

- [234] O.S. Roshchupkina, L.M. Gol'denberg, I.V. Nazarova, V.A. Dement'ev, I.E. Davidova, Vibrational spectra and conformational structure of polythiophene, *J. Appl. Spectrosc.* 52 (1990) 633-637.
- [235] J. Wu, G. Yue, Y. Xiao, J. Lin, M. Huang, Z. Lan, Q. Tang, Y. Huang, L. Fan, S. Yin, T. Sato, An ultraviolet responsive hybrid solar cell based on titania/poly(3-hexylthiophene), *Sci. Rep.* 3 (2013).
- [236] J.U. Lee, J.W. Jung, T. Emrick, T.P. Russell, W.H. Jo, Synthesis of C60-end capped P3HT and its application for high performance of P3HT/PCBM bulk heterojunction solar cells, *J. Mater. Chem.* 20 (2010) 3287-3294.
- [237] J. Bao, K. Furumoto, M. Yoshimoto, K. Fukunaga, K. Nakao, Competitive inhibition by hydrogen peroxide produced in glucose oxidation catalyzed by glucose oxidase, *Biochem. Eng. J.* 13 (2003) 69-72.
- [238] L. Gorton, A. Lindgren, T. Larsson, F.D. Munteanu, T. Ruzgas, Direct electron transfer between heme-containing enzymes and electrodes as basis for third generation biosensors, *Anal. Chim. Acta* 400 (1999) 91-108.
- [239] K. Zawada, J. Bukowska, An interaction of 1,10-phenantroline with the copper electrode in neutral and acidic aqueous solutions: a surface enhanced Raman scattering study *J. Mol. Struct.* 555 (2000) 425-432.
- [240] Y. Hitomi, H. Mukai, H. Yoshimura, T. Tanaka, T. Funabiki, Non-covalent modification of the heme-pocket of apomyoglobin by a 1,10-phenanthroline derivative, *Bioorg. Med. Chem. Lett.* 16 (2006) 248-251.
- [241] M.T. Ramírez-Silva, M.n. Gómez-Hernández, M.d.L. Pacheco-Hernández, A. Rojas-Hernández, L. Galicia, Spectroscopy study of 5-amino-1,10-phenanthroline, *Spectrochim. Acta A* 60 (2004) 781-789.
- [242] G. Jönsson, L. Gorton, An amperometric glucose sensor made by modification of a graphite electrode surface with immobilized glucose oxidase and adsorbed mediator, *Biosensors* 1 (1985) 355-368.
- [243] C. Pan, Y. Fang, H. Wu, M. Ahmad, Z. Luo, Q. Li, J. Xie, X. Yan, L. Wu, Z.L. Wang, J. Zhu, Generating electricity from biofluid with a nanowire-based biofuel cell for self-powered nanodevices, *Adv. Mater.* 22 (2010) 5388-5392.
- [244] P. Cinquin, C. Gondran, F. Giroud, S. Mazabrard, A. Pellissier, F. Boucher, J.P. Alcaraz, K. Gorgy, F. Lenouvel, S. Mathe, P. Porcu, S. Cosnier, A glucose biofuel cell implanted in rats, *PLoS One* 5 (2010) 1-7.

- [245] A. Ramanavicius, A. Kausaite, A. Ramanaviciene, Biofuel cell based on direct bioelectrocatalysis, *Biosens. Bioelectron.* 20 (2005) 1962-1967.
- [246] F. Giroud, C. Gondran, K. Gorgy, V. Vivier, S. Cosnier, An enzymatic biofuel cell based on electrically wired polyphenol oxidase and glucose oxidase operating under physiological conditions, *Electrochim. Acta* 85 (2012) 278-282.
- [247] V. Coman, R. Ludwig, W. Harreither, D. Haltrich, L. Gorton, T. Ruzgas, S. Shleev, A direct electron transfer-based glucose/oxygen biofuel cell operating in human serum, *Fuel Cells* 10 (2010) 9-16.
- [248] F. Tasca, M.N. Zafar, W. Harreither, G. Noll, R. Ludwig, L. Gorton, A third generation glucose biosensor based on cellobiose dehydrogenase from *Corynascus thermophilus* and single-walled carbon nanotubes, *Analyst* 136 (2011) 2033-2036.
- [249] A. Lindgren, T. Larsson, T. Ruzgas, L. Gorton, Direct electron transfer between the heme of cellobiose dehydrogenase and thiol modified gold electrodes, *J. Electroanal. Chem.* 494 (2000) 105-113.
- [250] T. Vidaković-Koch, I. Ivanov, M. Falk, S. Shleev, T. Ruzgas, K. Sundmacher, Impact of the gold support on the electrocatalytic oxidation of sugars at enzyme-modified electrodes, *Electroanal.* 23 (2011) 927-930.
- [251] D.S. Newburg, S.H. Neubauer, Carbohydrates in Milks: Analysis, Quantities, and Significance, in: R.G. Jensen (Ed.) *Handbook of Milk Composition*, Academic Press, San Diego, 1995, pp. 273-349.
- [252] C. Schou, M.H. Christensen, M. Schülein, Characterization of a cellobiose dehydrogenase from *Humicola insolens*, *Anglais* 330 (Pt 1) (1998) 565-571.
- [253] P. Ramírez, N. Mano, R. Andreu, T. Ruzgas, A. Heller, L. Gorton, S. Shleev, Direct electron transfer from graphite and functionalized gold electrodes to T1 and T2/T3 copper centers of bilirubin oxidase, *BBA-Bioenergetics* 1777 (2008) 1364-1369.
- [254] S. Shleev, V. Andoralov, M. Falk, C.T. Reimann, T. Ruzgas, M. Srnec, U. Ryde, L. Rulíšek, On the possibility of uphill intramolecular electron transfer in multicopper oxidases: electrochemical and quantum chemical study of bilirubin oxidase, *Electroanal.* 24 (2012) 1524-1540.

- [255] N. Mano, J.L. Fernandez, Y. Kim, W. Shin, A.J. Bard, A. Heller, Oxygen is electroreduced to water on a “wired” enzyme electrode at a lesser overpotential than on platinum, *J. Am. Chem. Soc.* 125 (2003) 15290-15291.
- [256] C. Tanne, G. Göbel, F. Lisdat, Development of a (PQQ)-GDH-anode based on MWCNT-modified gold and its application in a glucose/O₂-biofuel cell, *Biosens. Bioelectron.* 26 (2010) 530-535.
- [257] F. Hook, B. Kasemo, T. Nylander, C. Fant, K. Sott, H. Elwing, Variations in coupled water, viscoelastic properties, and film thickness of a Mefp-1 protein film during adsorption and cross-linking: A quartz crystal microbalance with dissipation monitoring, ellipsometry, and surface plasmon resonance study, *Anal. Chem.* 73 (2001) 5796-5804.
- [258] K. Haberska, O. Svensson, S. Shleev, L. Lindh, T. Arnebrant, T. Ruzgas, Activity of lactoperoxidase when adsorbed on protein layers, *Talanta* 76 (2008) 1159-1164.
- [259] C.-G. Gölander, E. Kiss, Protein adsorption on functionalized and ESCA-characterized polymer films studied by ellipsometry, *J. Colloid & Interface Sci.* 121 (1988) 241-253.
- [260] T.J. Halthur, U.M. Elofsson, Multilayers of charged polypeptides as studied by in situ ellipsometry and quartz crystal microbalance with dissipation, *Langmuir* 20 (2004) 1739-1745.
- [261] A.O. Lundgren, F. Björefors, L.G.M. Olofsson, H. Elwing, Self-arrangement among charge-stabilized gold nanoparticles on a dithiothreitol reactivated octanedithiol monolayer, *Nano lett.* 8 (2008) 3989-3992.
- [262] J. Lyklema, *Fundamentals of Interface and Colloid Science*, Academic Press, London, 2001.
- [263] A. Lindgren, L. Gorton, T. Ruzgas, U. Baminger, D. Haltrich, M. Schülein, Direct electron transfer of cellobiose dehydrogenase from various biological origins at gold and graphite electrodes, *J. Electroanal. Chem.* 496 (2001) 76-81.
- [264] P. Bingen, G. Wang, N.F. Steinmetz, M. Rodahl, R.P. Richter, Solvation effects in the quartz crystal microbalance with dissipation monitoring response to biomolecular adsorption. A phenomenological approach, *Anal. Chem.* 80 (2008) 8880-8890.

[265] P.E. Laibinis, M.A. Fox, J.P. Folkers, G.M. Whitesides, Comparisons of self-assembled monolayers on silver and gold: mixed monolayers derived from HS(CH₂)₂₁X and HS(CH₂)₁₀Y (X, Y = CH₃, CH₂OH) have similar properties, *Langmuir* 7 (1991) 3167-3173.

[266] J.M. Tour, L. Jones, D.L. Pearson, J.J.S. Lamba, T.P. Burgin, G.M. Whitesides, D.L. Allara, A.N. Parikh, S. Atre, Self-assembled monolayers and multilayers of α,ω -dithiols, and thioacetyl-containing adsorbates. Understanding attachments between potential molecular wires and gold surfaces, *J. Am. Chem. Soc.* 117 (1995) 9529-9534.

[267] P. Lamberg, Direct electron coupling of *Humicola insolens* cellobiose dehydrogenase by using structurally similar thiols (Manuscript), (2014).

ACKNOWLEDGMENTS

Finally, I came to my favourite part of the dissertation where I would like to thank to a number of people who helped me throughout this long (but for me it was like a moment!) scientific journey.

First of all, I would like to say many thanks to my Lithuanian and Swedish supervisors - prof. Arūnas Ramanavičius and prof. Tautgirdas Ruzgas who made this work possible. I would like to thank Arūnas for his encouragement to relate my life with science and for being my first teacher who introduced me to previously unknown (bio)electrochemistry word. I cannot express myself how much grateful I feel to Tautgirdas for his help in both science and life. Dear Tautgirdas, thank you for all your patience and time devoted to answer all my questions; your door was always open to me. You are the best mentor one can imagine! Also, I feel thankful for your constant encouragement and support, and for a possibility to spend almost three years in a beautiful Scandinavian country – Sweden where I have experienced lots of new things and probably one of the best moments in my life.

I would also like to thank prof. Thomas Arnebrant aka *my scientific grandpa* (since a *scientific daddy* is Taut) and my summer supervisor prof. Sergey Shleev for sharing great ideas and giving scientific advice.

I am very thankful to all co-authors for great collaboration. Especially, I would like to thank Yasemin for being the first person whom I started a *career* in scientific article writing with.

I would like to thank habil. dr. Almira Ramanavičienė for giving me clever advice and for wonderful working atmosphere in the office.

I would like to thank my lovely NanoTechnas family at Vilnius University for lots of fun, shared sweets, and many more things. Justyte, Jaroslavas, Asta, Lina, Ieva, Viktor, Jurgis, Anton, Natalija, Urte, Inga, et al., thank you all for the great time we have spent together.

I would like to thank people at the Department of Biomedical Sciences (Malmö University) for creating wonderful working atmosphere and helping me out during my stay in Malmö. So, Anton, Elena, Dmitry, Cathrin, Patrick,

Peter L. (scientific brother), Peter F. (our great conference supervisor), Grzegorz, Marité, Hala, Jildiz, Jonas, Anna R., Anna H., Eva N., Javier, Sebastian, Johan, Vitaly, Zoltan, Yana, Magnus, Alejandro thanks a lot again.

There are a few Lithuanian people I met in Malmö. I would like to thank them for chatting with me in Lithuanian, especially at the moments I was feeling homesick. So, Marija, Marius, Aušra, Jekaterina, Laura Ad., Laura Ab., thank you buddies aka *Lithuanian mafia!*

My separate thanks goes to my wonderful friend (aka German sister) Gesche for a lot of great time in Malmö while having interesting chats at lunch time, learning Swedish, travelling around, and many more things we were doing together during my stay in Malmö.

Dear Alayna, a creative and beautiful fashion girl, thank you a lot for your care and always relaxed atmosphere while staying at your apartment in Malmö! This let me feel like I was at home.

I am very grateful to Aušra Dapšienė not only for all her help with the English language but also for being a *person-diamond* so rarely encountered in my life.

Lithuanian Government, Erasmus study programme, Lithuanian and Swedish Scientific Councils, as well as Swedish Institute for financial support are acknowledged.

Last but not least, I would like to say special thanks to my dear family for making me constantly feel I was unconditionally loved and supported even though most of the time I spent behind the other side of the Baltic Sea. I cannot express my gratitude and love for you in words. *Ačiū už jūsų nuolatinę paramą, kantrybę ir supratimą!* Thus, I dedicate the thesis to my family and, especially, to little Kasparas for being an extraordinary optimist and inspirer. Dear Kasparas, yet being a small boy, you have shown me one should never give up in any situation!